

**SYNTHESIS AND CORROSION
BEHAVIOR OF NANOCRYSTALLINE
Fe-Cr ALLOYS**

THESIS

Submitted by

Rajeev Kumar Gupta

For the award of the degree of

Doctor of Philosophy

**Department of Mechanical and Aerospace
Engineering**

Monash University, Clayton, VIC-3800

2010

*Dedicated to my
Parents*

Declaration

This thesis contains no material which has been previously accepted for the award of any other degree or diploma in any University or Institute, and, to the best of my knowledge and belief this thesis contains no material previously published or written by any other person, except where due reference is made in next.

Rajeev Kumar Gupta

Copyright Notices

Notice 1

Under the Copyright Act 1968, this thesis must be used only under the normal conditions of scholarly fair dealing. In particular no results or conclusions should be extracted from it, nor should it be copied or closely paraphrased in whole or in part without the written consent of the author. Proper written acknowledgement should be made for any assistance obtained from this thesis.

Notice 2

I certify that I have made all reasonable efforts to secure copyright permissions for third-party content included in this thesis and have not knowingly added copyright content to my work without the owner's permission.

Rajeev Kumar Gupta

ACKNOWLEDGEMENTS

I am extremely grateful to record my acknowledgement to my supervisor Associate Professor R.K. Singh Raman for providing with an opportunity to work with him on this project and for guiding me throughout my work. I am most thankful to him: for his confidence in me and providing me with all the research facilities and for all his support.

I would like to thank Professor Carl C. Koch, Department of Metallurgical and Materials Engineering, North Carolina State University, USA for permitting me to use the facilities of his research laboratory and for his support to carry out my experimental work effectively. The support and guidance of Professor R.O. Scattergood, Department of Metallurgical and Materials Engineering, North Carolina State University, USA is highly appreciated. I would like to thank Prof. B.S. Murty, Department of Metallurgical and Materials Engineering, Indian Institute of Technology-Madras, India for permitting me to use the TEM facility in his research laboratory.

I would like to thank Australian Nuclear Science and Technology Organization (ANSTO) for providing me Secondary Ion Mass Spectrometry (SIMS) analysis facility. I highly appreciate the support that Mr. Armand has provided me in carrying out SIMS work.

I would like to thank Dr. Robert Jones of La Trobe University for his assistance and support in surface analysis using X-ray photoelectron spectroscopy (XPS).

The help rendered by my friend Kris Darling during my stay in North Carolina State University, USA is highly appreciated. I am thankful to him for creating such a wonderful friendly working environment. I really enjoyed the technical discussions with him.

I would like to thank department of Mechanical and Aerospace Engineering for providing me all the research facilities, infrastructure and scholarships to cover my tuition fee and living expenses.

Financial supports from Australian Institute of Nuclear Science and Engineering (AINSE) for carrying out SIMS analysis and Australian Research Network for Advanced Materials (ARNAM) for overseas travel grant are highly appreciated.

The research work reported here was supported by Australia Research Council under discovery grant.

I want to thank all my friends in Melbourne and overseas for being there for me in different aspects of my life. This includes: Vera, Dr. Bobby, Abhishek, Sarvesh, Parama, Dr. Kumar, Dr. Ravi, Dr. Sudhakar, Dr. Venu, Udaia, Sreenivasan, Richa and Tarun. Thanks to Abhishek for being part during long working hours and all discussions in the early days of PhD.

My sincere thanks to my best friend Rashmi for her constant support and trust. My special thanks to my sisters, brothers and all family members for their love, understanding and support. Lastly, and most importantly, I wish to thank my parents. They are whom I admire most for making me persistent, honest, and most importantly a human being.

ABSTRACT

Nanocrystalline (nc) materials, a single or multi-phase polycrystalline solids with a grain size of a few nanometers, typically less than 100 nm have attracted considerable attention of research community. However, investigation of corrosion/oxidation resistance of these materials has attracted limited research attention. Motivation of the current study is to understand the effect of nanocrystalline structure on the corrosion/oxidation resistance and to validate the hypothesis that passivity in the Fe-Cr based alloys can be achieved at lower Cr content if the grain size is reduced to the nano level. However, to investigate the oxidation/corrosion resistance bulk samples of nc materials are required and preparation of bulk samples is not a trivial task. Current study presents a technique to prepare consolidated bulk samples of Fe-Cr based nc materials after a systematic study of grain growth and mechanical (hardness) behavior of nc Fe-10Cr alloys.

Oxidation resistance of nc Fe-Cr alloys is compared with that of microcrystalline (mc) Fe-Cr alloys at various temperatures for a time period of up to 52 hours. Nanocrystalline Fe-Cr alloys showed considerably greater oxidation resistance than the mc alloys of the same compositions. This study presents novel results to prove that it is possible to develop a protective layer of chromium oxide at only 10 wt% chromium during oxidation of a nc Fe-Cr alloy. Thus the thesis provides evidence to validate the hypothesis that nc structure can confer considerable oxidation/corrosion resistance at much lower chromium contents (as compared to 18-20 wt% chromium in the common mc Fe-Cr alloys). Oxidation resistance of discs of nc and mc alloys was compared by subjecting them to oxidation in air, and post-oxidation characterization of the oxide scales by secondary ion mass spectrometry (SIMS). The thesis also presents a theoretical treatment to arrive at the minimum chromium content required for establishing a protective layer of chromium oxide in an Fe-Cr alloy of a given nanometric grain size.

The electrochemical corrosion of nc and mc Fe-Cr alloys prepared by high energy ball milling (followed by pre-annealing, compaction and sintering) was investigated at room temperature in various solutions using potentiodynamic polarization tests. Nanocrystalline Fe-Cr alloys have shown improved corrosion resistance over their mc counterparts as characterized by passivation potential, critical current density and passive current density. Interestingly passivation is achieved at comparatively lower potential in nc form of alloys. Compositional characterization of passive films carried out by X-ray photoelectron spectroscopy (XPS) have shown higher Cr content in the passive film of nc form of the alloys than that of their mc counterparts. Based on the XPS, polarization results and theoretical understanding, possible mechanisms for the observed enhancement in the corrosion resistance of the nc Fe-Cr alloys are suggested.

Keywords: Nanocrystalline, Fe-Cr alloys, High temperature corrosion resistance, corrosion, Electrochemistry, Ball milling, consolidation, Grain growth

Table of Contents

	Page
Acknowledgements	<i>i</i>
Abstract	<i>iii</i>
List of Tables	<i>viii</i>
List of Figures	<i>ix</i>
CHAPTER 1: INTRODUCTION	1
CHAPTER 2: LITERATURE REVIEW	3
2.1 Structure of nc-Fe and Fe-based materials	6
2.1.1 Grains and Grain boundaries	6
2.1.2 Composition of crystalline and intercrystalline region	9
2.1.3 Presence of dislocations	13
2.1.4 Nanocrystalline structure and phase change in nc vis-à-vis mc iron	14
2.2 Synthesis of Nanocrystalline Iron and Iron based alloys	16
2.2.1 Pulsed electrodeposition	18
2.2.2 Pulse Plasma Method	19
2.2.3 Chemical vapour condensation	20
2.2.4 Sputtering	20
2.2.5 Inert gas condensation	21
2.2.6 High Energy Ball milling	22
2.3 Consolidation of nc-Fe and Fe based alloys	27
2.3.1 Compaction under high pressure	28
2.3.2 Solid state sintering	29
2.3.3 Compaction at elevated temperature and high uniaxial pressure (Hot compaction)	30
2.3.4 Hot isostatic pressing (HIP)	31
2.3.5 In situ consolidation	32
2.4 Mechanical behaviour of nanocrystalline Fe and Fe based alloys	33
2.4.1 Yield Stress and Validity of Hall-Petch Relationship	35
2.4.2 Nanocrystalline Fe and Fe based alloys under tension and compression	38
2.5 Grain growth in nanocrystalline Fe and Fe based alloys	40
2.6 Electrochemical corrosion resistance of nanocrystalline materials	46
2.6.1 Factors affecting the corrosion resistance in nanocrystalline materials	47
2.6.2 Corrosion in Fe and Fe based Nanocrystalline materials	53
2.7 Role of grain size in oxidation resistance of Fe-Cr alloys	57
2.7.1 Inferior oxidation resistance caused by nanocrystalline structure	58
2.7.2 Improved oxidation resistance caused by the nanocrystalline structure	59
2.8 Nanocrystalline Fe based alloys	62
2.8.1 Nanocrystalline Fe-Cr alloys	62
2.8.2 Nanocrystalline Fe-Ni alloys	64

2.8.3 Nanocrystalline Fe-Cr-Ni alloys	67
2.9 Problems identified	69
CHAPTER 3 OBJECTIVES AND SCOPE	71
CHAPTER 4 EXPERIMENTAL DETAILS	74
4.1 MATERIALS	74
4.2 HIGH ENERGY BALL MILLING	75
4.2.1 Planetary Ball Mill	75
4.2.2 Shaker ball mill	76
4.3 Annealing of the ball milled powder	77
4.4 COMPACTION AND SINTERING	77
4.5 CHARACTERIZATION OF NANOCRYSTALLINE ALLOYS	78
4.5.1 X-ray diffraction analysis	78
4.5.2 Transmission electron microscopy (TEM)	80
4.6 DENSITY MEASUREMENT	80
4.7 HARDNESS TESTING	81
4.8 OXIDATION TEST	81
4.9 ELECTROCHEMICAL CORROSION TESTING	82
4.10 Secondary Ion Mass Spectrometry (SIMS)	83
4.10.1 SIMS instrument	83
4.10.2 Capabilities of SIMS instrument used in the present study	84
4.11 X-ray photoelectron spectroscopy (XPS)	85
CHAPTER 5: SYNTHESSES AND CHARACTERIZATION OF TEST ALLOYS	87
5.1 Introduction	87
5.2 Attempts to consolidate ball milled nanocrystalline alloys and challenges	88
5.3 Possible reasons for failure of initial attempts to consolidate the material and possible solutions	91
5.4 Grain growth behavior	92
5.4.1 Grain growth behavior of ball milled Fe ₁₀ Cr alloy	92
5.4.2 Grain growth behavior of ball milled Fe ₂₀ Cr alloy	96
5.5 Compaction	97
5.6 Preparation of Microcrystalline alloys	99
5.7 TEM characterization of test specimens	99
5.8 Conclusions	102
CHAPTER:6 OXIDATION RESISTANCE OF NANOCRYSTALLINE vis-à-vis MICROCRYSTALLINE Fe-Cr ALLOYS	103

6.1 Introduction	103
6.2 Results	105
6.2.1 Weight Gain Vs Time Plots and Colour Evolution during oxidation	105
6.2.2 Depth Profiles of Oxide Scales by Secondary Ion Mass Spectrometry (SIMS)	112
6.4 DISCUSSION	122
6.4.1 SIMS investigations and co-relation with kinetic curves	122
6.4.2 Correlation of Colour Evolution and Composition of Oxide Scales	125
6.4.3 Critical grain size and Cr content for protective Cr ₂ O ₃ layer formation	127
6.4.4 Possible mechanisms for the improved oxidation behavior of nanocrystalline alloys	132
6.5 Conclusions	134
CHAPTER 7 ELECTROCHEMICAL CORROSION BEHAVIOR of NANOCRYSTALLINE vis- à-vis MICROCRYSTALLINE Fe-Cr ALLOYS	135
7.1 INTRODUCTION	135
7.2 ELECTROCHEMICAL CORROSION BEHAVIOR IN 0.5 M H₂SO₄ SOLUTION	138
7.2.1 Potentiodynamic polarization tests	138
7.2.2 Surface characterization using XPS after electrochemical tests	141
7.3 ELECTROCHEMICAL CORROSION BEHAVIOR IN 0.05 M H₂SO₄ SOLUTION	148
7.3.1 Potentiodynamic Polarization Tests	148
7.3.2 Surface studies using SIMS after electrochemical tests	150
7.3.3 Surface studies using XPS after electrochemical tests	152
7.4 CORROSION RESISTANCE IN THE PRESENCE OF CHLORIDE IONS	155
7.4.1 Potentiodynamic Polarization Tests	155
7.4.2 Surface studies using XPS after electrochemical tests	157
7.4.3 Surface studies using SEM after electrochemical tests	159
7.5 Discussion	160
7.5.1 Value of the corrosion potential (E _{corr})	160
7.5.2 Improved corrosion resistance of nanocrystalline form of the alloys	161
7.5.3 Improved resistance of nanocrystalline alloys in the presence of chloride ions	163
7.6 conclusions	164
Chapter 8 Summary and Future work	165
References	168
Appendix A: Hardness of nanocrystalline Fe-Cr alloys	178
Appendix B: Oxidation Kinetics	180
Appendix C: Reproducibility of electrochemical corrosion data	183
Appendix D: Attempts at in-situ consolidation	186

List of Tables

	Page
Table 2.1 Pressure hysteresis of $\alpha \rightarrow \epsilon$ transformation [73]-----	15
Table 2.2 various techniques to synthesis nanocrystalline iron-----	17
Table 2.3: Consolidation of nc –Fe (hot compaction)-----	32
Table 2.3: Diffusion Coefficients of Cr in nanocrystalline and microcrystalline Fe, in comparison with the lattice and grain boundary (GB) diffusivities-----	48
Table 4.1 Properties of Fe and Cr -----	75
Table 4.2 Process variables used in the planetary ball mill -----	76
Table 4.3 Process variables used in the shaker mill-----	77
Table 4.4 Capabilities of Cameca ims 5f SIMS instrument -----	85
Table 5.1 Grain size and density of nanocrystalline Fe-10%Cr and Fe-20%Cr alloys after different processing steps!-----	99
Table 6.1 Diffusion coefficients of Cr in iron [382,383]-----	131
Table 7.1 Electrochemical corrosion parameters of nanocrystalline (nc) Fe-10Cr, microcrystalline (mc) Fe-10Cr, nanocrystalline Fe-20Cr and microcrystalline Fe-20Cr alloys in 0.5M H ₂ SO ₄ solution. Reported data, E _{corr} : corrosion potential, E _{pp} : Potential where passivation starts, E _b : Potential where trans-passive region starts, and i _{crit} : critical current density, the averages of several experimental results as shown in the Figure 2 of Appendix-C, and error standard deviations are shown in the brackets. -----	140
Table 7.2 Cr content expressed as Cr (Cr/(Fe+Cr)) in the passive film of various alloys -----	143
Table 7.3 Binding energies (eV) for the Fe 2p _{3/2} , Cr 2p _{3/2} and O1s levels -----	145
Table 7.4 Electrochemical data from anodic polarization tests of nc Fe-20Cr and mc Fe-20Cr alloys in 0.05M H ₂ SO ₄ solution. Reported data, E _{corr} : corrosion potential, E _{pp} Potential where passivation starts, E _b : Potential where trans-passive region starts, i _{crit} : critical current density, is average of a number of experimental results as shown in the Appnedix-C, Figure 4 and error shown in the brackets is standard deviation. -----	150
Table 7.5 Atomic ratio of Cr (Cr/(Fe+Cr)) in the passive film of nanocryatlline (nc) and (mc) Fe-20Cr alloy in 0.05M H ₂ SO ₄ solution-----	151
Table 7.6 Electrochemical data from anodic polarization tests of nc Fe-20Cr and mc Fe-20Cr alloys in 0.05M H ₂ SO ₄ +0.5M NaCl solutions. Reported data, E _{corr} : corrosion potential, E _{pp} : Potential where passivation starts, E _b : Potential where trans-passive region starts, i _{crit} : critical current density, are the averages of a number of experiments as shown in Figure 5 of Appendix C, and standard deviations of the data are shown in the bracket. -----	157
Table 7.7 Cr content as expressed as Cr (Cr/(Fe+Cr)) in the passive film of various alloy in 0.05M H ₂ SO ₄ +0.5M NaCl solution -----	159
Table 1 (Appendix A) Microhardness of nanocrystalline and microcrystalline Fe-10 Cr and Fe-20Cr alloy -----	178
Table 1 (Appendix C) Parabolic oxidation rate constants (k _p) values in g ² cm ⁻⁴ s ⁻¹ -----	182

List of Figures

	Page
Fig. 2.1 Two-dimensional model of a nanostructured material. The atoms in the centers of the crystals are indicated in black. The ones in the boundary core regions are represented as open circles [6, 50].....	9
Fig. 2.2 Schematic representation of the three-dimensional model used to evaluate the volume fractions of the microstructural elements. Shown figure is a cross-sectional view of the intersection of three adjoining tetrakaidecahedra (along a polyhedral edge), where the triple junction is considered a triangular prism extending into the page. Shaded regions represent the considered intercrystalline volumes.	12
Fig. 2.3 The effect of grain size (d) on calculated volume fractions (eqns. 2,3 and 4) for intercrystalline regions, grain boundaries, and triple junctions, assuming a grain boundary thickness (Δ) of 1 nm. [51].....	12
Fig. 2.4 Interplanar d spacing of n -Fe as a function of pressure for quasihydrostatic compression. The closed symbols indicate data taken upon compression while the open symbols represent data taken upon decompression. The solid lines are guides [72].	16
Fig. 2.5 Dependence of Fe nanocomposite particle size on decomposition temperature of $\text{Fe}(\text{CO})_5$ [118].....	20
Fig. 2.6 Schematic of inert gas condensation apparatus [6].....	21
Fig. 2.7 Schematic depicting the ball motion inside the planetary ball mill [131].....	22
Fig. 2.8 Kinetics of grain refinement: high energy ball milling. Grain size estimated from X-ray line broadening for Ru and AlRu.	24
Fig. 2.9 The stored enthalpy ΔH , the GBs enthalpy release ΔE_{GBs} and the elastic energy release of dislocations ΔE_{Ds} , as well as the GB enthalpy release per area $\Delta \gamma_{\text{GBs}}$ against the milling time [37].....	24
Fig. 2.10 Lattice strain vs. reciprocal grain size for bcc, hcp and fcc metals [133].....	24
Fig. 2.11 minimum grain size for nc elements vs. their melting temperatures [142].....	25
Fig. 2.12 Powder morphology evolution of $\text{Fe}_{50}\text{Cr}_{50}$ during MA process of a) 7 mn, b) 45 mn, c) 5h. [147].....	26
Fig. 2.13 Schematic representation of grain refinement mechanism during ball milling [154].....	27
Fig. 2.14 Schematic representation of Hot uniaxial press, showing different components: tungsten carbide die (A), punch (B), heating wires (C), powder sample (D), wedge (E), furnace insulation (F) and pressure (P).	31
Fig. 2.15 Variation of hardness with grain size	34
Fig. 2.16 Hall Petch relationship for Fe powders	36
Fig. 2.17 Stress/strain response of nc-Fe from powders with different milling time and grain size. The strain rate is 0.0001/s.....	40
Fig. 2.18 Grain growth with temperature	42
Fig. 2.19 Schematic diagram showing grain interior and boundaries as cathodic and anodic sites, respectively.....	49
Fig. 2.20 Potentiodynamic polarization plots of the nanocrystalline (NC) coating and the bulk steel (microcrystalline) in (a) Na_2SO_4 and (b) NaCl solution [312]	56
Fig. 2.21 Polarization curves of the twin layer, nanocrystalline surface and microcrystalline layer [263].....	56
Fig. 2.22 SEM morphologies of the samples in solution of 0.05M H_2SO_4 + 0.25M Na_2SO_4 at an anodic potential of about 0.9V (vs. SCE), the surface layer of the as-received microcrystalline sample (a), the nanocrystalline layer (b) [263].....	57

Fig. 2.23 Fe-Cr Phase Diagram[345].....	63
Fig. 2.24 Fe-Ni Phase Diagram[344].....	65
Fig. 2.25 Phase boundaries for Fe–Ni alloys processed by different methods: equilibrium, evaporation, sputtering, ball milling at low intensity and ball milling at high intensity [354].....	65
Fig. 2.26 Schematic of phase transformation during mechanical alloying of Fe-Ni powders [356].....	67
Fig. 2.27 The concentration range of stability of Ferrite and Austenite in Fe-Cr-Ni alloys [363, 364].....	68
Fig. 4.1 Schematic setup for a three electrode cell.....	82
Fig. 5.1 Reduction of grain size with the milling time.....	89
Fig. 5.2 Typical XRD peak profiles of ball milled Fe-Cr alloys.....	90
Fig.5.3 XRD profile of ball-milled nanocrystalline Fe-10Cr alloy annealed at 500°C for different time.....	93
Fig.5.4. XRD profile of ball-milled nanocrystalline Fe-10Cr alloy annealed at 600°C for different time.....	94
Fig.5.5. XRD profile for ball-milled nanocrystalline Fe-10Cr alloy annealed at 700°C for different time.....	94
Fig. 5.6 Grain growth in Fe-10Cr nanocrystalline alloy at: 500°C (a), 600°C (b) and 700°C (c). d, e and f represent grain growth data for pure Fe at 450°C, 530°C and 600°C, as reported by Malow et al [147].....	95
Fig. 5.7 Temperature dependence of grain size of nanocrystalline Fe-10Cr alloy annealed for 30min at different temperatures.....	95
Fig.5.8 XRD profile for ball-milled nanocrystalline Fe-20Cr alloy annealed at 600°C for different time.....	96
Fig. 5.9 Grain growth in nanocrystalline Fe-10Cr and Fe-20Cr alloys at 600°C.....	97
Fig.5.10 Schematic representation of compaction process. Arrow shown in the red shows the conventional compaction method.....	98
Fig. 5.11 TEM images of nanocrystalline Fe-10Cr alloy pellets (after compaction and sintering): a) Bright filed image, b) dark field image and c) selected area diffraction pattern.....	100
Fig. 5.12 TEM images of nanocrystalline Fe-20Cr alloy pellets (after compaction and sintering): a) Bright filed image, b) dark field image and c) selected area diffraction pattern.....	101
Fig. 5.13 TEM images of microcrystalline Fe-10Cr alloy pellets (after compaction and sintering): a) Bright filed image, b) dark field image, and c) selected area diffraction pattern.....	101
Fig.6.1 Oxidation kinetics of nanocrystalline (nc) and microcrystalline (mc) Fe-10Cr alloys, oxidised at 300°C: (a) weight-gain vs time plots for 3120min (insets showing colour of the oxidised samples after different durations of oxidation), and (b) weight-gain ² with time, suggesting parabolic kinetics for mc alloy but departure from parabolic kinetics for nc alloy. (c) weight-gain ² with time (up to 240 minutes) suggesting parabolic kinetics for both mc and nc alloys.....	107
Fig.6.2 Oxidation kinetics of nanocrystalline (nc) and microcrystalline (mc) Fe-10Cr alloys oxidised at 350°C for 3120min (insets showing colour of the oxidised samples after different durations of oxidation).....	108
Fig.6.3 Oxidation kinetics of nanocrystalline (nc) and microcrystalline (mc) Fe-10Cr alloys oxidised at 400°C for 3120min (insets showing colour of the oxidised samples after different durations of oxidation).....	109
Fig.6.4 Oxidation kinetics of nanocrystalline (nc) and microcrystalline (mc) Fe-20Cr alloys oxidised at 350°C for 3120min (insets showing colour of the oxidised samples after different durations of oxidation).....	111
Fig. 6.5 Comparison of oxidation resistance of nanocrystalline Fe10Cr alloy with that of microcrystalline Fe20Cr alloyl.....	111

Fig.6.6 Representative photographs of the colour of the oxide scales developed on nc and mc Fe-20Cr alloys at different stages of oxidation at 300 and 400°C: (a) nc, 300°C, 30 min, (b) nc, 300°C, 120 min, (c) mc, 300°C, 30 min, (d) mc, 300°C, 120 min, (e) nc, 400°C, 120 min, (f) mc, 400°C, 120 min	112
Fig.6.7 (a) SIMS depth profiles for Cr, O and Fe in the oxide scales developed during oxidation at 300°C of nanocrystalline (nc) and microcrystalline (mc) Fe-10%Cr and Fe-20Cr alloys oxidized for 30min.....	114
Fig.6.7 (b) SIMS depth profiles for Cr, O and Fe in the oxide scales developed during oxidation at 300°C of nanocrystalline (nc) and microcrystalline (mc) Fe-10%Cr and Fe-20Cr alloys oxidized for 120min.....	115
Fig.6.7 (c) SIMS depth profiles for Cr, O and Fe in the oxide scales developed during oxidation at 300°C of nanocrystalline (nc) and microcrystalline (mc) Fe-10%Cr alloys oxidized for 3120min	116
Fig.6.8 (a) SIMS depth profiles for Cr, O and Fe in the oxide scales developed during oxidation at 350°C of nanocrystalline (nc) and microcrystalline (mc) Fe-10%Cr and Fe-20Cr alloys oxidized for 30min.....	117
Fig.6.8 (b) SIMS depth profiles for Cr, O and Fe in the oxide scales developed during oxidation at 350°C of nanocrystalline (nc) and microcrystalline (mc) Fe-10%Cr and Fe-20Cr alloys oxidized for 120min.....	118
Fig.6.8 (c) SIMS depth profiles for Cr, O and Fe in the oxide scales developed during oxidation at 350°C of nanocrystalline (nc) and microcrystalline (mc) Fe-10%Cr and Fe-20Cr alloys oxidized for 3120m n.....	119
Fig.6.9 (a) SIMS depth profiles for Cr, O and Fe in the oxide scales developed during oxidation at 400°C of nanocrystalline (nc) and microcrystalline (mc) Fe-10%Cr and Fe-20Cr alloys oxidized for 120m n.....	120
Fig.6.9 (b) SIMS depth profiles for Cr, O and Fe in the oxide scales developed during oxidation at 400°C of nanocrystalline (nc) and microcrystalline (mc) Fe-10%Cr alloys oxidized for 3120min	121
Fig.6.10 Plots of the ratio of Cr required for transition from internal-external oxidation for alloys of grain sizes, d and $1.5\mu\text{m}$ against the alloy grain size, d (Plots generated using Equation (9) and using typical data of D_{gb} and D_b from the literature [381,382], $\delta=1\text{nm}$	131
Fig.6.11 SEM micrographs of nc and mc Fe10Cr alloys oxidized at 300C/52hours: (a) nanocrystalline alloy, (b) microcrystalline alloy	133
Fig. 7.1 Typical plots for change in open circuit potential with time for nanocrystalline (nc) and microcrystalline (mc) Fe-10Cr and Fe-20Cr alloys in 0.5M H ₂ SO ₄ solution. (Reproducibility of these results is presented in Appendix-C, Figure 1).....	139
Fig. 7.2 Cathodic and anodic polarization curves of nanocrystalline (nc) and microcrystalline (mc) Fe-10Cr and Fe-20Cr alloys in 0.5M H ₂ SO ₄ solution. Cathodic and anodic polarization curves were obtained separately by polarizing working electrode in negative and positive direction (with respect to OCP) respectively. (Reproducibility of these results is presented in the Appendix-C, Figure 2).....	140
Fig. 7.3 Potentiostatic polarization curves: nc Fe-10Cr, mc Fe-10Cr, nc Fe-20Cr and mc Fe-20Cr alloys were polarized at 775 mV, 1400 mV, -50 mV and 200 mV respectively (for 30 minutes)	141
Fig.7.4 Typical XPS survey scans of the nc Fe-10Cr, mc Fe-10Cr, nc Fe-20Cr and mc Fe-20Cr alloys after potentiostatic polarizations. nc Fe-10Cr, mc Fe-10Cr, nc Fe-20Cr and mc Fe-20Cr alloys were polarized at 775 mV, 1400 mV, -50 mV and 200 mV respectively (for 30 minutes)	142
Fig. 7.5 XPS regional scan of Fe 2p, Cr 2p, O1s for the four alloys: (A) Fe2p nc Fe-20Cr, (B) Cr 2p nc Fe-20Cr, (C) O1s nc Fe-20Cr, (D) Fe2p mc Fe-20Cr, (E) Cr 2p mc Fe-20Cr, (F) O1s mc Fe-20Cr, (G) Fe2p nc Fe-10Cr, (H) Cr 2p nc Fe-10Cr, (I) O1s nc Fe-20Cr, (J) Fe2p mc Fe-10Cr, (K) Cr 2p mc Fe-10Cr and (L) O1s mc Fe-20Cr.....	144
Fig. 7.6 XPS regional scan: curve fitting using casa XPS: (A) Fe 2p _{3/2} nc Fe-20Cr, (B) Cr 2p _{3/2} nc Fe-20Cr, (C) O 1s nc Fe-20Cr, (D) Fe 2p _{3/2} mc Fe-20Cr, (E) Cr 2p _{3/2} mc Fe-20Cr, (F) O 1s mc Fe-20Cr, (G) Fe 2p _{3/2} nc Fe-10Cr, (H) Cr 2p _{3/2} nc Fe-10Cr, (I) O 1s nc Fe-20Cr, (J) Fe 2p _{3/2} mc Fe-10Cr, (K) Cr 2p _{3/2} mc Fe-10Cr, (L) O 1s mc Fe-20Cr.....	147

Fig. 7.7 Typical plots showing change in open circuit potential with time of nc and mc Fe-20Cr alloys in 0.05M H ₂ SO ₄ solution. (Reproducibility of these curves is presented in the Appendix-C, Figure 3).....	149
Fig. 7.8 Anodic polarization curves of nanocrystalline (nc) and microcrystalline (mc) Fe-10Cr and Fe-20Cr alloys in 0.05M H ₂ SO ₄ solution. Anodic polarization curves were obtained separately by polarizing working electrode in positive direction (with respect to OCP. (Reproducibility of these results is presented in the Appendix-C, Figure 4)	149
Fig. 7.9 Potentiostatic polarization curves of nc and mc Fe-20Cr alloys in 0.05M H ₂ SO ₄ at 300 mV. Before potentiostatic polarization, each of the samples was polarized potentiodynamically to 300mV at a scan rate of 0.5 mV/sec.....	150
Fig. 7.10 SIMS depth profile for Cr in corrosion films developed on nanocrystalline (nc) and microcrystalline (mc) Fe-20Cr alloys after potentiostatic polarization tests as described in the section 7.3.2.	151
Fig. 7.11 Typical XPS survey scan spectrum of the nanocrystalline (nc) and microcrystalline (mc) Fe-20Cr alloys after potentiostatic polarization at 300mV/30 minutes in 0.05M H ₂ SO ₄ solution.....	153
Fig. 7.12 XPS regional scan of Fe 2p, Cr 2p, O1s for the four alloys (a) Fe2p nc Fe-20Cr, (b) Cr 2p nc Fe-20Cr, (c) O1s nc Fe-20Cr, (d) Fe2p mc Fe-20Cr, (e) Cr 2p mc Fe-20Cr and (f) O1s mc Fe-20Cr.....	154
Fig. 7.13 XPS regional scan: curve fitting using casa XPS: (a) Fe 2p _{3/2} nc Fe-20Cr, (b) Cr 2p _{3/2} nc Fe-20Cr, (c) O 1s nc Fe-20Cr, (d) Fe 2p _{3/2} mc Fe-20Cr, (e) Cr 2p _{3/2} mc Fe-20Cr and (f) O 1s mc Fe-20Cr.....	155
Fig. 7.14 Anodic polarization curves of nc and mc Fe-20Cr in 0.05M H ₂ SO ₄ +0.5M NaCl solution. (Reproducibility of these results is shown in Appendix-C Figure 5.)	156
Fig. 7.15 Potentiostatic polarization curves of nc and mc Fe-20Cr alloys, at -190 mV in 0.05M H ₂ SO ₄ + 0.5M NaCl solution. Before potentiostatic polarization, each of the samples was polarized potentiodynamically to -190 mV at a scan rate of 0.5 mV/sec.....	157
Fig. 7.16 Typical XPS survey scans spectra of the nc and mc Fe-20Cr alloys after potentiostatic polarization in 0.05M H ₂ SO ₄ + 0.5M NaCl solution at -190 mV.....	159
Fig. 7.17 SEM micrograph of mc and nc Fe-20Cr alloys after potentiodynamic polarization to 50 mV above the pitting potential: (a) microcrystalline Fe20Cr, (b) nanocrystalline Fe-20Cr alloy.	160
Fig.1 (Appendix A) Load Vs displacement curves obtained under different loading conditions	179
Fig. 2 (Appendix A) Variation of hardness with grain size, comparison of current finding with literature	179
Fig. 1 (Appendix B) kinetics of oxidation for mc Fe10Cr alloy (a) weight gain vs oxidation time plot for mc Fe10Cr alloy for a range of temperatures. (b) (Weight gain) ² vs time plot for mc Fe10Cr alloys for a range of temperature	181
Fig. 2 (Appendix B) kinetics of oxidation for nc Fe10Cr alloy (a) weight gain vs oxidation time plot for nc Fe10Cr alloy for a range of temperatures. (b) (Weight gain) ² vs time plot for Fe10Cr alloys for a range of temperature, there are two stages of oxidation distinguished by the unique parabolic rate constant and described as 1 and 2 in the above graph.....	181
Fig. 3(Appendix B) kinetics of oxidation for nc and mc Fe20Cr alloy (a) weight gain vs oxidation time plot for nc and Fe20Cr alloy for a range of temperatures. (b) (Weight gain) ² vs time plot for nc and mc Fe20Cr alloys for a range of temperature, there are two stages of oxidation distinguished by the parabolic rate constant and described as 1 and 2 in the above graph.....	182
Fig. 1 (Appendix C) Reproducibility tests in 0.5M H ₂ SO ₄ solution for OCP of: A) nc Fe20Cr, B) mc Fe20Cr, C) nc Fe10Cr and D) mc Fe10Cr.....	183

Fig. 2 (Appendix C) Reproducibility tests (potentiodynamic polarization) in 0.5M H ₂ SO ₄ solution: A) nc Fe ₂₀ Cr, B) mc Fe ₂₀ Cr, C) nc Fe ₁₀ Cr and D) mc Fe ₁₀ Cr	184
Fig. 3 (Appendix C) Reproducibility tests in 0.05M H ₂ SO ₄ solution for OCP of: A) nc Fe ₂₀ Cr, B) mc Fe ₂₀ Cr	184
Fig. 4 (Appendix C) Reproducibility tests (potentiodynamic polarization) in 0.05M H ₂ SO ₄ solution: A) nc Fe ₂₀ Cr, B) mc Fe ₂₀ Cr.....	185
Fig. 5 (Appendix C) Reproducibility tests (potentiodynamic polarization) in 0.05M H ₂ SO ₄ + 0.5 NaCl solution: A) nc Fe ₂₀ Cr and B) mc Fe ₂₀ Cr.....	185
Fig.1a (Appendix D) In-situ consolidated nc-Fe-20Cr-10Ni	187
Fig. 1b (Appendix D) After applying load of 12 tons	187
Fig.2 (Appendix D) TEM images of in-situ consolidated Fe ₂₀ Cr ₁₀ Ni alloy a) Bright filed image, b) dark field image, c) dark field image of other region at higher magnification and d) selected area diffraction pattern.....	187

CHAPTER 1

INTRODUCTION

The stainless steel is widely used in applications such as cookware, cutlery, hardware, surgical instruments, major appliances, industrial equipment, and as an automotive and aerospace structural alloy and construction material in large buildings and in making jewellery and watches, for high temperature application. The wide use of stainless steel is because of its excellent resistance to oxidation/electrochemical corrosion. In stainless steels chromium is the main alloying element which is a reactive element. However, chromium and its alloys passivate and exhibit excellent resistance to many environments. Corrosion resistance of stainless steel is because of the presence of Cr on the interface of environment, which forms a passive layer of chromium oxide at the interface and prevents corrosion [1,2]. Higher Cr contents is necessary so that a passive film of chromium oxide forms which prevents further surface corrosion and also blocks corrosion from spreading into the metal's internal structure.

Recently, nanostructured materials with a grain size below 100 nm are gaining importance due to their enhanced mechanical, electrical, optical and magnetic properties. It has been established that passivation of stainless steel depends largely upon the Cr content at metal/environment interface where oxidation or electrochemical corrosion is taking place [1,2]. Owing to unique structure of nanocrystalline structure, the diffusivity of Cr in Fe-Cr alloys is found to be considerably higher [3], therefore, it was hypothesized that nanocrystalline Fe-Cr alloys may exhibit passivity to oxidation/ electrochemical corrosion resistance at lower Cr contents. The aim of the present study also includes comparison of oxidization and electrochemical corrosion resistance of nanocrystalline and microcrystalline Fe-Cr alloys prepared by similar processing route. Instead of the possibility of achieving higher resistance to material degradation by reducing the grain size to nanometer size, oxidation/electrochemical corrosion

resistance of these novel materials has attained only a limited attention. Moreover, the reported data on the electrochemical corrosion resistance of nanocrystalline Fe-Cr alloys is limited to thin coating and is not consistent. To the best of author's knowledge oxidation resistance of Fe-Cr alloys has not, yet, been investigated.

This thesis contains a review of literature in the field, which is given in Chapter 2. Chapter 2 describes the structure of nanocrystalline materials and its relation to various properties such as oxidation and electrochemical corrosion resistance. The objectives and scope of the present investigation are presented in Chapter 3. In Chapter 4, the experimental details are provided. Chapters 5, 6 and 7 report the experimental results. Synthesis and characterization of nanocrystalline and microcrystalline test specimens (which is a non-trivial task) are described in the chapter 5. Chapter 6 reports the comparison between the oxidation resistance of nanocrystalline and microcrystalline Fe-Cr alloys, followed by the characterization of oxide layer (using secondary ion mass spectrometry), developed during oxidation. Chapter 6 further confirms the hypothesis that passivity against the oxidation can be achieved at lower Cr content by refining the microstructure to the nano level. Results related to the electrochemical corrosion resistance of nanocrystalline and microcrystalline Fe-Cr alloys are presented in the chapter 7. Nanocrystalline Fe-Cr alloys exhibit improved corrosion resistance over their microcrystalline counterparts; compositional characterization of corrosion film, developed during the electrochemical tests, shows relatively higher Cr enrichment of the passive film, developed on the nanocrystalline test specimen. Finally, all the results are summarized and future work based on the current study is proposed in chapter 8.

CHAPTER 2

LITERATURE REVIEW

Nanocrystalline (nc) materials are single or multi-phase polycrystalline solids with a grain size of a few nanometers, typically less than 100 nm. Materials with microstructural features of nanometric dimensions are referred to in the literature as nanocrystalline materials (a very generic term), nanocrystals, nanostructured materials, nanophase materials, nanometer-sized crystalline solids, or solids with nanometer-sized microstructural features. Nanostructured solids or nanocrystalline materials are, perhaps, the most accurate description. These materials can be zero dimensional (clusters), one dimensional (lamellar), two dimensional (filamentary) or three dimensional (equiaxed particles) [4,5]. Since the grain sizes are so small, a significant volume of the microstructure in nanocrystalline materials is composed of interfaces, mainly grain boundaries, i.e., a large volume fraction of the atoms reside in grain boundaries [6]. Consequently, nanocrystalline materials exhibit properties that are significantly different from and often improved over, their conventional microcrystalline (mc) counterparts. Nanocrystalline materials exhibit increased mechanical strength, enhanced diffusivity, better corrosion resistance (in some nanocrystalline material/environment systems), higher specific heat and electrical resistivity compared to conventional coarse grained counterparts. Therefore, nanocrystalline materials have attracted considerable research interest and the field of nanocrystalline materials has now become a major identifiable activity in materials science and engineering.

Despite the widespread opinion that nanocrystalline materials can only be produced artificially, they are not really new; they were in fact synthesized somewhere in Universe millions of years before our civilization sprang into being, and are detected in the sample of lunar soils [7]. Nanostructures, formed chemically under ambient conditions, are found in natural biological systems and these materials are

hard, strong and tough. Therefore various attempts have been made to mimic nature and to engineer these properties. Early in 1900, it was shown that finer grain size microstructure provides improved mechanical properties such as increased strength and toughness in structural materials. Finer dispersion of precipitates improves the mechanical properties, i.e., GP zones in Cu-Al alloys. These findings kindled research towards the synthesis of fine grain size material.

The synthesis of nanocrystalline material (nc) by Gleiter and co-workers [8-12] in 1980's can be viewed as one of the major breakthroughs in materials research in the past few decades. Gleiter [9] and co-workers have shown that nanocrystalline materials have properties significantly different from those of conventional microcrystalline materials ($>1\mu\text{m}$) or amorphous materials of similar chemical compositions. These results stimulated considerable research in the field of nanocrystalline materials. Various nanocrystalline materials have been synthesized after this.

Nanomaterials Fe and Fe based alloys, discovered first by Yoshizawa, Oguma and Yamauchi in 1988 [13,14], (where they expected that soft magnetic properties of bulk materials could be improved by making the crystal grains fine), are experiencing a rapid development in recent years due to their existing and/or future potential applications in a wide variety of technological areas such as structural, magnetic, corrosion-resistant alloys etc. This chapter is focused on the various aspects related to the synthesis, processing, electrochemical corrosion and oxidation behaviour of iron and iron-based nanocrystalline materials and divided into 8 sections.

The first section is focused on the structure of nanocrystalline materials. Grain and grain boundary structure, presence of defects and phase transformation in nanocrystalline metallic materials particularly, iron and iron-based nanocrystalline materials are also discussed in this section.

The second and third sections deal with the synthesis and consolidation of nanocrystalline Fe and Fe-based materials by various processing routes. Special attention is paid to the high energy ball-milling technique.

The mechanical properties of nanocrystalline materials are reviewed in section four which includes inverse Hall-Petch relationship, grain boundary sliding, grain-boundary diffusion, the triple junction effect, presence of nano-pores and impurities etc. Hardness, tensile and compressive strength of nanocrystalline materials are also discussed briefly in this section.

Presence of large fraction of grain boundaries offers large driving force for grain growth. Therefore, grain growth of nanocrystalline materials at elevated temperature has been an area of great interest. Section five describes the grain growth and related phenomena in nanocrystalline materials.

Electrochemical corrosion resistance of nanocrystalline materials is expected to be significantly different from microcrystalline materials because of higher diffusivity of impurities and alloying elements, and presence of larger fraction of grain boundaries and triple points (which provide more reactive sites). Engineering application of nanocrystalline materials is possible only if they exhibit a minimum level of corrosion resistance in service conditions. Therefore, investigation of corrosion behaviour of a material becomes essential for daily life application. Corrosion resistance of nanocrystalline metallic materials, particularly nanocrystalline Fe and Fe-based alloys is addressed in the section six.

Oxidation resistance of nanocrystalline alloys is described in section seven and is expected to be considerably different from that of microcrystalline materials of similar chemical compositions.

Section eight deals with examples of three important nanocrystalline Fe- based alloys, namely Fe-Cr, Fe-Ni and Fe-Cr-Ni.

2.1 Structure of nc-Fe and Fe-based materials

2.1.1 Grains and Grain boundaries

Nanocrystalline materials possess unusual mechanical, electrical, optical, magnetic and electrochemical (in comparison to their microcrystalline counterparts) properties because of large fraction of grain boundary area. The structure of grain and grain boundaries is crucial in determining the properties of materials, and, therefore, investigations of the properties of nanocrystalline materials have attracted considerable research interest. However, characterization of grain structure is not an easy task because of limitations of traditional experimental techniques. Transmission and scanning electron microscopy, tunneling microscopy, mossbauer spectroscopy, positron-lifetime spectroscopy, extended x-ray-adsorption fine structure (EXFAS), small angle X-ray and neutron diffraction and X-ray texture analysis etc. are the techniques used to investigate the microstructure of nanocrystalline materials. The key question is whether a novel state of matter exists in nanocrystalline materials where a large fraction of atoms reside in grain boundaries. Various opinions regarding the grain structure of nanocrystalline materials are available. However, a few investigations have suggested insignificant changes in grain boundary structure of nanocrystalline materials. The structure and width of grain boundaries in nanocrystalline materials are suggested to be similar to that in coarse-grained materials and the only difference between nano and microcrystalline material is their respective grain sizes [9,15-20]. Molecular dynamic simulations have shown that, the widely-held view of the Rosenchain's [21,22] "amorphous-cement" nature of grain boundaries (in coarse grain materials), holds true in

nanocrystalline materials as well [23]. An investigation of grain boundary diffusivity using radiotracers revealed that the self-diffusivities in nc-Fe are similar to those in conventional grain boundary diffusion which supports the view that the behaviour of grain boundaries in nc-Fe is similar to that of conventional grain boundaries [24].

However, a few investigations on nanocrystalline Fe have demonstrated that the grain boundaries in nanocrystalline Fe differ significantly from the grain boundaries in conventional polycrystalline Fe [25]. Based on X-ray diffraction and mossbauer spectroscopy of nanocrystalline iron (grain size ~ 6 nm, produced by inert gas condensation technique), Birringer et. al. [8] have suggested a “gas-like” structure in the case of nanocrystalline materials. The gas-like structure component may be attributed to the atoms located in the grain boundaries between the crystals. A “frozen-gas-like” structure of grain boundaries in nanocrystalline materials is discussed later which appears plausible given that 50% atoms in such a material are situated in highly distorted and defected environments of the grain boundaries and triple points [9,25]. Thermodynamic properties (specific heat at constant pressure, heat of fusion and stored enthalpy) of ball- milled Fe and other nanocrystalline materials, investigated by Fecht [26] suggest that the grain boundaries’ energy in nanocrystalline materials to be considerably greater than in the case of fully equilibrated grain boundaries in microcrystalline materials. Fecht [27] has described nanocrystalline material as a bimodal material with a grain boundary component and a crystalline component and described a new model to characterize the state of a grain boundary by extending the universal equation of state (EOS) which was developed by Smith et. al. [28-30]. In conventional polycrystalline materials, grain boundary energy, as determined by experiments, as well as static and dynamic simulations, is approximately 1 J/m^2 [31-35], whereas, this value soars to 4 J/m^2 in nanocrystalline materials having boundary-to-volume ratio of 0.15 [27,36,37]. Fecht [27] has termed grain boundaries in nanocrystalline materials as “nano-grain boundaries”. Fecht also showed that nano

grain boundaries inhibit grain growth because these are energetically stable, and suggested that idea of entropy stabilization of nano-grain boundaries at elevated temperature (against coarsening) holds true. This behaviour was also observed experimentally in nanocrystalline Pd [38,39]. Presence of metastable grain boundaries (in nc-Fe, ball- milled for longer period of time) with significantly different thermal properties has been reported by Zhao et al. [40].

Mossbauer spectroscopy reveals the reduced electron density of grain boundary component of nanocrystalline iron [41,42]. The grain boundary thickness measured, using mossbauer spectroscopy, was an order of 1 nm [43,44] . Many researchers have suggested that grain boundaries in nanocrystalline materials are more disordered than those in conventional microcrystalline materials [25,38,45-48]. In a recent study, diffusion coefficient of Cr in nanocrystalline Fe (at 300°C) is found to be around 10^4 times greater than that of grain boundary diffusion coefficient in microcrystalline Fe, which can be attributed to existence of novel grain and/or grain boundary structure in nanocrystalline materials [3].

From the above discussion it seems that the structure of nanocrystalline materials differs significantly from that of the microcrystalline materials. Structure and properties of nanocrystalline materials may also depend on the processing route and characterization techniques [49,50], as difference in the structure reported by various researchers may be because of difference in processing route and techniques used. The structure of nc-materials, in general, can be conceived as of two components: a crystalline component (CC), which is formed by small equiaxed single crystals each with random crystallographic orientations and the intercrystalline component (IC), which is formed by the boundaries between the crystallites (Figures 2.1). The second component is characterized by the reduced atomic density and inter-atomic spacing deviating from those in the perfect crystal lattice (as suggested in gas-

like or frozen-gas-like models, discussed earlier). The IC surrounds the nanometer-sized crystals and forms a network between them. As the grain size reduces, the IC increases and it may even exceed CC. This view is supported by various studies. Gleiter [9] proposed a “hard-sphere” two-dimensional model for nanocrystalline materials (Figure 2.1) which shows a schematic depiction of a nanocrystalline material. In Figure 2.1 the grain-boundary atoms are white and are not clearly associated with crystalline symmetry [9,51].

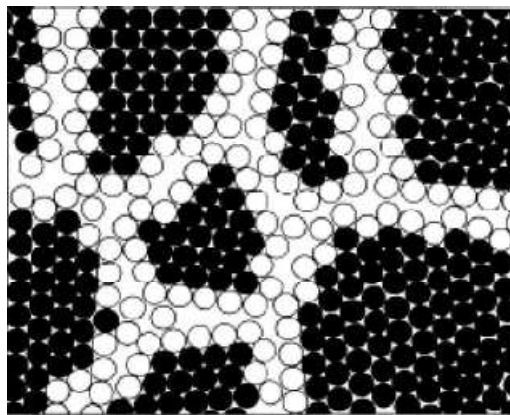


Fig. 2.1 Two-dimensional model of a nanostructured material. The atoms in the centers of the crystals are indicated in black. The ones in the boundary core regions are represented as open circles [9,52]

2.1.2 Composition of crystalline and intercrystalline region

Similar to the above discussion of IC and CC, nanocrystalline materials can be described as the materials with a large volume fraction of grain boundaries, composed of crystalline region and intercrystalline region. Volume fraction of IC and CC regions and their relationship to the grain size is determined. Mutschele and Kichheim [46] have used the following relation to evaluate the volume fraction (C_i) of nanocrystalline materials associated with intercrystalline regions,

$$C_i = 3\Delta/d \quad (1)$$

where, Δ is the average grain boundary thickness and d is the average diameter of the grains and grain size is considered to be cubes. Later, Palumbo et. al. [53] have shown that it is not suitable for

calculations of volume associated with triple junctions and to make it more general they assumed regular tetrakaidecahedron grain shape (as shown in figure 2.2), where the hexagonal faces represent grain boundaries, and edges correspond to triple junctions. The total intercrystalline volume fraction calculated by them is:

$$V_t^{ic} = 1 - \left[\frac{d - \Delta}{d} \right]^3 \quad (2)$$

where, d is the maximum diameter of an inscribed sphere, and the intercrystalline component assessed as an outer 'skin' of the tetrakaidecahedron having a thickness of $\Delta/2$, where Δ is the grain boundary thickness. The grain boundary component can be assessed as hexagonal prisms of thickness, $\Delta/2$, extending from the faces of the inner tetrakaidecahedron which defines the interface between perfect crystal and the interfacial 'skin'. This yields the following relation for grain boundary volume fraction (V_t^{gb}),

$$V_t^{gb} = \left[\frac{3\Delta(d - \Delta)^2}{d^3} \right] \quad (3)$$

The volume fraction associated with triple junctions (V_t^{tl}) is then given by,

$$V_t^{tl} = V_t^{ic} - V_t^{gb} \quad (4)$$

Above equations are valid under conditions where $d > \Delta$.

Using above equations and applying a boundary thickness (Δ) of 1 nm [46,54], the effect of grain size (d), in the range of 2 nm to 1000 nm, on the calculated volume fractions corresponding to intercrystalline regions, grain boundaries, and triple junctions, are shown in Figure 2.3. The total intercrystalline component is shown to be consistent with the previous suggestion [6] of a 20%-50% intercrystalline volume fraction with materials having a grain size less than 10 nm. The intercrystalline component increases from a value of 0.3% at a grain size of 1000 nm, to a maximum value of 87.5% at a 2 nm grain

size. The volume fractions associated with intercrystalline regions and perfect crystal are equivalent (i.e., 50%) at a grain size of ~ 5 nm. In assessing the individual elements of the intercrystalline fraction, it is noted that the triple junction volume fraction displays greater grain size dependence than that of the grain boundaries. In the range 100 nm to 2 nm, the triple junction volume fraction increases by three orders of magnitude, while the grain boundary volume fraction increases by little over one order of magnitude. In the nanocrystals range (i.e., $d \sim 10$ nm), the grain boundary fraction only increases from $\sim 27\%$ at 10 nm, to a maximum value of $\sim 44\%$ at 3 nm. Over the same range of grain sizes, the triple junction fraction increases from $\sim 3\%$ to a value of 50%. It is interesting to note that the grain boundary volume fraction decreases at grain sizes less than 3 nm, while the triple junction fraction continues to increase. The physical significance of this phenomenon is not yet known. As demonstrated in the Figure 2.3, the most significant contribution of triple junctions to bulk properties is expected to occur with materials having grain sizes < 10 nm. It should be noted that the determined triple junction volume fractions may represent a conservative estimate, since these junctions may be better represented as 'tubes' circumscribing the triangular prisms depicted in Fig. 2.2. On the basis of the calculated volume fractions, shown in Figure 2.3, it is apparent that variations in the bulk properties of nanocrystalline materials with grain size in the nanocrystals range (i.e., < 10 nm) are more likely dependent on grain size.

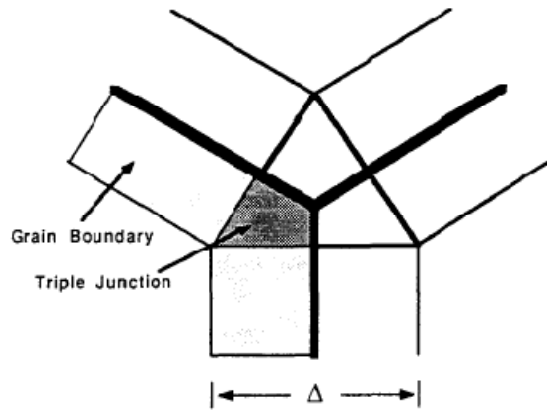


Fig. 2.2 Schematic representation of the three-dimensional model used to evaluate the volume fractions of the microstructural elements. The figure, shown, is a cross-sectional view of the intersection of three adjoining tetrakaidehedra (along a polyhedral edge), where the triple junction is considered a triangular prism extending into the page. Shaded regions represent the considered intercrystalline volumes.

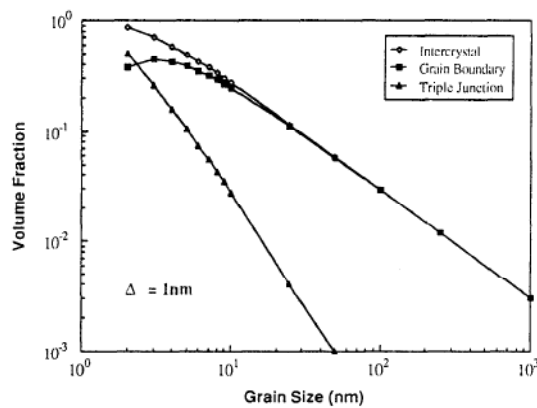


Fig. 2.3 The effect of grain size (d) on calculated volume fractions (eq. ns. 2,3 and 4) for intercrystalline regions, grain boundaries, and triple junctions, assuming a grain boundary thickness (Δ) of 1 nm. [53]

Similar to above model, EXAFS and Mossbauer spectroscopy of ball-milled iron also indicate the two phase structure of nanocrystalline Fe, interfacial region and crystalline phase with a very different atomic arrangement [55]. The interface volume fraction, which is less than 1% after 2 hours of milling, rises to 8.5% after 8 hours of ball-milling and no further increase is observed because crystallites are very near to their ultimate dimensions [55]. Mossbauer spectrum and EXAFS data of ball-milled iron show reduced co-ordination of the atoms located at the interfaces, with respect to bulk iron [55-57].

Similarly, extended x-ray-adsorption fine structure (EXFAS) investigation of nanocrystalline Fe and Pd indicate the large reduction in the atomic coordination number, supporting the idea of a very disordered structure at the interfaces [45,58-61]. Positron-lifetime spectroscopy measurements show a large density of vacancy-like defects in grain boundaries and relatively large effective free volume at the triple junctions arising from misorientation-induced atomic instability of these sites [44]. Elastic relaxation of the interfaces occurs with quite a different parameter than conventional coarse grain size polycrystalline materials [62]. Modelling of thermoplastic properties and structure [63] demonstrates that two phase model is the most appropriate to account for the vibrational density of states and excess energy density in terms of grain boundary parameter. Similar to many other researchers, computer simulation of nanocrystalline iron has shown [64,65] that boundary component in nanocrystalline material is very high and is a strong function of grain size. Boundary component proportion, excess lattice parameter, excess volume, average energy per atom is calculated with respect to the grain size. Interestingly, average energy per atom decreases with the grain size [64].

2.1.3 Presence of dislocations

Presence of dislocations and dislocation activity affects various properties of a material and investigation of nanocrystalline Fe and Fe-based alloys in terms of dislocations is necessary. As grain size is in nano-meter range, dislocation lines tend to be increasingly unstable and can annihilate at grain boundaries under the effect of their own stress fields. The annihilation process is supposed to start below a critical grain size. Consequently nanocrystalline materials may have reduced dislocation density or no dislocations at all. TEM of ball- milled nanocrystalline metal powders has shown absence of dislocations [66]. However, chemical composition of ball- milled powder and milling parameters are not described in this study. On the other hand, microstructure of ball-milled iron powder investigated, using

high resolution X-ray line profile analysis, has shown increased dislocation density in ball-milled nanocrystalline iron [67]. Molecular dynamic studies [68] on nanocrystalline iron shows that the required critical size for dislocation generation is 9 nm and any grain less than 9 nm is dislocation free even after compaction at very high pressures [68]. This result is consistent with the experimental results of the other researchers [69-71] where ball- milled nanocrystalline materials have been found to contain dislocations only if grain size is greater than 10 nm and are dislocation free for grain size values less than 10 nm.

2.1.4 Nanocrystalline structure and phase change in nc vis-à-vis mc iron

As a result of wide range of inter-atomic spacing and reduced density in the IC, the inter-atomic forces in IC are different in comparison to a CC of the same composition. If an external pressure is applied to nc-Fe, the interatomic spacing in IC is expected to be reduced by a greater amount than those in the CC. Trapp et al. [72] studied the relative compressibility of IC and CC using in- situ Mossbauer spectroscopy. Mossbauer spectra of nc-Fe pellets obtained at various pressures suggested an enhancement in compressibility of nc-Fe with pressure. The interfacial region (IC) of reduced atomic density was compressed readily. On annealing, the atomic structure of interfacial region changes to less compressible and probably denser structure. Another interesting observation was that this structural transformation of less dense IC to dense IC on pressure annealing occurred with little or no grain growth.

It is interesting to see how phase diagram of iron changes with grain size, and would be helpful to engineer new properties. It is well established that Fe exhibits three polymorphic phases at atmospheric pressure: BCC α -Fe is stable below 906°C; FCC γ -Fe is stable between 906°C and 1401°C; bcc δ -Fe is stable above 1401°C until melting at 1530°C. The α phase has a Curie temperature of 769°C where the

material changes from a ferromagnetic to a paramagnetic state. Apart from these three polymorphic phases, Takahashi et al. [73] postulated the existence of a hcp ϵ -Fe which is a high pressure phase and exists at pressure above 13 GPa at room temperature. Several investigators have reported that the bcc to hcp transformation in iron occurs over a wide range of pressures and is apparently very sluggish [73,74]. It has also been suggested that the transformation could be martensitic in nature [74]. Studies have been done on bcc to hcp transition of nc-Fe under high pressures. It has been found that the nc-Fe transforms from bcc to hcp at a lower pressure than that required for microcrystalline Fe [75]. On decompression the reverse transformation from hcp to bcc also occurs at a lower pressure. Though, the exact phase boundaries where both bcc and hcp Fe are stable, are not reported but, it is suggested that the hcp ϵ -Fe exists over a wide phase field and the phase field for nc-Fe is still wider. The BCC to HCP transformation pressures of for microcrystalline Fe (mc-Fe) and nanocrystalline Fe are given in Table 2.1 [75]. Chen et al. [74] who have also suggested the $\alpha \rightarrow \epsilon$ transformation of nc-Fe, observed that the hcp ϵ -Fe is stable even at a pressure of 46 GPa. They also reported a decrease in inter atomic spacing with increase in pressure (Figure 2.4).

Table 2.1 Pressure hysteresis of $\alpha \rightarrow \epsilon$ transformation [75]

	Compression Pressure (GPa)	
	mc-Fe	nc-Fe
Start of $\alpha \rightarrow \epsilon$	13	11
Finish of $\alpha \rightarrow \epsilon$	17	14
Start of $\epsilon \rightarrow \alpha$	8	7
Finish of $\epsilon \rightarrow \alpha$	5	1

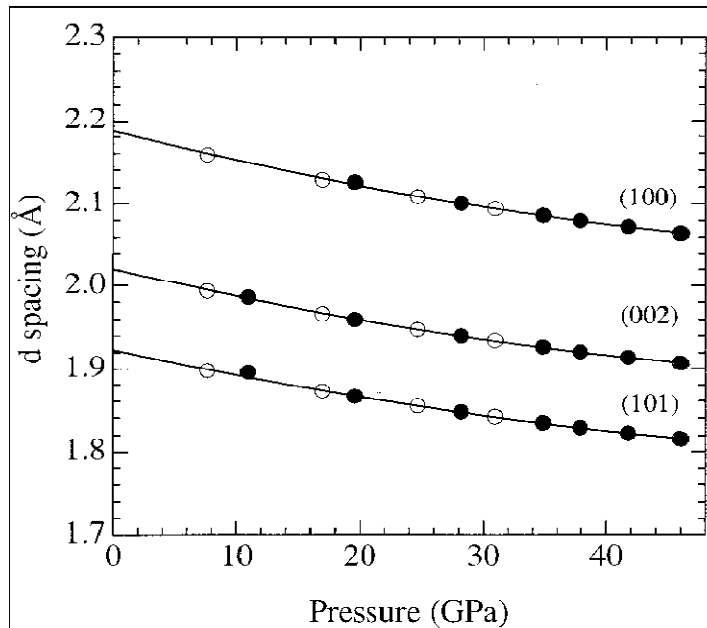


Fig. 2.4 Interplanar d spacing of n -Fe as a function of pressure for quasi hydrostatic compression. The closed symbols indicate data taken upon compression while the open symbols represent data taken upon decompression. The solid lines are guides [74].

2.2 Synthesis of Nanocrystalline Iron and Iron-based alloys

Novel fabrication technologies of nanocrystalline materials are versatile and include a wide range of vapour, liquid and solid state processing routes. Available techniques for the synthesis of nanocrystalline materials via vapour routes range from physical vapour deposition and chemical vapour deposition. The liquid route involves rapid solidification (and/or subsequent recrystallization from amorphous phase) and pulsed electrochemical deposition. The solid state route preparation takes place via severe plastic deformation, mechanical milling and mechanochemical synthesis. Each method has its own advantages.

Table 2.2 outlines the various processing routes and minimum grain size obtained for nc-Fe and Fe-based materials. It can be clearly observed that high energy ball-milling is the most widely used technique to synthesize nc-Fe and a prominent technique for synthesis of nanostructured materials [76,77]. This process is economical and can be easily scaled up for bulk production of nanocrystalline

materials. From Table 2.2, one can also observe that inert gas condensation and pulsed plasma deposition produces material with finer grain size.

Table 2.2 various techniques to synthesize nanocrystalline iron

Technique	Grain Size (nm)	Reference
Pulsed electrodeposition	16	[78,79]
Pulsed plasma deposition	2	[80]
Chemical vapour condensation	10	[81]
Severe plastic deformation (Cold rolled + torsion)	50	[82]
Sputtering	10	[83]
	20	[84]
Inert gas condensation	7	[72]
	5	[85]
	12	[86]
	31	[24]
	14	[87]
High Energy Ball milling	6	[88]
	8	[89]
	6	[90]
	18	[91]
	12	[92-94]
	16	[95]
	11	[96-99]
	6	[100]
	28	[101,102]
	20	[103]
	16	[104]
	20-30	[105]
	11	[106]
	10	[74]

2.2.1 Pulsed electrodeposition

Pulsed electrodeposition (PED) is one of the feasible techniques to synthesize nanocrystalline materials [107]. Apart from nc-Fe, several other nanocrystalline materials such as nano-Ni [108,109], nano-Pd [110], nano-Cu [111], nano-Co[112], nano-Zn [113] have been synthesized by PED technique. The critical nucleation radius, r_c (i.e, grains with $r > r_c$ are stable) in an electrochemical deposition can be obtained by Kelvin equation [114]

$$r_c = \frac{2\gamma V_m}{ze_0|\eta|} \quad \text{--- (5)}$$

where γ is the specific surface energy, V_m is the atomic volume in the crystal, z is the number of elementary charges e_0 , and η the over-voltage.

According to equation (5) the higher voltage results in smaller crystallites. A combination of high voltage and high current also results in high deposition rates. At high deposition rates, concentration of metal cations in the vicinity of the cathode is reduced so much that the process becomes diffusion-controlled. In order to control grain size, one has to apply a pulsed current, with correspondingly short pulse widths (a few milliseconds). In the break between two pulses (several tens of milliseconds), metal cations diffuse, as desired, from the bulk of the electrolyte into the vicinity of the cathode. But, simultaneously on the cathode, due to exchange currents, Ostwald ripening sets in when the larger grains grow at the expense of the smaller ones. To suppress this exchange process, appropriate organic complex formers such as, 3-mercapto-1-propanesulfonic acid, citric acid, citric acid-trisodiumsalt etc. are added to the electrolyte bath which protects nanocrystals during the break. Natter et al. gave a detailed account of PED of nc-Fe[79]. The crystallite size of Fe obtained by PED was about 16nm. Several nanocrystalline alloys and metals have been deposited by pulsed electrodeposition [109,115-119].

2.2.2 Pulse Plasma Method

α -Fe and γ -Fe phases are observed in nc-Fe (grain size of 2 nm), produced by pulsed plasma method [80]. In pulsed plasma method, the metal vapour from which the layer is synthesized is obtained by evaporating the electrode of a material placed in a high current pulse discharge (the pulse duration is typically 100 μ s, the current magnitude is 100 kA). The vapour produced in the form of a plasma pack is accelerated towards the substrate by an electrodynamic force at a velocity of about 10 km/s. Under these conditions, the layer grows from portions of plasma pack. The plasma pack incident, upon the substrate during the growth of the layer, plays a double role. It acts as a pulsed high energy source of heat; it heats up the substrate and a source of the metal vapours from which, the layer nucleates and grows on the substrate. Because of the pulse character of the plasma-substrate interaction ($t < 100 \mu$ s) and the incomparably long pauses between the consecutive plasma pulses (from 1 to several seconds), the heat- state on the substrate can be varied considerably. During the plasma action, the substrate surface and the near-surface region to a depth of the order of several micrometers are heated to a temperature of about 2000K, whereas, the temperature of the substrate, settled as a result of the action of the successive pulses of the plasma packs, is constant and substantially lower. This substrate temperature depends on the energy of the pulse discharge, the repetition frequency of the pulse discharges and the intensity of heat removal from the substrate. The chemical composition of the nc-Fe obtained by this technique is very close to the electrode composition. The nc-Fe obtained at a substrate temperature of 100°C consists of both α -Fe and γ -Fe. The γ -Fe content decreases with increasing substrate temperature, and above 150°C the nc-Fe obtained is completely α -Fe [80]. From these observations, it can be interpreted that the condensation of Fe vapours follows the allotropic transformations of the Fe and results in γ -Fe at high temperature. The transformation of γ -Fe to α -Fe depends on the cooling rates, which, in turn, is a function of substrate temperature. A higher substrate temperature results in lower cooling rates and thus aids in transformation of γ -Fe to α -Fe.

2.2.3 Chemical vapour condensation

Chemical vapour condensation involves synthesis of nanoparticles from organometallic precursors. The process involves controlled decomposition of a liquid precursor such as $\text{Fe}(\text{CO})_5$ and achieved grain size depends on decomposition temperature (Figure 2.5) [120]. A carrier gas (high purity He) is bubbled through the heated precursor which entrains a precursor vapour and passes through the heated furnace in which the precursor pyrolyses and condenses into clusters or particles that impinge upon the rotating chiller, which is cooled by liquid nitrogen. The passivation process is achieved by dosing oxygen before opening the chamber to air. The loose powder is smoothly stripped off the cold finger and stored in air [120,121]. In a modified technique, the pyrolyzed precursor is cooled in an empty chamber (protected with argon) without a chiller, which is maintained at room temperature[81, 122].

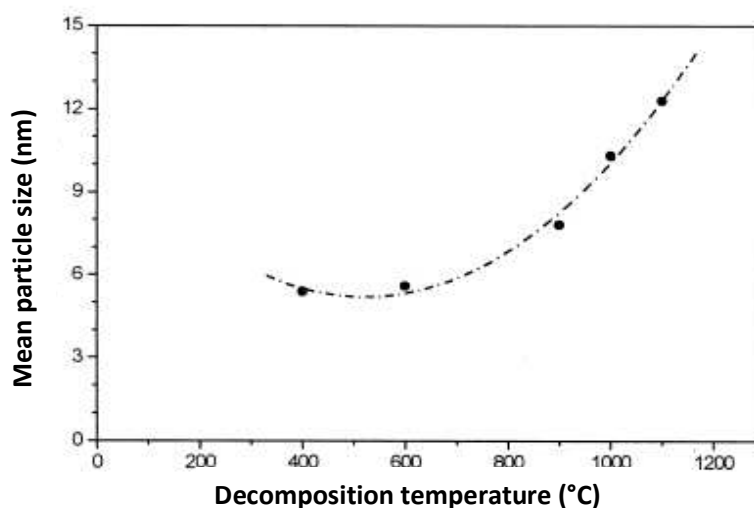


Fig. 2.5 Dependence of Fe nanocomposite particle size on decomposition temperature of $\text{Fe}(\text{CO})_5$ [120]

2.2.4 Sputtering

Sputtering is a vacuum evaporation process which physically removes portions of a coating material called the target, and deposits a thin, firmly bonded film onto an adjacent surface called the substrate. The process occurs by bombarding the surface of the sputtering target with gaseous ions under high voltage acceleration. As these ions collide with the target, atoms or occasionally entire molecules of the

target material are ejected and propelled against the substrate, where they form a very tight bond. The resulting coating is held firmly to the surface by mechanical forces. Hence this technique has been used to deposit thin films of Fe with a grain size of about 20 nm [83,84,123].

2.2.5 Inert gas condensation

Inert gas condensation technique is the one, first envisaged by Glieter [9], to synthesize nanocrystalline materials. A schematic of an ultra-high vacuum apparatus developed for this purpose is illustrated in Figure 2.6 [9]. The particles are produced by a two- step- process (Figure 2.6). The substance (e.g. Fe contained in a refractory metal boat) is evaporated by receptivity heating. The evaporated atoms transfer their thermal energy to the inert gas and condense in the form of small crystals. The crystals are, then, carried by a convective current of inert gas to a liquid-nitrogen, cooled cold finger. Subsequently, the inert gas is removed and the particles are scraped from the cold finger and funnelled into a piston and anvil-like device where they are compacted using high pressures. Cooling or heating of the specimen during compaction is easily possible. The powders become partially sintered during compaction. The nc-Fe produced by this technique exhibits a crystallite size of 5 to 30 nm [72].

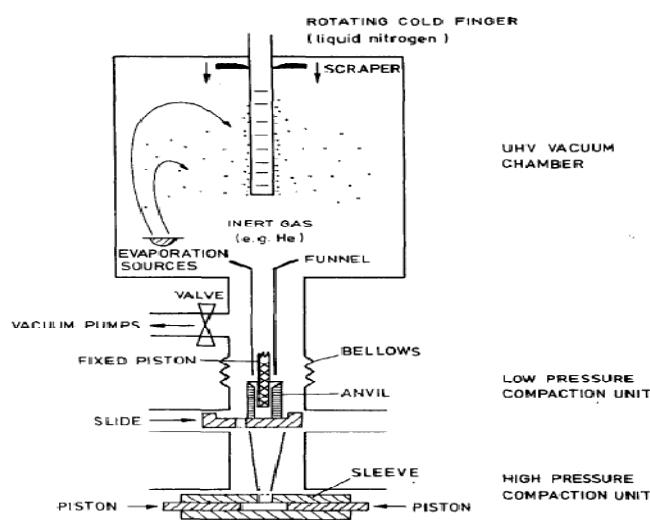


Fig. 2.6 Schematic of inert gas condensation apparatus [9]

2.2.6 High Energy Ball- milling

High energy ball- milling, also known as mechanical alloying (MA) is a solid-state powder processing technique involving repeated welding, fracture and rewelding of powder-particles in a high-energy ball mill. This technique was originally developed to produce oxide-dispersion strengthened (ODS) nickel- and iron-base superalloys for applications in aerospace industry. Later, MA has shown to be capable of synthesizing a variety of equilibrium and non-equilibrium phases including nanocrystalline and amorphous materials [124,125], and, recently, it became the most versatile and economical process for synthesis of nanocrystalline materials, due to its simplicity, low cost and ability for large production [76,77,126-128]. Synthesis of nanocrystalline metals and alloys, using high energy ball -milling and related phenomena, have recently been reviewed [76,77,92,129-132]. Vibratory mill, planetary ball mill, attritor ball- mill and rod mill are the main milling devices that have been employed for synthesis of nc- metals and alloys [76]. During ball- milling, the energy is transferred from the ball movement to powder particles and grain refinement takes place. A schematic of the ball movement in a high energy planetary ball mill is presented in Figure 2.7.

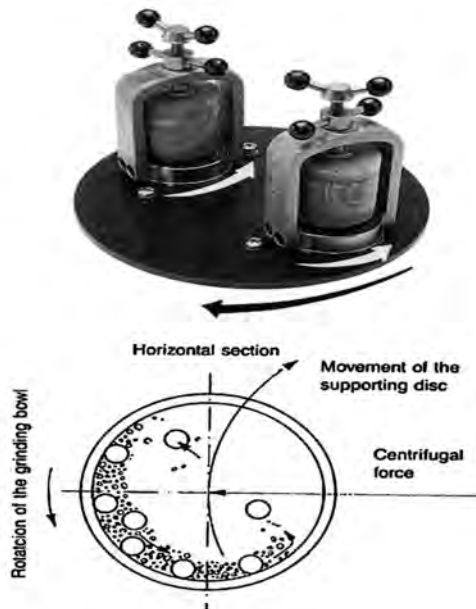


Fig. 2.7 Schematic depicting the ball motion inside the planetary ball mill [133]

The minimum achievable grain size and quality of nanocrystalline materials, formed, depends on number of parameters like, type of ball mill, milling container, ball to powder ratio, milling speed, milling time, grinding medium, extent of filling the vial, milling atmosphere, process controlling agents, milling temperature, type of material being milled, etc. [76,134-136]. These parameters are crucial and should be chosen according to the nature of material under consideration and the purpose of milling.

Milling time is one of the most important factors in ball- milling. Grain size decreases with increasing milling time and becomes constant after reaching to a minimum value of grain size (d_{min}) [94,103,134,137]. The time required to obtain d_{min} depends on the nature of material being milled, type of mill used, the intensity of milling, the ball-to-powder weight ratio, and the temperature of milling. Figure 2.8 shows the grain refinement with milling time. Grain refinement kinetics is very fast in the early hours of milling and becomes sluggish with time. Milling, after obtaining a minimum grain size (d_{min}), may not lead to any significant grain refinement, but it would add on to the further contamination with increase in milling time [132,138,139]. However, in some systems [37,140,141], milling, after attaining minimum grain size (d_{min}), modifies grain and grain boundary structure, consequently, lattice strain and the stored enthalpy; values start decreasing after attaining a maximum value. Effect of longer periods of ball-milling on the microstructural and property evolution in Fe is investigated and it is found that various properties start decreasing (after attaining a maxima) after a critical period of milling. This decrease in values can be attributed to the grain boundary relaxation. [40,131,134,141-143]. Figure 2.9 shows values of various thermodynamic parameters in Fe as function of milling time. Figure 2.10 presents effect of grain size (which is a function of milling time) on the lattice strain.

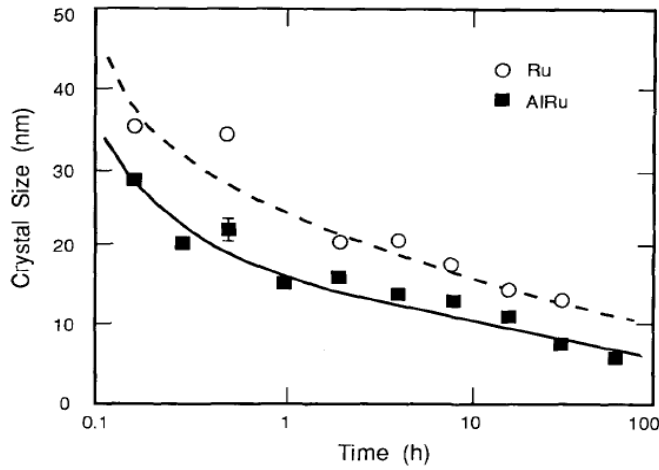


Fig. 2.8 Kinetics of grain refinement: high energy ball milling. Grain size estimated from X-ray line broadening for Ru and AlRu.

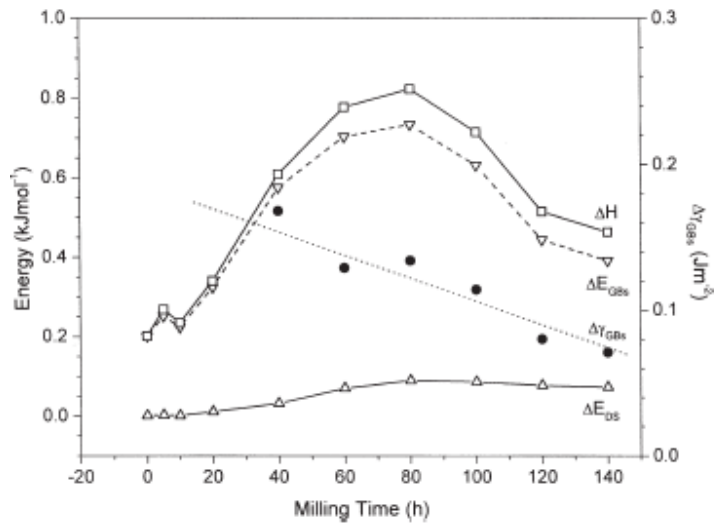


Fig. 2.9 The stored enthalpy ΔH , the GBs enthalpy release ΔE_{GBs} and the elastic energy release of dislocations ΔE_{Ds} , as well as the GB enthalpy release per area $\Delta \gamma_{GBs}$ against the milling time [40]

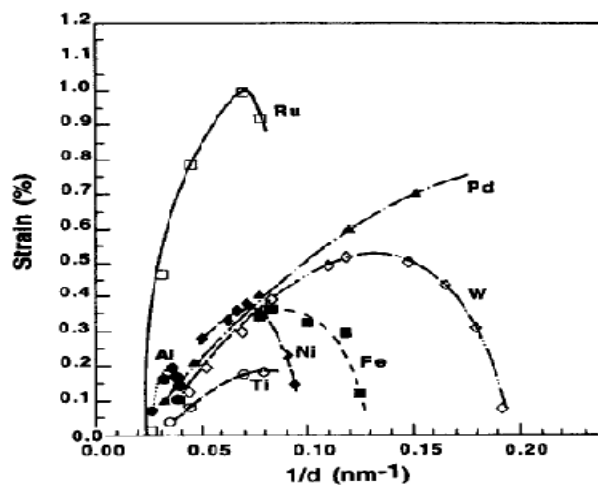


Fig. 2.10 Lattice strain vs. reciprocal grain size for bcc, hcp and fcc metals [135]

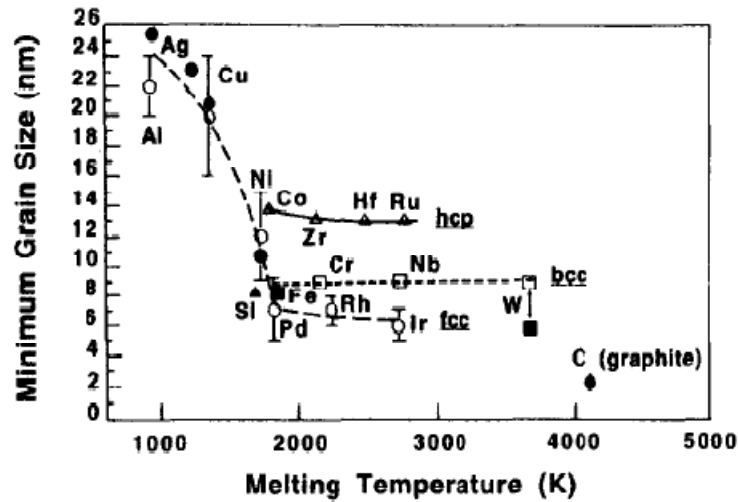


Fig. 2.11 minimum grain size for nc elements vs. their melting temperatures [144]

Minimum level of grain size (d_{min}), obtained by ball milling, largely depends on crystal structure and melting temperature of material in the order, FCC<BCC<HCP (Figure 2.11) [134,135,140,145]. Milling temperature is the other important factor that affects the achievable minimum grain size of the material. Based on the concept that the minimum grain size, obtained by ball milling, is governed by a balance between the hardening rate introduced by dislocation, generation and the recovery rate arising from dislocation, annihilation and recombination, it was shown that lower milling temperature accelerates the kinetics of grain refinement [103,146]. The technique of ball-milling was modified by performing the milling at liquid nitrogen temperature; cryomilling [147,148], which is particularly useful for the FCC material. The major concern of the ball-milling technique is the contamination from grinding media which is however, circumvented by employing balls and vial of appropriate material. Cryomilling can also be effective in reducing contamination as grain refinement is achieved at much lesser time and contamination, assisted by diffusion, is less because temperature does not rise during the whole period of milling

Simultaneous grain refinement and modification of particle size and morphology happens during the high energy ball- milling. Flattening, cold welding, fracturing and re-welding of powder particles during high energy ball- milling repeatedly keep happening. After certain alloying time, particle size distribution becomes more uniform (Figure 2.12) [139,149-152]. Progress of ball- milling in terms of particle, size shape and structure has been investigated, recently, and formation of lamellar structure in Fe-Cr alloys has been shown. Interlamellar spacing decreases with progress of alloying which loses its identity after milling for longer time [139,149,153,154].

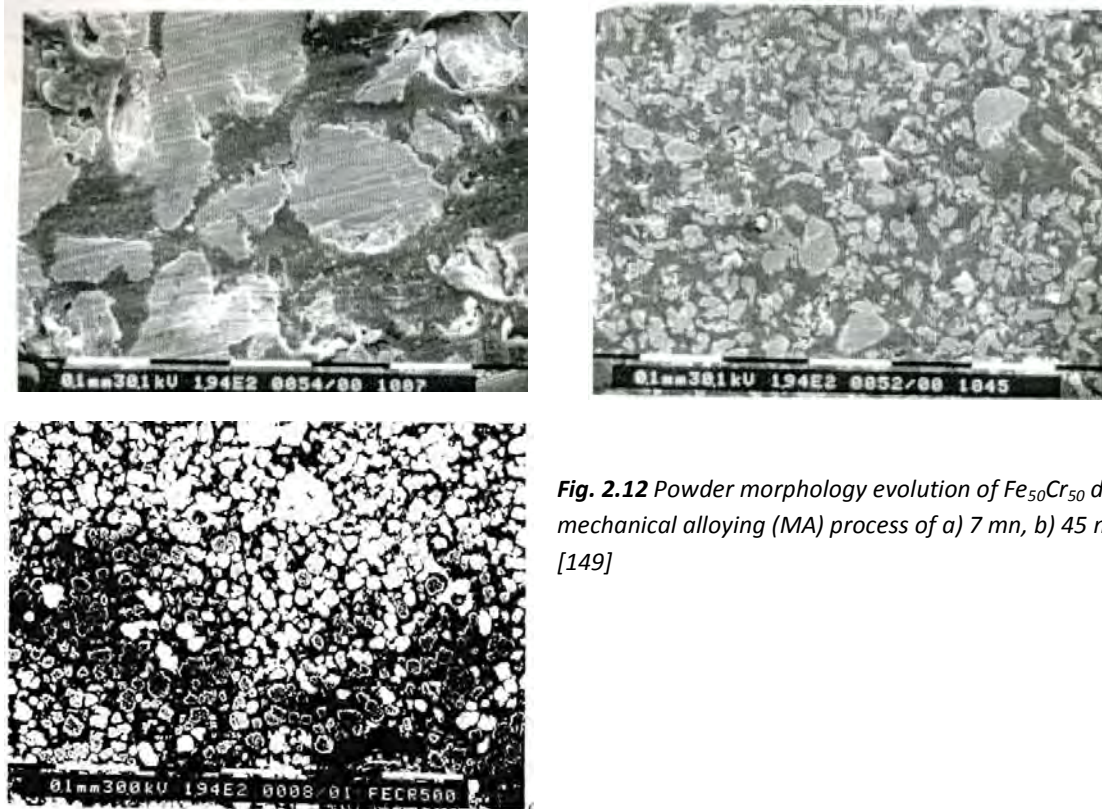


Fig. 2.12 Powder morphology evolution of Fe₅₀Cr₅₀ during mechanical alloying (MA) process of a) 7 mn, b) 45 mn, c) 5h. [149]

Formation of nanocrystalline material (grain refinement to the nano level) by ball- milling is a complicated process and has to be understood, precisely. Based on the energy balance of shear bands, a mathematical model for refinement of nanocrystalline grain size during ball -milling was proposed by

Li et al. [137]. Later, Fecht [155] summarized the phenomenology of the development of nanocrystalline structure as a result of a three-stage process, i.e.,

Stage 1: localization of deformation into shear bands with high dislocation density,

Stage 2: dislocation, annihilation and recombination to form a nanometer-scale sub-grains, which extends throughout the sample with further milling,

Stage 3: transformation of sub-grain boundary structure to randomly orientated high-angle grain boundaries. Superplastic deformation process such as grain boundary sliding causes this self-organization into a random nanocrystalline state.

The schematic presentation of the process at the microscopic level is given in Figure 2.13, which is based on the work of Xuan et al. [129,156]. Recent, atomic level observation of ball milled, nc-Fe reveals formation and migration of partial disclinations during deformation that allows crystallite solids to rotate and rearrange at nanometer level. Such rearrangement may be critical in the formation of nanocrystalline metals by mechanical milling [157].

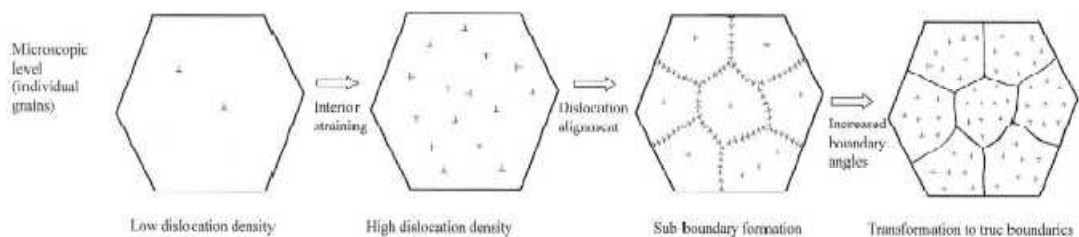


Fig. 2.13 Schematic representation of grain refinement mechanism during ball- milling [156]

2.3 Consolidation of nc-Fe and Fe based alloys

Synthesis of nc-Fe by most of the techniques described in section 3.0 results in nc-Fe either in powder form or a thin film. Consolidation of powder produced by ball- milling is necessary, particularly for the study of various properties. High mechanical strength, lack of ductility and poor thermal stability of

nanocrystalline materials make consolidation into fully dense bulk products or coatings much more challenging and different from conventional microcrystalline materials [158]. As unique properties of nanocrystalline materials are derived from their fine grain size, therefore, it is of crucial importance to retain the microstructure at a nanometer scale during consolidation to form bulk materials.

It is also noticed that pores are generated in bulk nanocrystalline materials, consolidated from nanocrystalline powders prepared by several routes. Such nano-pores may result in poor mechanical properties under compression or tension. Issues related to consolidation of nc-materials are discussed by J.R. Groza [159]. Consolidation of nc-BCC materials like Fe becomes even more challenging because of lack of ductility and is described here briefly.

2.3.1 Compaction under high pressure

Compaction comprises sliding and rearrangement of particles, elastic deformation, and plastic deformation at the interfaces and within the particles. Green density is related to applied pressure (Shapiro and Kolthoff [160]):

$$\ln\left\{\frac{1}{1-D}\right\} = kP + A \quad \text{-- (6)}$$

Where D is the relative green density, P is compaction pressure, k and A are constants. K is related to yield strength and work hardening.

During compaction, density increases and bonding between particles takes place; bonding results from the plastic deformation at particle interfaces due to high pressure at particle interfaces. Bond strength depends on shear stress at particle contact. Bonding between the particles in compacted samples may be very weak. However, cold welding in some cases may increase the bond strength [161].

For plastic deformation to occur, applied pressure should exceed the yield strength of material. It will be discussed in section 5 that the nanocrystalline materials possess very high yield stress, therefore, compaction becomes difficult [158]. Depending upon grain size as well as on synthesis techniques, iron is compacted at very high pressure and mostly at elevated temperature (Table 2.3).

Depending upon grain size, nc-Fe possesses hardness value of approximately 10 GPa. Therefore, applied pressure should be more than 3.33 GPa, in any case. Gupta et al. [162] have shown that an applied pressure of 2.7 GPa at room temperature was not sufficient to compact Fe-10Cr (with a grain size of 13 nm). Compaction was performed under uniaxial pressure of 2.7 GPa, after annealing (softening) of the powder at 600°C for 30 minutes. Softening takes place because of grain growth during annealing. Explosive compaction [163], as employed by Ramesh et al. [164] would be another method to consolidate material at room temperature but grain growth during sintering cannot be avoided.

2.3.2 Solid state sintering

A good green density does not mean good strength. The compacted material needs to be sintered to increase bond strength between particles. Sintering commonly refers to the processes involved in the heat treatment of powder compacts at elevated temperatures, usually at $T > 0.5 T_m$, i.e., the temperature range where mass transport by diffusion is appreciable. However, in nc materials severe grain growth is expected at $0.5T_m$. Successful sintering usually results in dense polycrystalline solids. However, sintering can proceed only locally (i.e. at contact point of grains), without any appreciable change in the average -overall density of a powder compact. The driving force for sintering is a decrease in the surface free energy of powdered compacts, by replacing solid-vapour interfaces (of surface energy Γ_{sv}) with solid-solid (Γ_{ss}) interfaces, where $\Gamma_{ss} < \Gamma_{sv}$. Thermodynamically, then, sintering is an

irreversible process in which a free energy decrease is brought about by a decrease in surface area [162, 165].

Sintering time and temperature are the factors that determine the density and interparticle bonding of the sintered compacts. Time and temperature is chosen such that densification rate is higher than the grain growth rate. Fe and Fe- based alloys have been compacted and sintered successfully at temperature below $0.5 T_m$ [162].

2.3.3 Compaction at elevated temperature and high uniaxial pressure (Hot compaction)

This technique combines the compaction and sintering into one single operation. A high pressure is applied at an elevated temperature. Schematic representation of a hot uniaxial press is given in Figure 2.14. Simultaneous application of pressure and temperature results in direct increase in the driving force for the densification. Material softens because of grain growth and thermal effect. Plastic flow is easier and pores collapse readily. Good bonding between particles is obtained because of removal of interfaces, higher plastic deformation and diffusion across them. In hot compaction, temperature can be lower than the sintering temperature i.e., two step consolidation process (compaction and sintering). Good density and strength is obtained with minimum grain growth.

Malow et al. [97] have received almost 100% density by compacting nc-Fe at 500°C/2.7 GPa. Results obtained are listed in table 2.3. Elkedim et al [166] have reported 98.9% of the theoretical density in nc-Fe after compaction at 400°C and under 2 GPa uniaxial pressure for 1 hour [166]. Austenitic stainless steel was compacted by Omuro et al. [167] at a much lower pressure at 1000°C.

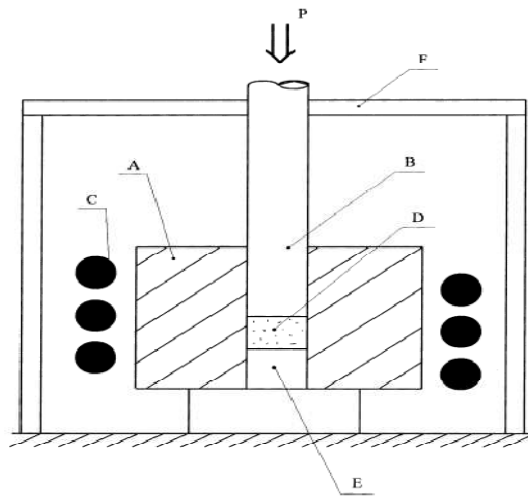


Fig. 2.14 Schematic representation of Hot uniaxial press, showing different components: tungsten carbide die (A), punch (B), heating wires (C), powder sample (D), wedge (E), furnace insulation (F) and pressure (P).

2.3.4 Hot isostatic pressing (HIP)

Hot isostatic pressing is similar to hot compaction with the only difference that applied pressure is same in all the directions. This process has been used to compact complicated shapes. Generally, the HIP process is used at high temperatures and relatively low pressures, and the produced samples have a density close to 100% of the theoretical density. In the case of nanocrystalline materials, conventional HIP can not be used because of severe grain growth at high temperature. In order to consolidate nanocrystalline materials, relatively low temperature and high pressure will be useful. A new alternative route, Warm-HIP, is developed for nanocrystalline materials. Warm-HIP is the process where isostatic pressure is applied and processing temperature is kept below $0.5T_m$ so that the grain size in nano regime can be retained. The application of both elevated pressure and temperature during Warm-HIP, assures that the particles undergo plastic deformation, and the bonding between particles, largely by surface diffusion, results in chemical bonding. In a study, pure nc- Fe (grain size = 7.5 nm), produced by high energy ball milling for 150 hours, was subjected to warm-HIPping. Warm-HIP compaction was

performed at 250°C temperature and 200 MPa pressure for 3 hours. Warm-HIPped samples have 95% of theoretical density and grain size lesser than 50 nm.

2.3.5 In- situ consolidation

This technique developed by Youssef et al. [168] seems very attractive for FCC metals like copper. Nanocrystalline Cu is synthesized by a special method of combining liquid-nitrogen - temperature (cryo) and room-temperature (RT) milling [168,169]. Direct application of this technique for BCC materials like nc-Fe does not seem possible because of lack of ductility

Table 2.3 Consolidation of nc –Fe (hot compaction)

Material)	Pressure(GPa)/ Temp(°C)	Grain size (nm)	Density (%)	Reference
Fe	1.4/300	14	95.0	[85]
Fe	2.0/400	28	98.9	[101,170]
Fe	1.5/200/5	58	93.0	[86]
Fe	3.1/130	38	96.0	[24]
Steel	1.1/425	30	>97	[171]
Fe	2GPa/RT+ 1GPa/600°C	--	--	[104]
Fe	Warm-HIP, 300MPa/580°C	41	95	[172]
Austenitic SS	100MPa/1000°C	40.8	96	[167]

2.4 Mechanical behaviour of nanocrystalline Fe and Fe based alloys

Fine grain size, large grain boundary area, triple points, grain and grain boundary structure make nc-materials completely different from their conventional polycrystalline counterparts. Nanocrystalline metallic materials are much stronger and apparently less ductile than conventional ones. This difference is mainly because of unique grain structure, defects, defect activity and their arrangement in nc-materials. For example, paucity of dislocations in nanocrystalline materials is well documented [71]. Dislocation pile-up in deformed specimen has not been reported so far and any dislocation activity is primarily believed to originate and terminate at grain boundaries. Dislocation activity decreases remarkably, while grain boundary sliding [173] and/or coble creep [174] can dominate which may cause softening [145]. Therefore, unique mechanical behaviour of nanocrystalline material is worth to be investigated, keeping the structure of nanocrystalline material in mind. Various attempts to understand the mechanical behaviour of nanocrystalline materials have recently been reviewed [175-181].

Investigations of mechanical properties of nanocrystalline materials using conventional experimental techniques have been challenging. Preparation of porosity free bulk samples of nanocrystalline materials for tensile tests or compression tests is still not an easy task. Most of the tensile tests or compression tests are limited to ductile materials only. Recently Koch et al. [182] have suggested techniques which could be useful to investigate the mechanical behaviour of nanocrystalline materials. Hardness measurement is a widely used technique because of its simplicity and easy sample preparation. Hardness of material can directly related to the yield stress of material as following: $H_v = 3\sigma$ [183]. Therefore, hardness measurements can be a convenient means of establishing Hall-Petch relationship in fine grained materials [184, 185] and, most of the investigations on the mechanical behaviour of nanocrystalline materials are based on the hardness measurement.

Hardness of nc-Fe increases with decrease in grain size [80-85,97,98,104,151,171,186-188] and data reported by various researchers are plotted in Figure 2.15 which, clearly shows that hardness of these materials is several times higher than that of conventional microcrystalline materials of similar compositions. High hardness in nanocrystalline materials is expected according to Hall-Petch relationship but, many investigations on nanocrystalline materials show deviation from this Hall-Petch relationship. This section is focused on hardness, plastic deformation and young modules of nanocrystalline Fe and Fe- based alloys. Author's understanding is that the following factor may play important role in determining the mechanical properties of nanocrystalline materials:

1. large fraction of grain boundary and small grain size
2. Paucity of dislocations, dislocation size and distribution of dislocation
3. Softening due to triple points and grain boundaries (Grain boundary itself may be more disordered and with different mechanical properties)
4. Grain boundary sliding, grain boundary rotation, Coble creep diffusion
5. Effect of porosity and impurities introduced during processing of material and possibility of presence of nano-pores

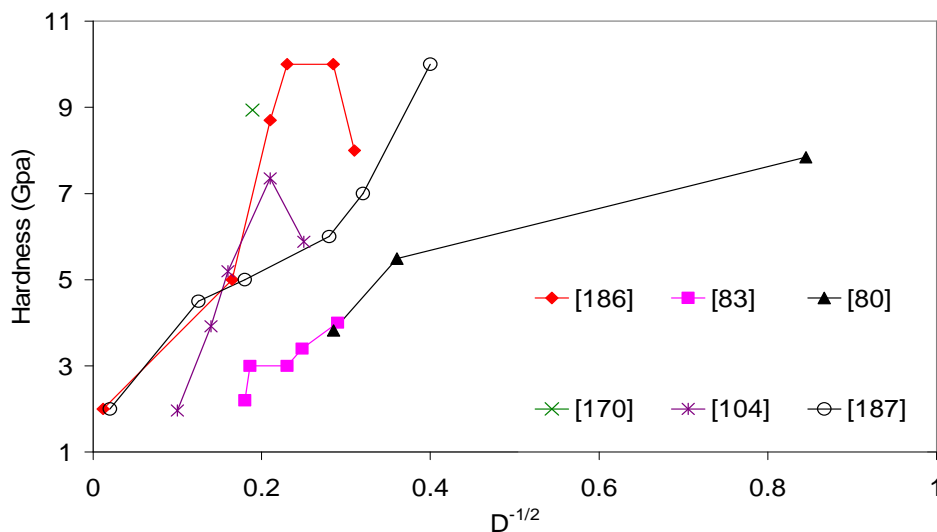


Fig. 2.15 Variation of hardness with grain size (D is the grain size in nm)

2.4.1 Yield Stress and Validity of Hall-Petch Relationship

Conventional microcrystalline materials exhibit increased yield strength with the grain refinement following well-known Hall-Petch [189,190] relationship:

$$\sigma = \sigma_0 + k_0 d^{-1/2} \quad \text{--- (7)}$$

Where, σ_0 is the friction stress resisting the motion of gliding dislocation and k , the so called “locking parameter”, is the Hall-Petch slope, which is associated with a measure of resistance of the grain boundary to slip transfer. In analogy, hardness can be related to grain size by:

$$H_v = H_o + k_H d^{-1/2} \quad \text{--- (8)}$$

where, H_o and k_H are constants. Hardness is a measure of the resistance of a material to the plastic deformation under the application of indenting load.

Various investigations have verified the validity of Hall-Petch relationship in nc-Fe in nano grain size regime [151,186,187]. However, some deviation from Hall-Petch relationship is also reported [176,180,188,191-196]. For validity of Hall-Petch relationship, the pile-up of dislocations at grain boundaries is the mechanistic process underlying in enhanced resistance to plastic flow. Thus grain boundaries act as efficient obstacles to dislocations, nucleated mostly from Frankel-Read sources. Consequently, a dislocation pile-up can be formed against the grain boundaries inside the grains [185]. Neith and Wadsworth [194] have suggested that the Hall-Petch relation continues to be applicable to the description of the strength of nc-materials as long as the grain size of the nc-materials can sustain the dislocation pile-up. However, the reason of deviation from Hall-Petch relationship in very fine grained nc materials is not well understood. One probable reason may arise as dislocations are believed to be absent or very less and/or dislocation source does not operate in small grained-materials [194,197]. The minimum stress required to activate any common dislocation source (Frank-Read source, for example) is inversely proportional to the distance between the two pinning points and, in

nanocrystalline materials, the stress required to operate Frankel-Read source increases dramatically and applied stress is not enough to operate the Frankel-Read source in very fine nc regime [191]. The other reason of the deviation may be the unique grain boundary structure and/or presence of large fraction of grain boundaries (so-called as “intercrystalline component”). This view is supported as the harnesses of annealed and ball -milled Fe of same grain size has shown different values (Figure 2.16 [151]). Interestingly, hardness of ball milled -Fe increased after annealing, though it was expected to decrease, as a result of loss of work- hardening during annealing. In the two cases, grain boundary fraction is the same because the grain size is same. One can conceive of change in the grain boundary structure as the probable reason of this strange behaviour as ball-milling forms distorted grain boundary region which becomes more crystalline during annealing

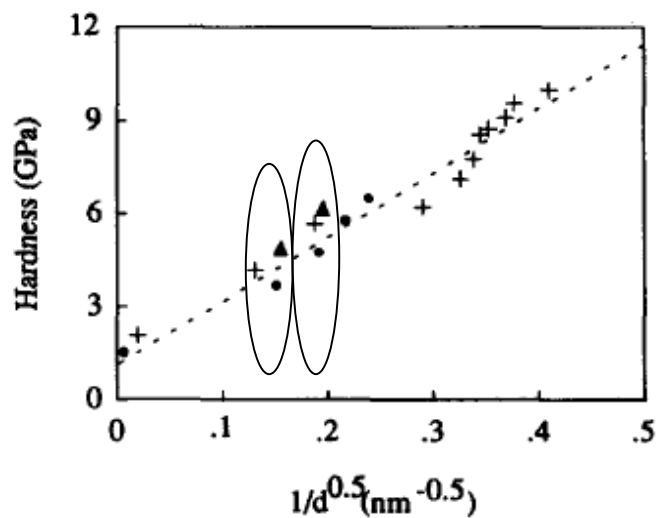


Fig. 2.16 Hall-Petch relation for milled Fe powders. ●: mechanically alloyed (MA) powders; ▲: after MA and annealing; +: from Jang and Koch [151]

A few investigations (for instance Khan et al. in nc-Fe [198]) have reported decrease in hardness beyond a critical grain size. This behaviour, reported in nanocrystalline materials, is termed as Inverse Hall-Petch relationship [51,53,104,186,199,200] and was first observed in Cu and Pd [201]. However, earlier

researches have theoretically interpreted that Hall-Petch relationship may not be valid for materials having very fine grain size [202,203].

Attempts have been made to describe the softening in nanocrystalline materials. Pile-up model for nanocrystalline materials has been questioned [185]. Nieth and Wordsworth [194] have suggested that below a certain grain size, change in deformation mechanism(because of breakdown of dislocation pileup) may be one of the possible reasons for softening. Suryanarayana et al. [204] have suggested that decrease in grain size leads to increase in grain boundary fraction, triple junction fraction and change in grain boundary structure and, hence, softening [201]. Based on the model of bow-out of dislocation, a modified Hall-Petch relation is proposed by Lian and Baudalet [196] which was experimentally supported for a long range of grain size in nano regime [187,205]. Scattergood and Koch [193] proposed an approach, based on the dislocation-network model, to interpret the negative slope of the HP relation for nanocrystalline materials. They assumed that dislocation line tension is size-scale dependent. Lu and Sui [206] have presented a qualitative model explaining the abnormal Hall-Petch relationship on the basis of decrease in excess volume and interfacial excess energy when grain size approaches to nano size. Normal-abnormal HP relationship transition grain size is found to be < 6 nm [187,206]. The structure and energetic states of the nc interfaces and therefore various properties of the nc materials are strongly dependent on the sample preparation and on the consequent heat treatments [206]. Fougere et al. [207] have noticed that occurrence of the H-P softening is associated with the annealing of the NC materials.

The validity of inverse hall pitch relationship has continued to be controversial. Many investigations of nc-Fe show no softening. Malow and Koch [97] have not found any decrease in hardness; it keeps increasing till 10 nm grain size. While, Khan [104] et al. have reported softening merely at a grain size of

35 nm in ball- milled Fe. Little strange behaviour has been reported by Fougere et al. [85] where hardness increases drastically with increase in grain size (in nano-regime). Level of porosity present in the specimen also depends on the grain size. Increase in hardness with increase in grain size may be only due to decreased porosity after a certain grain size level.

Fe based nc-alloys are prepared and solid solution strengthening and softening is studied. Mechanical strength changes according to type of solute atoms [208] and it is similar to that in conventional microcrystalline materials. As seen in Figure 2.15, discrepancies in literature data indicate that significant effects on the reported results come from impurities and processing parameters, all affecting the actual microstructure of the specimens.

2.4.2 Nanocrystalline Fe and Fe- based alloys under tension or compression

Majority of investigations on mechanical properties of nanocrystalline iron have been focused on the hardness measurement due the simplicity. Unfortunately, hardness represents complex stress states and its interpretation in terms of basic deformation or fracture mechanisms and ductility is, therefore, difficult. Tensile tests would yield more straightforward information. However, only a few studies have dealt with the tensile behaviour of nc-materials, specifically for nc-Fe or Fe -based alloys. It is interesting to see that materials which are ductile in coarse grain form exhibit none or little ductility for grain size < 30 nm [209-215]. Oddly, some of intermetallics have shown ductility under compression tests [216-220]. Some of these materials which have shown ductility in compression test, failed at nearly zero strain during tensile testing [217, 220]. It is debatable if decrease in ductility is because of inherent crystal property or due to artifacts present in the test specimen. Explanation that loss in ductility is due to artifacts has recently been supported by Khaled et al. [168], where, they have shown improved

ductility in artifact free in-situ consolidated copper. To the great extent, artifacts present in test specimen are responsible for the lower ductility.

Malow and Koch [96-98] have studied deformation behaviour of nc-Fe under tension and compression where nc-Fe shows no plastic deformation for grain size <20 nm [98]. However, samples of relatively larger grains (>20 nm) have shown localized plastic deformation. Close observation of fracture morphologies indicate deformation and fracture by shear mechanisms. The fracture stress increased with the grain size, which is opposite to predictions made by Hall-Petch relationship [98]. However, this observation may be deceptive and, the reason may be just poor interparticle bonding and presence of porosity in specimen of finer grain size.

Compressive tests performed on nc-Fe and its alloys have shown a very high compressive strength with none or very less ductility [96,104,171,192]. Malow et al. [96] have used automated ball indentation (ABI) technique to study compressive strength of nc-Fe. Compressive flow stress for a range of strain rates was found to be around 3 GPa for grain size of around 21 nm. A very small strain hardening is observed; value of strain rate sensitivity is determined and compared with the literature. Deformation morphology has shown localized deformation in shear bands, which represents local ductility. Compression tests made by Khan et al. [104] have also shown significant increase in fracture toughness and strength in nanocrystalline Fe [104]. Nc-Fe loses its ductility gradually with decrease in grain size and shows almost brittle behaviour for grain size of 16 nm (Figure 2.17). Strain sensitivity of nc-Fe has also been reported. Based on various experimental results for a range of strain rates, KHL model was modified for nanocrystalline iron [104]. Generalized Hooks law predicts the materials behaviour before yielding. KHL model [198,221,222], modified by grain size effect is used to reflect the stress/strain behaviour of nc-Fe after yielding:

$$\sigma = \left[\left(a_0 + \frac{k_0}{\sqrt{d}} \right) + B \left(1 - \frac{\ln \dot{\epsilon}}{\ln D_0^p} \right)^{n_1} \dot{\epsilon}^{n_0} \right] \dot{\epsilon}^C (1 - T^{*m}) \quad \text{--- (9)}$$

$$T^* = \frac{T - T_r}{T_m - T_r} \quad \text{--- (10)}$$

where. σ , ϵ and $\dot{\epsilon}$ are von Mises equivalent stress, strain and strain rate respectively. T_m is melting temperature and T_r is room temperature. a_0 , k_0 , B , n_0 , n_1 , C , D_0^p and m are materials constants. d is grain size.

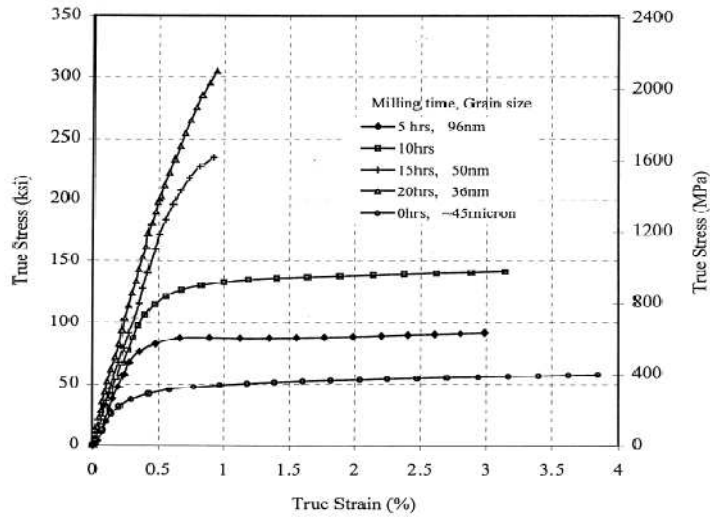


Fig. 2.17 Stress/strain response of nc-Fe from powders with different milling time and grain size. The strain rate is 0.0001/s

2.5 Grain growth in nanocrystalline Fe and Fe based alloys

In general, grain growth in microcrystalline materials is driven by the resultant decrease in the interfacial energy and hence the total energy of the system. Nanocrystalline materials possess highly disordered and large grain boundary area (described earlier as IC area), which provides large amount of driving force for grain growth. Therefore, nanocrystalline materials are highly susceptible to grain growth [9, 52]. Understanding of thermal stability becomes prime issue for engineering applications and processing of these materials. A number of investigations on thermal stability of nanocrystalline materials have

been carried out. Recently, Surayanarayana [49] and Weissmuller [223] have carried out a general review of the grain growth in NC materials, whereas, the grain growth of ball -milled nanocrystalline metallic materials has been reviewed by Witkin et al [129].

Significant grain growth occurs at room temperature in low melting point nc- materials like Sn, Pb, Al and Mg [52, 224]. However, materials with melting point greater than 600°C possess some stability against grain growth. Nanocrystalline iron shows considerable stability against grain growth at elevated temperatures. Some of the interesting results on the grain growth of nc-Fe are compiled and grain size is plotted against annealing temperature (Figure 2.18). Natter et al. [225] have studied crystallite growth of pulsed electrodeposited nc-Fe by in-situ X-ray and observed no significant grain growth till 400°C. At around 410°C, transition in grain growth kinetics is observed and a sudden large grain growth is reported thereafter [225]. In contrast to this data, other investigations have shown even improved thermal stability at higher temperature.

For example, Malow and Koch have reported no excessive grain growth till 500°C [99] but, a sudden large grain growth between 500 and 530°C; the grain size becomes 23 nanometre, during annealing at 500°C, while for the same annealing period, an increase in annealing temperature by 30°C leads a grain growth to 48 nm. Similar transition in grain growth mechanism has been reported for other materials, like, Co, and it is explained on the basis of excess volume theory [226] which, seems convincing and can be applied to nc-Fe as well.

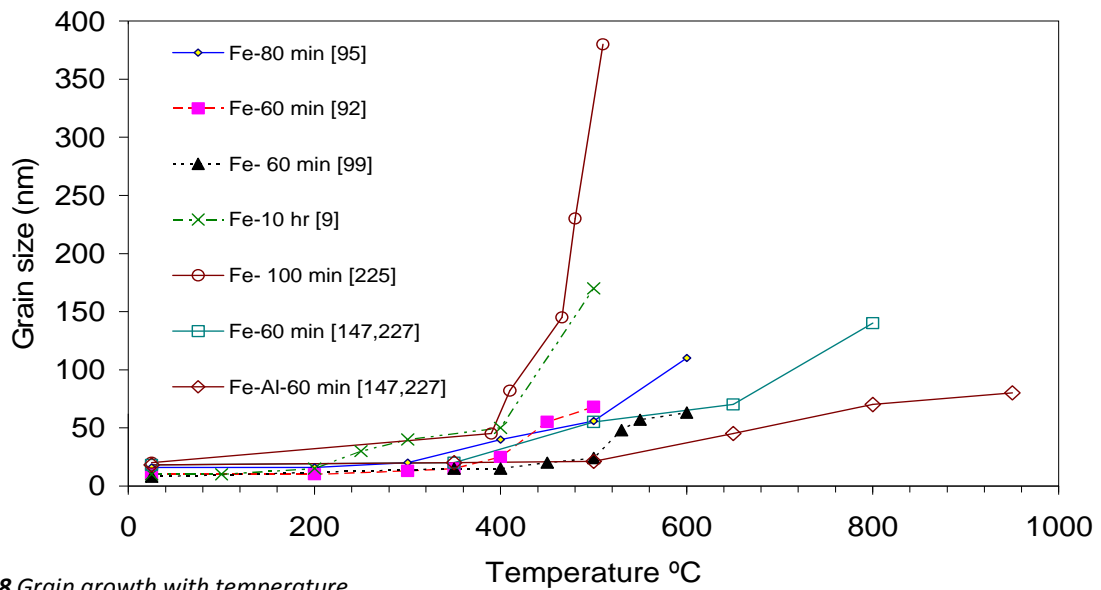


Fig. 2.18 Grain growth with temperature

In contrast to earlier consideration of poor thermal stability of nc-materials, recent studies show quite good thermal stability and this could be attributed to the presence of impurities that come inherently from processing route [92,95,99,167,227]. Multi-component materials such as alloys or materials containing second phase particles have inherent thermal stability because of pinning of grain boundary motion, for example, addition of Cr or Al enhances thermal stability [162,227,228]. A number of factors have been shown to influence the thermal stability of these materials. Grain boundary segregation [229], solute drag [230], pore drag [231], second phase (Zener) drag [232], chemical ordering [233], grain size distribution, equiaxed grain morphology, low energy grain boundary structures are some of the important factors responsible for the thermal stability of NC materials. Impurities that get introduced during processing of material plays crucial role in thermal stability [234]. Further alloying enhances the thermal stability [162,167,227].

A mathematical relationship is desired to fit the available data and for understanding of grain growth mechanism. A few grain growth laws have been proposed on the basis of basic understanding of grain

growth. Available grain growth data give better fit to following expression when annealing temperature is not very high:

$$D^{1/n} - D_0^{1/n} = kt \quad \text{--- (11)}$$

where D_0 is the initial grain size, n is time exponent, k is temperature dependent constant which can be expressed as following:

$$k = k_0 \exp\left(-\frac{Q}{RT}\right) \quad \text{--- (12)}$$

k_0 in above equation is the frequency term and R is the gas constant. Q is activation energy of grain growth and T is the temperature.

In many cases pinning forces impede grain growth so that grain boundary migration stops before the grain boundary curvature is completely eliminated. The rate of growth is then proportional to the difference between the curvature of the actual grain size at the the given annealing time ($1/D$) and curvature of the grain size that corresponds to the limiting curvature where the growth stops ($1/D_m$):

$$(D_0 - D)/D_m + \ln[(D_m - D_0)/(D_m - D)] = kt \quad \text{--- (13)}$$

where, D_m is the maximum grain size that results due to the pinning force.

It is clear from the above equations that kinetics of grain growth largely depends on two important parameters namely, activation energy (Q) and time exponent (n). A value of time exponent and activation energy depends on the temperature and material. Grain growth data are fitted to above two expressions and values of Q and n are determined over a wide range of time and temperature. In pure metals, value of time exponent n would be 0.5 where the grain growth is controlled by the driving forces raised by curvature of grain boundaries. However, large deviation from $n=0.5$ is noticed in nc-materials. Malow and Koch [98] have reported the value of n in nc-Fe to be constant at 0.1 (for temperature < 0.4

T_m), followed by considerable increase in n to 0.33 with an increase in temperature from 0.4 to 0.45 T_m [99]). These values are compared with the conventional polycrystalline Fe. Value of n for nanocrystalline Fe approaches to 0.5 as annealing temperature increases. For Fe-10Cr alloy n was found to be 0.09 for various temperature ranges ($T < 0.5T_m$) [162].

Most of the studies report a rapid grain growth in the beginning of annealing, followed by the regime of the sluggish grain growth. Calculated grain size using the Equation (11) with value of n close to 0.1 shows that grain size stabilizes soon and no significant grain growth takes place in the later stages of annealing. Most of the investigations agree with the theoretical derivation. However, later it was reported by Malow and Koch that annealing of nc-Fe at 450 °C for 142 hours leads to grain size of 64 nm which should be around 28 nm, according to equation 11 [99]. As a matter of fact, it was realized that grain growth kinetics is time dependent and they have divided the grain growth into two regions with different value of activation energy and time exponent [99]. Two mechanisms are proposed: one of them follows the equation 19 with n value increasing with T/T_m ; second mechanism that operates at higher temperature takes pinning force into account (Equation 21). Similar results have been reported by Natter et al. [223]. Value of activation energy at lower temperature is found much lower than that at higher temperature. At higher temperature value of activation energy is much closer to that in polycrystalline iron and lattice self diffusion. This value is close to values for diffusion of solute atoms present as impurity. Hence increased value can be attributed to the solute diffusion -dependent grain growth [99, 234].

Grain growth data reported by different investigators are scattered (Figure 2.18). Gleiter has obtained grain size of 170 nm for nc-Fe after annealing at 500° C for 10 hours [9]. Malow and Koch have heat - treated nanocrystalline Fe at the same temperature but for 25 hours and the grain size obtained is much

smaller than reported by Gleiter. Difference in data may be because of dependence of grain growth on the processing parameters. Impurities, introduced during processing, play an important role. For instance, if material is prepared by ball-milling, milling time, ball used, rotation speed etc. will determine the impurities introduced and hence the grain growth. For the same reason, electrodeposited nc-Fe has shown larger grain growth than one produced by ball-milling (Figure 2.18).

Final grain structure cannot be ignored in the study of grain growth. Grain structure is a strong function of types of interfaces, dislocations etc. which can be critical to the grain size. For example, grain growth in ball-milled copper is more than that in electrodeposited copper [235]. Bonetti et al. synthesized nc-Fe by using vibratory and planetary ball mills [92] and studied the difference in grain growth behaviour in two cases. Further, it was found that the grain growth kinetics of pre-annealed (annealed at 297°C for 1 hour) nc-Fe powder is slower than that of as-milled samples [92]. After heat treatment grains of the pre-annealed nc-Fe powders at 397°C were found to be 40% smaller than those of milled samples. High energy ball milling produces highly disordered grain boundaries. A low temperature, prior to annealing, could possibly cause re-arrangement of dislocations, decreasing the grain boundary energy. Moreover, a low temperature annealing could also result in migration of impurities to the grain boundaries, causing grain boundary pinning during subsequent thermal treatment [92]. Another important observation was that the nc-Fe, obtained by planetary ball-milling, showed a relatively faster grain growth than that obtained by vibratory ball mill [92]. The grain size of pre-annealed nc-Fe after subsequent annealing for 1h at 500°C is about 70 nm [92]. Though studies are not present but, from the basic understanding it is clear that uniform distribution of grain size suppresses grain growth. Hence long annealing time to ensure uniform homogeneous distribution of grains size would suppress the grain growth to a large extent.

2.6 Electrochemical corrosion behavior of nanocrystalline materials

In recent years, there has been considerable research interest in understanding the corrosion resistance of nanocrystalline metals and alloys. Most of the early research has been focused on Ni [236-242], Ni-P [243-245], Ni-S [246], Co [119,247-249], Cu [250-254] and their alloys. Electrochemical behaviour of a material depends largely on the nature of material and environment. Hence generalization of corrosion behaviour is not easy. Various parameters such as grain size, distribution of precipitates, surface defects, solute atoms, impurities, electronic structure etc. makes the electrochemical behaviour in nc-materials different from conventional materials. Surface defects viz., grain boundaries, dislocations and triple points serve as anodic sites [255-257] and result in higher anode area which results in higher corrosion rate. Therefore, it was believed that corrosion rate of nanocrystalline material would be higher [236,243,258-264]. However, grain boundaries are also preferential sites for precipitation and enhances diffusion rate by providing channels for faster diffusion which may improve the corrosion resistance of nanocrystalline materials.

In contrast to above discussion, corrosion resistance of some materials is reported to be superior in nanocrystalline form [265-268]. For example, improved corrosion resistance is reported in nanocrystalline Zr -based alloys [265,269-272] and Fe-B-Si intermetallics system to gaseous corrosion, and that of an iron aluminide[266] system to electrochemical dissolution.

Corrosion is a very complex process and various parameters work together. To make a general overview, material/environment system can be characterized as following:

1. No passivation (corrosion products are soluble)

2. A passive film is formed on the material/environment interface which protects further corrosion (these materials can be further divided as (a) pure metals for example, Al in a few environments (b) alloys where diffusion of alloying elements plays a major role in the passivation for example, Fe-Cr system).

Fe is a material which shows passivation due to the formation of an oxide layer in oxidizing environment like, H_2SO_4 . The addition of Cr improves corrosion resistance by formation of passive layer of chromium

2.6.1 Factors affecting the corrosion resistance in nanocrystalline materials

Further, to avoid confusion, parameters which can make difference in the corrosion of nanocrystalline and microcrystalline materials are briefly described here:

2.6.1.1 Diffusivity of alloying elements and impurities

Material environment systems, where solute atoms play crucial role (by forming passive film or destroying passive film), the corrosion kinetics, highly, depends on diffusion process. Diffusion of elemental and ionic species in alloys may occur with the assistance of lattice defects such as vacancies/dislocations or other high defect areas such as grain boundaries. Grain boundary diffusivity is known to be far greater than equivalent lattice/volume diffusion, particularly, in the lower temperature regime (the 'low temperature regime', i.e., typically, $<0.5-0.8T_m$, varies, depending on the alloy and the diffusing species in consideration). Since nanocrystalline materials have considerably high volume fraction of grain boundaries, types of corrosion of such materials that is assisted by diffusion has been reported to be strongly influenced due to their nanostructure. However, the nature of the influence of nanostructure on the diffusion-assisted corrosion depends on the nature of the predominantly diffusing

species in a given alloy-environment system. For example, corrosion resistance of a nanocrystalline Ni-P [243] alloy is reported to be considerably lower and that of nanocrystalline Co-P [248] is higher than their microcrystalline counterparts. This behaviour is attributed to the influence of phosphorus in Ni-P and Co-P, the predominantly diffusing species, on corrosion. For the systems, where predominantly diffusing species provide corrosion resistance (such as by formation of a protective film), nanocrystalline structures have beneficial effects. For example, the corrosion/oxidation resistances of an iron-aluminide and an FeBSi alloy in the nanocrystalline state are reported [265,266] to be superior to those of in their microcrystalline state. This behaviour is attributed to Al and Si, the well-known protective oxide film formers, being the predominantly diffusing species respectively in the two alloys, and the nanostructure facilitating their diffusion and early formation of protective films (of Al/Si oxide).

Diffusivity of alloying or impurity elements in nanocrystalline materials is much higher than the polycrystalline materials. Examples of such materials may be stainless steel, Ni-P, Co-P etc. An example of enhanced diffusivity of Cr in nanocrystalline iron is presented here, where diffusion coefficient of nanocrystalline material is four orders of magnitude higher than grain boundary diffusion coefficient [3] (supporting the view of distorted grain boundaries in nanocrystalline material).

Table 2.4 Diffusion coefficients of Cr in nanocrystalline (NC) and microcrystalline (MC) Fe, in comparison with the lattice and GB diffusivities of Cr in α -Fe [3]

Temperature	NC iron (D_n) m^2/s	MC iron (D_m) m^2/s	Lattice (D_v) m^2/s	GB (D_b) m^2/s
300°C	1.7×10^{-17}	--	1.2×10^{-26}	8.6×10^{-22}
340°C	1.6×10^{-16}	--	3.7×10^{-25}	1.7×10^{-20}
380°C	2.8×10^{-15}	3.6×10^{-19}	7.6×10^{-24}	2.3×10^{-19}
840°C	--	2.2×10^{-15}	1.5×10^{-15}	3.7×10^{-12}

2.6.1.2 Higher nucleation sites for nucleation of passive film

Grain boundaries are anodic in nature and also provide heterogeneous sites for nucleation of secondary phase, i.e. passive film. Therefore, nanocrystalline materials are composed of comparatively large fraction of nucleation sites leading to a uniform and rapid growth of passive film. Large fraction of closely- distributed grain boundary enhances the passive film growth rate. *Schematic representation is shown below in Figure 2.19*

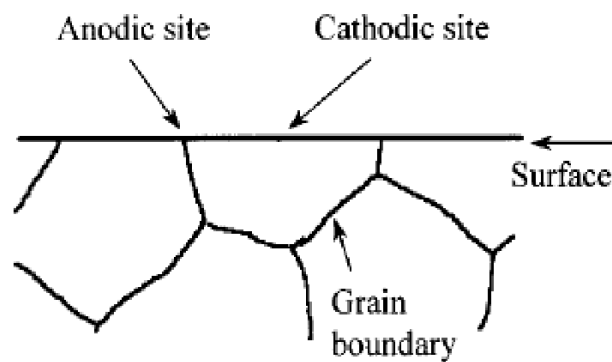


Fig. 2.19 Schematic diagram showing grain interior and boundaries as cathodic and anodic sites, respectively.

2.6.1.3 Anode-to-cathode area ratio

Grain boundaries suffer localized corrosion because these are highly anodic to the adjacent area within the grains. The thermodynamic driving force for corrosion is equal to difference in equilibrium potentials of grain boundaries, anodic sites (E_a) and grains, cathodic sites (E_c):

$$\Delta E = E_a - E_c \quad \text{--- (22)}$$

In microcrystalline alloys where anode-to-cathode area ratio is greater, the severity (depth) of localized galvanic corrosion will be considerably high [273,274]. With considerable increase in grain boundary (anodic) area in the nanocrystalline materials, the cathode-to-anode area ratio is expected to be less favourable for the progress of localized galvanic corrosion, and, some investigations have shown that

localized corrosion is circumvented [119,252]. Ultra fine grain (UFG) copper, made by severe plastic deformation, has high dislocation density within the grains, which makes the grains more anodic and, thus, localized corrosion is prevented. But, annealing for short duration of time annihilates dislocations and localized corrosion at grain boundaries is observed [252]. The larger the value of ΔE , the higher the localized corrosion rate is. In Nanocrystalline materials where grain boundary energy is greater than that of microcrystalline alloys, large value of ΔE can lead to higher intergranular corrosion, in spite of lower cathode-to-anode area ratio. Most of the experimental results showing decrease in intergranular corrosion in nanocrystalline materials are based on SEM observation which may be beyond the resolution limit. Careful observation, using high resolution techniques down the nano-meter range (like AFM or high resolution SEM), would reveal the actual picture.

2.6.1.4 Change in thermodynamic properties

Nanocrystalline material possesses highly disordered grain boundaries and large amount of defects, which can change the Gibbs free energy, which, in turn, is directly related to corrosion potential of the material ($\Delta G = -nFE$). Kirchheim [260] et al. have measured difference between nanocrystalline and single crystalline materials and shown that following relationship holds true:

$$\Delta E = -\frac{\mu_{nc} - \mu_{sc}}{nF} = -\frac{\Delta G}{nF} \quad \text{--- (23)}$$

Where μ_{nc} and μ_{sc} are chemical potential of the metals in nc and single crystal form. Various studies have shown the change in corrosion potential in nc material. For example a little increase in corrosion potential is noticed in Co [119] and Ni [236,275].

2.6.1.5 Adsorption

Higher adsorption of gases may change the kinetics of reactions involving gaseous reactant, for example, reduction of hydrogen ion, H^+ , occurs in three steps and any of them may be rate determining:

- a) $H^+ + e^- = H_{ads}$
- b) Two of these adsorbed hydrogen atoms must react to form hydrogen molecule: $H_{ads} + H_{ads} = H_2$
- c) A third step requires sufficient molecules to combine and nucleate a hydrogen bubble on the surface.

Any of these steps can control the rate of reaction and can cause activation polarization. Enhanced kinetics of step 'b' leads to increase in hydrogen ion reduction rate and therefore, overall rate and corrosion potential of reaction [1]. In some metals, enhanced adsorption is noticed and change in value of E_{corr} in Ni- based alloys is explained on the basis of change in kinetics of above reactions [236,275,276].

2.6.1.6 Passive film

Passive film itself may be different in nanocrystalline material. In pure metals, it may be more uniform and compact (due to the presence of large number of nucleation sites). Adherence of passive film and microstructure would be different that can bring appreciable change in corrosion rate.

Zhang et al. [277] have tried to explain high temperature corrosion of Zr assuming that the reduced grain size can affect the oxidation rate constant. They presented a mathematical model, based on Wanger's theory and electron theory of solid and, shown that oxidation rate constant can be described as:

$$k = D \times (1 + Z) \times Z \times C_o \times \left(1 - \frac{C_o^a}{C_o^b}\right) \times 2 \quad \text{--- (17)}$$

$$\text{Where, } D = r \frac{Nk_B T l_{eff}}{m v_F n} \times (1 + Z) \text{ and } \frac{1}{l_{eff}} = \frac{1}{R} + \frac{1}{l_{bulk}} \quad \text{--- (18)}$$

Details of above equation can be found in [277]. Value of k is size depend and it is shown that in nanocrystalline metals, electronic mean free path can be influenced by the grain size and it reduced in nanocrystalline materials, which leads to lower oxidation constant and therefore improved resistance towards oxidation. Based on the above model, two experimental results are explained successfully.

2.6.1.7 Electronic Structure of nanocrystalline metals and alloys

It has been shown that passivity of metals also depends on electronic structure. Passivation phenomenon in metals and alloys, in general, falls into four categories: (1) metal modification, (2) reaction rate, (3) oxide film and (4) adsorption. These phenomena have been reviewed by the Uhlig in 1960's [278]. It has been shown that the electronic interactions within the metals affects the corrosion rate of materials by modifying the reactivity, type and structure of passive film formed on the metal or alloy surface. In nanocrystalline materials, the expected change in electronic structure and, therefore, accelerated adsorption and chemisorption phenomenon would lead to a different passivation mechanism and hence corrosion rate.

2.6.1.8 High Fraction of triple points

Bollman [279, 280] has demonstrated that the triple-points in polycrystalline materials can be interpreted as line defects with structural characteristics dependent on the specific interaction of adjoining grain boundary dislocation of arrays. The effect of triple points on the corrosion behaviour of

microcrystalline material is investigated [281] and this can be important in nanocrystalline materials where large fraction of triple points are present. The effect of triple points on corrosion of nanocrystalline materials has yet to be investigated.

Higher grain boundary area fraction enhances diffusion of alloying elements and impurities and at the same time increases anode-to-cathode area ratio which is not favourable for localized corrosion of grain boundaries. It also provides active sites for preferential attack and accelerates overall corrosion rate. Structure of grain boundary in nanocrystalline, material may lead to high adsorption and chemisorption rates which may further affect corrosion rate in material. All these parameters act simultaneously and have to be investigated in each material/environment system.

2.6.2 Corrosion in Fe and Fe- based Nanocrystalline materials

Corrosion of Iron and Fe-Cr alloys in their microcrystalline form is well characterized. Passivation is privileging corrosion resistance mechanism in anodic region of Fe and Fe-Cr alloys and inhibits the further corrosion of these alloys. As discussed above, the four phenomena are responsible for passivation [278,282-289]. Oxide film theory [278,285,290,291,292] suggests that diffusion barrier, imposed by oxide passive film (Fe_2O_3 in iron and $\text{Fe}_2\text{O}_3/\text{Cr}_2\text{O}_3$ in Fe-Cr alloys) prevents corrosion, therefore, enhanced diffusivity of Cr and more number of nucleation sites for passive film formation improve corrosion resistance of nanocrystalline Fe-Cr alloys [284]. In fine grain size materials larger number of grain boundaries provide path for faster diffusion of impurities and solute atoms, which largely affects the corrosion behaviour of material. A Fe-Cr alloy during oxidation forms an outer layer of Fe_2O_3 , and an inner layer of Cr_2O_3 [293]. The kinetics of formation of protective layer of Cr_2O_3 depends on the supply of chromium by diffusion in the alloy matrix, which is governed profoundly by grain size of the alloy. Typical 18Cr-8Ni stainless steels develop duplex oxide scales during oxidation [294]. The outer

scale is always Fe_2O_3 , whereas, the composition of the inner scale varies with alloy grain size. A fine grain ($\sim 17\mu\text{m}$ or less) alloy easily develops a uniform layer of Cr_2O_3 . For an alloy with grain sizes greater than $\sim 40\mu\text{m}$, this protective layer of Cr_2O_3 was difficult to form due to insufficient chromium supply, and an inner layer of $(\text{Fe,Cr})_3\text{O}_4$ continued to grow. The diffusion of elements is significantly higher in nc-form. Diffusion coefficient of Cr in Fe-Cr alloy at 300°C is reported to be higher than that of grain boundary diffusion coefficient at 600°C [3]. Therefore, formation of protective Cr_2O_3 layer is much faster and it may develop at much lower chromium contents as well as at much lower temperatures, thus enabling less expensive stainless steel.

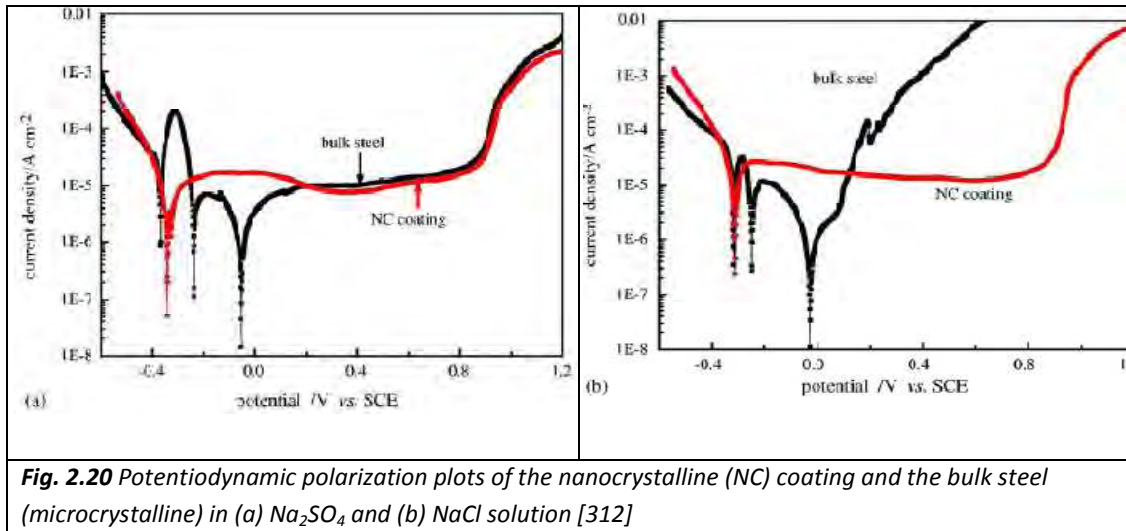
Metal modification theories and adsorption theories of passivation [278,295-303] suggest that passive film formed on Cr, Fe and Fe-Cr alloys is probably chemisorbed and/or adsorbed oxygen. The film supposedly served, diminishes chemical reactivity of the metal/environment interphase. The adsorbed oxygen film, sometimes less than a monolayer thickness, is the primary source of passivity in transition metals and their alloys; the unfilled “*d*” electron levels of the metal favouring a chemisorbed bond. These theories have been discussed in literature. To the interest of current study, change in the electronic structure and, therefore, adsorption and chemisorption phenomena [304] in nanocrystalline material may significantly change the corrosion mechanism and corrosion rate in nanocrystalline materials. Nanocrystalline materials are suggested to have electronic structure, different from the microcrystalline materials of similar compositions [305,306]. Some investigations have shown enhanced adsorption and chemisorption in nanocrystalline form of the material [307]. However, none of these factors has been well understood in case of nanocrystalline Fe and Fe-based alloys. Research in this area is in early stages and more work is required to understand these phenomena and their relevance to corrosion mechanism.

Recently, some attention has been paid to investigate corrosion properties of nanocrystalline Fe and Fe-based alloys [101,170,308-310]. Immersion tests, potentiodynamic polarization curves and EIS scans have shown improved corrosion resistance of nc-Fe in both HCl and H₂SO₄ solution [308], though mechanism of corrosion in nc-Fe is not understood precisely. Kedim et al. [170] have reported passivity both in nc and mc- Fe in 0.5M sulphuric acid (pH=0.3) solution [170] and increase in passivation domain width is observed in nc-Fe. Similar results are found in an earlier investigation by Kedim et al. [101] in 0.1 M sulphuric acid solution but microcrystalline Fe does not show passivation. Passive region seen in nc-Fe is not predicted by Pourbaix diagram. In most of the above examples of nc-Fe some sort of technique that involves severe plastic deformation is used to make nc-surface.

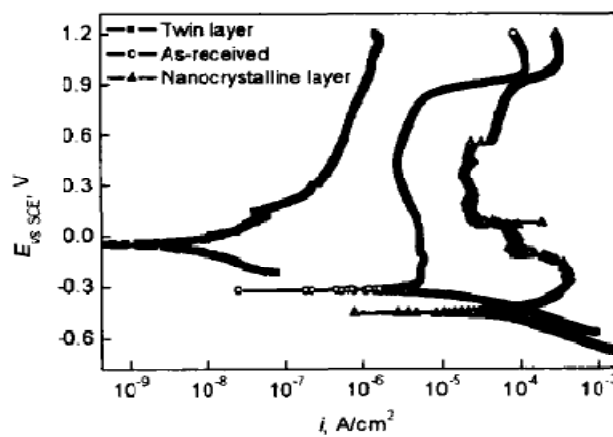
In recent years, attempts have been made to understand corrosion behaviour of nanocrystalline steels and to compare with their microcrystalline counterpart. The nc-steels for such studies have generally been produced by surface mechanical treatment and have shown improved corrosion behaviour in various solutions [311-317]. However, decrease in corrosion resistance of nc mild steel is reported [316]. Potentiodynamic polarization and EIS tests have demonstrated improved corrosion resistance of nanocrystalline stainless steel in NaCl solution. Nanocrystalline 316 stainless steels show lower susceptibility to pitting corrosion and higher re-passivation power in NaCl solution. This is attributed to faster corrosion rate of Cr and easy formation of protective film in case of nanocrystalline steel. Improved corrosion resistance can be explained on the bases of above discussion, rapid formation of compact and uniform passive layer [311,314,317].

Electron Work Function, EWF, (measured by Scanning Kelvin probe), of passive film is greater in case of nanocrystalline material, which shows better electrochemical stability and improved protective role of passive film [317]. Nanocrystalline 309 stainless steel shows improved corrosion resistance in 0.5M NaCl

+ 0.05M H₂SO₄ solution, whereas the resistance is similar to its microcrystalline counterpart in 0.25M Na₂SO₄ + 0.05M H₂SO₄ solution (Figure 2.20).



Opposite to above studies, Lu et al. [263] have found that corrosion resistance of nanocrystalline 316 steel in 0.05M H₂SO₄ + 0.25M Na₂SO₄ decreases and is attributed to the higher corrosion rate at grain boundaries and triple points, present in the nanocrystalline form (Figure 2.21). Figure 2.22 shows the preferential corrosion of grain boundaries in microcrystalline steel while localized corrosion of grain boundaries in nanocrystalline is circumvented because of higher anode-to-cathode area ratio. The whole surface corrodes uniformly and higher anode area ratio leads to increase in overall corrosion-rate.



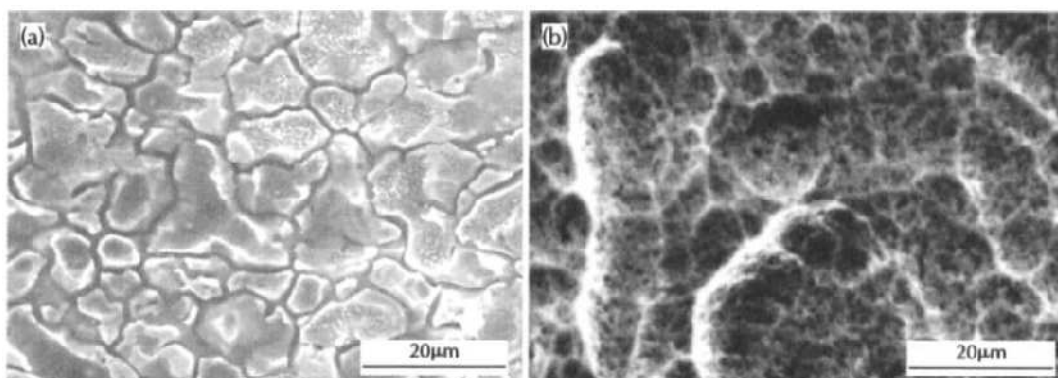


Fig. 2.22 SEM morphologies of the samples in solution of $0.05M H_2SO_4 + 0.25M Na_2SO_4$ at an anodic potential of about $0.9V$ (vs. SCE), the surface layer of the as-received microcrystalline sample (a), the nanocrystalline layer (b) [263]

Corrosion resistance of Nanocrystalline Fe and steels is investigated in various solutions and, in most of the cases, improved corrosion resistance is observed in nanocrystalline form which can be understood on the basis of easy passive film formation. Higher diffusion rate of Cr in nanocrystalline forms lead to the formation of a uniform and Cr rich layer and hence improved corrosion resistance. However, the role and validity of reaction velocity, metal modification, and adsorption theories in nanocrystalline Fe and Fe- based have to be investigated for the better understanding of passivation mechanism. Intergranular corrosion has to be investigated with high resolution techniques, i.e., AFM.

2.7 Role of grain size in oxidation resistance of Fe-Cr alloys

The unique structure, high grain boundary area fraction, diffusion of impurities and alloying elements, and change in thermodynamic properties of nanocrystalline materials may also lead to considerable difference in oxidation behaviour when compared to their microcrystalline counterparts with same chemical compositions.

The effect of the alloy grain on the high-temperature oxidation resistance has attracted much attention during the past few decades. Giggins and Pettit [318] reported that a reduction in grain size caused improvement in the oxidation resistance of Ni-Cr alloys. Merz [319], and Basu and Yurek [320] reported that the formation of protective Cr_2O_3 scales on stainless steels is facilitated by the decrease in grain size. However, the grain refinement was limited to a few microns in these studies. Suggested factors for improved oxidation resistance are the faster grain boundary diffusion of Cr and more number of probable nucleation sites for the protective oxides. On this basis, the grain refinement to nano-scale level should result in an extra-ordinary improvement in oxidation resistance. However, thermodynamically unstable nature of nanocrystalline structure may enhance the oxidation rate. The possible factors affecting the oxidation rate and causing superior or inferior oxidation resistance are elaborated below:

2.7.1 Inferior oxidation resistance caused by nanocrystalline structure

Presence of large fraction of grain boundaries and lower co-ordination number of atoms present in nanocrystalline materials may lead to increased oxidation rate. X-ray absorption fine structure (XAFS) measurements, performed on nanocrystalline Ni, showed a lower co-ordination number of nanocrystalline Ni in comparison to microcrystalline Ni, indicating a greater susceptibility to oxidation [321]. Geng et al. [322] have also shown greater oxidation of nc Ni than its microcrystalline counterpart. Possible mechanism for the increase in oxidation rate can be understood on the basis of:

1. Increased reactivity of the nanocrystalline alloys as greater surface area is occupied by grain boundaries (i.e., high energy sites).

2. Increase in oxide nucleation sites and, therefore, formation of oxide scale with comparatively finer grain size through which diffusion of oxygen and metal is faster because of enhanced diffusion through the grain boundaries [322].
3. In the case of metals and alloys where the solute atoms are sufficiently low and internal oxidation continues, the oxidation rate may be enhanced because of increased diffusivity of oxygen through grain boundaries leading to severe internal oxidation near the grain boundaries.

2.7.2 Improved oxidation resistance caused by the nanocrystalline structure

Nanocrystalline structure, in general, causes improvement in oxidation resistance of alloys where solute atoms have beneficial role on oxidation resistance. Improvement in oxidation resistance of majority of engineering alloys where solute atoms have beneficial role on oxidation is noticed in their nanocrystalline form. Improved oxidation resistance of FeBSi [265], Ni-based alloys [323-327], Zr and its alloys [277,328], Cr-33Nb, Fe-Co based alloys [329], and Cu-Ni-Cr alloys [330] is reported in their nanocrystalline form (in comparison to their microcrystalline counterparts). Mechanistic role of nanocrystalline structure in oxidation resistance is discussed below:

a) Higher diffusivity of atoms and formation of a protective scale

Certain alloys can develop a continuous layer of the protective oxide of more reactive alloying element which forms basis for the development of oxidation/corrosion resistance of alloys. Such alloys are Fe, Ni, Co based, with Al, Cr or Si as the reactive alloying additives. Oxidation behaviour of binary alloys such as Fe-Cr alloys have been studied widely. It has been established for several binary alloys such as Fe-Cr, Co-Cr, Ni-Cr etc. that when time-dependent inward flux of oxygen is less than the time-dependent outward flux of solute, a continuous layer of oxide is formed at or very near the surface. This is called “external oxidation”. If, on the other hand, the

inward flux of oxygen exceeds the outward flux of solute, internal oxidation occurs, producing a more-or-less disconnected dispersion of oxide (particularly, in alloy with small solute contents). For external oxidation to occur, a critical concentration of solute is required which has been calculated by Wagner [331-333] in various conditions. Critical amount of solute for such a transition depends on the diffusion coefficient of solute in the alloy. Given that the nanocrystalline material comprises a high volume fraction of grain boundaries, diffusion coefficient of solute may increase to the level that critical solute concentration for internal to external transition may be substantially low.

That the nanocrystalline structure may facilitate the formation of protective oxides has been examined for nanocrystalline FeBSi alloy [265] and Al in Ni-11Cr-8Al [323,325,326]. Such reports, though extremely limited, point to an alternative hypothesis that it may be possible to achieve corrosion resistance at considerable low concentrations of reactive elements.

b) Lateral growth of passive film

Lobb and Evans [334] have reported an improvement in the oxidation resistance of fine grained conventional microcrystalline as a result of grain boundary area which acts as the preferential nucleation site for Cr_2O_3 . This effect may be considerably increased in the case of nanocrystalline alloys which comprise comparatively large fraction of grain boundaries and triple points. This view is supported by other authors in a few nanocrystalline alloy systems [265,327].

c) Enhanced adsorption and chemisorption phenomena

Nanocrystalline surfaces may possess significantly different adsorption and chemisorptions phenomena which form initial stage of oxidation.

d) *Structure of oxide scale*

Nanocrystalline structure of substrate may influence various physical properties of oxide film viz, crystal size morphology and crystallographic orientation of oxides formed, lattice mismatch with the base metal, adhesion of oxide layer and hence can influence the stresses in the scale and oxidation behaviour. For example, fine grained oxide scales often show a fast creep rate at high temperatures, releasing the stresses accumulated in the scales and, therefore, decrease in scale spallation tendency. Change in the surface grain structure causes more adherent passive layer resulting in improved oxidation resistance [326,327]. Experimentally, it has shown that higher electron work function leads to stronger adhesive forces forming a more adhesive passive layer.

Based on Wagner's theory [331-333] and electron theory of solids, Zhang et al. [277] have proposed a model which shows that reduced conductivity caused by reduced grain size suppresses the transport of the oxidizing species across the passive film, resulting in improved oxidation resistance of Zr and Zr based alloys [277]. However, this model has not been examined for other alloys.

It is important to note that the above factors can operate both indifferently and in combination. However, there are concerns regarding studies carried out so far on these topics, i.e., these studies have generally been performed at substantially high temperatures where grain growth would be taking place during the oxidation tests. Further nanocrystalline samples used in different studies were processed by quite different routes than their microcrystalline counterparts. Such differences may lead to considerable variations in defect contents, phases etc. between the nanocrystalline and microcrystalline test materials. It is likely that the factors other than grain size may affect the observed difference in oxidation behavior.

2.8 Nanocrystalline Fe based alloys

Nanocrystalline alloys are very interesting, particularly for their extended solid solubilities. Therefore, phase diagram of nanocrystalline alloy may differ from their conventional counterpart. Various Fe-based alloys have been prepared and studied [335] for example, Caer[154] et al. have shown mixing of iron with elemental powder mixtures. In the current study example of Fe-Cr, Fe-Ni and Fe-Cr-Ni alloys are discussed briefly.

2.8.1 Nanocrystalline Fe-Cr alloys

Feritic steels with high Cr contents find several applications because of their high abrasion resistance, and good corrosion resistance in oxidizing acids, numerous salt solutions, and in marine or industrial environment. These properties can be further enhanced by reducing their grain size to nano range (less than 100 nm). Mechanical alloying has been used as a viable process to synthesise nanocrystalline Fe-Cr alloy powders [336-340]. Structural and compositional changes during mechanical milling of Fe-Cr system have been studied using various characterization techniques like SEM, TEM, XRD, AFM and Mössbauer spectroscopy [139,153,337,341,342]. The difference in lattice parameter of Fe and Cr is only ~0.5%. Hence, it is difficult to monitor the progress of alloying during ball -milling through XRD analysis.

The Fe-Cr phase diagram shows a miscibility gap below 830°C over a wide range of composition (Figure 2.23). Thus Fe-Cr solid solutions can be decomposed into Fe-rich and Cr-rich solid solutions over a temperature range of 400°C and 830°C. Below 400°C, the diffusion of one species to other is to cause partitioning. However, a possibility of partition exists even at low temperature during high energy ball -milling and may inhibit the formation of homogeneous alloy. The Fe-Cr phase diagram also shows the existence of sigma phase over a narrow composition range (~ 42 to 49 wt.% Cr). The sigma phase drastically deteriorates the mechanical properties and will also affect the corrosion properties of the

alloy. Costa et al. used Sn as additive in Fe-Cr alloy to inhibit the formation of sigma phase, and it is effective in both nanocrystalline and conventional coarse grain alloy [343,344].

Consolidation of nanocrystalline Fe-Cr alloy without significant grain coarsening is a challenging task. Most of the investigations are limited to the characterization and study of magnetic properties. Not many attempts are made to consolidate these materials. Gupta et al. [162] have consolidated pre-annealed Fe-10Cr under 2.7 GPa pressure and then sintered at 600°C for 1 hour and achieved a good density. This technique would be an alternative of hot compaction. Thermal stability has also been studied [162] and it shows that Fe-10Cr alloy does not show excessive grain growth till 600°C. *Nano-indentation and microhardness tests give a hardness value of 6.5 GPa and young modules approximately equal to 165 GPa (Unpublished work)*. Increasing Cr content leads to increasing hardness and decrease in grain size [345]. This alloy shows improved corrosion resistance in nanocrystalline form. Faster diffusion kinetics of Cr improves resistance towards gaseous and aqueous corrosion [3,314].

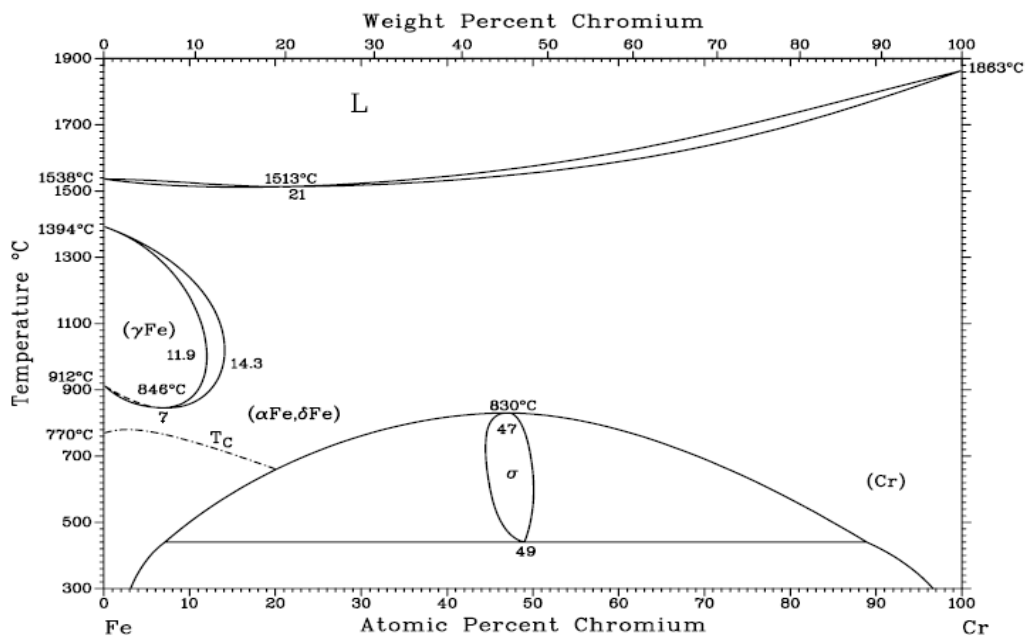


Fig. 2.23 Fe-Cr Phase Diagram[346]

Magnetic properties of nanocrystalline Fe-Cr alloys can be explained assuming two phase models (IC and CC), as discussed in section 2. Properties of Fe-Cr nanograin are close to conventional microcrystalline alloy, but the intergranular region is very disordered, therefore, weakly magnetic. Global magnetization of the nanocrystalline Fe-Cr alloy samples is lesser than microcrystalline material. Mechanically alloyed Fe-Cr alloy seems to show same kind of SGL behaviour (but in some composition range) as in microcrystalline behaviour. Freezing temperature of nc-Fe-Cr alloys is reduced [340].

2.8.2 Nanocrystalline Fe-Ni alloys

The Fe-Ni alloys belong to a technologically important class of alloy systems called permalloy have attracted considerable attention for their special magnetic, thermal and mechanical properties [347-351]. Severe plastic deformation of these alloys in various kinds of high-energy mechano-activators and electrodeposition enables one to obtain alloy with new structures and properties [352,353]. The addition of nickel to a plain-carbon steel tends to stabilise the austenite phase over a wide temperature range, by raising the A_4 temperature and depressing the A_3 as shown in the Fe-Ni phase diagram (Figure 2.24). Thus, the addition of 25% nickel to pure iron renders it austenitic, even after slow cooling to ambient temperatures. The effect of nanocrystallization on martensitic transformation and magnetic properties of Fe-Ni alloys is interesting. High energy ball -milling is the predominant technique adapted to synthesize nanocrystalline Fe-Ni alloys. A detailed study of Fe-Ni alloys synthesized by high energy ball- milling suggests extended single phase solid solution phase fields (α -FeNi and γ -FeNi) [353-356]. Figure 2.25 shows the phase boundaries for Fe-Ni alloys processed by different methods.

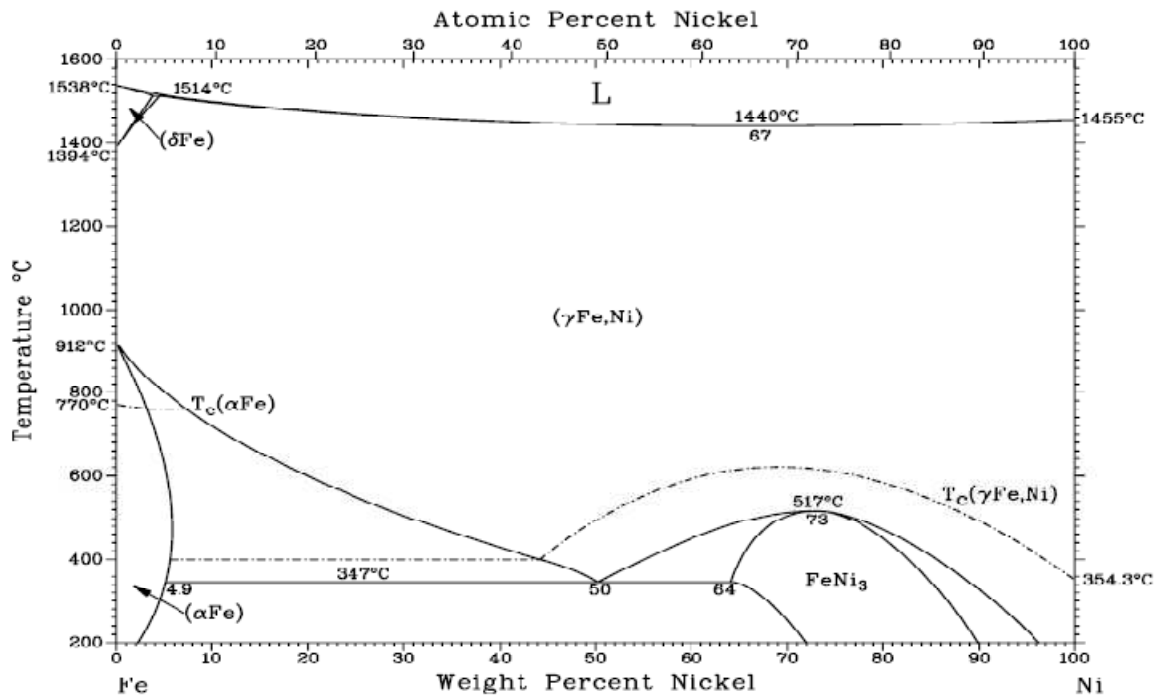


Fig. 2.24 Fe-Ni Phase Diagram[346]

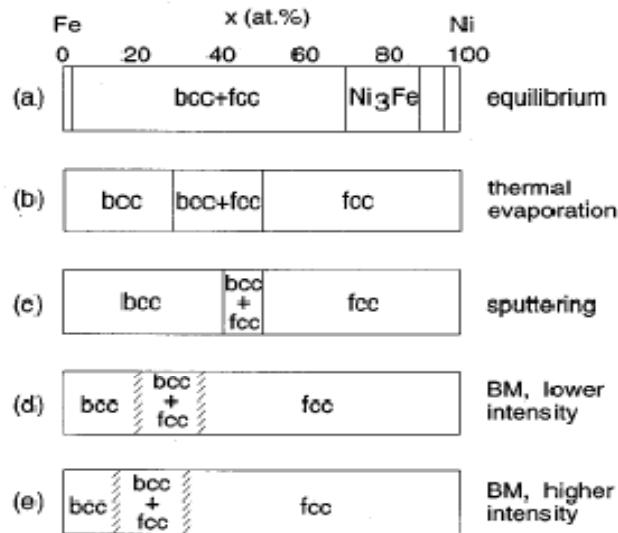


Fig. 2.25 Phase boundaries for Fe–Ni alloys processed by different methods: equilibrium, evaporation, sputtering, ball- milling at low intensity and ball- milling at high intensity [355]

Martensitic formation has also been observed during mechanical alloying of Fe-Ni [356-358]. The grain size of Fe-30Ni is 20 nm and Fe-35Ni is 18 nm after 20 h of milling, but, in spite of the same milling procedure, different microstructures are obtained with further milling. Therefore, the nickel content and its minor variation are crucial for the transformation tendency during mechanical alloying of Fe-Ni powders. The schematic of phase formation of Fe-30Ni and Fe-35Ni is presented in Figure 2.26. It can be seen that the martensitic transformation takes place during mechanical alloying of Fe-30Ni, while the reverse transformation of martensite into austenite occurs with further milling of Fe-35Ni powder. However, the reverse transformation temperature of mechanically alloyed nanocrystalline Fe-Ni is higher than the microcrystalline alloys [359].

The coercivity of ball-milled Fe-Ni alloy is of the order of 4-40 A/cm, which is treated as high [360]. However, the coercivity of ball-milling Fe-Ni could be due to strain induced during high energy ball-milling. Nanocrystalline materials are expected to have excellent soft magnetic characteristics [361] which means low coercivity. A recent investigation of Fe-Ni alloys shows lower value of coercivities (at lower temperature as low as 5K). The temperature dependence of saturation magnetization follows Bloch behaviour with a Bloch constant, which is higher, compared to that for typical ferromagnetic metals and alloys [362].

Ni-Fe nanocrystalline alloy with a grain size of about 30nm was synthesized by electrodeposition [115]. Grain size dependence of strength has been found to undergo a transition at a grain size of 14nm, below which the alloy shows an inverse Hall-Petch relationship.

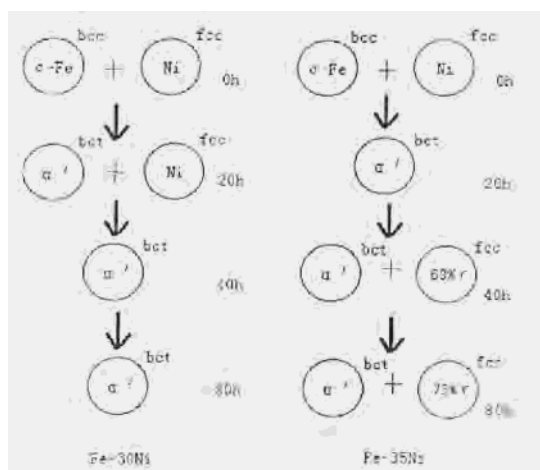


Fig. 2.26 Schematic of phase transformation during mechanical alloying of Fe-Ni powders [357]

2.8.3 Nanocrystalline Fe-Cr-Ni alloys

Fe-Cr-Ni alloys and stainless steels are the most common containing various amounts of Cr and Ni. Corrosion resistance is attained with additions of a minimum of 13 wt. % Cr. However, alloys with up to 26% Cr may be required for application in harsh environments. Nanocrystalline Fe-Cr-Ni alloys or stainless steels are expected to exhibit superior corrosion resistance because of their superior passivation characteristic. [273]. There have been limited studies on nanocrystalline stainless steel. Leinartas et al.[363] deposited a nanocrystalline coating with 14.2 wt.% Cr and 9.4 wt.% Ni. The target used was AISI 316 stainless steel with 20.1 wt.% Cr and 9.4 wt.% Ni, suggesting a deficiency of Cr in the deposited film. Interestingly, in spite of this Cr deficiency, the anodic activity and breakdown potential indicated superior corrosion resistance of the nanocrystalline Fe-Cr- Ni alloy compared to AISI 316 stainless steel in both chloride and sulfate solutions [363]. Stainless steels can suffer to pitting in chloride environment, which includes breakdown of passivity, pit, nucleation and growth of and re-passivation phenomena [273]. Halide anions have an exceptional capability to break down the passivity. The local breakdown in passivity causing pitting is highly sensitive to certain microstructural inhomogeneities such as inclusions, secondary precipitates that cause electrochemical heterogeneities. However, the grain boundary area available on nanocrystalline alloys provides greater nucleation sites,

resulting in formation of relatively homogeneous and uniform passive film compared to the conventional microcrystalline alloys, which provide greater resistance to pitting [363].

Nanocrystalline stainless steels have been produced generally by different severe plastic deformation techniques. Primary investigations show that in-situ consolidation of nanocrystalline stainless steel is possible and it could be consolidated by hot compaction [167]. Improved corrosion behavior in both HCl and H₂SO₄ solution is observed and this is attributed to the ease of formation of the passive film of chromium oxide [311-315]. Similar to other nanocrystalline materials, stainless steels in nanocrystalline form show better mechanical properties.

As in the case of Fe-Cr alloys, nanocrystalline stainless steels also show certain deviation from equilibrium phase diagram (Figure 2.27). Enayati and Bafandeh [364] have shown that ball milled- Fe-18Cr-8Ni and Fe-15Cr-15Ni alloy is a single phase BCC solid solution, which differs from those predicted by equilibrium phase diagrams, formed by ball- milling of various compositions of Fe, Cr and Ni, identified and then annealed at 700°C. Gamma phase stability and grain growth increase with Ni content in the material. For lower chromium content (Fe-18Cr-8Ni) grain size of both α and γ phases are below 100 nm after heat treatment at 700°C.

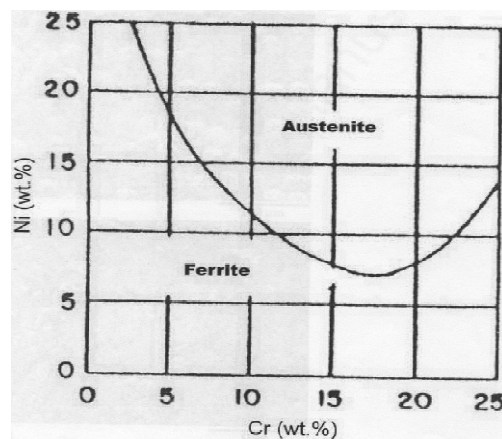


Fig. 2.27 The concentration range of stability of Ferrite and Austenite in Fe-Cr-Ni alloys [364,365]

2.9 Problems identified

This Literature review has presented a comprehensive and systematic study based on the investigations performed on the nanocrystalline metals and alloys. Structure of nanocrystalline materials is discussed which suggests the possibility of a structure composed of crystalline and intercrystalline regions with paucity of dislocations (below a critical grain size). Grain boundaries of nanocrystalline materials (nano grain boundaries) may be significantly different than the conventional grain boundaries. Hardness of these materials is several times higher than the conventional microcrystalline materials, although, in most of the cases these materials possess poor ductility. Grain growth at elevated temperatures, shown by most of the nanocrystalline alloys, limit their real life applications. Mechanism of grain growth is not precisely understood and, moreover, the data available in literature are not consistent.

Any engineering material in service condition is exposed to the environment and should exhibit enough resistance against the environmental degradation. However, limited attention is paid towards environmental degradation of these materials and a large discrepancy in reported data is noticed. There is a need of a thorough study to understand the difference between the corrosion/oxidation resistance of nanocrystalline and microcrystalline materials. Literature review clearly shows a possibility of improvement in corrosion resistance of some engineering metals and alloys by reducing their grain size to nano level.

Synthesis of these materials in the bulk form has been one of the biggest challenges. Synthesis of material in powder or in the form of thin film is possible but preparation of bulk samples with no artefact will be area of interest for the next couple of decades.

In view of the current review, following problems are identified and will be of interest in this research:

1. Effect of nanocrystalline structure on the oxidation resistance of Fe-Cr alloy has not been investigated yet. Therefore, this study will present a comprehensive investigation on the role of grain size on the oxidation resistance of Fe-Cr alloys.
2. The data reported in the literature on the electrochemical corrosion behaviour of nanocrystalline materials are not consistent and effect of grain size on electrochemical behavior of Fe-Cr based alloys has not been understood precisely. Present study compares the electrochemical corrosion resistance of Fe-Cr based alloys in their nanocrystalline and microcrystalline forms.
3. Synthesis of nanocrystalline samples has been a major challenge which limits the investigation of various properties as well as real life applications of these materials. This study presents a technique to consolidate the nanocrystalline powder of Fe-Cr material (produced by high energy ball- milling) after a systematic study of grain growth and hardness of these materials.
4. Structure of the nanocrystalline alloys is not understood precisely. However, understanding of the structure is important in order to determine various properties of these materials.
5. Data reported on the various mechanical properties is not consistent. Inverse Hall Pitch relationship is reported in some cases while many researchers do not support it. Neither the data are consistent nor has any theoretical understanding been developed. More over, these materials possess very poor ductility and, thus, underlying mechanism has to be understood and attempts should be made to improve the ductility.
6. Grain coarsening due to elevated temperatures is a major challenge and systematic experimental and theoretical investigations are necessary in order to understand the mechanism and to suppress the grain coarsening at higher temperatures.

CHAPTER 3

OBJECTIVES AND SCOPE

The present study has the primary motivation of demonstrating an effective resistance to corrosion (both high temperature oxidation and electrochemical corrosion) at considerably lower chromium levels in nanocrystalline alloys than in conventional microcrystalline alloys. High-Cr Microcrystalline Fe-Cr alloys (such as stainless steels) are the most commonly employed corrosion resistant materials. Stainless steels develop an inner layer of Fe/Ni/Cr oxide during initial stages of oxidation that eventually converts into a protective oxide, i.e. Cr_2O_3 . The kinetics of transition of Fe/Ni/Cr oxide into a protective layer of Cr_2O_3 depends on the supply of chromium by diffusion from the alloy matrix, which is governed profoundly by grain size of the alloy. Consistent with the mechanism that a fine grain structure should facilitate development of a protective scale, a fine grain ($\sim 17\mu\text{m}$ or less) 18Cr-8Ni stainless steel was reported to easily develop a uniform layer of Cr_2O_3 , whereas, it was difficult for a steel with a grain size greater than $\sim 40\mu\text{m}$ to develop the protective layer of Cr_2O_3 (due to insufficient chromium supply). In the light of the predominant role of diffusion in development of the protective layer of Cr_2O_3 , the phenomenon of grain boundary diffusion-assisted formation of protective layer in nanocrystalline materials may be advantageously exploited. For example, it may be possible to develop a protective film of Cr_2O_3 , even in alloys with much lower chromium contents (say, alloys with $<5\%$ Cr, as opposed to stainless steels which generally possess a minimum of 12 % Cr).

Electrochemical corrosion resistance (similar to oxidation resistance) also depends upon the development of Cr rich oxide layer at the alloy surface in contact with the electrolyte. Development of Cr rich passive film in the case of electrochemical corrosion is less clearly understood. However,

nanocrystalline structure may facilitate the Cr enrichment of corrosion film which may lead to improved corrosion resistance of nc form of the Fe-Cr alloys.

However, bulk monolithic samples of nanocrystalline alloys are required to investigate the corrosion properties. Preparation of bulk samples of nanocrystalline alloys is not a trivial task.

In view of the discussion, above, the objective of the current study can be summarized as:

1. To develop a suitable processing technique to prepare the test specimen of nanocrystalline Fe-Cr alloys
2. Preparation of test specimens of microcrystalline Fe-Cr alloys (by the same processing route for the purpose of consistency in properties resulting from processing)
3. Comparison of oxidation resistance of nanocrystalline and microcrystalline Fe-Cr alloys
4. Comparison of electrochemical corrosion resistance of nanocrystalline and microcrystalline Fe-Cr alloys
5. Understanding the mechanism of the observed differences (if any) in the oxidation as well as electrochemical corrosion resistance of nanocrystalline and microcrystalline Fe-Cr alloys

The present study provides a fair comparison between the oxidation /electrochemical corrosion resistance of nanocrystalline and microcrystalline Fe-Cr alloys and helps in developing the fundamental understanding of the observed differences between the electrochemical corrosion/ oxidation resistance of these materials. To the best of author's knowledge this will be the first study comparing the oxidation resistance of nanocrystalline and microcrystalline Fe-Cr alloys where, it has been established that nanocrystalline Fe-Cr alloys show, up to an order of magnitude, improvement in oxidation resistance in comparison to their microcrystalline counterparts. Most interestingly, the level of corrosion resistance

obtained in Fe-20Cr alloy in its microcrystalline form, can be achieved only by addition of 10% Cr (Fe-10Cr alloy) if the grain size is reduced to 50nm. This finding would have significant industrial impacts as the desired oxidation resistance can be achieved at lower Cr contents which may form basis for developing stainless steels with much lower Cr content and cutting down the cost in producing stainless steel. Development of the suitable processing route to synthesize nanocrystalline Fe-Cr alloys should certainly kindle the investigations of various properties of these materials and should be a milestone in ensuring the real life application of these novel materials. The scope of the present work can be summarized as:

1. Use of high energy ball- milling in synthesis of Fe-Cr alloy, and development of suitable processing route to synthesize bulk specimens from ball -milled alloy powders.
2. Study of grain coarsening behaviour of ball- milled nanocrystalline Fe-Cr alloys
3. Comparison of oxidation behaviour of nanocrystalline and microcrystalline alloys which would be the first study investigating the oxidation resistance of nanocrystalline alloys
4. Comparison of electrochemical corrosion resistance of nc and mc Fe-Cr alloys which becomes essential as the data reported in the literature are not consistent. The present research includes the first study investigating the electrochemical corrosion resistance of bulk nanocrystalline Fe-Cr alloys and comparing the corrosion resistance of nc and mc Fe-Cr alloy specimens, prepared by the same processing route i.e. high energy ball- milling annealing-compaction-sintering.
5. Achieving passivity against oxidation/electrochemical corrosion at relatively lower Cr content.
6. Developing the fundamental understanding of observed difference in oxidation/electrochemical corrosion resistance of nanocrystalline and microcrystalline alloys, on the basis of the analysis of the oxidation/corrosion films and fundamentals of oxidation/corrosion.

CHAPTER 4

EXPERIMENTAL DETAILS

The objectives of the present work (as discussed in the previous chapter) can be divided into three parts: (A) preparation of test specimens which includes synthesis of nanocrystalline alloy powders using high energy ball -milling, understanding of grain growth behaviour of nanocrystalline Fe-Cr alloys, consolidation of ball- milled powder to desired grain size and density, and characterization of the ball-milled nanocrystalline alloy powders and consolidated test specimens, (B) Comparison of oxidation resistance of nanocrystalline and microcrystalline Fe-Cr alloys at various temperatures, followed by characterization of the resulting oxide layer using secondary ions mass spectrometry (SIMS), and (C) Comparison of electrochemical corrosion resistance of nanocrystalline and microcrystalline Fe-Cr alloys using potentiodynamic polarization tests, followed by the chemical compositional analysis of corrosion film (developed over the samples during electrochemical tests) using XPS.

The test materials and experimental techniques required to achieve these objectives are described here:

4.1 MATERIALS

In order to prepare specimens of nanocrystalline and microcrystalline Fe-Cr alloys, the elemental powders of Fe and Cr were ball- milled in high energy ball mill. All the elemental powders used were 99.9% pure and were $\leq 10\mu\text{m}$ in size. These powders were obtained from Alfa-Aesar. Physical properties of Fe and Cr are presented in the Table 4.1.

Table 4.1 Properties of Fe and Cr

	Crystal structure	Vickers hardness (MPa)	Melting point (°C)	Density (g/cc)	Atomic radius (Å)
Fe	BCC	608	1535	7.874	1.72
Cr	BCC	1060	1857	7.19	1.85

4.2 HIGH ENERGY BALL- MILLING

High energy ball - milling was used to produce various compositions of the nanocrystalline Fe-Cr alloys. Alloys thus produced were in the powder form. Two types of ball mill were used in the present study. Planetary ball mill was used initially to develop basic understanding of the ball-milling process. A shaker ball mill was used in the later stage and the specimens used for the oxidation and aqueous corrosion tests, in the present study, were prepared using a shaker ball mill. Details of the experiments are given below:

4.2.1 Planetary Ball Mill

High energy ball -milling experiments were carried out in Fritsch Pulverisette P-5 planetary ball mill with tungsten carbide (WC) as milling media and a ball to powder ratio (BPR) of 10:1, and at a speed of 300 rpm. Milling operation was carried out in the presence of toluene as process control agent (PCA). Toluene prevents oxidation, excessive cold welding and agglomeration during high energy ball- milling. The process variables that have been used in the present study are summarized in Table 4.2.

Fe-Cr alloy powders with a grain size of approximately 13nm were produced using high energy ball - milling which needs to be compacted. As will be discussed in the Chapter 5, attempts to consolidate

these alloy powders were not successful. Therefore, next set of experiments were performed using a shaker mill.

Table 4.2 Process variables used in the planetary ball mill

Parameter	Process variable
Type of mill	Fritsch Pulverisette P-5 planetary ball mill
Milling container (Vial)	Tungsten Carbide (WC)
Grinding ball	Tungsten Carbide (WC)
Size of ball	10 mm \emptyset
Ball to powder ratio (BPR)	10:1
Extent of filling the vial	1/3
Milling speed	300 rpm
Milling time	20h
Milling medium	toluene

4.2.2 Shaker ball mill

As starting materials, high purity powders of Fe (99.9% purity and particle size < 10 μm) and Cr (99.9% and particle size <10 μm) were loaded into a tool steel vial under vacuum with 440C stainless steel balls (6.4-7.9mm in diameter). Ball-to-powder weight ratio was kept at 10:1. High energy ball- milling was carried out for 20 hours in SPEX Model 8000 shaker mill which was air cooled. For ball- milling, the metal powders were loaded into the vial in the controlled atmosphere glove box where oxygen content can be mainlined as less as 80ppb. Powders were loaded in the glove box and then vacuum (in the vial) was created in the transfer chamber of the glove box.

The process variables that have been used in the present study are summarized in Table 4.3.

Table 4.3 Process variables used in the shaker mill

Parameter	Process variable
Type of mill	SPEX Model 8000 shaker mill
Milling container (Vial)	440C grade steel
Grinding ball	440C grade steel
Size of ball	6.4 and 7.9 mm ϕ
Ball to powder ratio (BPR)	10:1
Extent of filling the vial	1/3
Milling time	20h
Milling medium	vacuum

4.3 Annealing of the ball- milled powder

In order to investigate the grain growth behaviour of ball- milled nanocrystalline Fe-Cr alloys annealing experiments were performed at a range of temperatures and durations of time. Annealing of the ball-milled powders was performed at a range of temperatures and for varying periods of time in a tube furnace in a forming gas atmosphere. For each set of the experiment, tube furnace was evacuated three times and then purged with the forming gas.

4.4 COMPACTION AND SINTERING

Compaction of powders was performed using an 80 ton hydraulic press. 12 mm ϕ pellets were produced under uniaxial compaction pressure of 3 GPa. Sintering of compacted pellets was carried out in a tube furnace with forming gas atmosphere at different temperatures (depending on the requirement of producing nanocrystalline or microcrystalline material) for 1 hr (nanocrystalline) and 3 hrs (microcrystalline).

4.5 CHARACTERIZATION OF NANOCRYSTALLINE ALLOYS

4.5.1 X-ray diffraction analysis

XRD is a relatively less time-consuming but, indirect tool for the measurement of average grain size in nanocrystalline materials in comparison to transmission electron microscope (TEM). The sample preparation for XRD is simple and averaging of several grains is inherent. In addition, the reliability of the TEM results depends on whether the thin area is representative of the original microstructure of the entire sample particularly when the microstructure is inhomogeneous. Also, the sample preparation and TEM analysis is a difficult task in many cases. Therefore, XRD has generally been preferred over TEM in the determination of grain size and lattice strain in nanocrystalline materials. X-ray peak broadening analysis is appropriate for crystallite sizes in the range of 10-300 nm. In case of crystals larger than 300 nm, inaccuracy is expected to be large.

X-ray diffraction (XRD) has been extensively used in the present work to perform crystallite size measurements and qualitative/quantitative phase analysis. The XRD studies were performed using CuK_α ($\lambda = 0.1540537$ nm) radiation. Qualitative phase analysis was performed by the standard method of comparative peak matching with standard JCPDS files.

The average grain size is determined from x-ray diffraction (XRD) analysis in terms of diffraction line broadening. The broadening of diffraction lines increases with decrease in the grain size. XRD peaks are broadened due to: (a) instrumental effects, (b) crystallite size in the nanometer range and (c) lattice strain in the material. The individual contributions of these effects to the total broadening can be separated using standard techniques and their modifications. The grain size determined by different

methods may vary slightly (full width at half maximum (FWHM) of the Bragg peaks or the integral widths) but, the results often do not differ too much. The experimental profile is a convolution of the instrumental broadening profile and the structurally broadened profile. The simplified methods for subtracting the effect of instrumental broadening are based on assumptions on the shapes of the experimental profile and reference profile. Following methods are used commonly:

- Lorentzian

$$\beta_{obs} = \beta_{size} + \beta_{strain} + \beta_{inst} \quad \text{--- (4)}$$

- Gaussian

$$\beta_{obs}^2 = \beta_{size}^2 + \beta_{strain}^2 + \beta_{inst}^2 \quad \text{--- (5)}$$

where, β_{obs} is observed (experimental) broadening, β_{size} is broadening due to the grain size, β_{strain} is broadening due to lattice strain, and β_{inst} is instrumental broadening.

In the current study, value of β_{inst} was obtained by measuring the full width at half maximum of a microcrystalline Fe-Cr alloy sample produced upon annealing at 840°C for 10 hours in forming gas atmosphere. This annealing for the long duration would remove lattice strain and effect of grain size on peak broadening and the obtained peak broadening will be due only to β_{inst} .

Scherrer, first, observed that small crystallite size could give rise to line broadening. He derived a well known equation for relating the crystallite size to the broadening which is called the “Scherrer Formula”

$$D_v = \frac{K\lambda}{\beta_{size} \cos \theta} \quad \text{--- (6)}$$

D_v = Volume weighted crystallite size, K = Scherrer constant, somewhat an arbitrary value that falls in the range 0.87-1, λ = The wavelength of radiation and β_{size} =The integral breadth of the reflection and is measured on 2θ scale in radians, λ is the wavelength and ϑ is the angular position.

Grain size was calculated using the Scherrer equation. However, Scherrer equation does not account for the internal lattice strain which also causes line broadening of the diffraction peaks. However, $\beta_{lattice}$ was assumed to be negligible as it has been established by various researchers [98] that the effect of lattice strain broadening on the calculated grain size is negligible in the case of iron. Grain size, determined, using XRD technique (neglecting the lattice strain), was consistent with the grain size measured, using TEM technique (described later) which confirms that the use of Scherrer equation for the calculation of the grain size of ball milled Fe-Cr powder is appropriate.

4.5.2 Transmission electron microscopy (TEM)

Nanocrystalline and microcrystalline nature of the compacted test specimens was determined also, using Philips CM 20 transmission electron microscope (TEM). The compacted test specimens (produced by high energy ball -milling followed by pre-annealing, compaction and sintering) were polished to the thickness of 40 μm and then ion- milled. The ion-milled specimens were analyzed using TEM in bright field, dark field and selected area diffraction modes. An acceleration voltage of 200 kV was used in all the experiments.

4.6 DENSITY MEASUREMENT

A Micromeritics 1330 Gas Pycnometer was used to determine the density of test specimens. Gas Pycnometer allows rapid and accurate determination of density of samples of the order of 0.5 to 4 gms.

By using helium gas as the means of determining the volume of a sample of known mass, density can be determined without recourse to density gradient columns and other techniques which require the sample to be immersed in a solvent.

Weight of the pellets was measured using Cahn balance. Average density and standard deviation was reported after 30 measurements on each specimen.

4.7 HARDNESS TESTING

Vickers micro-hardness testing was determined using 20g load. 10 readings were taken on each sample and the average of hardness values was reported.

4.8 Oxidation test

The compacted and sintered discs of nanocrystalline (nc) Fe-Cr alloys were polished to 1 μ m SiO₂ finish and subjected to oxidation in air for durations up to 52 hours at the temperatures where grain boundary of such alloys is known to predominate the lattice diffusion, i.e., 300 - 400°C. For particular investigation of the role of nanometric vis-à-vis micrometric grain size in the development of passive films, a microcrystalline (mc) alloy with much larger grain size (1.5 μ m) was simultaneously subjected to the same oxidation treatment along with the nc Fe-Cr alloy.

Weight of the test specimens increases during the oxidation experiments and it is measured at regular time intervals using a Cahn balance with a precision limit of 0.1 mg. In order to minimize the possible errors duplicate specimens were subjected simultaneously to each oxidation test. However, in the case of Fe₂₀Cr alloys, and nc Fe₁₀Cr alloy the weight change data at 300°C is close to the precision limit of the balance.

4.9 ELECTROCHEMICAL CORROSION TESTING

The test specimens (pellets of Fe-Cr alloys) were polished to 2500-grit paper finish, cleaned and subjected to potentiodynamic polarization tests. A conventional three-electrode electrochemical cell was used, with the Fe-Cr alloy samples as working electrode (test specimen), a graphite rod as counter electrode and a saturated calomel electrode (SCE) as the reference electrode. All the potentials, reported in this study, are with respect to SCE. Potentiodynamic polarization tests were carried out in 0.5M H₂SO₄, 0.05M H₂SO₄ and 0.5M H₂SO₄ + 0.05M NaCl solutions using PAR-2273 potentiostat, employing a scan rate of 0.5mV/sec. A schematic of the experimental setup is presented in Figure 4.1. Prior to all experiments, the working electrode was cathodically polarized at -1.0V for 120 seconds to remove any existing oxide film. Open circuit potential (OCP) was stabilized after the cathodic cleaning. Cathodic and anodic polarization parts, reported here, were generated separately. These experiments were repeated at least four times to ensure the reproducibility of the data.

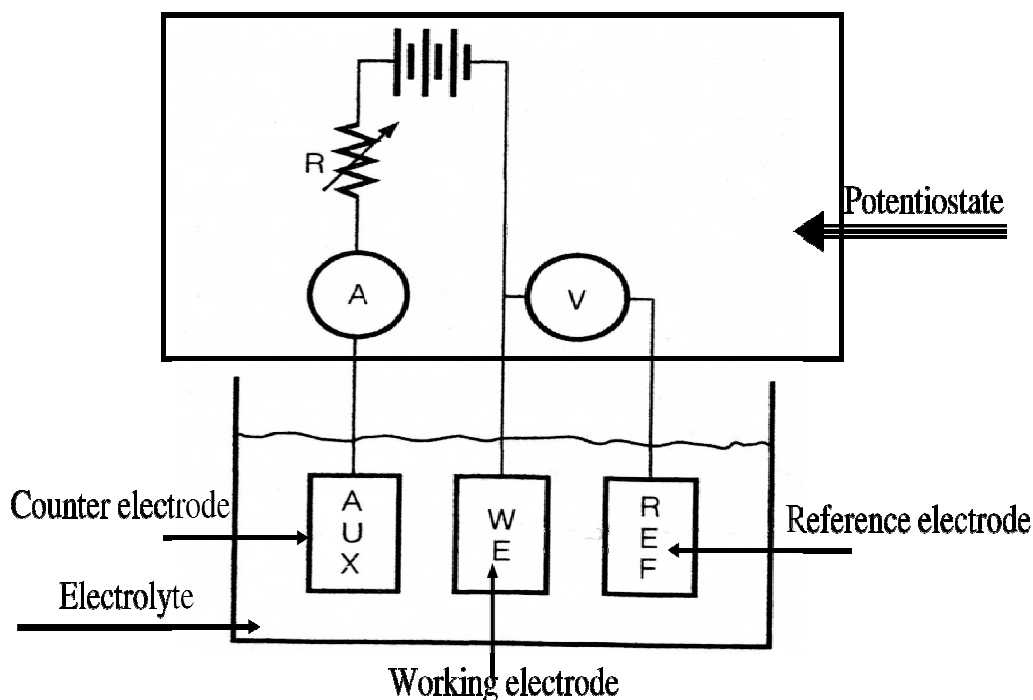


Fig 4.1 Schematic setup for a three electrode cell

4.10 Secondary Ion Mass Spectrometry (SIMS)

In order to understand the role of the nanostructure on oxidation or electrochemical corrosion resistance, thin oxide films formed at the initial stages of oxidation or corrosion need to be characterized for the chromium content. For this purpose specimens oxidized for various durations at the three oxidation temperatures were investigated using SIMS.

4.10.1 SIMS instrument

SIMS is a destructive surface analytical technique. A primary ion beam (O or Cs) bombards the surface, causing ions (anions and cations), atoms and molecules to be ejected ('sputtered') from the surface. The energy of the primary ions can be of the order of a few 100 eV to 10s of keV (which is enough to eject atoms and molecules from the surface layers.) The actual depth of interaction is usually a few nm.

As the primary beam raster across, the small surface area sputters out **the secondary ions**. Continuous detection of the sputtered secondary ions allows SIMS to provide a depth profile of the underlying layers to a depth of 10 microns with a depth resolution of 2-5nm.

Cameca ims (5f) SIMS instrument, used in the present study, is referred to as "dynamic" as it can both sputter at high rates and analyse the liberated ionised species simultaneously. The main difference between the TOF-SIMS and dynamic SIMS is that TOF-SIMS are generally restricted to shallow surface analysis due to their very low sputter rates. Depth profiling using TOF-SIMS can be prohibitively time-consuming.

Main steps of SIMS analysis process are as follows:

- Primary ions are produced by a cesium or oxygen source and are accelerated along the primary column and focused onto the sample surface.

- Sputtered secondary ions pass through a secondary column, where they are collected and separated by charge
- The secondary ions are then collected and focussed through the mass spectrometer
- The analysed ions are then directed into detectors, and a signal is measured. The electron multiplier amplifies the incoming signal for each element to be large enough to be measured.

4.10.2 Capabilities of SIMS instrument used in the present study

SIMS is one of many surface analytical tools available for surface analysis. SIMS possesses an excellent dynamic detection range, extending from atomic weight-percent down to parts per billion (ppb).

Quantification is available with appropriate reference standards. Furthermore, data can be acquired as a function of depth, allowing profiles to be built up through progressively deeper layers from the surface.

Spatial information can also be collected, allowing imaging of the spatial distribution of species to a resolution of about 2-5 μ m. Analysis of species in the mass range 1 to 500 amu is available and mass resolutions of up to $\sim dM/M=10000$ are achievable.

Capabilities of the SIMS instrument used in the present study are summarized in the Table 4.4.

Table 4.4 Capabilities of Cameca ims 5f SIMS instrument

Sources:	Oxygen and cesium
Elemental Mass Range:	Hydrogen to Uranium (1 to 500amu)
Detection limits:	Down to ppm - ppb
Depth Profiling Capability:	Simultaneous with sputtering to a depth of 10 microns
Depth Resolution:	1-2nm
Lateral Spatial Resolution:	2-5 microns (imaging)
Elemental mapping (imaging):	Yes, area up to 500X500 microns
Quantitative analysis:	Yes, With standards (reference samples)

In the present study the thin oxide films formed over nanocrystalline and microcrystalline alloys were characterized by SIMS depth profiling, using Cs⁺ ion primary beam 2 nA (for characterization of specimens after electrochemical tests) and 10 nA (for the characterization of oxidized specimens), depth profiling of craters of 250 μ m \times 250 μ m area.

4.11 X-ray photoelectron spectroscopy (XPS)

Fe-Cr alloys were polarized (from OCP) to the potential where the passive current density is minimum and held at that potential until steady state is reached (typically it took 30 minutes in the present study). Potential is in the passive region and, therefore, preferential-dissolution/-adsorption mechanism does not take place. Samples were washed by distilled water and dried in air at room temperature. Passive film formed on the surface was analysed by XPS. All spectra were generated using a Kratos Axis Ultra Spectrometer with monochromatized Al K α (1486.6 eV). A charge neutralizer was employed to minimize the photoemission charging effect. Quantitative and qualitative analysis was performed using CasaXPS software. The survey scans were generated under the conditions: energy range: 1600-0 eV, pass energy=

160 eV, step size=0.7 eV, sweep time= 180 sec and x-ray spot size=700×300 μm. Regional scans were performed for O 1s, Cr 2p, and Fe 2p. The conditions for regional scans were similar to those for wide scans except the pass energy (20 eV).

CHAPTER 5

SYNTHESES AND CHARACTERIZATION OF TEST ALLOYS

5.1 Introduction

Nanocrystalline alloys have been produced by processes such as sputtering, electron beam evaporation, pulse laser ablation [366], gas condensation [9,72] and sol-gel [367] method. However, the use of these techniques for processing nanocrystalline materials is limited to thin films or small samples [366], whereas, it is necessary to produce/process bulk samples for corrosion or mechanical testing. Electrodeposition [368] and severe plastic deformation [132,169] have been recognized as the two relatively successful routes for the processing of nanocrystalline materials.

Pulsed electrodeposition has been employed relatively successfully for processing nanocrystalline materials in bulk, most notably, Ni-Fe and Ni-Co alloys [369-371]. However, synthesis of nanocrystalline alloys or metals by electrodeposition often requires organic additives, for the purpose of biasing nucleation over growth of the depositing grains. These additives are believed to cause poor mechanical properties (such as embrittlement), typically observed in nanocrystalline electrodeposits [366].

Among the plastic deformation techniques, advanced ball -milling has been most widely used because of simplicity and potential to scale up for large production [169,372,373]. However, ball-milled powders required to be compacted. Groza [159] has reviewed various techniques employed for compaction of different nanocrystalline materials, viz., high pressure / lower temperature compaction, in-situ consolidation [168], hot compaction [374], hot isostatic pressing [172], explosive compaction [163]. However, compaction of nanocrystalline Fe-Cr alloys appears to be a non-trivial task. The difficulties arise due to the restrictions on plastic deformation posed by the body centred cubic (BCC) structure

causing high hardness, which necessitates high pressures/temperatures for consolidation and sintering, for example, pure iron with an average grain size of 10 nm shows a hardness value of 10 GPa [191]. Plastic deformation, a necessary condition for effective compaction requires applied pressure to be in excess of yield stress and approximately $1/3^{\text{rd}}$ of the hardness (i.e., 3.5 GPa), facilities, which are not easily available in most research laboratories. Plastic flow, high densification and inter-particle bonding can be achieved by compaction/sintering at high temperatures. However, processing at excessively high temperatures will lead to the common instances of grain growth.

It may be possible to produce nanocrystalline Fe-Cr alloys with close to green density and without too excessive grain growth, by employing a suitable combination of temperature and pressure in hot compaction process. The other possibility could be, to soften the material, by prior thermal treatment before compaction. The latter may be less effective but, attractive for the situations where hot compaction facilities are not readily available.

This chapter presents a description of the success in exploring the suitable processing window for nanocrystalline Fe-Cr alloys.

5.2 Attempts to consolidate ball- milled nanocrystalline alloys and challenges

Nanocrystalline powders of Fe-Cr alloys with a nominal Cr content of 2, 3, 5, 10 and 20 weight percent were prepared using planetary ball mill at the nano-micro laboratory at Indian Institute of Technology-Madras, India. As starting materials, high purity powders of Fe and Cr were used. The high energy ball - milling was performed in toluene medium using planetary ball mill and tungsten carbide (WC) balls at a rotating speed of 300 RPM. Ball to powder weight ratio was 10:1. On the basis of reported literature [88-

100], ball- milling was carried out for 20 hours to ensure the formation of nanocrystalline alloy. Temperature after each hour of milling cycle was found to rise to $\sim 80^{\circ}\text{C}$. To avoid excessive temperature rise (during longer period of ball- milling) ball mill operation was stopped after each one hour, and the ball mill was cooled using a fan for 45 minutes, before starting further milling.

Optimum milling time is important to obtain a minimum grain size. To monitor the grain size reduction with milling time, the samples of ball- milled Fe-Cr alloys were taken after 5, 10, 15 and 20 hours of milling and the grain size was measured using XRD analysis (details of XRD analysis are given in chapter 4). As evident from the Figure 5.1, the grain size decreased until 15 hours of ball milling, after which there was no appreciable reduction in the grain size. Therefore, ball milling of 20 hours is supposed to be optimum to find the minimum grain size.

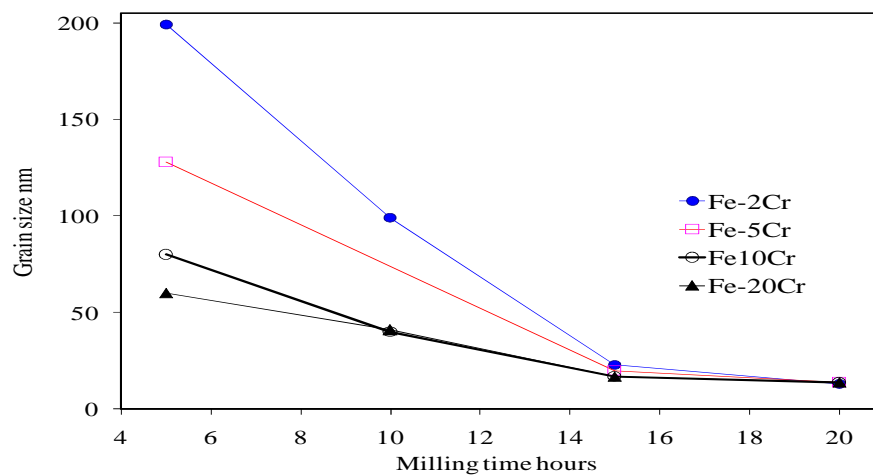


Fig. 5.1 Reduction of grain size with the milling time

Nanocrystalline Fe-Cr alloys, thus, produced were in powder form. For the determination of corrosion properties, these alloys are required to be compacted. Initial attempts were made to compact the nanocrystalline alloy powders using the uni-axial compaction machine which can apply a maximum of 750 MPa pressure. However, compaction was not successful at this pressure. Unfortunately, application of the pressure beyond 750MPa was not possible using the available facilities.

These unsuccessful attempts to produce compacted pellets of nanocrystalline Fe-Cr alloys prompted collaboration, formed with the research group of Prof Carl C. Koch at North Carolina State University, USA, whose laboratory has the necessary facilities and expertise. Nanocrystalline Fe-Cr alloys with various Cr contents were prepared using SPEX shaker high energy ball mills. As starting materials, high purity powders of Fe (99.9% purity and particle size < 10 μm) and Cr (99.9% and particle size <10 μm) were loaded into a tool steel vial under vacuum with 440C stainless steel balls (6.4-7.9mm in diameter). Ball-to-powder weight ratio was kept at 10:1. High energy ball -milling was carried out for 20 hours in SPEX Model 8000 shaker mill which was air cooled. Details of ball- milling are provided in chapter 4.

However, the results of milling time vs grain size from the overall unsuccessful attempts at IIT-M were useful in selecting a suitable milling time in future experiments. The grain size, as determined by the XRD, was found to be 13 (± 4) nanometers for Fe10Cr alloy and 14 (± 4) nanometers for Fe20Cr alloys. XRD peak profiles of various nanocrystalline Fe-Cr alloys powders produced by ball- milling for 20 hours are shown in Figure 5.2. Peak broadening is clearly visible.

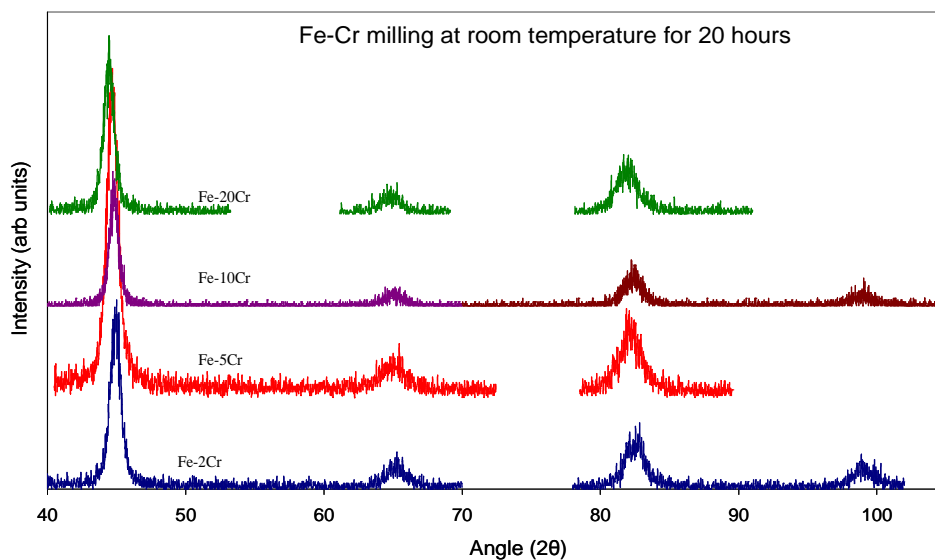


Fig. 5.2 Typical XRD peak profiles of ball milled Fe-Cr alloys

Attempts were made to compact the nanocrystalline alloy powders, thus, produced under maximum achievable pressure (3GPa, with the available tungsten carbide dies and punches). However, these attempts, using much greater pressure than previously applied, were not successful, as the pellets were fragmented. Not a single unbroken pellet could be produced.

In further attempts of compaction, a hot compaction unit was developed which enables appreciating 1.5GPa pressure at 500°C. However, compaction at the temperature higher than 500°C was not possible as this compaction machine became too hot and application of high pressure would damage the compaction machine. Pellets, then produced, were also having porosity and cracks. Moreover, hot compaction procedure is cumbersome as it also involves a lot of time and man power, and it was not safe for a person to work alone.

After all the unsuccessful attempts we were left with the following possibilities:

1. Explosive compaction [163], which was not available.
2. Development of some new processing technique.

5.3 Possible reasons for failure of initial attempts to consolidate the material and possible solutions

The reasons for unsuccessful compaction were explored, as discussed below:

- a) A thin coating of the oxides on the ball- milled nanocrystalline powders might form which could have added on to the brittleness of the material. This surface brittleness will not allow the plastic deformation at the interface of particles, and as a consequence compaction will be hindered. However, the oxide layer if, any, was too thin to be detected by XRD.

- b) It was realized that the necessary condition for compaction is that the applied pressure at the particle interfaces should exceed the yield stress of the material. The nanocrystalline materials have high yield stress ($1/3^{\text{rd}}$ of hardness), typically > 3 GPa which is more than the applied pressure. However, these materials can be compacted if the hardness could be reduced by some prior thermal treatment.
- c) Any prior annealing at excessively high temperatures may cause grain coarsening. Compaction at very high temperature can not be performed as severe grain growth will take place at such temperatures.
- d) However, it may be possible to select a temperature regime where the material still remains in the nano regime but the hardness is reduced to the level where the powder could be compacted.

In order to determine the right processing temperature and pressure, it becomes necessary to understand the grain growth behaviour and hardness of the material. Therefore, a systematic study to investigate the grain growth and hardness of the material was carried out.

5.4 Grain growth behaviour

5.4.1 Grain growth behavior of ball milled Fe10Cr alloy

Ball- milled nanocrystalline powders of nc Fe10Cr alloys were annealed in forming gas atmosphere at various temperatures for various periods of time in order to investigate the grain growth behaviour. Grain size of annealed nanocrystalline alloy after each annealing experiment was determined using XRD analysis.

Figures 5.3-5.5 respectively show XRD patterns of Fe-10Cr annealed at 500, 600 and 700°C for different times. Diffraction line broadening of Bragg reflection peaks have been found to decrease with the increase in annealing time and temperature, as shown in Figures 5.3-5.5. Initial grain growth is rapid at each of the three temperatures. However, the intensity of the initial grain growth increases with temperature (Figure 5.6). Annealing at 500°C marks a rapid grain growth which was limited to the first 15 minutes, and no significant grain size changes in the course of further annealing. At 600 and 700°C, grains continued to grow with time, even beyond 15 minutes.

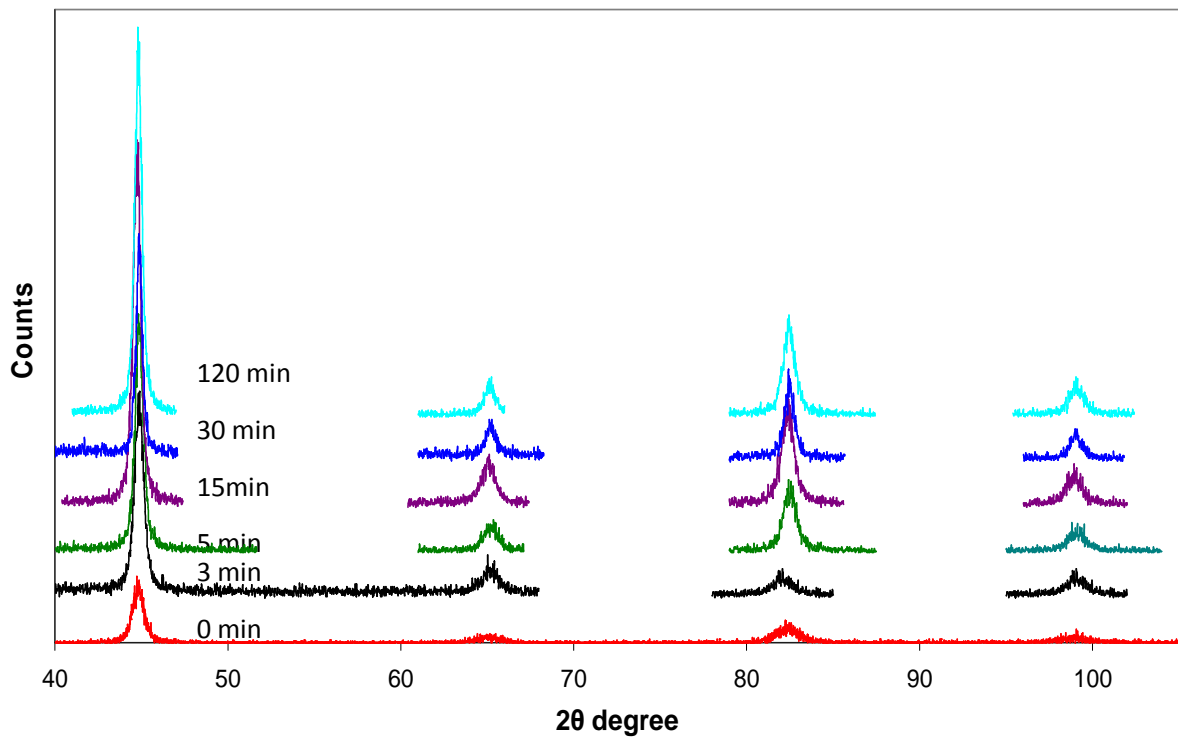


Fig.5.3 XRD profile of ball-milled nanocrystalline Fe-10Cr alloy annealed at 500°C for different time

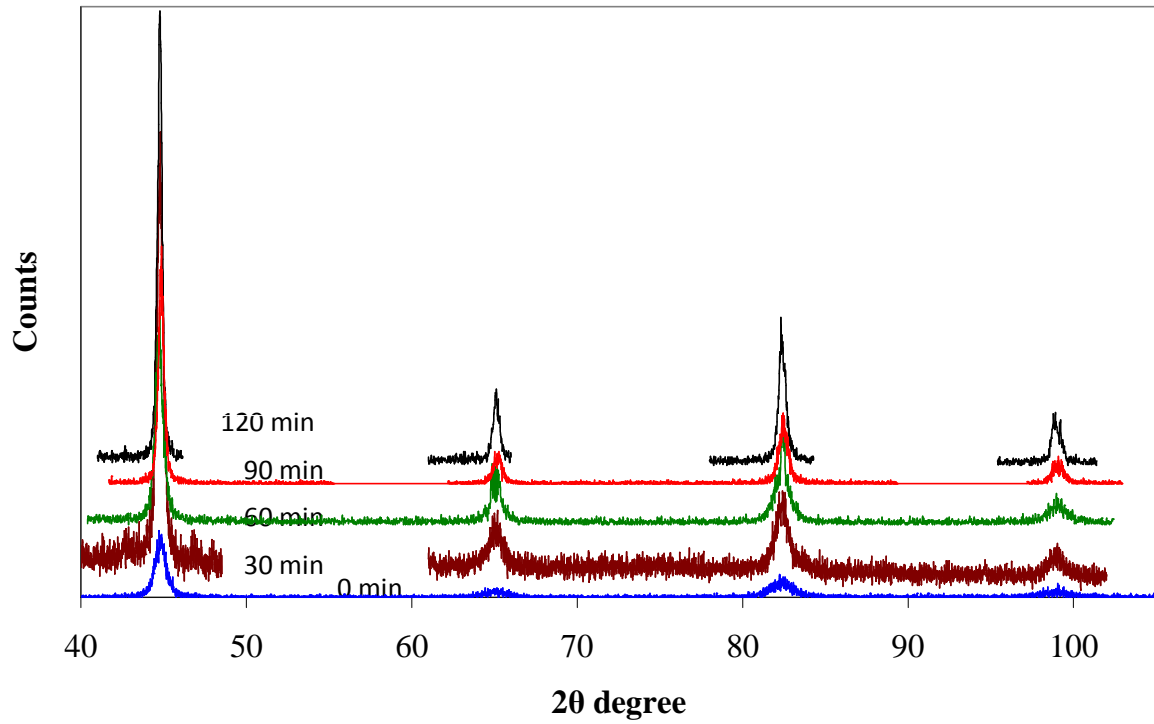


Fig.5.4. XRD profile of ball-milled nanocrystalline Fe-10Cr alloy annealed at 600°C for different time

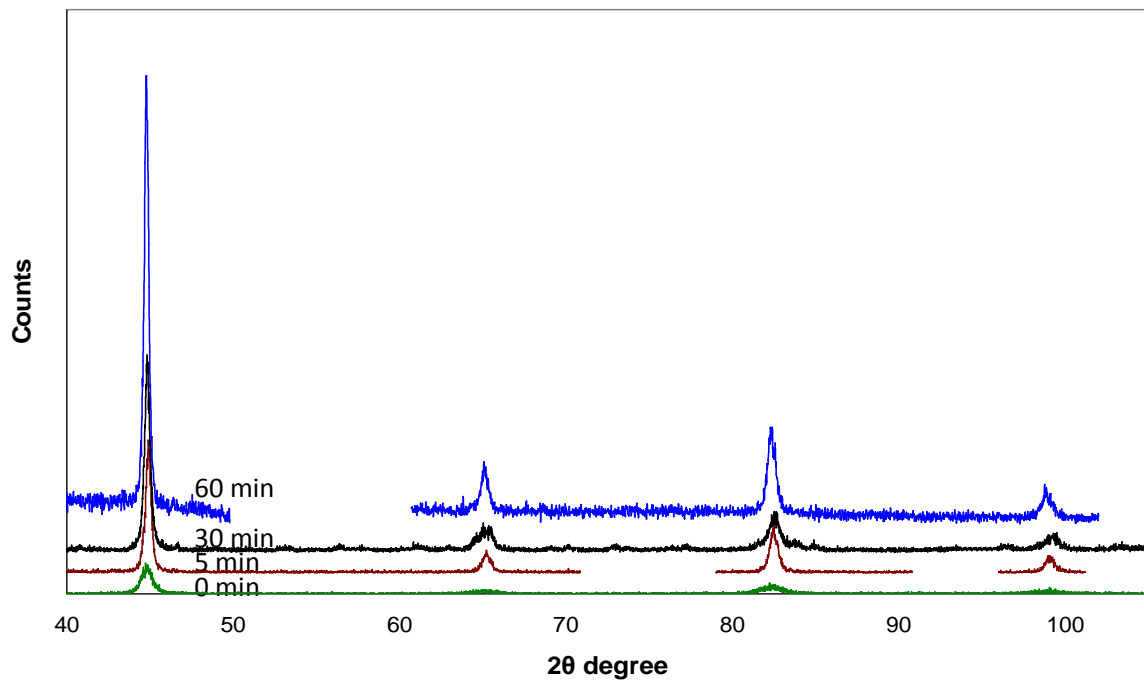


Fig.5.5. XRD profile for ball-milled nanocrystalline Fe-10Cr alloy annealed at 700°C for different time

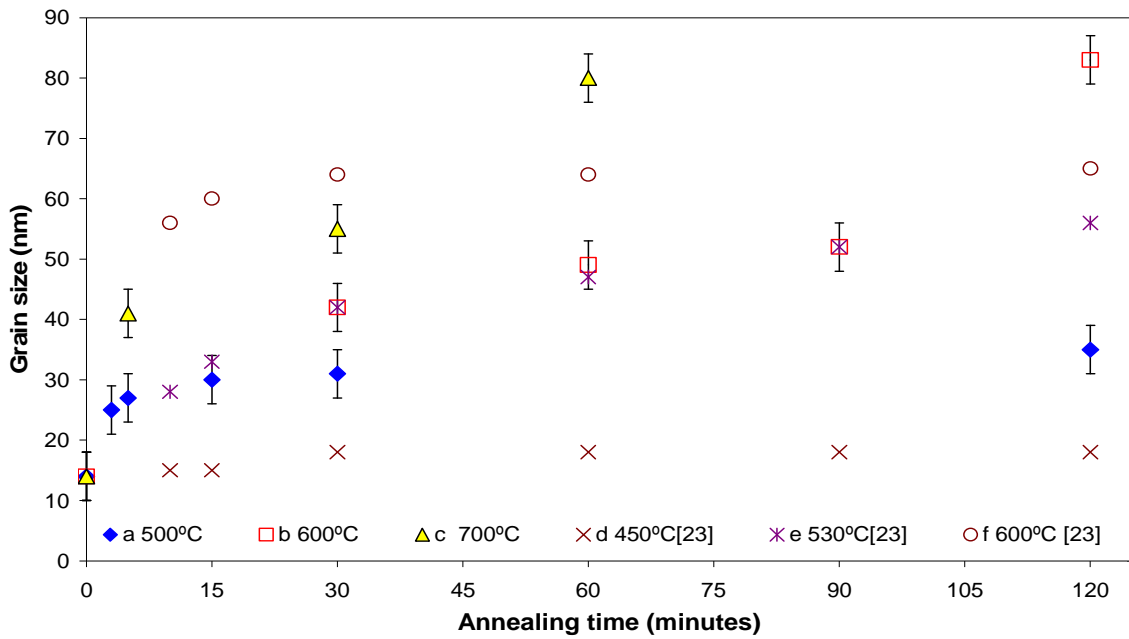


Fig. 5.6 Grain growth in Fe-10Cr nanocrystalline alloy at: 500°C (a), 600°C (b) and 700°C (c). d, e and f represent grain growth data for pure Fe at 450°C, 530°C and 600°C, as reported by Malow et al [149].

Grain growth is a strong function of temperature, as suggested from the increasing intensity of the initial grain growth with temperature (Figure 5.7). Grain size data for nanocrystalline Fe-10Cr alloy annealed for 30min at different temperatures, shown in Figure 5.7, suggest a rapid grain growth at 600 and 700°C.

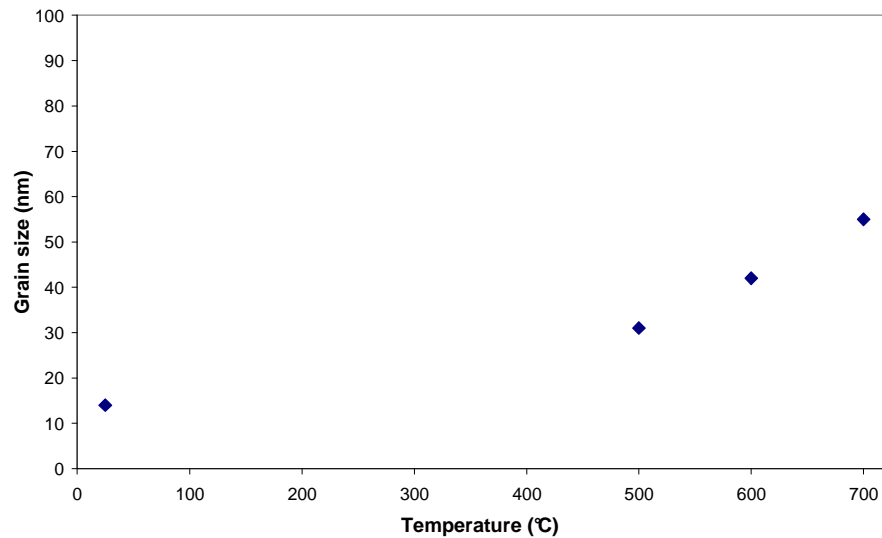


Fig. 5.7 Temperature dependence of grain size of nanocrystalline Fe-10Cr alloy annealed for 30min at different temperatures.

5.4.2 Grain growth behavior of ball milled Fe20Cr alloy

Similar to nanocrystalline Fe-10Cr alloy, grain growth behaviour of nc Fe20Cr alloy was also investigated at 600°C. A typical XRD scan showing decrease in the grain size (as indicated by the decrease in peak broadening) with the progress of annealing at 600°C is presented in the Figure 5.7. Grain size obtained during subsequent annealing of the powder was also determined using XRD analysis. As evident from the Figure 5.8 grain growth behaviour of Fe-20Cr alloy is similar to that of the nc Fe10Cr alloy at 600°.

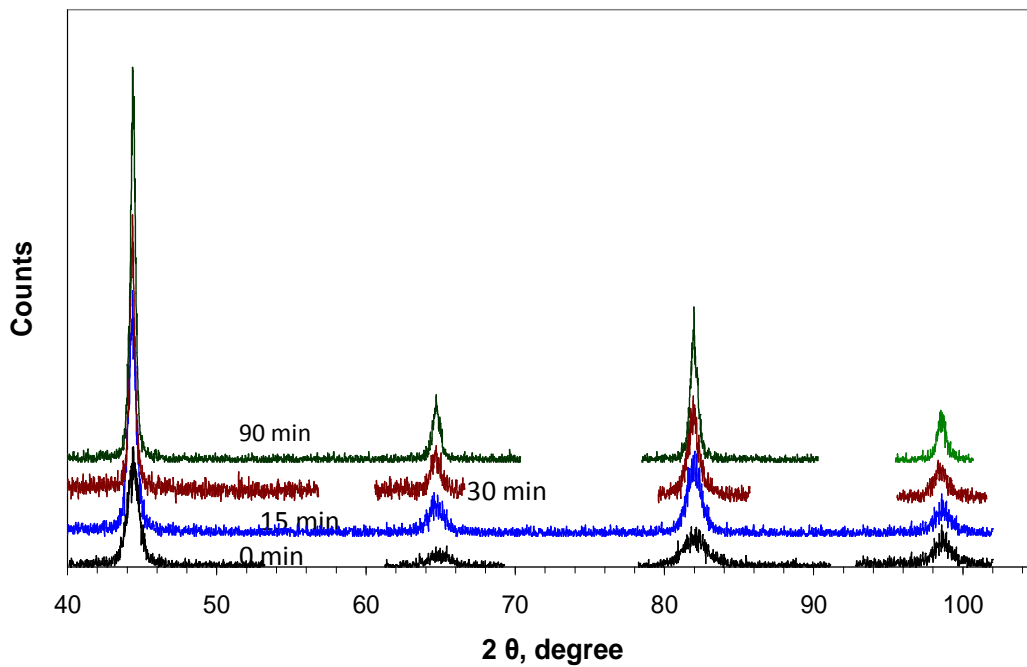


Fig.5.8 XRD profile for ball-milled nanocrystalline Fe-20Cr alloy annealed at 600°C for different time

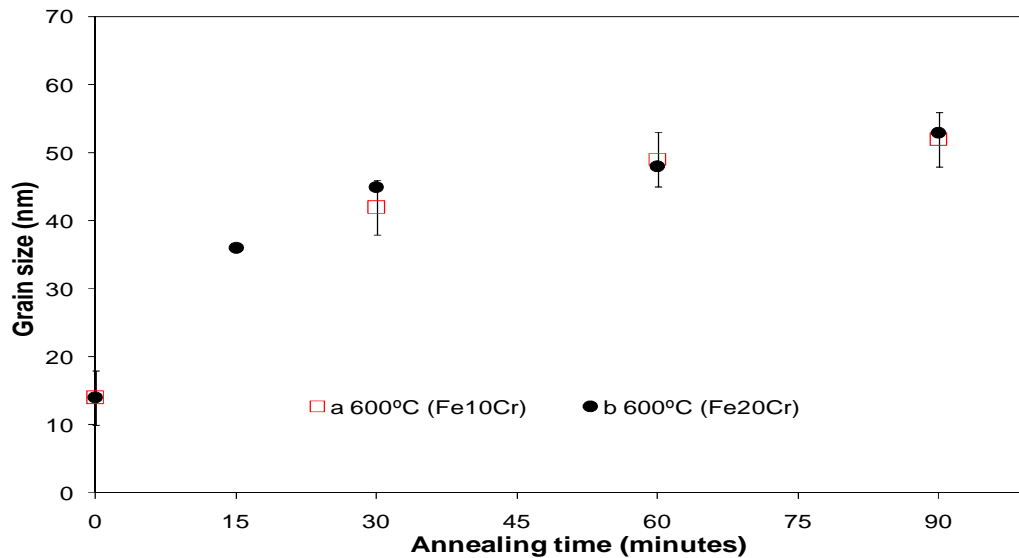


Fig. 5.9 Grain growth in nanocrystalline Fe-10Cr and Fe-20Cr alloys at 600°C

5.5 Compaction

Compaction of the ball- milled powder under a uniaxial pressure of 3 GPa at room temperature was not successful, as this resulted in disintegration of the pellets. It became obvious that it would be necessary to reduce hardness and improve ductility of the powder, before it was subjected to the pressure compaction. Based on the grain growth data, shown in Figure 5.6 and change in the hardness with grain size (caused by annealing), as shown in Appendix A, an annealing at 600°C for 30 minutes was selected with a view to prior softening of the powder without any considerable grain growth. The ball-milled powder was subjected to this annealing (600°C/30min), and then was successfully compacted under a pressure of 3 GPa. The resulting compacted pellets (diameter = 12 mm, thickness = 1.5 mm) had a green density of approximately 100% of the theoretical density, as determined using a pycnometry. Compacted pellets were sintered for 1h at 600°C. This temperature appears to be a proper choice in order to avoid excessive grain growth. Grain size and density of the nanocrystalline materials after various steps are shown in Table 5.1

A schematic representation of the compaction procedure is shown in the Figure 5.9. It may be important to note that the level of grain coarsening that was realized, following this procedure, could not have been avoided even if hot compaction were used. A hot compaction at 600°C for an hour would have resulted in the grain size very close to one, obtained in this procedure (as clear from the grain growth data shown in Figure 5.7). Moreover obtained density in the current method is pretty close to the theoretical density of the material. Besides, the conventional compaction method, as shown in the Figure 5.9, would result in the final grain size very similar to that achieved using the present technique. However, the required applied pressure would have been considerably large to achieve satisfactory level of density. Therefore, a step of prior annealing as used for the first time in the present study was a satisfactory choice to compact the nanocrystalline materials.

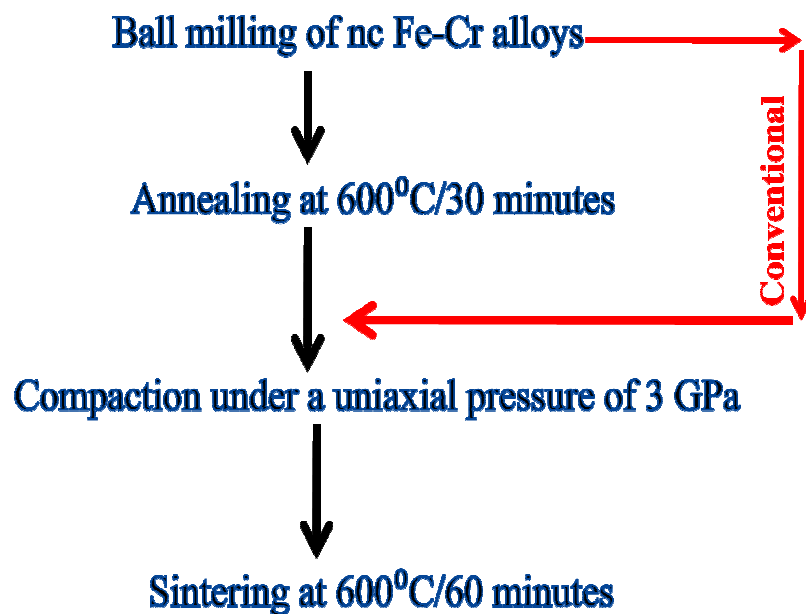


Fig.5.10 Schematic representation of compaction process. Arrow shown in the red shows the conventional compaction method.

Pre-annealing is also beneficial for the purpose of removing any oxide layer coating on the ball- milled nanocrystalline alloy powders formed during ball- milling. Annealing performed at 600°C for 30 minutes

in the forming gas (which contains 2% hydrogen) atmosphere was expected to reduce the oxides to their respective metals and thus facilitating compaction of oxide-free surface of powder particle.

Table 5.1 Grain size and density of nanocrystalline Fe-10%Cr and Fe-20%Cr alloys after different processing steps

	Grain size, ball-milled powder (nm)	Annealing, ball-milled powder	Grain size, ball-milled and annealed powder (nm)	Green density of compacted pellets (% of theoretical density)	Sintering, compacted pellets	Grain size, sintered pellet (nm)	Sintered density of compacted pellets (% of theoretical density)
ncFe10Cr	13 (± 4)	600°C, 30 min	40 (± 4)	99.0 (± 0.6)	600°C, 60 min	52(± 4)	99.6 (± 0.3)
ncFe20Cr	14(± 4)	600°C, 30 min	42(± 4)	99.0 (± 0.6)	600°C, 60 min	53(± 4)	99.6 (± 0.3)

5.6 Preparation of Microcrystalline alloys

For the purpose of converting nanocrystalline alloy powders into microcrystalline discs, ball-milled powders of Fe-Cr alloys were annealed at 800°C for 30 minutes and compacted under a uniaxial pressure of 2.5 GPa followed by sintering at 840°C. Grain size of microcrystalline material determined by optical microscopy was 1500 nm. Grain size was further examined using TEM and is presented in the next section.

5.7 TEM characterization of test specimens

TEM samples were prepared from the compacted discs of nanocrystalline and microcrystalline Fe10Cr and Fe20Cr alloys (these were dense enough for the preparation of TEM samples). TEM images of nanocrystalline and microcrystalline Fe10Cr and Fe20Cr alloys are presented in the Figures 5.11-5.13.

The TEM images show that grain size in the nanocrystalline materials is, indeed, in the nano range and is in good agreement with grain size obtained from the XRD analysis. Selected area diffraction patterns of nanocrystalline and microcrystalline alloys differ significantly. As evident from the Figures 5.11c and 5.12c, a ring pattern is attributed to nanocrystalline structure while a dotted selected area diffraction pattern (Figure 5.13c) is characteristic of a microcrystalline structure.

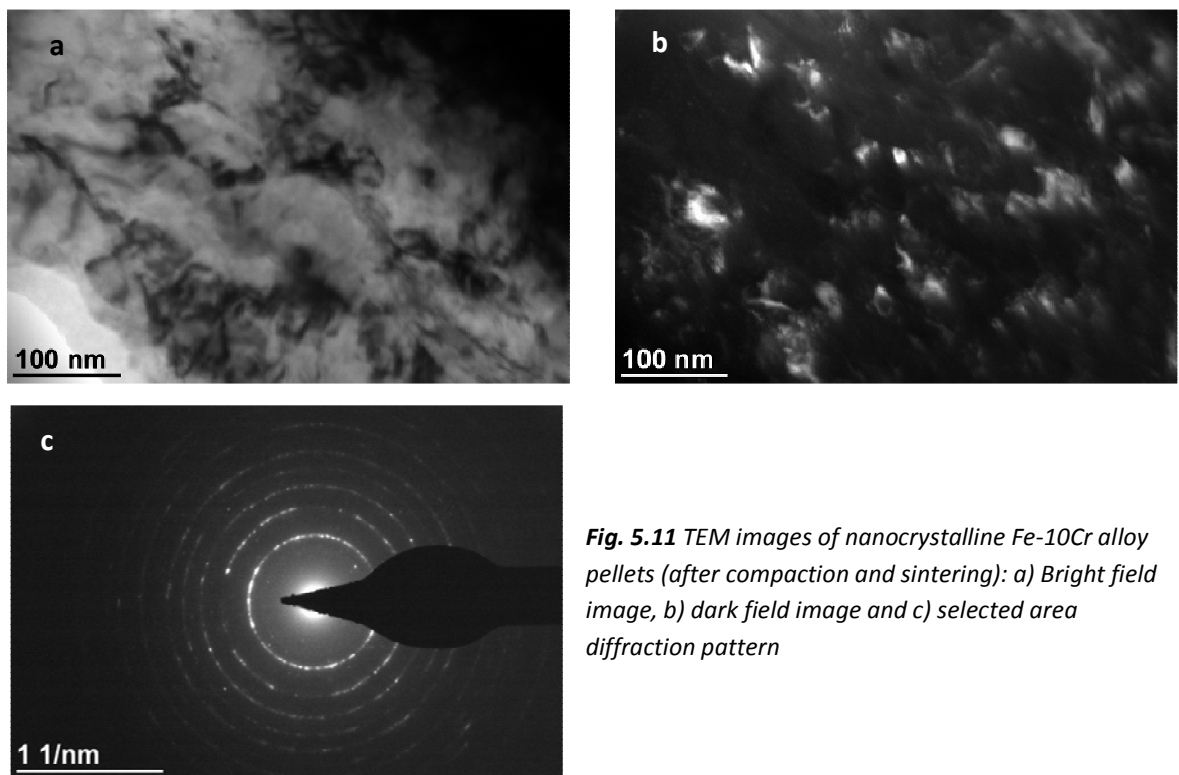


Fig. 5.11 TEM images of nanocrystalline Fe-10Cr alloy pellets (after compaction and sintering): a) Bright field image, b) dark field image and c) selected area diffraction pattern

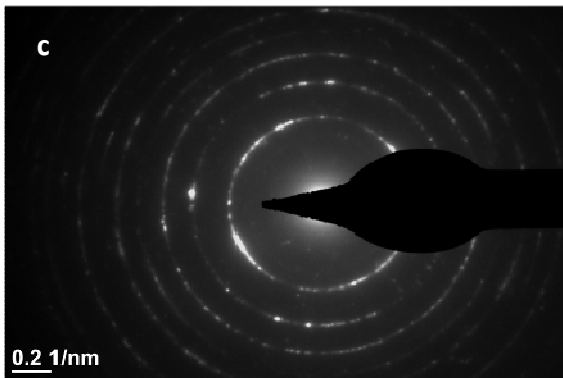
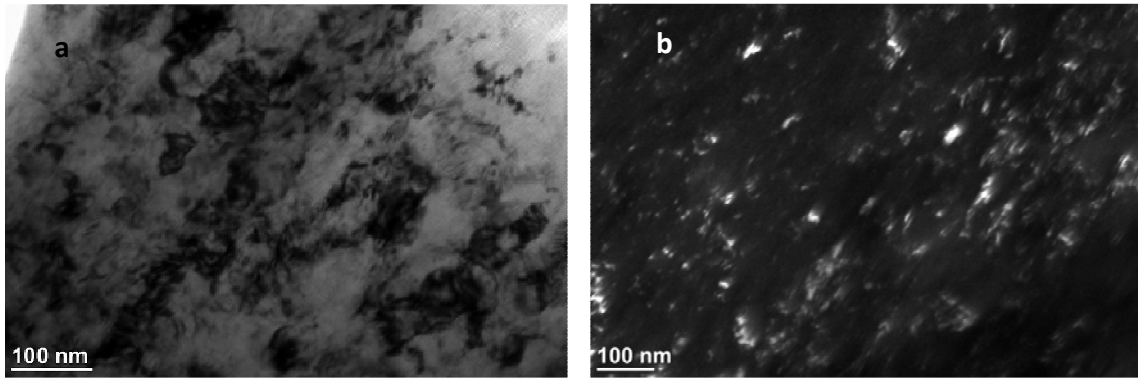


Fig. 5.12 TEM images of nanocrystalline Fe-20Cr alloy pellets (after compaction and sintering): a) Brightfield image, b) dark field image and c) selected area diffraction pattern

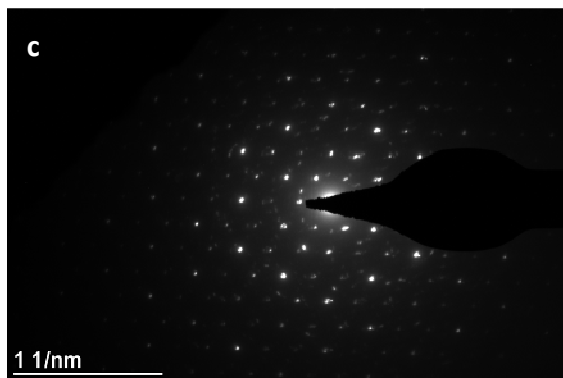
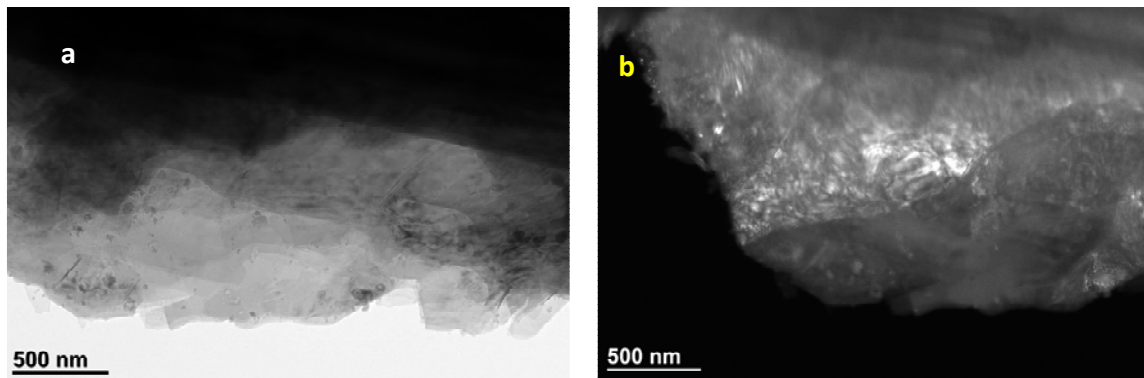


Fig. 5.13 TEM images of microcrystalline Fe-10Cr alloy pellets (after compaction and sintering): a) Brightfield image, b) dark field image, and c) selected area diffraction pattern

5.8 Conclusions

- 1) Nanocrystalline Fe-10Cr and Fe-20Cr alloys were produced in the powder form using high energy ball- milling.
- 2) Grain growth behaviour and hardness of nanocrystalline Fe-10Cr and Fe-20Cr alloys were investigated.
- 3) Ball-milled nanocrystalline alloys specimens with a grain size of 52 nm and density close to theoretical density were produced. It was found that a step of prior annealing tremendously facilitated room temperature compaction.
- 4) It was possible to prepare the TEM specimens out of compacted specimens. Grain size of nanocrystalline alloys, measured using TEM, was in nano-range and was in good agreement with the XRD data.

CHAPTER 6

OXIDATION RESISTANCE OF NANOCRYSTALLINE *vis-à-vis* MICROCRYSTALLINE Fe-Cr ALLOYS

6.1 Introduction

Given that the grain boundaries are high energy areas, corrosion rate of nanocrystalline materials in simplistic terms would be expected to be considerably greater than that of a microcrystalline material of similar composition, and this view is often supported in the literature [243,260-262]. However, the corrosion resistance of some materials is reported to be superior in nanocrystalline form when compared with that in microcrystalline state [250,266,267,375]. Such contrasts in the nature of the influence of nanostructure may depend on the type of corrosion (gaseous or aqueous) and the environment-material system.

The nature of the influence of nanostructure on the diffusion-assisted corrosion (*viz.*, high temperature oxidation) depends on the role of the predominantly diffusing species in a given alloy. For example, oxidation resistances of an iron-aluminide and an Fe-B-Si alloy in the nanocrystalline state are reported to be superior to that in their microcrystalline state [265,266]. This behaviour is attributed to Al and Si, the well-known protective oxide film formers, being the predominantly diffusing species respectively in the two alloys, and the nanostructure facilitating their diffusion and expedited formation of protective films (of Al/Si oxide).

Given the extremely fine grain size of nanocrystalline alloys, the degree of grain boundary diffusion will be very high. Hence, it may be possible to develop a protective film of Cr_2O_3 in nanocrystalline Fe-Cr

alloys, even at much lower chromium contents as opposed to the much greater minimum chromium contents (>18-20 wt% chromium) required for the development and maintenance of the Cr_2O_3 layers in common stainless steels. A few studies have been carried out on the electrochemical corrosion resistance of nanocrystalline coatings of stainless steels (high chromium Fe-Cr alloys) [311,312,314]. These studies are limited to aqueous electrochemical corrosion and to the coating of high-Cr Fe-Cr alloys.

Before the proposed investigation of the role of nanocrystalline (nc) structure in formation of a protective film/passivity, it may be imperative to have an overview of the role of grain size in development of the inner layer of oxidation resistant oxide. As suggested earlier, for a given combination of alloy-environment-temperature, where predominantly diffusing species can form a protective film and provide oxidation resistance, a decrease in grain size will facilitate protective film formation. Iron-chromium alloys (such as stainless steels) are the most commonly employed corrosion resistant microcrystalline materials. A common high-Cr alloy (viz., 18Cr-8Ni stainless steel) forms, during oxidation, an outer layer of Fe_2O_3 , and an inner layer of the mixed oxide of Fe, Ni and Cr that eventually converts into a protective oxide, i.e., Cr_2O_3 [293]. The kinetics of transition of the mixed Fe-Ni-Cr oxide into protective layer of Cr_2O_3 depends on the supply of chromium to alloy-oxide interface by diffusion in the alloy matrix, which is governed profoundly by grain size of the alloy. As clearly demonstrated in the literature [294], a fine grained ($\sim 17\mu\text{m}$ or less) alloy easily developed a uniform layer of Cr_2O_3 , whereas for an alloy with grain sizes greater than $\sim 40\mu\text{m}$, this protective layer of Cr_2O_3 was difficult to form during air-oxidation, and the inner layer of mixed oxide continued to grow due to insufficient chromium supply [376]. Low-chromium Fe-Cr alloys fail to form a protective layer of Cr_2O_3 [376-379]. Singh Raman et al. [376-379] have investigated the role of grain size (15-60 μm) in oxidation resistance of such low-Cr alloys. Grain boundary diffusion in microcrystalline low-chromium alloys is never enough for the

formation of a contiguous protective layer of Cr_2O_3 . In fact, the alloy suffers extensive internal oxidation along grain boundaries, and a decrease in grain size rather increases the grain boundary internal oxidation. Comparing the grain size effect in low- and high-chromium alloys, it is imperative to note that the high-chromium alloys too undergo internal oxidation, however, the internal oxide precipitates that form in close proximities due to a high supply of chromium, quickly, to form a contiguous protective layer [379].

This chapter investigates the hypothesis that nanocrystalline structure may confer considerable corrosion resistance to iron-chromium alloys at much lower chromium contents. Oxidation resistance of *nc* and *mc* FeCr alloys is compared at various temperatures. Nanocrystalline alloys have shown improved oxidation resistance in comparison to their microcrystalline counterparts. Mechanistic aspects of the improved oxidation resistance of *nc* Fe-Cr alloys is discussed based on the theoretical understanding and SIMS investigations.

6.2 Results

6.2.1 Weight Gain Vs Time Plots and Colour Evolution during oxidation

6.2.1.1 Nanocrystalline vis-à-vis Microcrystalline Fe-10%Cr Alloys

To compare the influence of nanocrystalline (*nc*) and microcrystalline (*mc*) structures on oxidation resistance, the compacted and sintered pellets of both *nc* and *mc* materials were oxidized at 300, 350 and 400°C in air for durations up to 3120 min.

Weight gain curves representing the oxidation kinetics of nanocrystalline Fe10Cr alloys are represented in Figures 6.1 to 6.3. Oxidation kinetics of nanocrystalline (*nc*) and microcrystalline (*mc*) Fe-10Cr alloy at 300°C (Figure 6.1) shows the *mc* alloy to be oxidizing at a considerably greater rate than the *nc* alloy.

After 3120 min of oxidation, weight gain of microcrystalline Fe-10Cr alloy was found to be nearly seven times greater than that of the nanocrystalline alloy of same composition. Colours of the oxide scales after different durations of oxidation (shown as insets in Figure 6.1) were considerably different. Besides the considerably higher weight gain of the *nc* alloy, other striking features of the oxidation kinetics and oxide scale colour evolution are:

- (a) Both *nc* and *mc* Fe-10Cr alloys follow parabolic kinetics during the first 240min of oxidation (as evidenced by the weight-gain² vs time plots in Figure 6.1b). However, during subsequent oxidation, nanocrystalline Fe-10Cr alloy shows a considerable departure from the parabolic behaviour whereas, microcrystalline alloy of the same composition continued to follow parabolic kinetics (Figure 6.1c). The marked departure of the nanocrystalline Fe-10Cr alloy from the parabolic behaviour is accounted for by the insignificant increase in weight-gain of this material after the first 240min of oxidation (Figure 6.1a). Such behaviour would generally be attributed to some critical change in the chemical characteristics of the oxide scale that can influence the diffusion-assisted parabolic kinetics. Hence, chemical compositions of the oxide scales formed on both *nc* and *mc* alloys before and after 240min of oxidation were characterized, and the results are described in *section 6.4*.
- (b) Interestingly, the considerable change in the oxidation kinetics between nanocrystalline (*nc*) and microcrystalline (*mc*) Fe-10Cr alloys after 240min of oxidation is also manifest in some stark difference in colour of the oxidized samples (insets in Figure 6.1b). Colour of both *nc* and *mc* alloys are similar (brownish gold) after 30 and 120 min of oxidation. However, this brownish gold colour changes to greenish-blue in the case of the microcrystalline alloy oxidized for 3120min whereas the nanocrystalline alloy in the same oxidation period had turned red.

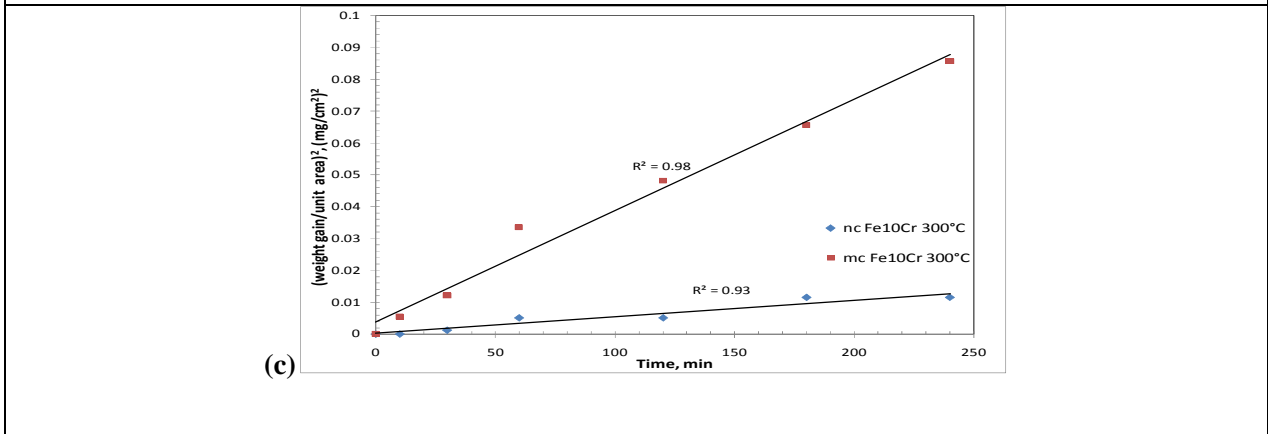
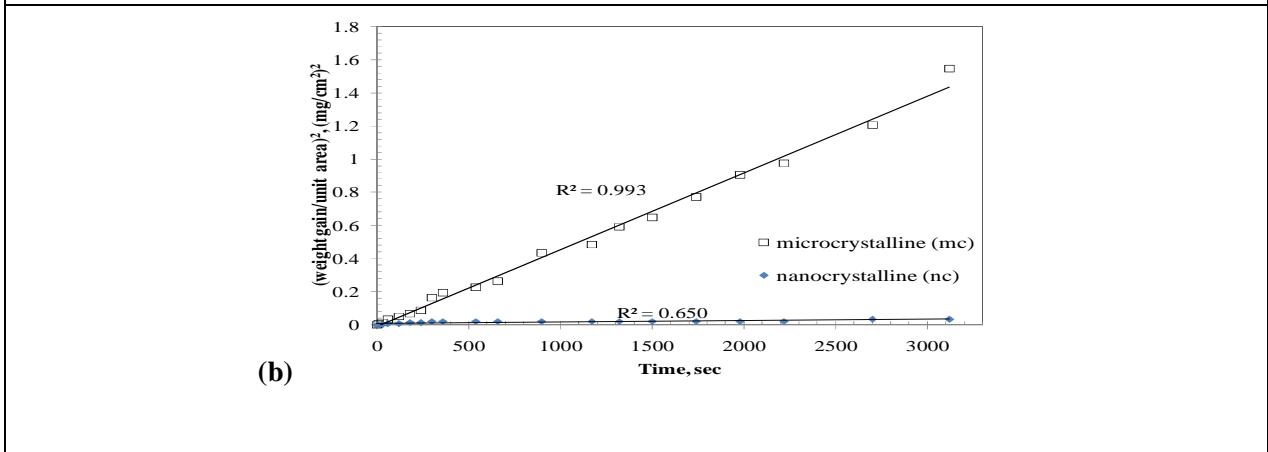
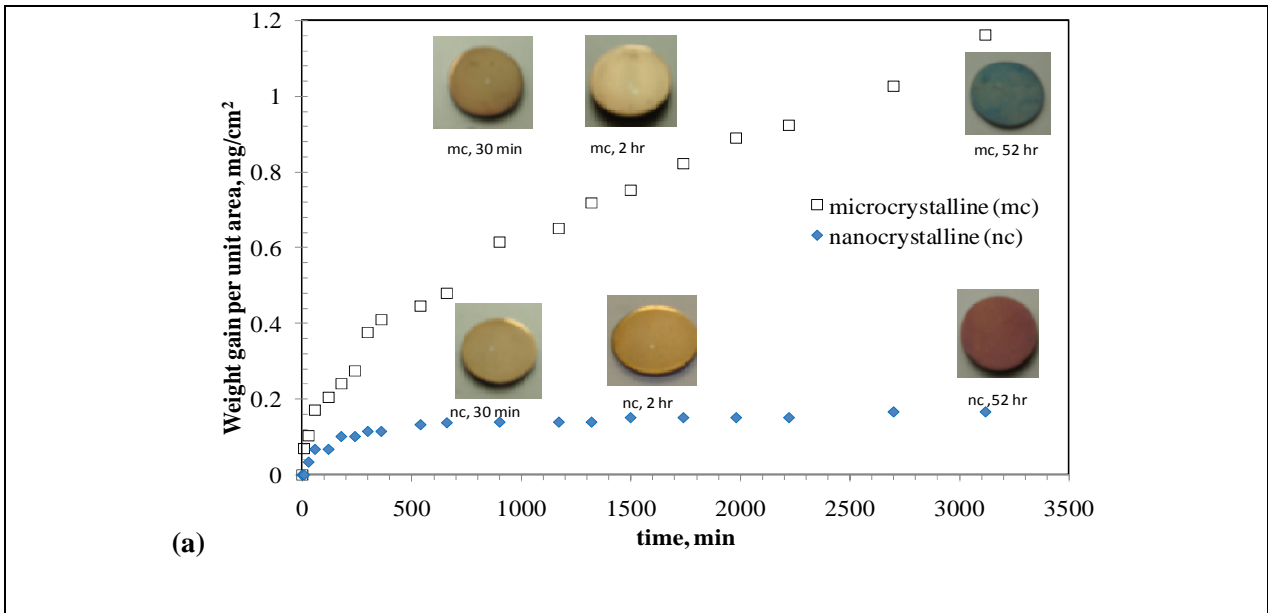
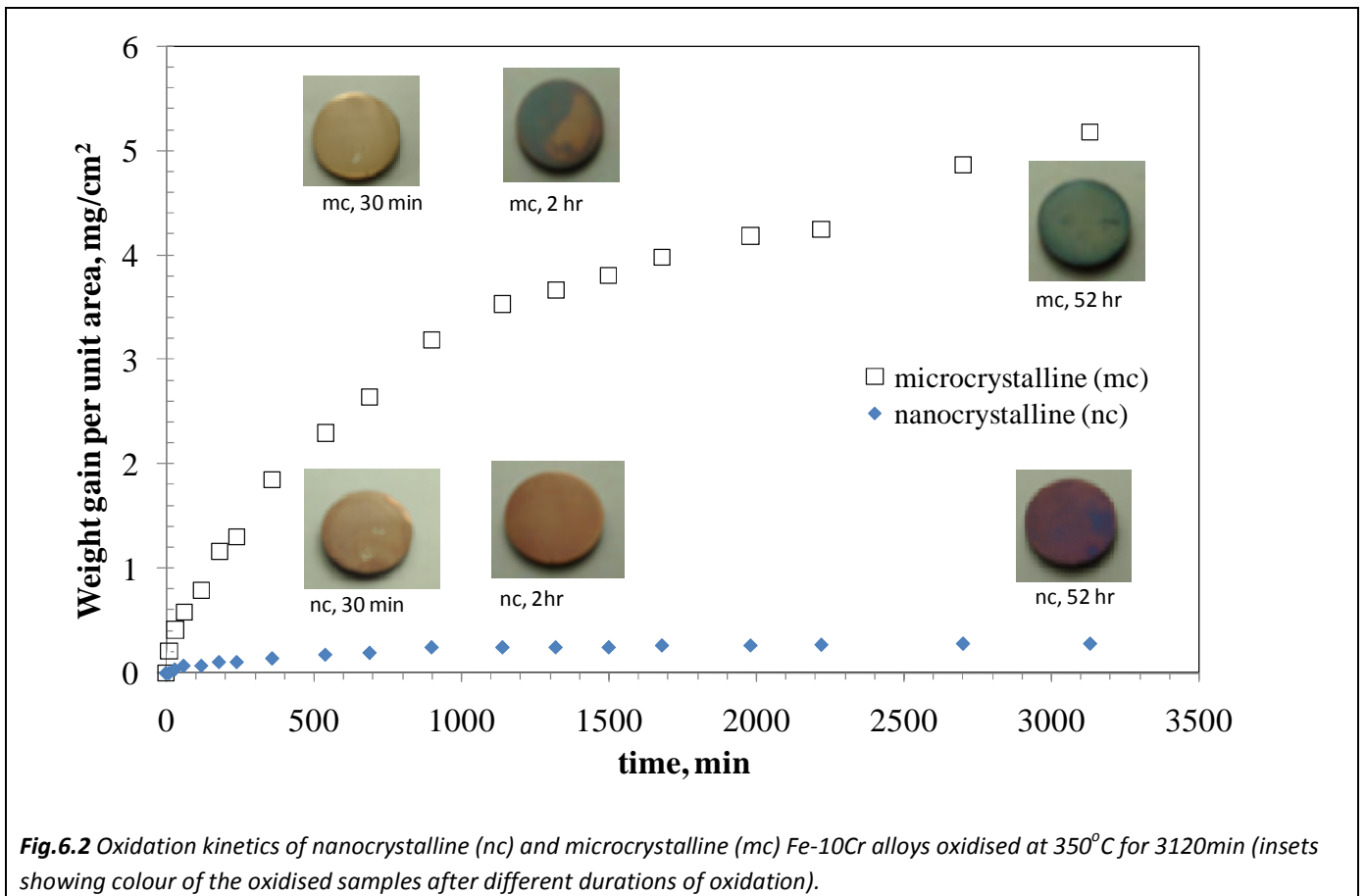


Fig.6.1 Oxidation kinetics of nanocrystalline (nc) and microcrystalline (mc) Fe-10Cr alloys, oxidised at 300°C: (a) weight-gain vs time plots for 3120min (insets showing colour of the oxidised samples after different durations of oxidation), and (b) weight-gain² with time, suggesting parabolic kinetics for mc alloy but departure from parabolic kinetics for nc alloy. (c) weight-gain² with time (up to 240 minutes) suggesting parabolic kinetics for both mc and nc alloys

Oxidation kinetics of nanocrystalline (*nc*) and microcrystalline (*mc*) Fe-10Cr alloys at 350 and 400°C are presented in Figures 6.2 and 6.3. The trend of greater oxidation rate of the *mc* alloy, as seen at 300°C is also followed at the two higher temperatures. However, the influence of *nc* structure in improving the oxidation resistance was extraordinarily enhanced at these higher temperatures as indicated by the comparative weight gains after 3120 minutes of oxidation: weight gain of microcrystalline Fe-10Cr alloy was found to be 18 times greater than that of the nanocrystalline Fe-10Cr alloy at 350°C, and nearly 17 times greater at 400°C.



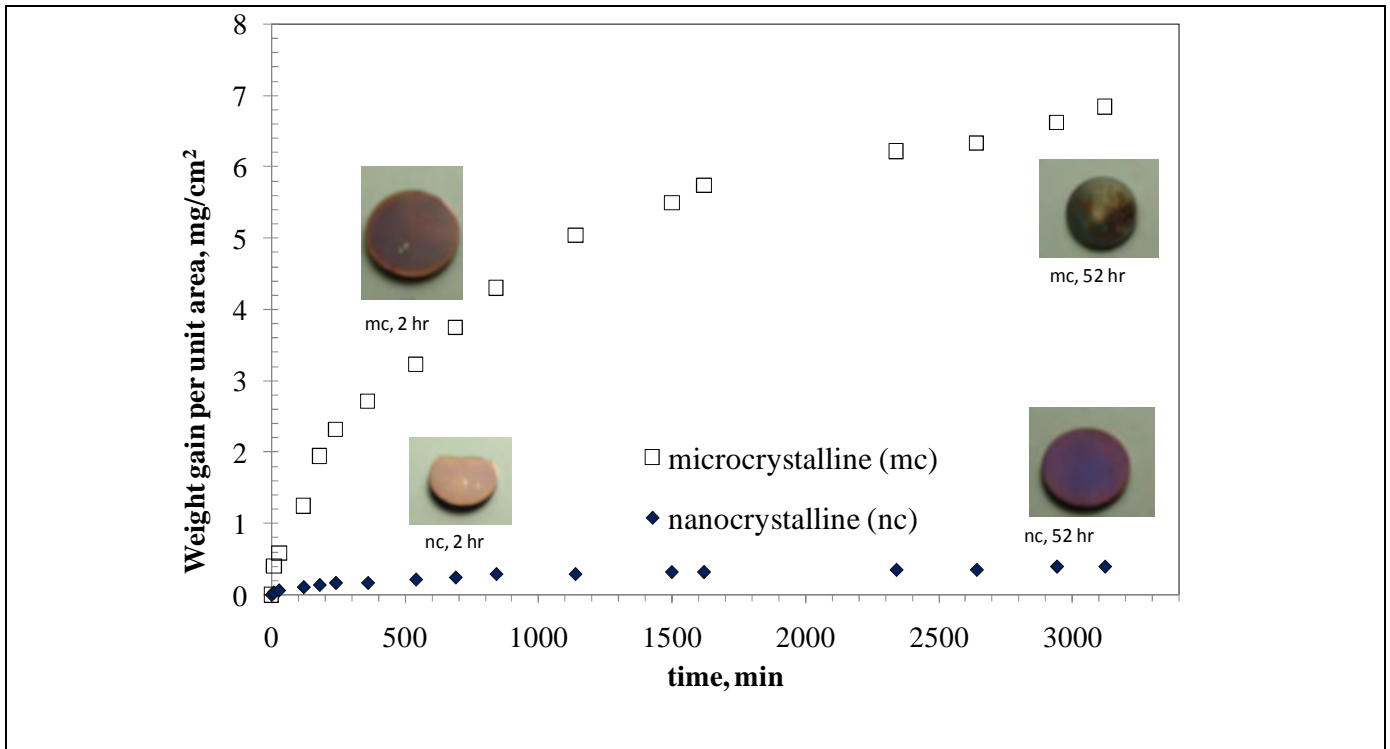


Fig. 6.3 Oxidation kinetics of nanocrystalline (*nc*) and microcrystalline (*mc*) Fe-10Cr alloys oxidised at 400°C for 3120min (insets showing colour of the oxidised samples after different durations of oxidation)

Figures 6.2 and 6.3 also consist as insets the corresponding colour evolution of the oxide scales during oxidation of *mc* and *nc* Fe-10Cr alloys at 350 and 400°C. At 350°C, colour of both *nc* and *mc* alloys are similar (brownish gold) after 30 min which is similar to the colours of the two samples at 300°C after 30min. However, with increasing oxidation temperature there is a systematic decrease in the oxidation time when the difference in colour between the *mc* and *nc* alloys sets in. The transition time is shorter (i.e., 30-120min) at 350°C than that at 300°C (i.e., where the colour change set in after 120min). Colour of the nanocrystalline specimen oxidised at 350°C for 120min was pale red, which intensified over most of the surface during subsequent oxidation up to 3120min (Figure 6.2). The major parts of the 120min-oxidised microcrystalline specimen surface was greenish-blue. The entire surface of this specimen turned greenish-blue during subsequent oxidation up to 3120min. In the case of specimens oxidized at 400°C, a distinct colour difference sets in between *nc* and *mc* specimens even during 2h-oxidation and

the difference became prominent between 2h and 52h (Figure 6.3). Most notably, most of the surface of the *mc* alloy oxidised for 3120min was covered with dark oxidation product with very little bluish-green area, whereas the colour of the *nc* alloy was similar to the corresponding sample oxidized at 350°C.

6.2.1.2 Nanocrystalline vis-à-vis Microcrystalline Fe-20%Cr Alloys

For developing an understanding of how the considerably greater oxidation resistance of *nc* Fe10Cr alloy (in comparison with *mc* Fe-10Cr alloy) compares with the resistance of an alloy with much higher Cr content, samples of nanocrystalline and microcrystalline Fe-20Cr alloys were also oxidized at 300, 350 and 400°C for durations up to 3120min. The weight gains of these alloys at 300°C were too low to be detected by the gravimetric balance used for this study. However, it was possible to characterize the chemical composition of the thin oxide scales developed at the two higher temperatures. Oxidation kinetics of *nc* and *mc* Fe-20Cr alloys at 350°C (Figure 6.4) suggest only a little improvement in oxidation resistance due to nanocrystalline structure. However, what is most relevant to note is that the weight gain at the end of 3120min-oxidation of *mc* Fe-20Cr alloy is similar to that of the nanocrystalline Fe-10Cr alloy at 350°C (shown in Figure 6.5), suggesting the degree of oxidation resistance conferred due to nanocrystalline structure at only 10% chromium to be similar to that of the alloy with twice as much chromium but microcrystalline structure.

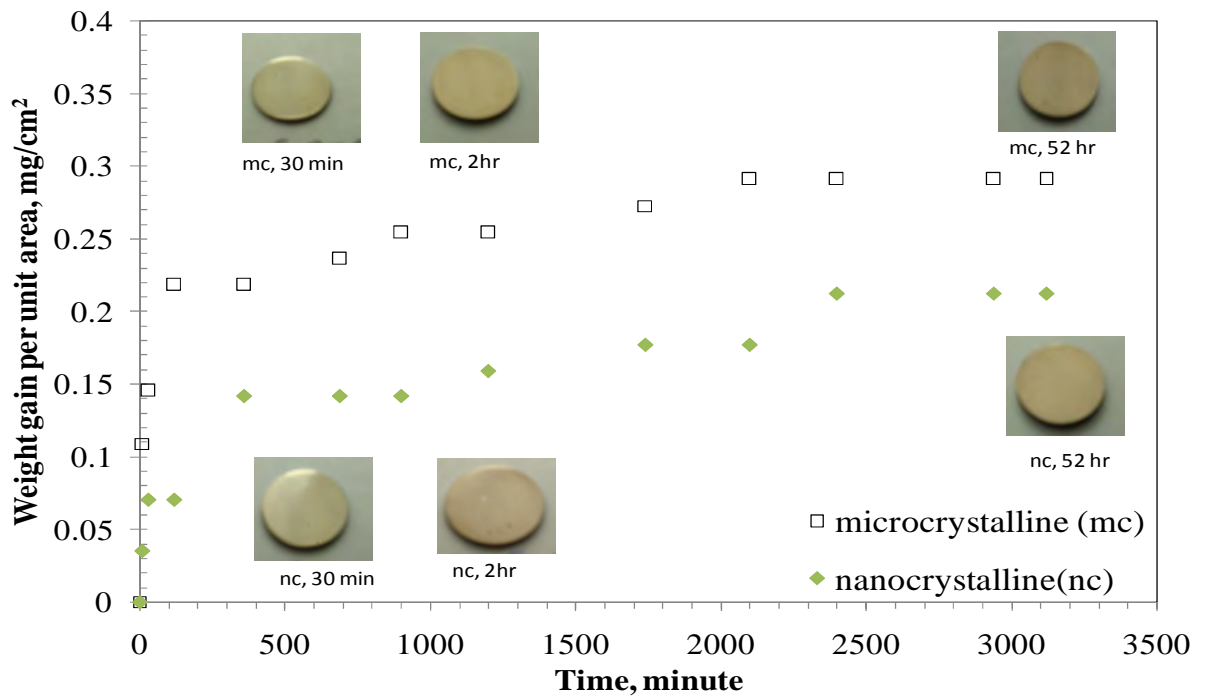


Fig. 6.4 Oxidation kinetics of nanocrystalline (nc) and microcrystalline (mc) Fe-20Cr alloys oxidised at 350°C for 3120min (insets showing colour of the oxidised samples after different durations of oxidation).

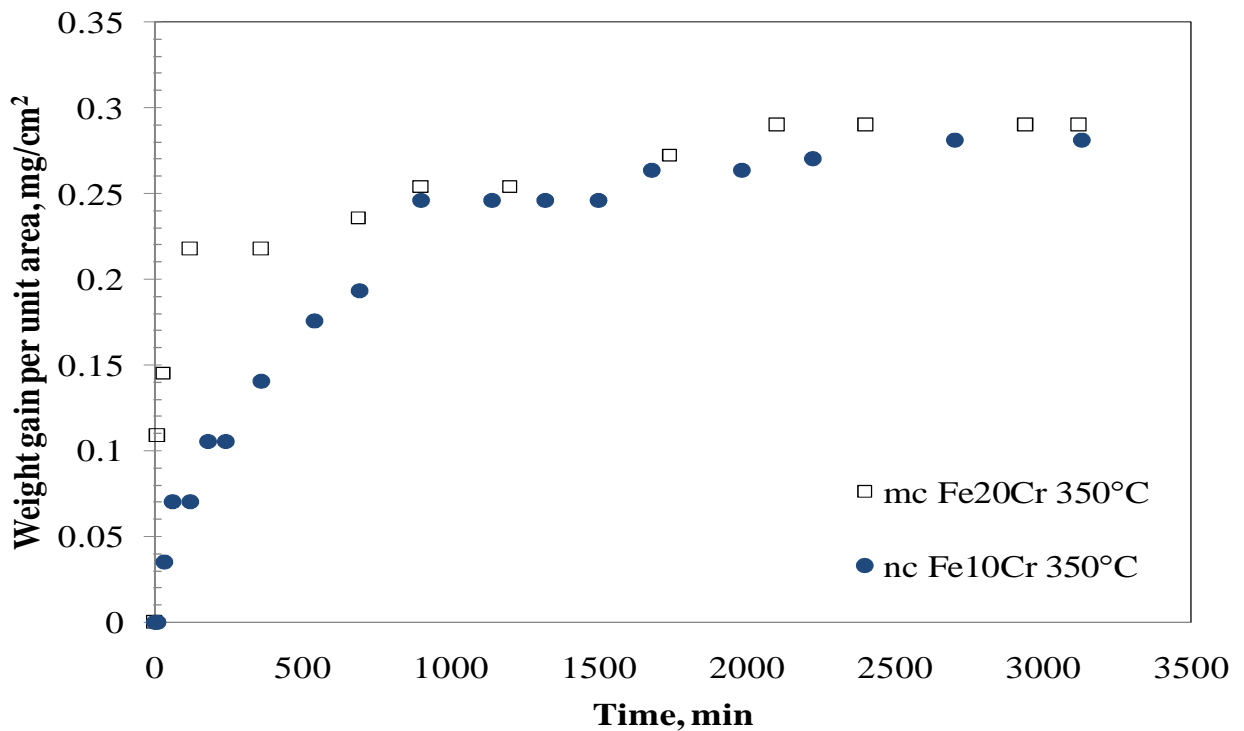


Fig. 6.5 Comparison of oxidation resistance of nanocrystalline Fe10Cr alloy with that of microcrystalline Fe20Cr alloy

Figure 6.4 also consists, as insets, the colour of the oxide scales during oxidation of *mc* and *nc* Fe-20Cr alloys at 350°C. Representative photographs of the colour of the oxide scales at different stages of oxidation at 300 and 400°C are presented in Figure 6.6. There is little difference between the colours of the two alloys at various stages of oxidation at each of the three temperatures. However, the bright appearance of the alloys at the earlier stages of oxidation turned somewhat dull with increasing duration of exposure.

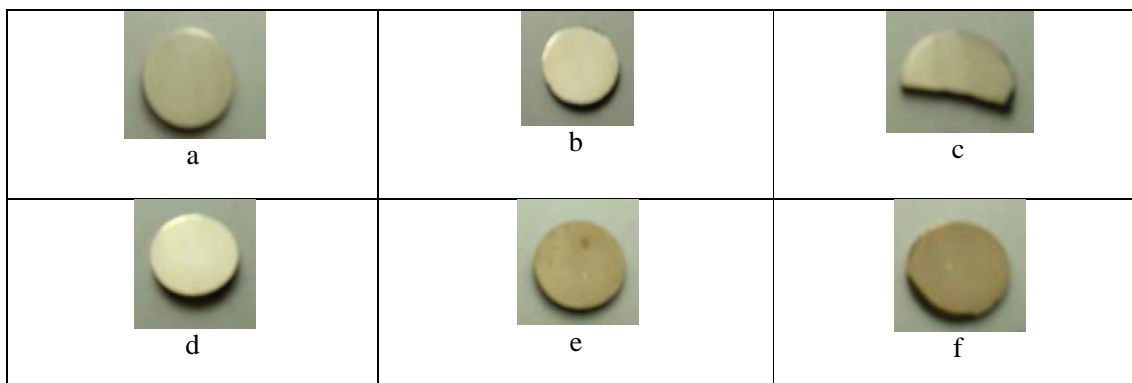


Fig. 6.6 Representative photographs of the colour of the oxide scales developed on *nc* and *mc* Fe-20Cr alloys at different stages of oxidation at 300 and 400°C: (a) *nc*, 300°C, 30 min, (b) *nc*, 300°C, 120 min, (c) *mc*, 300°C, 30 min, (d) *mc*, 300°C, 120 min, (e) *nc*, 400°C, 120 min, (f) *mc*, 400°C, 120 min

6.2.2 Depth Profiles of Oxide Scales by Secondary Ion Mass Spectrometry (SIMS)

In order to investigate the reason for the considerable difference in oxidation rates of Fe-10Cr alloy due to nanocrystalline and microcrystalline states (Figures 6.1-6.3), it became essential to characterize the elemental distribution in the oxide scales. As described in *section 6.1* above, oxidation resistance of Fe-Cr alloys is associated primarily to the Cr content of the thin inner oxide scale and the eventual development of the protective layer of Cr₂O₃. Depth profiles of chromium, oxygen and iron in the oxide scales were generated using secondary ion mass spectrometry (SIMS).

Depth profiles for Cr, O and Fe for the *nc* and *mc* Fe-10Cr alloys oxidized at 300°C for 30, 120 and 3120 min are presented respectively in Figure 6.7a, 6.7b and 6.7c. Similar profiles for specimens oxidized at 350 and 400°C for different durations are presented respectively in Figures 6.8a-c and 6.9a-b. Comparison of Cr, O and Fe profiles (Figures 6.7-6.9) suggests the oxide film developed on *mc* Fe-10Cr alloy to be considerably thicker than that on *nc* Fe-10Cr alloy at the three test temperatures as well as at various oxidation times. However, Fe and O depth profiles of the alloys oxidized for short durations (30 and 120min) suggest much greater Fe and O contents in the outer scales of *nc* Fe-10Cr alloy (Figures 6.7 a&b, 6.8a&b and 6.9a&b).

Depth profiles for Cr (as evident from the Figures 6.7-6.9) show that Cr enrichment in the nanocrystalline form of the Fe10Cr alloy is much higher than that of microcrystalline counterpart for all the oxidation conditions. Enrichment of Cr is one of the reasons of enhanced oxidation resistance exhibited by nanocrystalline form of the alloys. Interestingly, *nc* Fe20Cr alloy also shows more Cr enrichment in comparison to *mc* Fe20Cr alloy but, level of enrichment obtained in case of Fe20Cr alloy is not as great as that in Fe10Cr alloy. This will be discussed later in the discussion section.

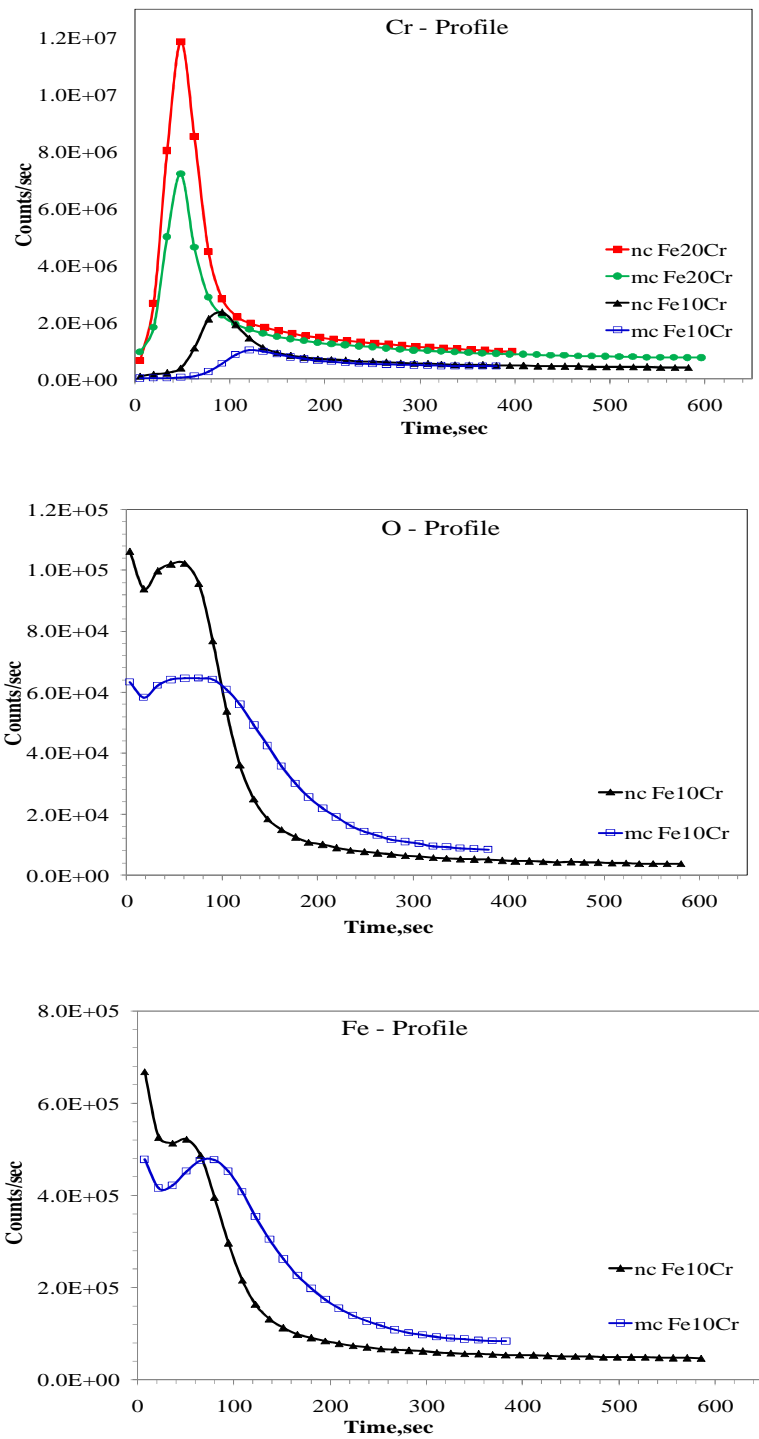


Fig.6.7 (a) SIMS depth profiles for Cr, O and Fe in the oxide scales developed during oxidation at 300°C of nanocrystalline (nc) and microcrystalline (mc) Fe-10%Cr and Fe-20Cr alloys oxidized for 30min

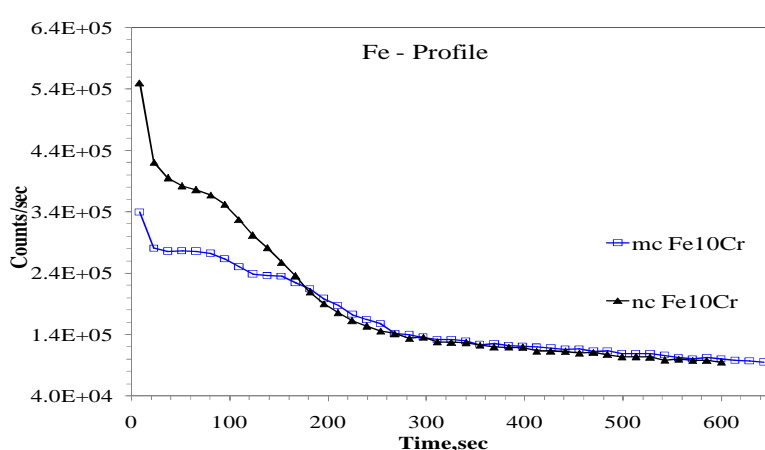
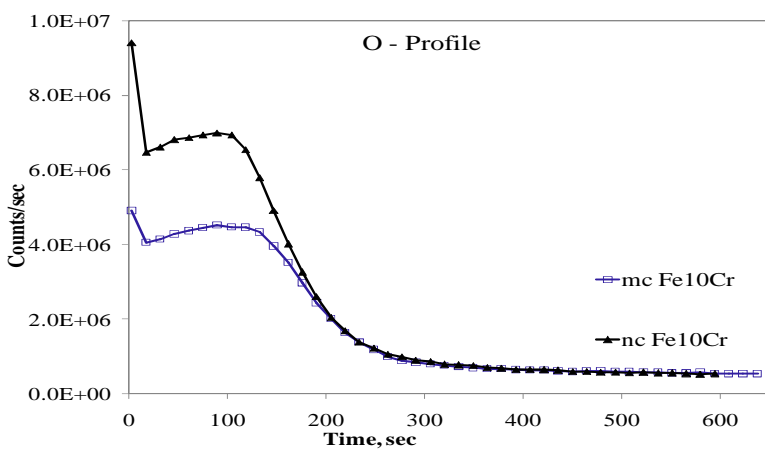
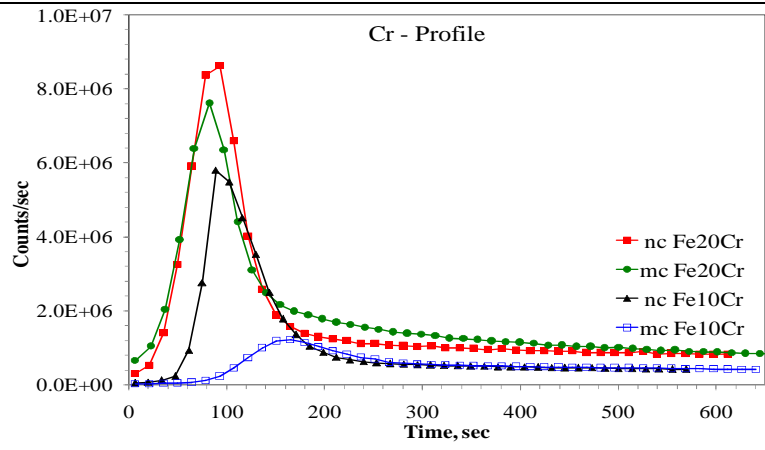


Fig.6.7 (b) SIMS depth profiles for Cr, O and Fe in the oxide scales developed during oxidation at 300°C of nanocrystalline (nc) and microcrystalline (mc) Fe-10%Cr and Fe-20Cr alloys oxidized for 120min

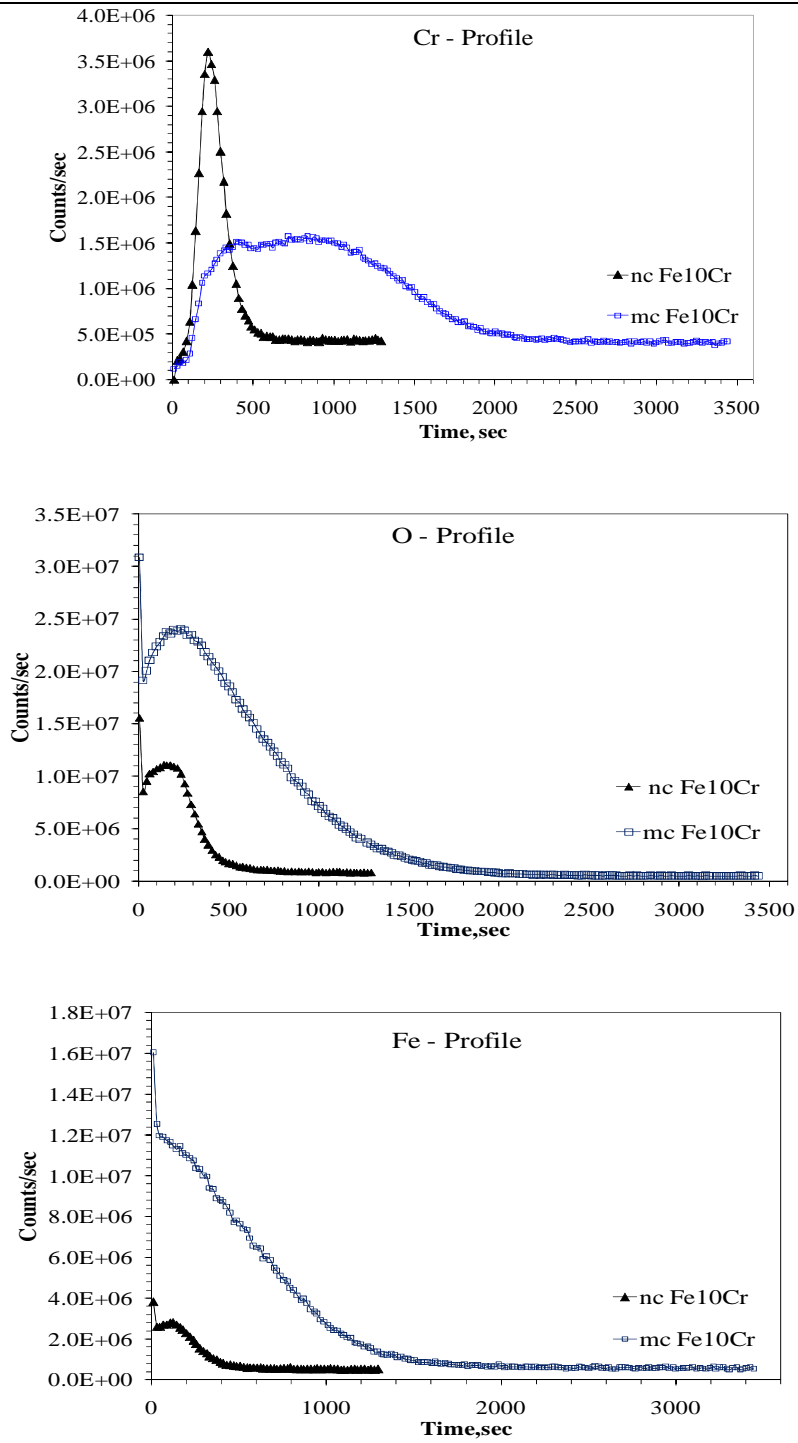


Fig.6.7 (c) SIMS depth profiles for Cr, O and Fe in the oxide scales developed during oxidation at 300°C of nanocrystalline (nc) and microcrystalline (mc) Fe-10%Cr alloys oxidized for 3120min

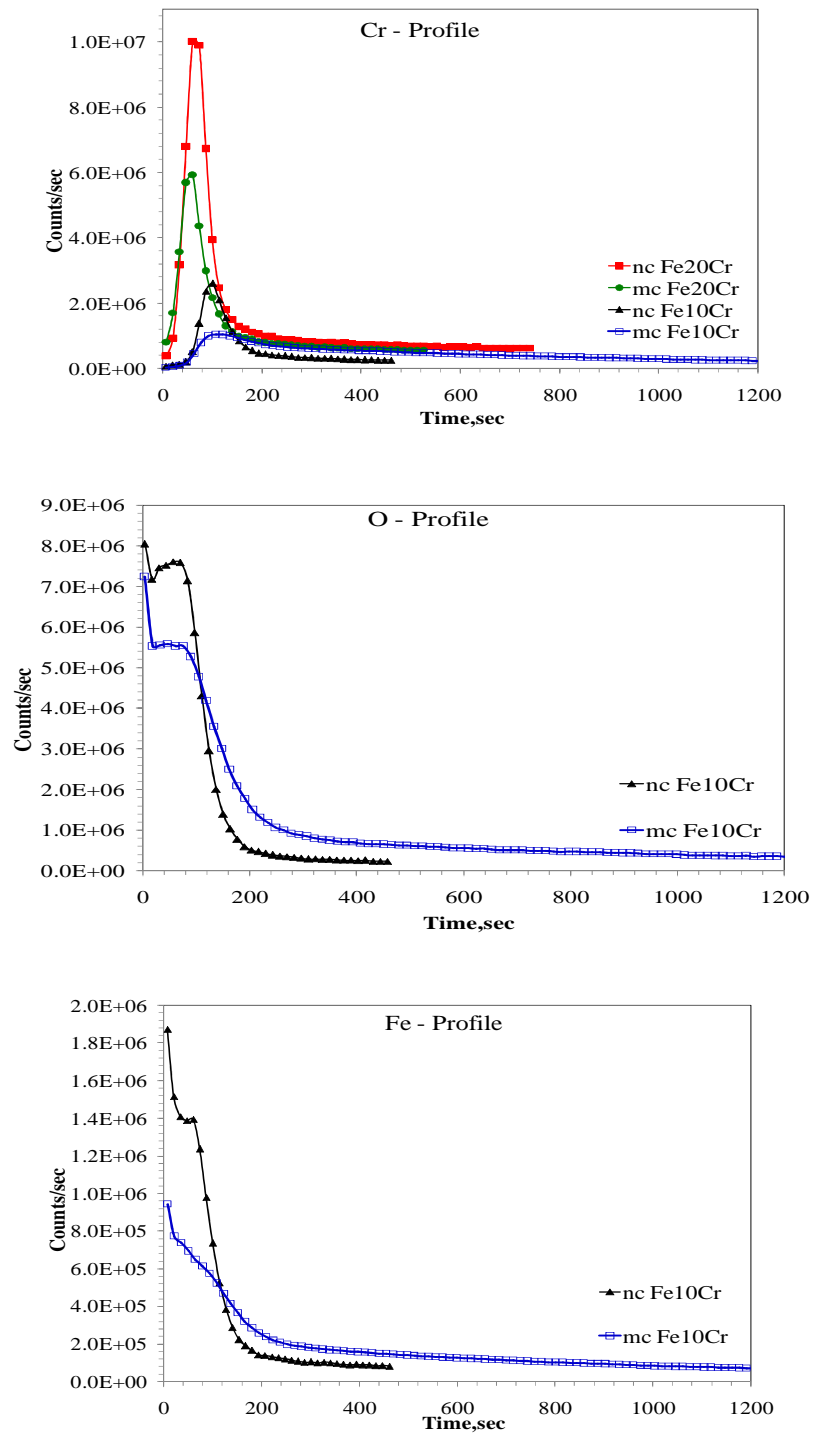


Fig.6.8 (a) SIMS depth profiles for Cr, O and Fe in the oxide scales developed during oxidation at 350°C of nanocrystalline (nc) and microcrystalline (mc) Fe-10%Cr and Fe-20Cr alloys oxidized for 30min

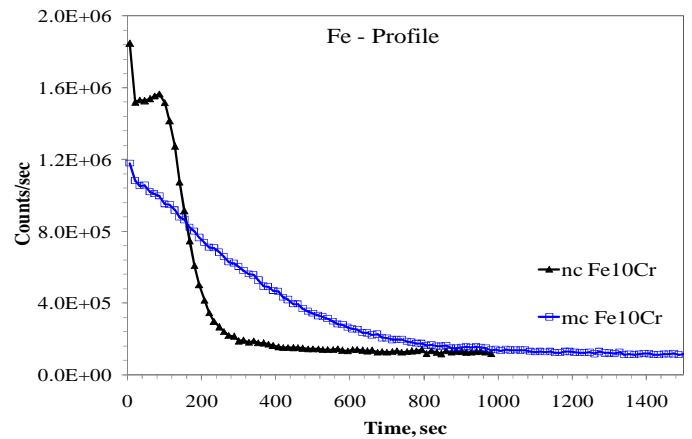
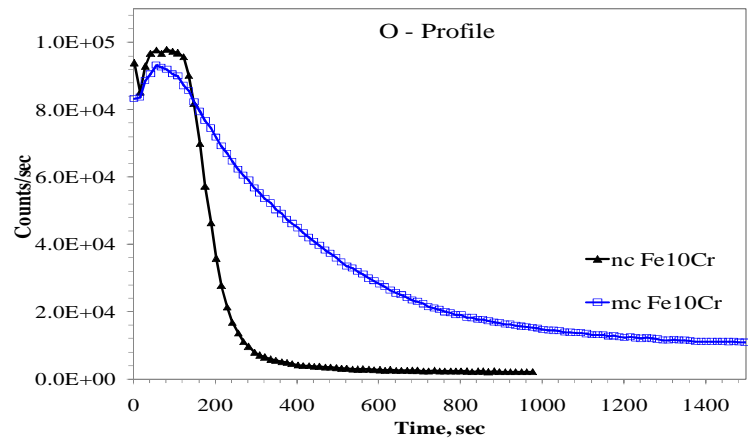
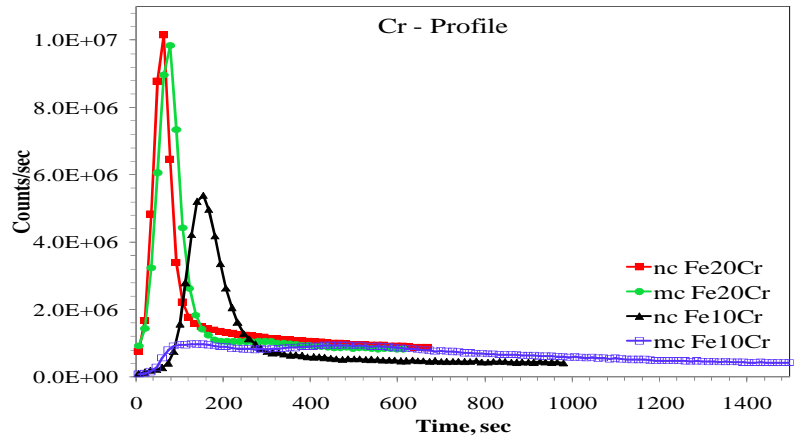


Fig.6.8 (b) SIMS depth profiles for Cr, O and Fe in the oxide scales developed during oxidation at 350°C of nanocrystalline (nc) and microcrystalline (mc) Fe-10%Cr and Fe-20Cr alloys oxidized for 120min

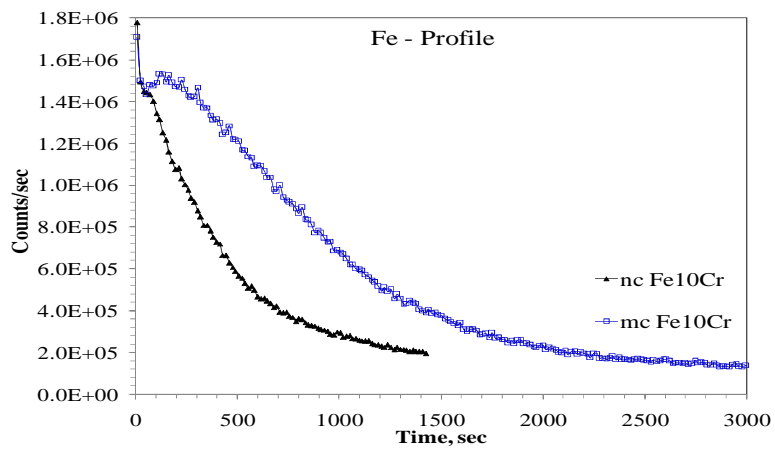
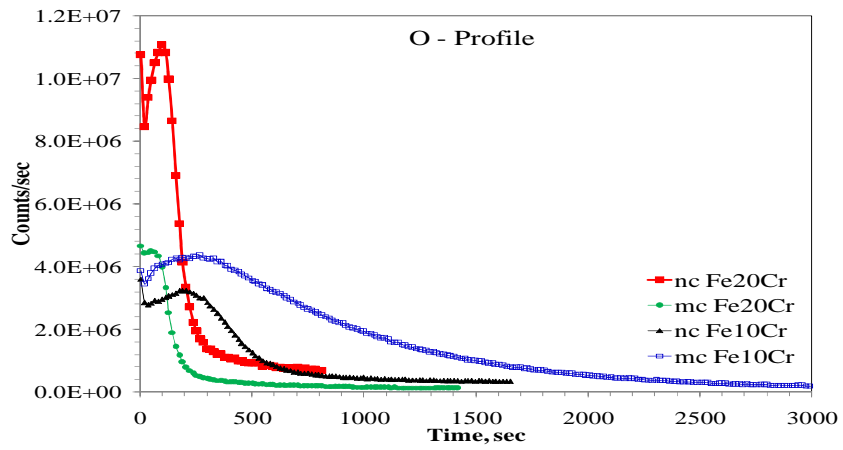
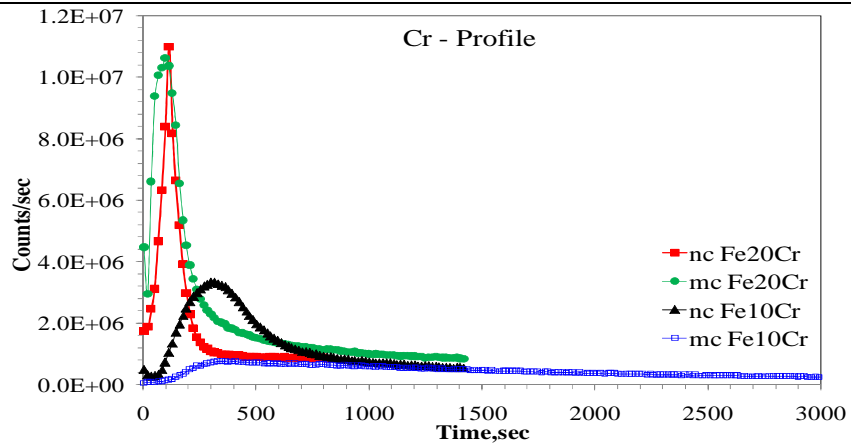


Fig.6.8 (c) SIMS depth profiles for Cr, O and Fe in the oxide scales developed during oxidation at 350°C of nanocrystalline (nc) and microcrystalline (mc) Fe-10%Cr and Fe-20Cr alloys oxidized for 3120min

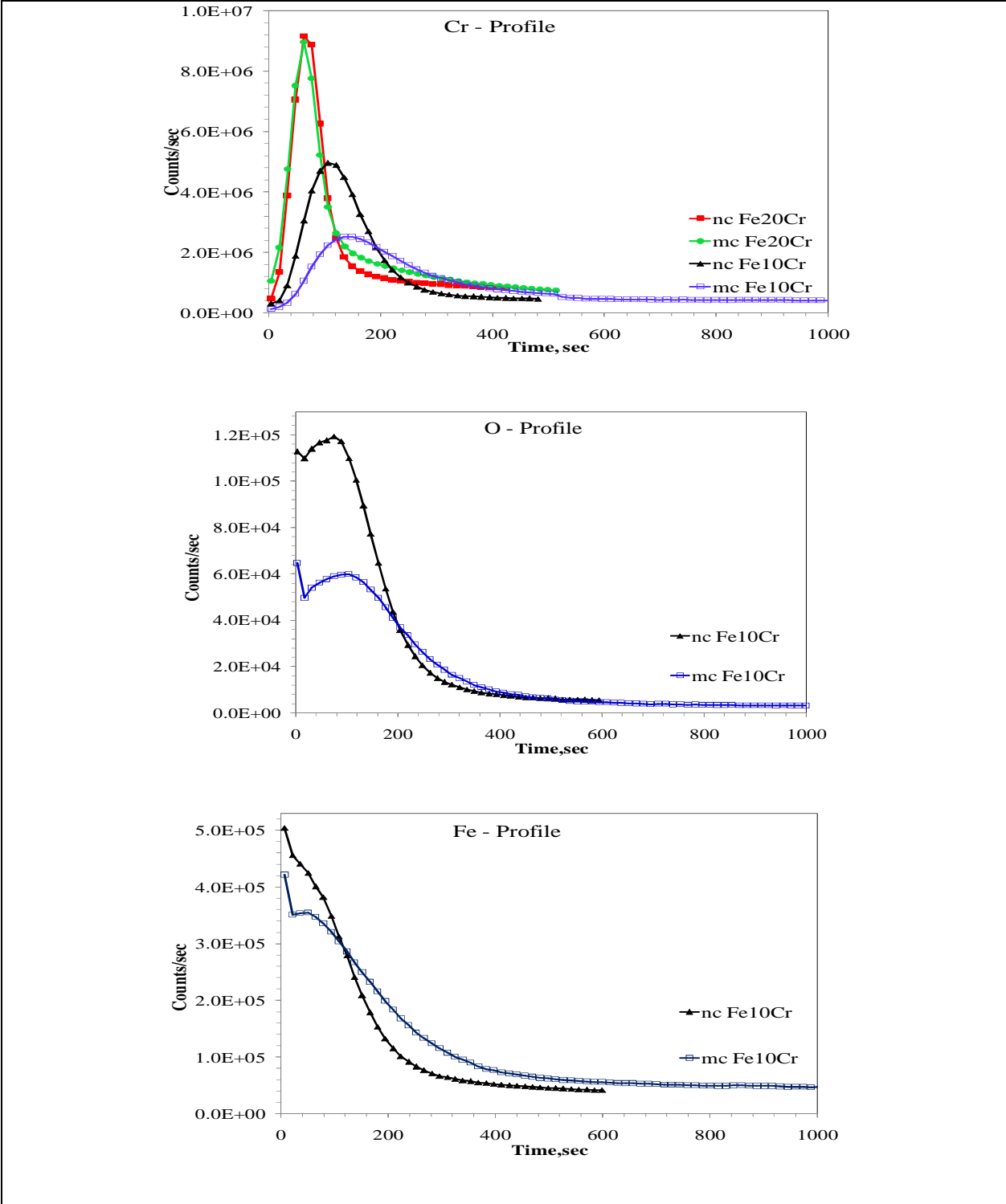
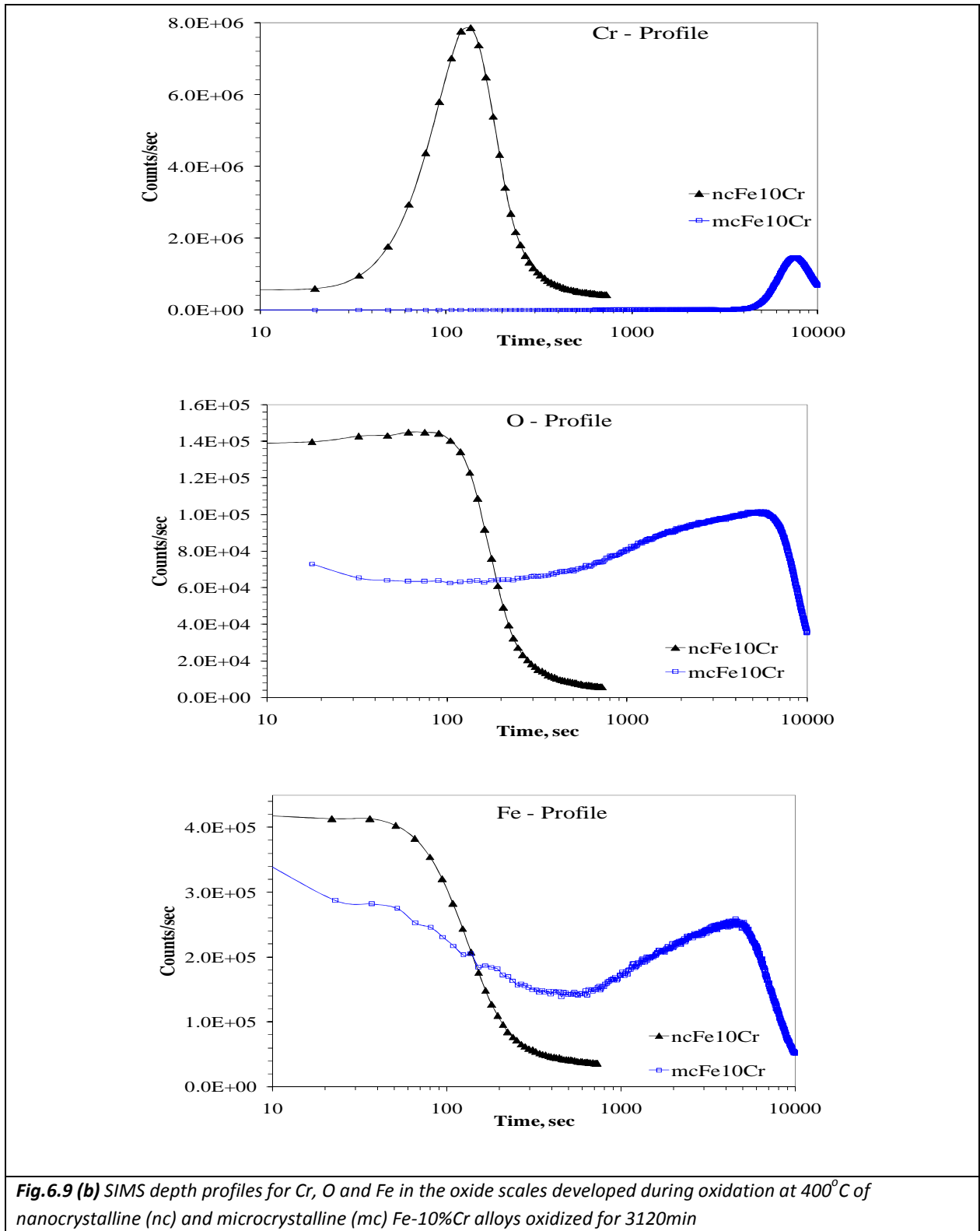


Fig.6.9 (a) SIMS depth profiles for Cr, O and Fe in the oxide scales developed during oxidation at 400°C of nanocrystalline (nc) and microcrystalline (mc) Fe-10%Cr and Fe-20Cr alloys oxidized for 120min



6.4 DISCUSSION

6.4.1 SIMS investigations and co-relation with kinetic curves

The most relevant findings of the SIMS analyses are the depth profiles of chromium and their stark consistency with the trends of oxidation kinetics as well as the colour evolution of the oxide scales. At each of the oxidation temperatures and at each oxidation duration (Figures 6.7-6.9), the highest Cr content of the inner layer of *nc* Fe-10Cr alloy was invariably found to be considerably higher than the highest Cr content in the inner layer of *mc* Fe-10Cr alloy. This may provide a ready explanation for the greater oxidation resistance of the *nc* Fe-10Cr alloy (as shown in Figures 6.1-6.3), since oxidation resistance of Fe-Cr alloys is governed primarily by the Cr content of the thin inner oxide scale [293,294,376,377].

A careful comparison of the Cr depth profiles of the oxide scales formed in different oxidation durations also indicates the time domains for the considerable change in oxidation kinetics (i.e., deviation from parabolic kinetics) of *nc* alloy to be consistent with the eventual extraordinary enrichment of chromium in the inner oxide scales on the *nc* alloy. For example, after 30min of oxidation at 300°C, the highest chromium content of the inner scale on *nc* Fe-10Cr alloy is twice as high as that for the *mc* Fe-10Cr alloy (Figure 6.7a). However, in the case of the samples oxidised for 120min (Figure 6.7b), the highest chromium content of the inner layer of *nc* alloy grew to ~6 times greater than that of the inner layer of the *mc* alloy. At this considerably higher Cr content of the oxide layer on *nc* Fe-10Cr alloy, the inner oxide layer is assumed to be of Cr₂O₃. In order to examine the validity of formation of a protective layer of Cr₂O₃, chromium content of the inner layer, developed on *nc* Fe-10Cr alloy, was compared with that of the inner layer, developed under the same conditions (30min/300°C) on the microcrystalline (*mc*) Fe-20Cr alloy (i.e., an Fe-Cr alloy with 20%Cr is known to have sufficient chromium to develop the protective Cr₂O₃ layer) [293,294]. As the chromium depth profiles in Figure 6.7b would suggest the

chromium content of the inner oxide layers of the *nc* Fe-10Cr and *mc* Fe-20Cr alloys are comparable, and hence both the alloys are assumed to have developed protective Cr₂O₃ layers. However, it took some time and sufficient diffusion-assisted chromium enrichment before a Cr₂O₃ layer could eventually be established on the *nc* Fe-10Cr alloy. Once this layer was established, the subsequent oxidation rate decreased drastically (Figure 6.1a and 6.1b), which also accounts for the insignificant weight-gain and departure from parabolic kinetics during oxidation beyond 240min and until 3120min (Figure 6.1a and 6.1b). In fact, it would be fair to suggest that most of the weight gain of *nc* Fe-10Cr alloy occurred until the time when the protective Cr₂O₃ layer was yet to be established. Because of its high chromium content, *mc* Fe-20Cr alloy had quickly established the Cr₂O₃ layer, allowing little weight gain throughout the 3120min oxidation, as was the case for *nc* Fe-10Cr alloy after the initial period of eventual establishment of Cr₂O₃ layer. Thus, results of SIMS analyses have served to establish that it is possible to develop a protective layer of chromium oxide during the oxidation of nanocrystalline Fe-Cr alloys at a considerably low chromium content (10% in this case).

The trend of considerably greater chromium contents in the inner scales of nanocrystalline Fe-10Cr alloy than microcrystalline Fe-10Cr alloy, after different oxidation times at 300°C, holds good also for oxidation of the *nc* and *mc* alloys at 350 and 400°C (Figures 6.8 and 9). In fact, SIMS depth profiles for Cr, O and Fe suggest that thickness of both the inner Cr₂O₃ layer and the external iron oxide layer, developed on the nanocrystalline Fe-10Cr alloy at 400°C in 3120min, to be extraordinarily smaller than that of *mc* Fe-10Cr alloy as well as the chromium content of the inner scale on the microcrystalline Fe-10Cr alloy to be extraordinarily lower (Figures 6.8a and 9b).

As the reported literature would suggest [376-379], inner oxide layer of the microcrystalline alloys with low-Cr (<12%) would at best be a mixed spinel type Fe-Cr oxide, which would provide limited oxidation

resistance (because such low-chromium-alloys would fail to develop a Cr_2O_3 layer). In the present study, for example, a comparative assessment of the Fe, O and Cr depth profiles of the microcrystalline samples oxidised at 300°C for 30, 120 and 3120 min (Figures 6.7a, 6.7b and 6.7c) would, indeed, suggest that the inner layer consists of the mixed oxide of Fe and Cr and the external layer of iron oxide. Both these layers have grown considerably in thickness during oxidation for 3120 min (Figure 6.7c). Therefore, the considerably greater oxidation rate of the samples of microcrystalline Fe-10Cr alloy (as compared to nanocrystalline Fe-10Cr alloy), as shown in Figures 6.1, is explained on the basis of the considerably lower Cr content in the inner oxide layer (Figures 6.7a, 6.7b and 6.7c) and their inability to develop the protective oxide layer of Cr_2O_3 . This explanation, also, holds good for oxidation of microcrystalline Fe-10Cr alloy at 350 and 400°C (Figures 6.8 and 6.9). In fact, the chromium content of the inner scale of Fe-Cr mixed-oxide, developed on the microcrystalline Fe-10Cr alloy in 120 and 3120min at 400°C , was found to be extraordinarily lower (Figures 6.9a and 6.9b).

The greater Fe content in the oxide scale on *nc* Fe-10Cr alloy is attributed to a greater grain boundary oxidation of the dominant alloy constituent (i.e., Fe) in the initial stages, owing to the far greater grain boundary area at the surface of a nanometric grain size alloy as compared to the *mc* alloy of the same composition. However, as is suggested from the depth profiles of specimens oxidized for a long duration of 3120 min, with highly enhanced enrichment of chromium in the oxide scale and an eventual development of the highly protective chromium-rich scale evolving on *nc* alloy, the iron content of the scales formed on *nc* alloy decreases drastically and becomes considerably lower (Figures 6.7c, 6.8c and 6.9b) as compared to that in the scales in the initial stages as well as compared to the Fe content in the *mc* alloy oxidized for the corresponding durations (Figures 6.7a&b, 6.8a&b and 6.9a&b).

6.4.2 Correlation of colour evolution and composition of oxide scales

As suggested earlier, it has been possible to find a consistency in the explanations for the oxidation kinetics and the corresponding colour change of the *nc* and *mc* Fe-10Cr alloys (seen in Figures 6.1-6.4).

In spite of their identical chromium contents, discs of *nc* and *mc* Fe-10Cr alloys after oxidation at 300, 350 and 400°C for 3120min have distinctly different colours (Figures 6.1-6.3). However, the discs of both *nc* and *mc* alloys have similar colour in the initial stages of oxidation. During subsequent oxidation, the difference in colour between the *nc* and *mc* alloys sets in. Oxidation duration, when the difference in colour sets in, decreases with increasing oxidation temperature (Figures 6.1-6.3). Besides, in the area of the difference in colour between the *nc* and *mc* alloys, it is interesting to note that in spite of insignificant weight-gain during 120-3120min, the colour of *nc* alloys changed dramatically, suggesting the colour change of the *nc* alloy to be associated with some chemical change in the external layer.

Like, in the case of oxidation kinetics, it seems possible to correlate the difference in colour of the oxide films on *nc* and *mc* Fe-10Cr alloys with the chemical composition of the oxide films and the ease/ability to form the protective layer. For example, at 300°C, in initial stages (30min), both *nc* and *mc* alloys form oxide films that consist, predominantly, of the external layer of iron oxide and the inner layer of Fe-Cr mixed oxide (as suggested by the SIMS depth profiles in Figures 6.7-6.9). In fact, the depth profiles of a 30-min oxidised *nc* sample (Figure 6.11a) and the associated description in *the previous section* suggest the iron content of the external scale of *nc* alloy to be greater than that of the *mc* alloy, owing to the greater grain boundary oxidation of the former. The standard Fe-O phase diagram [380] would suggest this external layer to be of magnetite (Fe_3O_4), which, when sufficiently thick, is dark in colour. However, the oxide films on both *nc* and *mc* alloys oxidized for 30 min at 300°C are thin, and hence the samples do not appear dark. Both *nc* and *mc* specimens were brownish gold after 120min of oxidation. However, the oxidised *mc* alloy is somewhat dark. As described in *the previous section*, by 120min, the inner layer

eof protective layer of Cr_2O_3 had established, and had drastically constricted the outward iron diffusion, allowing only an insignificant weight-gain during subsequent oxidation. Due to the drastically - constricted outward iron diffusion, the magnetite layer, which is in direct contact with oxygen would eventually convert into hematite (as per the Fe-O phase diagram), which is red in colour. This explains the colour transformation of the *nc* alloy to red in the course of 120-3120min, in spite of little weight-gain during this period (Figure 6.1b). On the other hand, as described in the previous section, *mc* Fe-10Cr alloy fails to develop the inner protective layer of Cr_2O_3 , but, forms, in the initial stages, an inner layer of Fe-Cr mixed oxide, which is greenish-blue. As the Fe-Cr mixed oxide layer thickens with time (as suggested by SIMS profile in Figure 6.7a, 6.7b and 6.7c), the colour of the entire sample becomes greenish-blue.

The above description of the correlation of the difference in colour of 300°C-oxidised samples with the establishment of Cr_2O_3 layer on *nc* Fe-10Cr alloy and lack of its formation on *mc* Fe-10Cr alloy holds good also for the samples oxidised at 350 and 400°C (Figures 6.2-6.3). However, time taken for the inception of distinct difference in colour between the *mc* and *nc* alloys decreases with increase in oxidation temperature, viz., Cr_2O_3 establishing, after 120min at 300°C, 30-120min at 350°C and within 30min at 400°C. Colour change of the oxidised samples as well as the colour difference between *nc* and *mc* alloys samples during oxidation at 350 and 400°C for different durations, apparently, finds explanation in the ability/inability to establish Cr_2O_3 layer, which is a function of temperature- and time- dependent diffusion of chromium.

For example, *nc* and *mc* specimens that showed most stark difference in colour between them when oxidised at 400°C for 3120 min (Figure 6.3) also had most drastic difference in chromium contents and thickness of the two oxide scales (as suggested by SIMS depth profiles in Figure 6.9b). The chromium

diffusion in alloy and enrichment in the inner layer was facilitated more at 400°C, effecting an early establishment of the inner Cr₂O₃ layer in the case of *nc* alloy, which also causes an early conversion of the external magnetite layer to hematite and explains an early transformation of most of the initially - formed brownish gold oxide scale to a red colour (Figure 6.3). However, in spite of the well-established protective layer of Cr₂O₃ layer, a significant amount of chromium, enriched in the inner layer, seems to have diffused outward at the higher temperature, causing partial transformation of the external magnetite layer into Fe-Cr mixed oxide, thus, explaining why the *nc* specimen oxidised at 400°C for 3120min also has bluish patches in addition to the red areas (Figure 6.3). On the other hand, the Fe-Cr mixed oxide that usually forms on *mc* Fe-10Cr alloy, developed relatively quickly during oxidation at 400°C because of the greater diffusivity at this temperature, as is evident from the SIMS depth profiles for 120min-oxidised *mc* specimen that suggest much greater Cr content than for specimens oxidised for shorter durations (Figures 6.7b, 6.8b and 6.9b). This layer provides some protection in the early stages and the scale is a mix of Fe-Cr mixed oxide and hematite (as suggested by the bluish red appearance of the scale after 120min of oxidation (Figure 6.3). However, the Fe-Cr mixed oxide being considerably less protective, it fails to provide much protection beyond the early stages and allows substantial outward diffusion of iron, resulting, presumably, in formation of some thick magnetite that accounts for the dark areas in the scale (seen in the case of specimen oxidised for 3120 min at 400°C (Figure 6.3).

6.4.3 Critical grain size and Cr content for protective Cr₂O₃ layer formation

Given that the present study has established that it is possible to develop a protective scale of Cr₂O₃ at a considerably low chromium content on a nanocrystalline Fe-Cr alloy, attempts have been made to develop a theoretical understanding of the minimum chromium content required for transformation of the layer of Fe or Fe-Cr oxide into the Cr₂O₃ at a given nanometric grain size.

During oxidation, several of the binary alloys with certain alloying elements (viz., Cr, Al and Si) can form a continuous layer of the oxide of more reactive solute, conferring substantial oxidation resistance. In the case of these alloys, since the time-dependent inward flux of oxygen is generally less than the time-dependent outward flux of solute, all the oxidation reaction commonly results in the formation of a continuous layer of surface oxide (called external oxidation) [380]. If, on the other hand, the inward flux of oxygen exceeds the outward flux of solute, isolated oxide particles form in the sub-surface and this phenomenon is called internal oxidation [380]. From a fundamental point of view, internal and external oxidation processes are best studied using binary alloy systems, where one of the components is noble and does not undergo oxidation even at low partial pressures of oxygen. However, oxidation of engineering alloys is somewhat complicated due to the formation of an outer layer of the relatively active component, which (to an extent) fixes the nominal oxygen partial pressure at the interface of this oxide with the underlying metal. This section presents a theoretical treatment of the minimum chromium content required for transformation of the layer of Fe or Fe-Cr oxide (that generally forms on low chromium alloy) into the Cr_2O_3 at a given nanometric grain size. In Fe-Cr alloys, transition is also required from internal to external oxidation which establishes a continuous layer of Cr-oxide layer. Availability of sufficient chromium at the alloy-oxide interface is essential for the effectiveness of both the transition types to a continuous Cr_2O_3 layer. Establishment of such continuous oxide layer of solute depends on the several factors which include: (a) the concentration and diffusion of the solute in the alloy, (b) the diffusion of the oxygen in the alloy, (c) diffusion of oxygen in the external oxide film and (d) the growth rate of solute-oxide layer. In practice this means that, under a particular set of conditions, continuous and protective scale of solute-oxides form at and above a critical concentration of solute, which has been calculated by Wagner and co-workers [331-333, 381]. Wagner [331-333, 381] has shown that the transition from internal to external oxidation largely depends on the diffusivity of solute

atoms. For a compact external scale, the critical concentration of solute above which external oxide scale can form is expressed as:

$$N_B = \frac{V}{Z_B M_O} \sqrt{\left(\frac{\pi k_p}{D_B}\right)} \quad (6.1)$$

where, V is the molar volume of the alloy, Z_B the valance of the B atoms, M_O the atomic weight of oxygen, D_B the diffusion coefficient of B and k_p is the parabolic rate constant for the exclusive formation of the B oxide.

Diffusion in a material can be characterized as the combined effect of diffusion through the grain boundaries and lattice diffusion and can be written as:

$$D = fD_{gb} + (1-f)D_b \rightarrow D = f(D_{gb}-D_b)+D_b \quad (6.2)$$

where, f is the grain boundary fraction, D_{gb} is the grain boundary diffusion coefficient and D_b is bulk diffusion coefficient of B in alloy. Assuming the shape of grains cubic, the grain boundary area fraction f can be calculated as:

$$f = (2 \times \delta) / d \quad (6.3)$$

where δ is grain boundary thickness, and d is the grain size.

Using Equations 6.3, 6.4 and 6.5, the critical concentration of B required for the external oxidation can be written as:

$$N_B = \left(\frac{V \cdot \sqrt{\pi k_p}}{Z_B M_O}\right) \cdot \left(\frac{1}{\sqrt{f(D_{gb}-D_b)+D_b}}\right) = \left(\frac{V \cdot \sqrt{\pi k_p}}{Z_B M_O}\right) \cdot \left(\frac{\sqrt{d}}{\sqrt{2\delta(D_{gb}-D_b)+d \cdot D_b}}\right) \quad (6.4)$$

At a given temperature and external oxygen partial pressure, N_B is a function of only grain size, diffusion coefficients, grain size and grain boundary width, provided the oxides of the two alloy constituents have

similar compositions. The critical concentration of B required (N_{oB}) where only bulk diffusion can control the oxidation can be calculated as:

$$N_{oB} = \frac{V}{Z_B M_o} \sqrt{\frac{\pi k_p}{D_b}} \quad (6.5)$$

From equation (6.4) and (6.5), for material B of grain size, d , the ratio (X) of critical concentration required for external oxidation when grain boundary oxidation predominates to that when the bulk diffusion coefficient dominate, and can be given as:

$$X = \frac{N_B}{N_{oB}} = \sqrt{\frac{d}{2\delta\left(\frac{D_{gb}}{D_b} - 1\right) + d}} = \sqrt{\frac{1}{f\left(\frac{D_{gb}}{D_b} - 1\right) + 1}} \quad (6.6)$$

Values of D_{gb} and D_b are known for each material which depends largely upon temperature. Value of X can be calculated as a function of time and temperature.

Data for N_b are available for range of grain size and temperature. Given that the critical amount of Cr required for a material with grain size d_0 is w , the ratio for the critical amount of Cr required for a grain size of d to that for the grain size d_0 can be expressed as X' (using equation 6.6):

$$X' = \frac{N_B}{w} = \sqrt{\frac{d(2\delta(D_{gb} - D_b) + d_0 \cdot D_b)}{d_0(2\delta(D_{gb} - D_b) + d \cdot D_b)}} \quad (6.7)$$

Using Equation 6.7 and the diffusion coefficient data provided in Table 6.1, it has been possible to calculate the effect of grain size on the minimum amount of Cr required for transition from internal to external oxidation. For typical values of D_{gb} and D_b from literature [382, 383], $\delta=1\text{nm}$, $d_2=1.5\mu\text{m}$, the ratio of Cr required for transition from internal-external oxidation for alloys of grain sizes, d and $1.5\mu\text{m}$ is plotted as a function of grain size, d (Figure 6.10). The data presented in Figure 6.10 would suggest that by reduction of grain size from $1.5\mu\text{m}$ to 55 nm the minimum amount of Cr required for transition from

internal to external oxidation during oxidation at 350°C can theoretically be reduced by 75%. Thus, the observation in the present study that a 52nm-grain sized nanocrystalline Fe-Cr alloy at 10wt% chromium establishes an effective ‘external’ oxidation layer of Cr₂O₃ and provides as effective an oxidation as a 1.5µm microcrystalline Fe-20Cr alloy (after initial stages) is also theoretically valid. In fact, a 52nm-grain -sized nanocrystalline Fe-Cr alloy should be able to develop an ‘external’ oxidation layer of Cr₂O₃ even at 5wt% chromium.

Table 6.1 Diffusion coefficients of Cr in iron [382,383]

Temperature	Lattice (D_b) m^2/s	GB (D_{gb}) m^2/s
300 °C	1.2×10^{-26}	8.6×10^{-22}
380°C	7.6×10^{-24}	2.3×10^{-19}
840°C	1.5×10^{-15}	3.7×10^{-12}

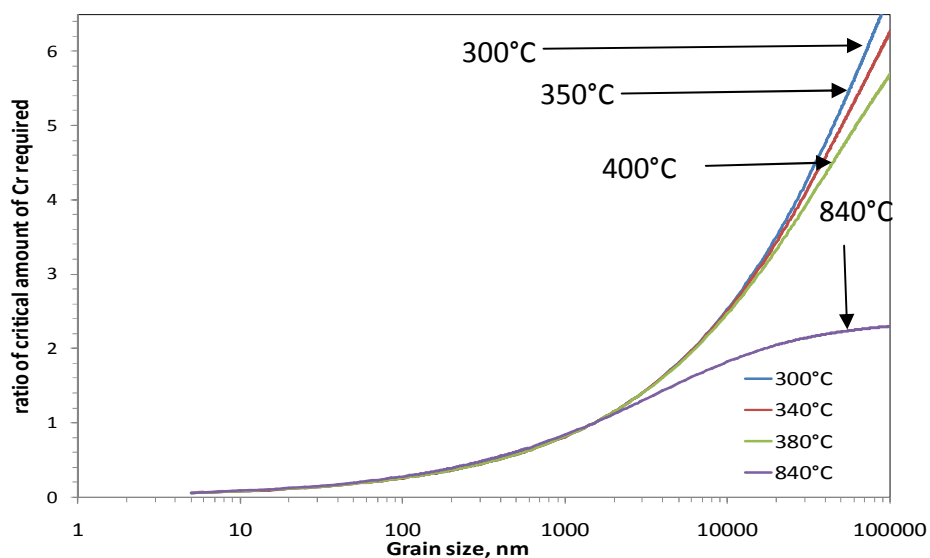


Fig.6.10 Plots of the ratio of Cr required for transition from internal-external oxidation for alloys of grain sizes, d and 1.5µm against the alloy grain size, d (Plots generated using Equation (6.7) and using typical data of D_{gb} and D_b from the literature [382, 383], $\delta=1nm$).

6.4.4 Possible mechanisms for the improved oxidation behaviour of nanocrystalline alloys

During oxidation, iron-chromium alloys initially develop a layer of iron oxide or iron-chromium mixed oxide, depending on the alloy chromium content. The ease of chromium enrichment governs the eventual transformation of the entire scale thickness or its inner part into a continuous layer of chromium oxide which confers protection against corrosion and oxidation. The results of the present study, discussed earlier, have established and explained the role of nanometric vis-à-vis micrometric grain size in conferring ability/inability to a few Fe-Cr alloys for establishing a protective layer of Cr_2O_3 as a function of chromium content, oxidation time and oxidation temperature. Summarized below are the two most obvious roles of nanometric grain size in the oxidation resistance of Fe-Cr alloys:

1. Considerably greater Cr diffusivity of Cr facilitating formation of Cr_2O_3 layer at smaller grain size has been known for high Cr microcrystalline Fe-Cr alloys [3,48,380,384-387]. However, the results presented here have shown that it is possible to establish Cr_2O_3 layer at a considerably lower Cr content in the case of nanocrystalline Fe-Cr alloys. It is described here that critical amount of Cr required for the passivity comes down and an increase in the oxidation resistance in nanocrystalline alloys is shown.
2. Oxidation resistance of a nanocrystalline alloy may be inferior due to the large fraction of high energy sites, i.e., grain boundaries and triple points [322,380,387]. The SIMS depth profiles of the present study have, indeed, suggested a greater iron oxidation in the initial stages.
3. Considerably greater grain boundary areas may provide extraordinarily greater number of nucleation sites, leading to a homogenous and compact passive film [265,334,388].

4. The large fraction of grain boundaries and triple points increases the surface energy of nanocrystalline materials which may facilitate the adsorption and chemisorptions phenomena, which is a critical initial step in oxidation [9,380].
5. Morphology and structure of oxide scales developed on nanocrystalline alloy may be considerably different (viz., oxide crystal size, crystallographic orientation, lattice mismatch with the base metal, adhesion of oxide layer). These factors affect the oxidation behaviour and mechanical breakdown of the oxide scales. For example, the fine grained oxide scales often show a fast creep rate at high temperatures, releasing the stresses accumulated in the scales and, therefore, decrease in scale spallation tendency [380,385,387,389]. Grain size of the oxide developed on nanocrystalline alloy was found to be finer than that of microcrystalline alloy in the present study. Scanning electron microscope (SEM) images showing the grain size of oxides developed on nc and mc Fe10Cr alloys after oxidation at 300°C for 52 hours are shown in the Figure 6.11.

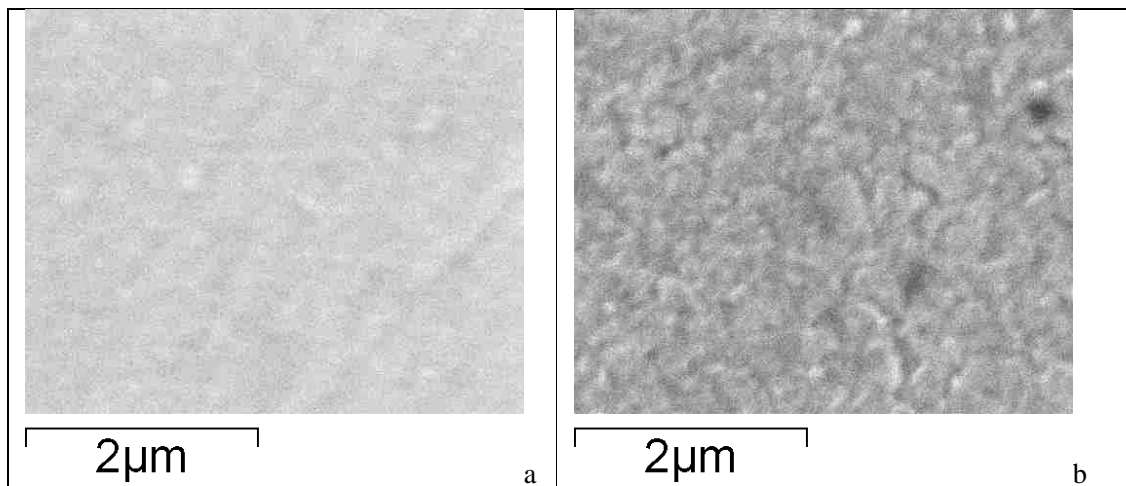


Fig. 6.11 SEM micrographs of nc and mc Fe10Cr alloys oxidized at 300°C/52 hours: (a) nanocrystalline Fe-10Cr alloy, (b) microcrystalline Fe-10Cr alloy

6.5 Conclusions

- (1) It has been possible to validate the hypothesis that nanocrystalline structure may confer considerable oxidation resistance and that with nanocrystalline alloys with lower chromium contents it is possible to develop corrosion resistance as good as that of the common high chromium Fe-Cr alloys.

- (2) The extraordinary difference in oxidation resistance of nanocrystalline and microcrystalline Fe-10%Cr alloys is also manifest in stark difference in colour of the oxidized alloys, which is duly corroborated by the difference in chemical composition of the two scales.

- (3) The experimental results suggesting extraordinary oxidation resistance of nanocrystalline Fe-10Cr alloy is consistent with the theoretical determination of combined effect of grain size and the minimum chromium required for the diffusion-assisted establishment of the protective layer chromium oxide in Fe-Cr alloys.

CHAPTER 7

ELECTROCHEMICAL CORROSION BEHAVIOR of NANOCRYSTALLINE vis-à-vis MICROCRYSTALLINE Fe-Cr ALLOYS

7.1 INTRODUCTION

Nanocrystalline (nc) materials are characterized as materials with grain size less than 100 nm and a high-volume fraction of the grain boundary which may comprise as much as 50% of the total crystal volume [9]. The small grain size and the high-volume fraction of grain boundaries result in the corrosion behaviour of a material in nanocrystalline state to be different from that in the microcrystalline (mc) state.

Given that the grain boundaries (i.e., high energy areas with a much greater degree of disorder) are nearly always anodic, the corrosion rate of nanocrystalline materials in simplistic terms would be expected to be considerably higher than that of a microcrystalline material of similar chemical composition, and this view is often supported in the literature [119,236,243,259,260,264]. However, the corrosion resistance of some materials is reported to be superior in nanocrystalline form when compared with their microcrystalline state. Such contrasts in the nature of the influence of nanostructure may depend on the environment-material system.

The primary factors in the case of pure metals are the anodic behaviour of grain boundaries and the influence of anode-cathode area ratio, whereas the beneficial or deleterious role of alloying elements would be the additional factor in the case of alloys. Therefore, corrosion properties of nanocrystalline

materials can differ significantly from those of their microcrystalline counterparts. The decrease in the extent of localized corrosion at grain boundaries, in the case of nanocrystalline Cu and Co (as opposed to their microcrystalline counterparts), is reported [119,248,252] and can be attributed to: (a) decrease in the difference in the electrochemical potentials of grain and grain boundaries and (b) the greater anode-to-cathode area ratio in nanocrystalline materials.

Considerable difference in the corrosion potential (E_{corr}) of some material in nanocrystalline and microcrystalline state is reported which is attributed to the enhanced hydrogen reduction reaction and/or to the greater magnitude of free energy per unit surface area of nanocrystalline materials [119,236,243,259,260,275].

The effect of the nanostructure on the forms of corrosion, that are primarily diffusion-assisted, depends on the nature of the predominantly diffusing species. For example, corrosion resistance of FeAl₈ alloy [390], iron aluminide [266] and FeBSi [265] is reported to be superior in their nanocrystalline form, which is attributed to the diffusion of the Al/Si, the well-known protective oxide film formers being the predominantly diffusing species respectively in the two alloys, and the nanostructure facilitating their diffusion and early formation of protective films (of Al/Si oxide).

A few studies [263,311,312,317] have also been carried out to compare the electrochemical corrosion of nanocrystalline and microcrystalline iron-chromium alloys. Electrochemical corrosion resistance of a nanocrystalline surface of 316 stainless steel, developed upon surface mechanical attrition treatment, was found to be considerably inferior to the microcrystalline unmodified bulk. Interestingly, this behaviour is attributed to the considerable increase in the 'fast diffusion channels' for ions, i.e., grain boundaries and triple junctions in the nanocrystalline material [263]. In another example, a

nanocrystalline surface of 304-stainless steel, developed upon sandblasting, showed a considerably inferior corrosion resistance to the microcrystalline substrate [311]. However, a prior annealing of the sandblasted surface considerably improved the resistance, to the extent that the annealed surface shows a corrosion resistance superior to the substrate. On the other hand, grain refinement of stainless steels to nano level is reported to improve the corrosion resistance [312,317]. Corrosion resistance of a nc thin film / coating of 309 stainless steel, that was developed by DC magnetron sputtering, showed a superior electrochemical corrosion resistance than the microcrystalline bulk of 309 steel [312], which has been attributed to the greater chromium diffusion in the nanocrystalline structure. It is interesting to note that the processing routes employed for developing the nc structure of steels, in the examples described above, are considerably different from those employed for producing cast stainless steels samples used in these studies for the purpose of comparison with corresponding microcrystalline alloys. In fact, in one of these studies [312] the crystal structure of the nanocrystalline thin films is described to be ferritic, whereas that of the microcrystalline alloy to be austenitic, and as a result, the two materials would have shown distinctly different polarization behaviour (the latter producing two anodic peaks as opposed to the only one peak for the former). Moreover the nanocrystalline surfaces used for the corrosion studies are in the form of the thin surface films. Therefore, it may not be inappropriate to suggest that the effects of nanocrystalline structure on corrosion, as claimed in the studies discussed earlier [263,311,312,314,317], are also due to other factors, such as the levels of point and other defects present in the nanocrystalline alloys, produced by different processing routes as well as the difference in density and phase compositions in the nano and microcrystalline samples. In fact, one of the studies justifies this view since a considerably defective nanocrystalline structure developed upon sandblasting also showed a considerably inferior corrosion resistance to the microcrystalline (mc) substrate whereas, prior annealing-out of these defects improved the resistance to be superior to the microcrystalline substrate.

For an appropriate comparison of the role of nanocrystalline vis-à-vis microcrystalline structure in electrochemical corrosion of Fe-Cr alloys, it is necessary that the materials with the grain size in two distinctly apart regimes be processed by the similar route. This chapter presents a comparison between the electrochemical corrosion resistance of nanocrystalline and microcrystalline Fe-Cr alloys prepared by same processing route, i.e., ball-milling, followed by annealing/compaction/sintering. Electrochemical corrosion resistance of nanocrystalline and microcrystalline alloys has been investigated in sulphuric acid and so too the effect of chloride ions on the electrochemical corrosion resistance. Steels with sufficient Cr can form passive layer in sulphuric acid solution which is disrupted by Cl ions. Hence tests in the Cl⁻ containing environment provide the idea about the robustness of passive film. A significant difference in the electrochemical corrosion behaviour of the nanocrystalline and microcrystalline materials is found. Further mechanistic aspects of difference in corrosion resistance are discussed after the XPS analysis of the corrosion film, developed over the alloys in various solutions.

7.2 ELECTROCHEMICAL CORROSION RESISTANCE IN 0.5 M H₂SO₄ SOLUTION

7.2.1 Potentiodynamic polarization tests

Open circuit potential (OCP) with increasing duration of immersion of the nanocrystalline (*nc*) and microcrystalline (*mc*) Fe-10%Cr and Fe-20%Cr alloys in 0.5M H₂SO₄ solution is shown in Figure 7.1. These curves are obtained by several experiments to ensure that the difference does not fall in the error limit. OCP of nanocrystalline Fe-10Cr alloy is 15 mV more than its microcrystalline counterpart, while Fe-20Cr alloy shows an increase of 10 mV in its nanocrystalline form.

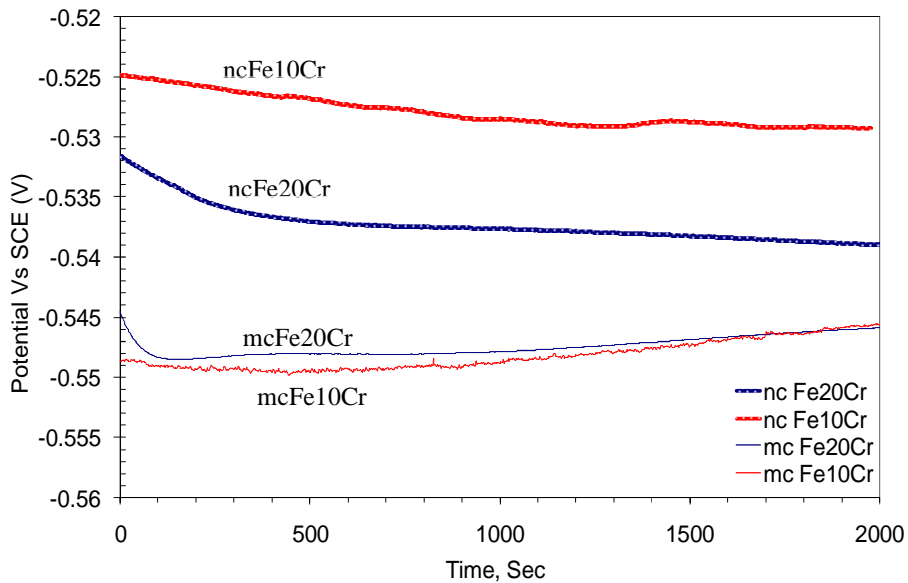


Fig. 7.1 Typical plots for change in open circuit potential with time for nanocrystalline (nc) and microcrystalline (mc) Fe-10Cr and Fe-20Cr alloys in 0.5M H₂SO₄ solution. (Reproducibility of these results is presented in Appendix-C, Figure 1.)

Potentiodynamic polarization curves of the nanocrystalline and microcrystalline Fe-10%Cr and Fe-20%Cr alloys in 0.5M H₂SO₄ are shown in Figure 7.2. The cathodic arm of the polarization curves of the four test materials is similar suggesting the same cathodic reactions with the similar kinetics. For an alloy with a given chromium content, the nanocrystalline structure is shown to improve the corrosion resistance, as suggested, by the comparison of the critical current density, passivation current density, passivation potential and the extent of passivation regime (Figure 7.2 and Table 7.1) for the nanocrystalline and microcrystalline Fe-10Cr and Fe-20Cr alloys. However, their anodic behaviour is considerably different, as evident from the anodic polarisation data presented in Table 7.1. During the anodic polarization, the effect of chromium content appears to pre-dominate the effect of nanocrystalline structure since both nanocrystalline and microcrystalline Fe-20Cr alloys show: (a) lower critical current densities, (b) lower passivation currents and (c) extended potential regimes for passivation, when compared to the Fe-10Cr alloys (Table 7.1).

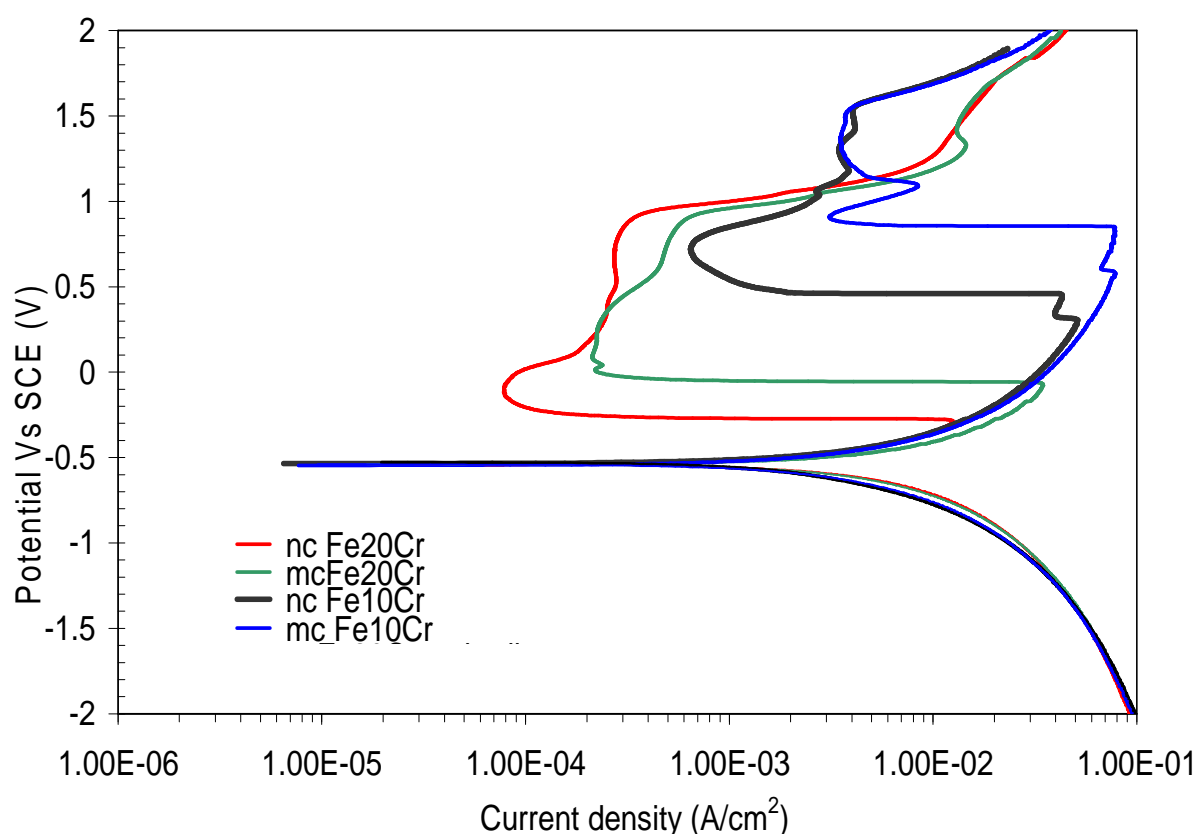


Fig. 7.2 Cathodic and anodic polarization curves of nanocrystalline (nc) and microcrystalline (mc) Fe-10Cr and Fe-20Cr alloys in 0.5M H₂SO₄ solution. Cathodic and anodic polarization curves were obtained separately by polarizing working electrode in negative and positive direction (with respect to OCP) respectively. (Reproducibility of these results is presented in the Appendix-C, Figure 2)

Table 7.1 Electrochemical corrosion parameters of nanocrystalline (nc) Fe-10Cr, microcrystalline (mc) Fe-10Cr, nanocrystalline Fe-20Cr and microcrystalline Fe-20Cr alloys in 0.5M H₂SO₄ solution. Reported data, E_{corr} : corrosion potential, E_{pp} : Potential where passivation starts, E_b : Potential where trans-passive region starts, and i_{crit} : critical current density, the averages of several experimental results as shown in the Figure 2 of Appendix-C, and error standard deviations are shown in the brackets.

	E_{corr} (mV)	E_{pp} (mV)	E_b (mV)	i_p ($\mu\text{A}/\text{cm}^2$)	i_{crit} (mA/cm^2)
nc Fe-10Cr/0.5M H ₂ SO ₄	-530 (± 5)	435(± 20)	1565 (± 20)	680(± 200)	40 (± 6)
mc Fe-10Cr/0.5M H ₂ SO ₄	-545 (± 5)	815(± 15)	1565(± 20)	3894(± 500)	84(± 8)
nc Fe-20Cr/0.5M H ₂ SO ₄	-545 (± 5)	-290(± 25)	900(± 10)	77 (± 20)	10 (± 3)
mc Fe-20Cr/0.5M H ₂ SO ₄	-540 (± 5)	-65 (± 15)	900(± 10)	275 (± 30)	36(± 4)

7.2.2 Surface characterization using XPS after electrochemical tests

Alloys were polarized to the potential where passive current density is minimum (potentials were chosen from the Figure 7.2) and held at the chosen potential for 30 minutes. Polarization potential for nanocrystalline Fe-10Cr, microcrystalline Fe-10Cr, nanocrystalline Fe-20Cr and microcrystalline Fe-20Cr were 775mV, 1400 mV, -50 mV and 200 mV (all potentials are with respected to SCE) respectively. Evolution of the current density with time is presented in Figure 7.3 and values of steady state passive current densities after 30 minutes of polarization are shown in Table 7.2. As evident from Figure 7.3 and Table 7.2 that the current densities obtained after 30 minutes of polarization in the case of nanocrystalline form of the alloys are lower than their microcrystalline counterparts which is consistent with the superior corrosion resistance of nanocrystalline alloys as suggested by potentiodynamic polarization tests.

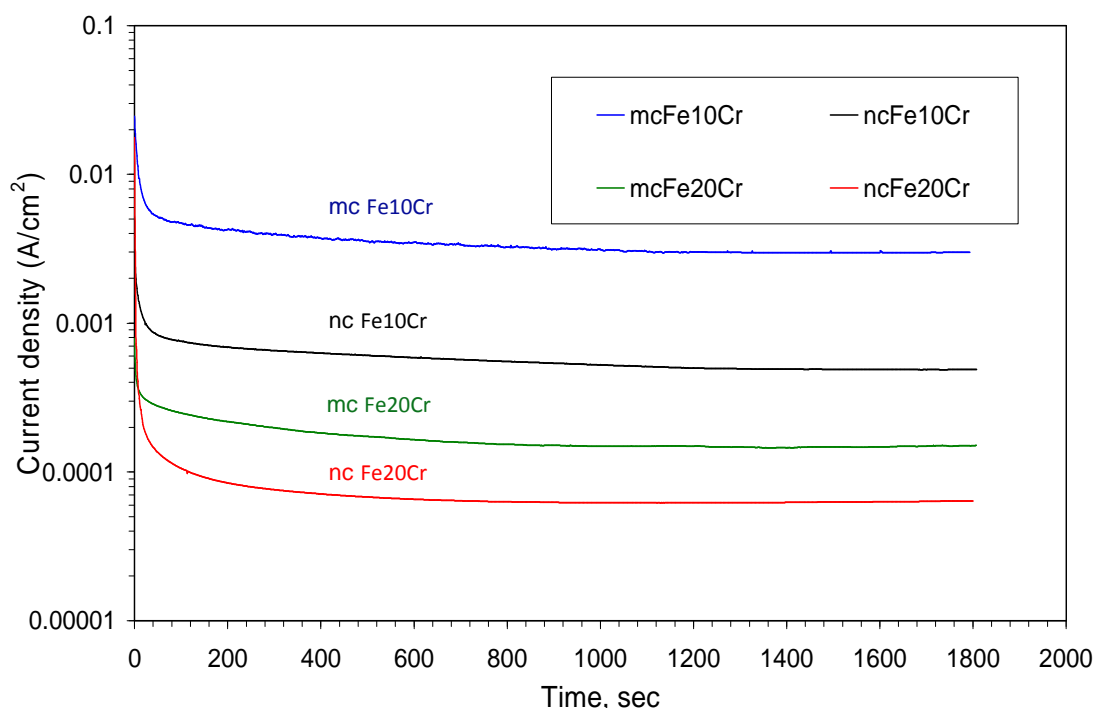


Fig. 7.3 Potentiostatic polarization curves: nc Fe-10Cr, mc Fe-10Cr, nc Fe-20Cr and mc Fe-20Cr alloys were polarized at 775 mV, 1400 mV, -50 mV and 200 mV respectively (for 30 minutes).

XPS survey scans and detailed regional scans presented in Figure 7.4 and Figure 7.5, respectively, for the thin corrosion film developed during potentiostatic polarization of the nanocrystalline and microcrystalline Fe-Cr alloys were obtained at a takeoff angle of 0° . The aim of the survey scans was to compare the relative elemental content in the corrosion films. In the binding energy region of 1100-0 eV, the spectra show the peaks of mainly Fe, Cr, O and S. Atomic fractions of the Fe and Cr were determined using casaXPS software and thus atomic ratio of Cr with respect to combined Fe and Cr (i.e., $Cr/(Fe+Cr)$) were calculated as presented in Table 7.2. It is evident from the Table 7.2 that the corrosion film developed on nanocrystalline form of the Fe-Cr alloys to have significantly higher Cr to (Fe+Cr) ratio in comparison to that in their microcrystalline counterparts. For example Cr to (Fe+Cr) ratio in the corrosion film developed on nanocrystalline Fe-10Cr alloy is considerably higher (0.8) than that in microcrystalline Fe-10Cr (0.3). Cr to (Fe+Cr) ratio also suggests a chromium enrichment in the corrosion film since the ratio in the Fe-10Cr alloy is only 0.11. This ratio is 0.21 in the Fe-20Cr alloy. Unlike Fe-10Cr alloy, the difference in $Cr/(Fe+Cr)$ ratio in the corrosion films developed on nanocrystalline and microcrystalline Fe-20Cr alloys is less pronounced.

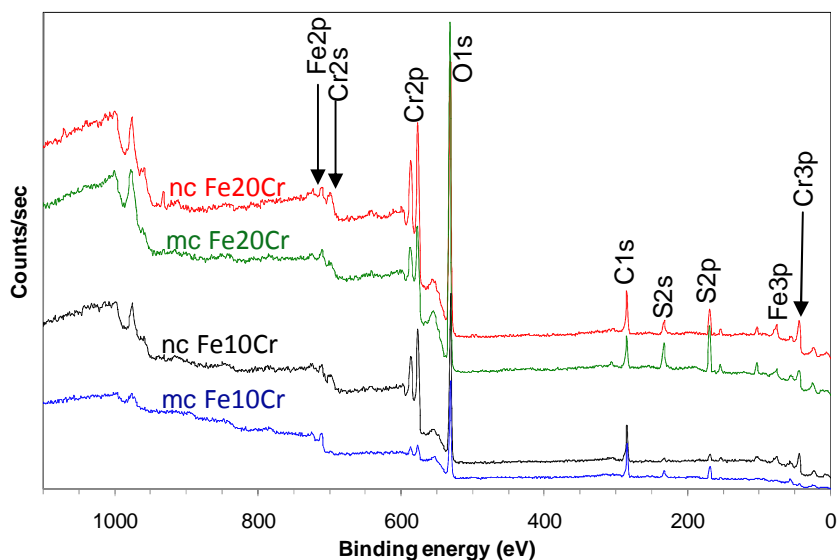


Fig. 7.4 Typical XPS survey scans of the nc Fe-10Cr, mc Fe-10Cr, nc Fe-20Cr and mc Fe-20Cr alloys after potentiostatic polarizations. nc Fe-10Cr, mc Fe-10Cr, nc Fe-20Cr and mc Fe-20Cr alloys were polarized at 775 mV, 1400 mV, -50 mV and 200 mV respectively (for 30 minutes).

Cr contents of the corrosion films are consistent with the potentiodynamic polarization results which suggest a greater difference in the anodic polarization curve of nanocrystalline and microcrystalline Fe-10Cr alloy than the nanocrystalline and microcrystalline Fe-20Cr alloys (Figure 7.2 and Table 7.2).

Table 7.2 Cr content expressed as Cr (Cr/(Fe+Cr)) in the passive film of various alloys

	Passivation potential*	i_p ($\mu\text{A}/\text{cm}^2$)**	i_p ($\mu\text{A}/\text{cm}^2$)***	Cr/(Fe+Cr) ^a	Cr/(Fe+Cr) ^b
nc Fe-10Cr	775 mV	650	488	0.78	0.79
mc Fe-10Cr	1400 mV	3270	2996	0.31	0.29
nc Fe-20Cr	-50 mV	79.3	63.9	0.90	0.91
mc Fe-20C	200 mV	215	150	0.83	0.85

* Potential at which alloy was potentiostatically held for 30 minutes

** Passive current density obtained from potentiodynamic polarization (Figure 7.2)

*** Steady state current density obtained after 30 minutes of polarization (Figure 7.3)

^a Survey scans obtained at a takeoff angle of 0°.

^b Survey scans obtained at a takeoff angle of 30°

The results discussed so far were generated with a takeoff angle of 0°. Survey scans of nanocrystalline and microcrystalline Fe-10Cr and Fe-20Cr alloys were also obtained at a takeoff angle of 30° so that only a thinner layer could be analysed and the effect of base metal could be minimized. However, Cr/Fe+Cr ratio obtained using a takeoff angle of 30° (as presented in the Table 7.2) are similar to the ratios obtained using the takeoff angle of 0°.

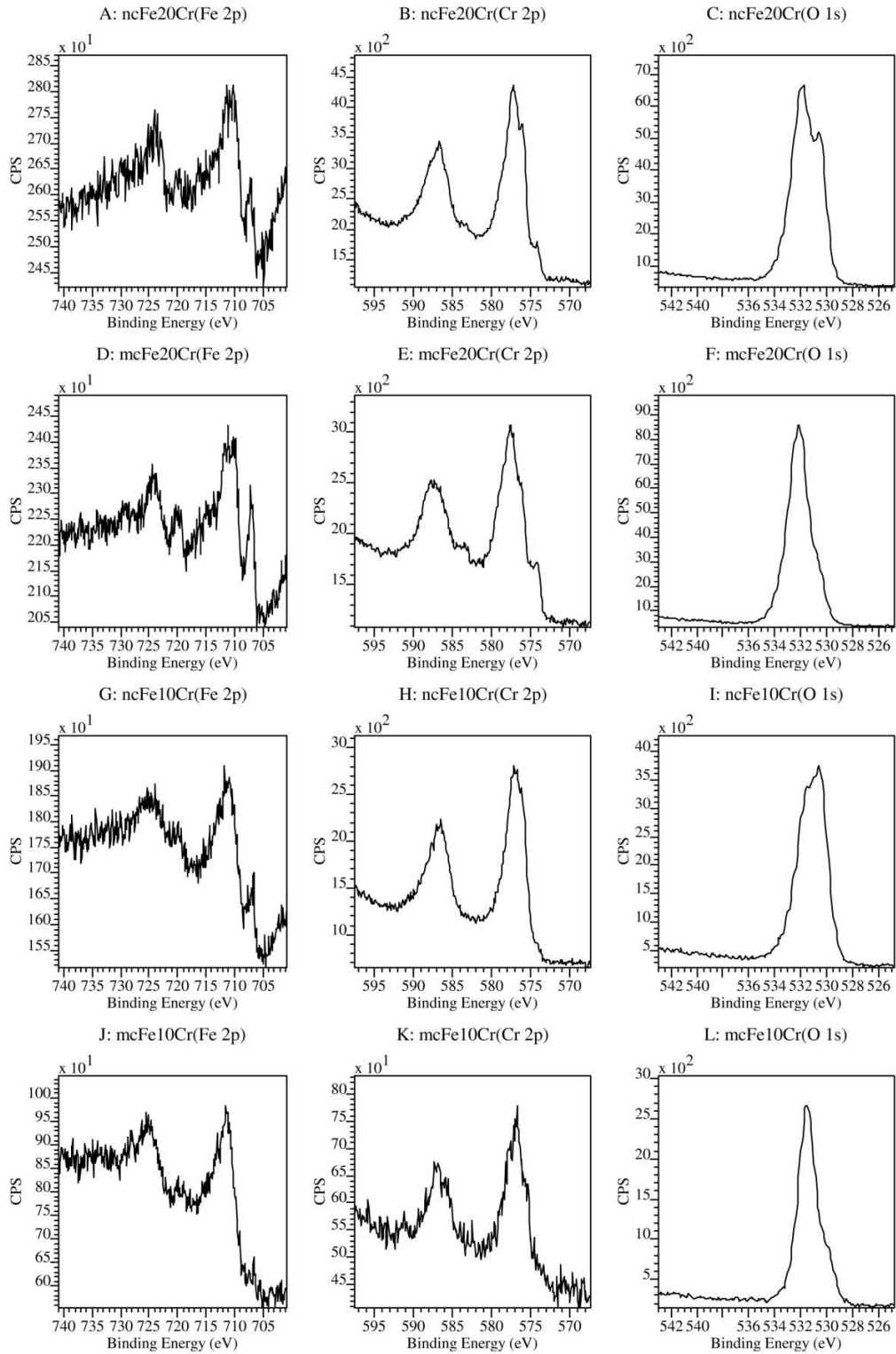


Fig. 7.5 XPS regional scan of Fe 2p, Cr 2p, O1s for the four alloys: (A) Fe2p nc Fe-20Cr, (B) Cr 2p nc Fe-20Cr, (C) O1s nc Fe-20Cr, (D) Fe2p mc Fe-20Cr, (E) Cr 2p mc Fe-20Cr, (F) O1s mc Fe-20Cr, (G) Fe2p nc Fe-10Cr, (H) Cr 2p nc Fe-10Cr, (I) O1s nc Fe-20Cr, (J) Fe2p mc Fe-10Cr, (K) Cr 2p mc Fe-10Cr and (L) O1s mc Fe-20Cr

The high resolution regional scans of O 1s, Fe 2p and Cr 2p that were obtained to quantify the chemical composition of the passive films are presented in the Figure 7.5. Chromium would be the primary element in the passive film of stainless steels.

Quantification of the different contributions, observed in Cr 2p_{3/2}, Fe 2p_{3/2} and O 1s ionisations, were performed by peak fitting, using casa XPS software. Curves with the peak fitting are presented in Figure 7.6. Four species considered for the Cr 2p_{3/2} are: the metallic contribution at a binding energy of 474.0 ±0.3 eV, Cr₂O₃ at (576.3 ±0.3 eV), Cr(OH)₃ at (577 ±0.3 eV), and Cr₂O₇²⁻ at (579.3 ±0.3 eV).

Three species considered for the Fe 2p_{3/2} spectra are: metallic Fe contribution at a binding energy of 706.8 ±0.3, Fe²⁺ at 709.5 ±0.3 and Fe³⁺ at 711.1 ±0.3eV.

Similarly, three contributions for O1s curve fitting considered are: O²⁻, OH⁻ and hydrated H₂O at binding energies of 529.9 ±0.3, 531.4 ±0.3 and 533 ±0.3 eV respectively. Binding energies of these species as reported in the literature are presented in the Table 7.3

Table 7.3 Binding energies (eV) for the Fe 2p_{3/2}, Cr 2p_{3/2} and O1s levels

Substance	Present study	Hermas [391]	Brooks et al [392]	Grosvenor [393]	Lin et al [394]	Langevoort [395]
Cr	574.0 (±0.3)	574.0(±0.2)	574.1		--	574.4
Cr ₂ O ₃	576.3 (±0.3)	576.1(±0.2)	576.3		--	576.8
Cr(OH) ₃	577.0 (±0.3)	577.1(±0.2)	577.0		--	--
Cr ₂ O ₇ ²⁻	579.3 (±0.3)	578.5(±0.2)	579.3		--	--
Fe	706.8 (±0.3)	--	--		-	706.8(±0.2)
Fe ²⁺	709.5 (±0.3)	--	--	709.0(±0.1)	709.7	709.7

Fe ³⁺	711.1 (±0.3)	--	--	711.1(±0.4)	711.1	711.2
O ²⁻	529.9 (±0.3)	530.1(±0.2)	529.9	529.9(±0.1)	529.7	530.6
OH ⁻	531.4 (±0.3)	531.5(±0.2)	531.4	531(±0.2)	531.2	
H ₂ O	533.0 (±0.3)	533.3(±0.2)	533.0		532.4	

The Cr 2p spectra for the corrosion films, developed over the four materials (nanocrystalline and microcrystalline Fe-10Cr and Fe-20Cr alloys), have shown a broad distinct peak with a small shoulder related to Cr metal towards the low energy side. Figure 7.6 clearly shows that Cr in all the four materials to be present in the forms of metallic Cr, Cr₂O₃, Cr(OH)₃ and Cr₂O₇²⁻. The metallic Cr peaks for the corrosion film of Fe-20Cr alloys are considerably more pronounced than the corresponding peaks for the Fe-10Cr alloys (Figure 7.6). The presence of metallic Cr indicates a thin corrosion film that allows the underlying alloy to be picked up. In the case of mc Fe-10Cr alloy, a relatively thick porous iron oxide layer forms, and, thus, metallic Cr from the substrate could not be picked up.

Fe is present in the form of metallic Fe, Fe²⁺ and Fe³⁺. Metallic Fe shows a trend similar to the metallic Cr in all the four alloys indicating a thin layer in Fe-20Cr alloys (Figure 7.6).

Oxygen spectra show a considerable difference in the nanocrystalline and microcrystalline Fe-20Cr alloys. A peak, appearing at lower binding energy corresponding to oxides, dominated in the nanocrystalline form of the alloys in both the compositions of the alloy.

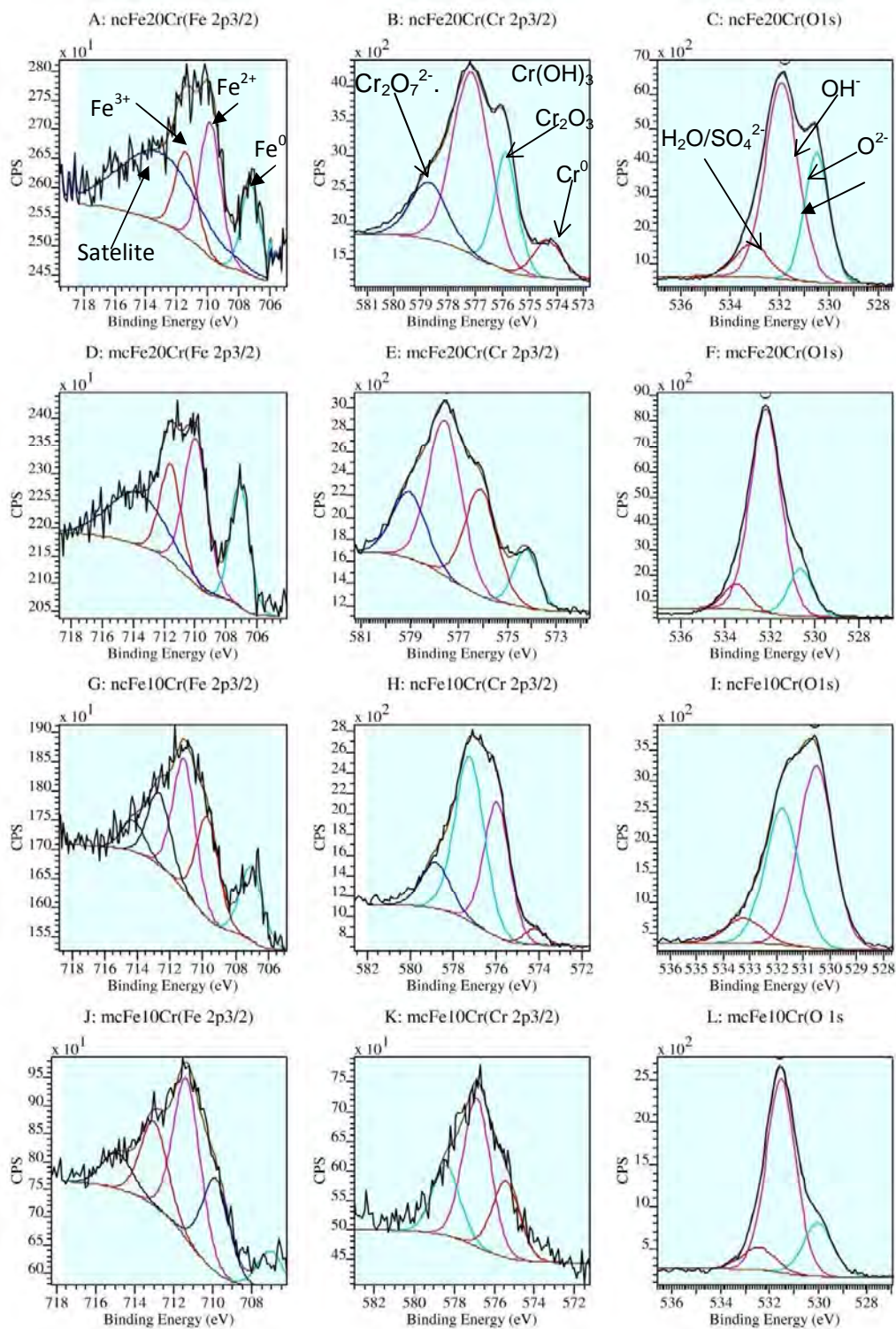


Fig. 7.6 XPS regional scan: curve fitting using casa XPS: (A) Fe 2p_{3/2} nc Fe-20Cr, (B) Cr 2p_{3/2} nc Fe-20Cr, (C) O 1s nc Fe-20Cr, (D) Fe 2p_{3/2} mc Fe-20Cr, (E) Cr 2p_{3/2} mc Fe-20Cr, (F) O 1s mc Fe-20Cr, (G) Fe 2p_{3/2} nc Fe-10Cr, (H) Cr 2p_{3/2} nc Fe-10Cr, (I) O 1s nc Fe-20Cr, (J) Fe 2p_{3/2} mc Fe-10Cr, (K) Cr 2p_{3/2} mc Fe-10Cr, (L) O 1s mc Fe-20Cr

7.3 ELECTROCHEMICAL CORROSION RESISTANCE IN 0.05 M H₂SO₄ SOLUTION

Section 7.2 clearly demonstrates the improved electrochemical corrosion resistance of nanocrystalline form of the alloys. However, the passive current density, critical current density and passivation potentials in the case of Fe-10Cr alloys (as clear from the Figure 7.2 and Table 7.1) are very high whereas, both the current densities (passive and critical current density) and passivation potentials are significantly lower in the case of Fe-20Cr alloys. Therefore, for further investigation of the role of grain size on the electrochemical corrosion only Fe-20Cr alloy is investigated.

Electrochemical corrosion resistance of nanocrystalline and microcrystalline Fe-20Cr alloy has also been compared at lower sulphuric acid concentration i.e. 0.05M H₂SO₄. Effect of Cl⁻ ions on the corrosion behaviour of nanocrystalline and microcrystalline Fe-20Cr alloys has also been investigated in 0.05M H₂SO₄.

7.3.1 Potentiodynamic Polarization Tests

Open circuit potential (OCP) with immersion time for the nanocrystalline (nc) and microcrystalline (mc) Fe-20%Cr alloys in 0.05M H₂SO₄ solution are shown in Figure 7.7. After an initial decrease, a little increase in the OCP is observed after ~200 seconds. OCP of nanocrystalline Fe-20Cr alloy is only 8 mV less negative than that for mc alloy.

The potentiodynamic polarization curves of nanocrystalline and microcrystalline Fe-20Cr alloys, polarized anodically in 0.05 M H₂SO₄, at room temperature, are presented Figure 7.8. Nanocrystalline Fe-20Cr alloy shows considerable improvement in corrosion resistance as characterized by: (a) lower critical

current density, (b) lower passive current density and (c) extended potential regimes for the passivation, when compared to the mc Fe-20Cr alloy (Figure 7.8 and Table 7.4).

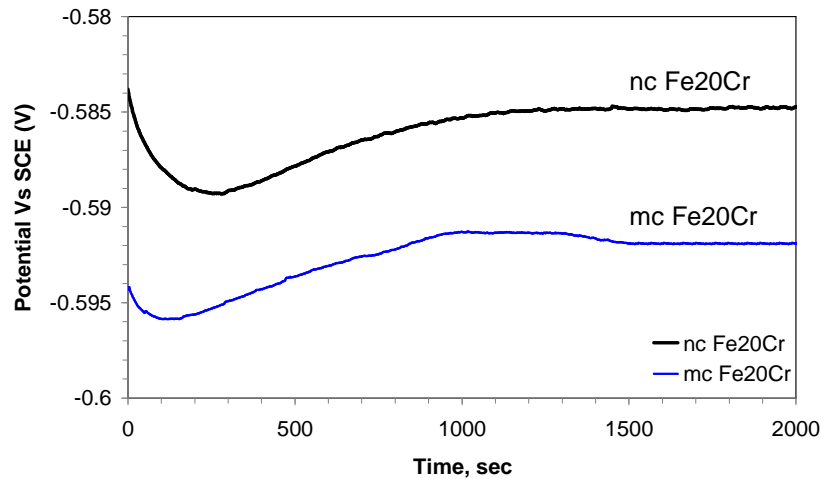


Fig. 7.7 Typical plots showing change in open circuit potential with time of nc and mc Fe-20Cr alloys in 0.05M H_2SO_4 solution. (Reproducibility of these curves is presented in the Appendix-C, Figure 3)

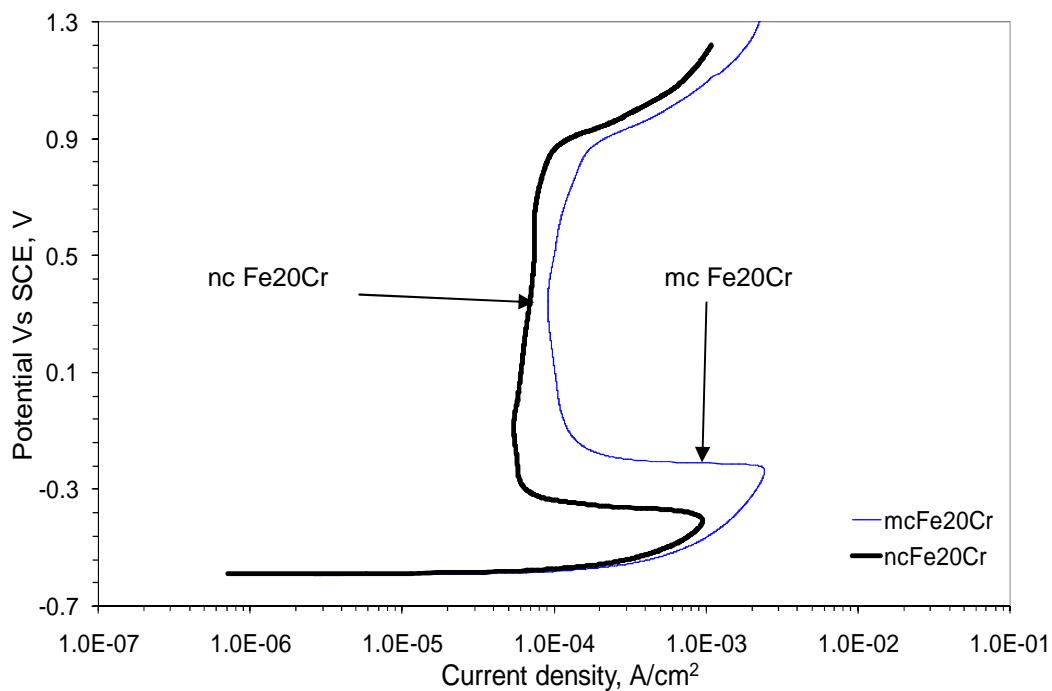


Fig.7.8 Anodic polarization curves of nc and mc Fe-20Cr in 0.05M H_2SO_4 solution. Anodic polarization curves were obtained by polarizing working electrode in positive direction from OCP. (Reproducibility of these curves is presented in Appendix-C, Figure 4.)

Table 7.4 Electrochemical data from anodic polarization tests of nc Fe-20Cr and mc Fe-20Cr alloys in 0.05M H₂SO₄ solution. Reported data, E_{corr} : corrosion potential, E_{pp} Potential where passivation starts, E_b : Potential where trans-passive region starts, i_{crit} : critical current density, is average of a number of experimental results as shown in the Appendix-C, Figure 4 and error shown in the brackets is standard deviation.

Test Materials	E_{corr} (mV)	E_{pp} (mV)	E_b (mV)	i_p ($\mu\text{A}/\text{cm}^2$)	i_{crit} (mA/cm^2)
nc Fe-20Cr	-590 (± 5)	-400 (± 5)	880(± 8)	50(± 5)	0.85 (± 0.09)
mc Fe-20Cr	-590 (± 5)	-220 (± 15)	880(± 8)	91(± 10)	3.4 (± 0.8)

7.3.2 Surface studies using SIMS after electrochemical tests

Nanocrystalline and microcrystalline Fe-20Cr alloys were polarized to the 300mV (in 0.05M H₂SO₄ solution) which is in the passive region and held at this potential for 30 minutes to obtain steady state conditions. Current densities obtained, as a function of time at 300 mV for nanocrystalline and mc Fe-20Cr alloys, are presented in Figure 7.9, and the steady state current densities, obtained after 30 minutes of polarization, are presented in Table 7.5. The steady state current density for nanocrystalline Fe-20Cr alloy is lower than that of mc Fe-20Cr alloy which is consistent with the superior corrosion resistance of nanocrystalline Fe-20Cr alloy, as suggested by the potentiodynamic polarization test results (Figure 7.8 and Figure 7.9).

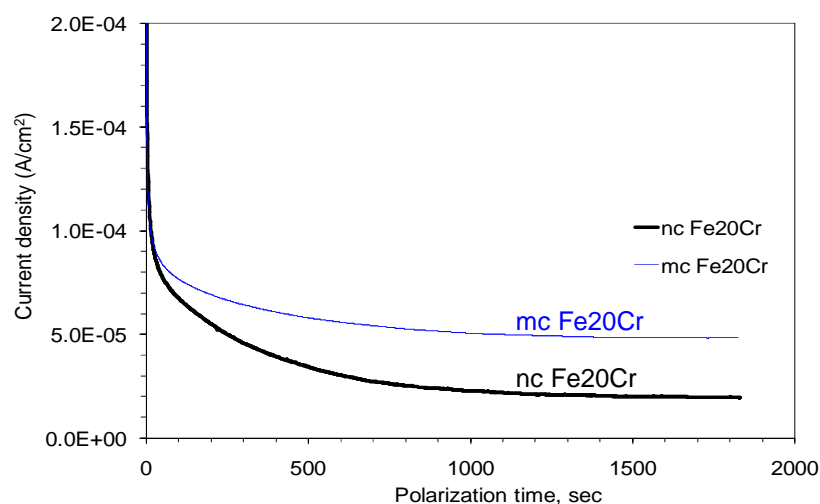


Fig. 7.9 Potentiostatic polarization curves of nc and mc Fe-20Cr alloys in 0.05M H₂SO₄ at 300 mV. Before potentiostatic polarization, each of the samples was polarized potentiodynamically to 300mV at a scan rate of 0.5 mV/sec.

Table 7.5 Atomic ratio of Cr ($Cr/(Fe+Cr)$) in the passive film of nanocrystalline (nc) and (mc) Fe-20Cr alloy in 0.05M H_2SO_4 solution

Test Materials	Passivation potential*	i_p ($\mu A/cm^2$)**	i_p ($\mu A/cm^2$)***	Cr/(Fe+Cr), atomic ratio of Cr ^a	Cr/(Fe+Cr), atomic ratio of Cr ^b
nc Fe-20Cr	300 mV	54	20	0.73	0.77
mc Fe-20Cr	300 mV	91	49	0.62	0.66

* Potential at which alloy was polarized for 30 minutes

** Passive current density obtained from potentiodynamic polarization (Figure 7.8)

*** Passive current density obtained after 30 minutes of polarization (Figure 7.9)

^a Survey scans obtained without beam tilt

^b Survey scans obtained at a take off angle of 30°

After the potentiostatic polarization the passive film, developed over the alloy surface, was examined using SIMS depth profiling in the corrosion films (Figure 7.10). Profile suggests Cr content of the passive film, developed over nanocrystalline Fe-20Cr alloy, to be greater than that in mc Fe-20Cr alloy. With the progress of sputtering (as the base alloy is approached), the Cr content of the passive film, developed on the two alloys, decreases and becomes equal in the base alloy (as expected).

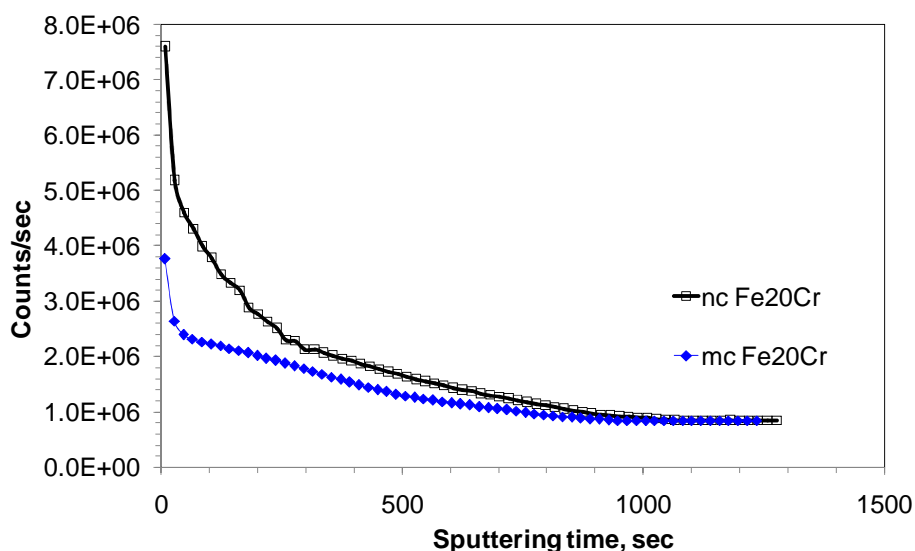


Fig. 7.10 SIMS depth profile for Cr in corrosion films developed on nanocrystalline (nc) and microcrystalline (mc) Fe-20Cr alloys after potentiostatic polarization tests as described in the section 7.3.2.

7.3.3 Surface studies using XPS after electrochemical tests

Sample preparation for the XPS analysis is the same as SIMS. Nanocrystalline and microcrystalline Fe-20Cr alloys were polarized to the 300mV in 0.05M H₂SO₄ solution, which is in the passive region and held at this potential for 30 minutes to obtain steady state conditions (Figure 7.9).

XPS survey scans of the corrosion film, developed during potentiostatic polarization of the nanocrystalline and microcrystalline Fe-20Cr alloys, were obtained at a takeoff angle of 0° (Figure 7.11). The aim of the survey scans was to compare the relative elemental content in the corrosion films developed on the two alloys. In the binding energy region of 1100-0 eV, the spectrum shows the peaks of mainly Fe, Cr, O and S. XPS spectra also suggests relatively a higher Cr content for the corrosion film developed on the nanocrystalline Fe-20Cr alloy in comparison to mc Fe-20Cr alloy (Figure 7.11). Atomic ratio of Cr with respect to combined Fe and Cr (i.e., Cr/(Fe+Cr)) were calculated using the atomic fractions obtained from the survey scans and are presented in Table 7.5, which shows that the corrosion film developed on nanocrystalline form of the Fe-Cr alloy has significantly higher Cr to (Fe+Cr) ratio in comparison to that in its microcrystalline counterpart. Atomic ratio of Cr in both nanocrystalline and microcrystalline Fe-20Cr alloy (without any electrochemical treatment) is 0.21, whereas, XPS analysis of the corrosion film suggests significant Cr enrichment of the corrosion film, as the atomic ratio of Cr for the corrosion film of nanocrystalline (0.73) and microcrystalline (0.62) alloy to be considerably higher than the base alloy (0.21). Cr enrichment of the corrosion film developed on nanocrystalline Fe-20Cr alloy is greater than that developed on microcrystalline Fe-20Cr alloy.

In order to minimize the effect of base metal on the XPS, analysis survey scans of nanocrystalline and microcrystalline Fe-20Cr alloys were also performed at a takeoff angle of 30°. Cr/(Fe+Cr) ratios obtained,

using a takeoff angle of 30°, are presented in Table 7.5, which are consistent with the analysis performed at the takeoff angle of 0°.

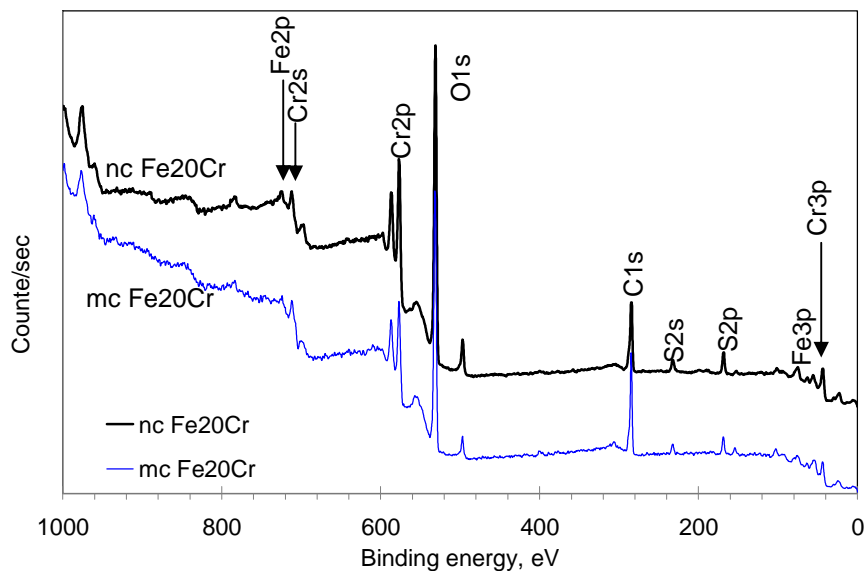


Fig. 7.11 Typical XPS survey scan spectrum of the nanocrystalline (nc) and microcrystalline (mc) Fe-20Cr alloys after potentiostatic polarization at 300mV/30 minutes in 0.05M H₂SO₄ solution.

The high resolution regional scans of O 1s, Fe 2p and Cr 2p were obtained at a takeoff angle of 0° to characterize the chemical compositions of the corrosion films and are presented in the Figure 7.12. Characterization of the different contributions, observed in Cr 2p_{3/2}, Fe 2p_{3/2} and O 1s ionisations were performed by peak fitting using casa XPS software (Figure 7.13).

Four species were considered for the Cr 2p_{3/2}: the metallic contribution at a binding energy of at 474.0 eV, Cr₂O₃ (576.3 ±0.3 eV), Cr(OH)₃ (577 ±0.3 eV), and Cr₂O₇²⁻(579.3 ±0.3 eV). Three species were considered for the Fe 2p_{3/2} spectra: metallic Fe contribution at a binding energy of 706.8 ±0.3, Fe²⁺ and Fe³⁺ at a binding energy of 709.5 ±0.3 – and 711.1 ±0.3 respectively. Similarly, three contributions for O1s curve fitting were considered: O²⁻, OH⁻ and hydrated H₂O at binding energies of 529.9 ±0.3, 531.4 ±0.3 and 533 ±0.3 eV respectively. Binding energies of various species, considered as reported in the literature, are presented previously in the Table 7.3

Figure 7.13 clearly shows that Cr in both the alloys is present in the forms of metallic Cr, Cr₂O₃, Cr(OH)₃ and Cr⁶⁺ specie (Cr₂O₇²⁻). Presence of metallic Cr indicated a thin corrosion film as thickness of passive film is lesser than the depth analysed by the XPS (which is approximately 10nm).

Fe is present in the form of metallic Fe, Fe²⁺ and Fe³⁺. Metallic Fe shows a trend similar to the metallic Cr in the two alloys indicating a thin layer in Fe-20Cr alloys (Figure 7.13).

Oxygen spectra show a considerable difference in the nanocrystalline and microcrystalline Fe-20Cr alloys. A peak, appearing at lower binding energy corresponding to oxides, dominated in the nanocrystalline form of the alloy.

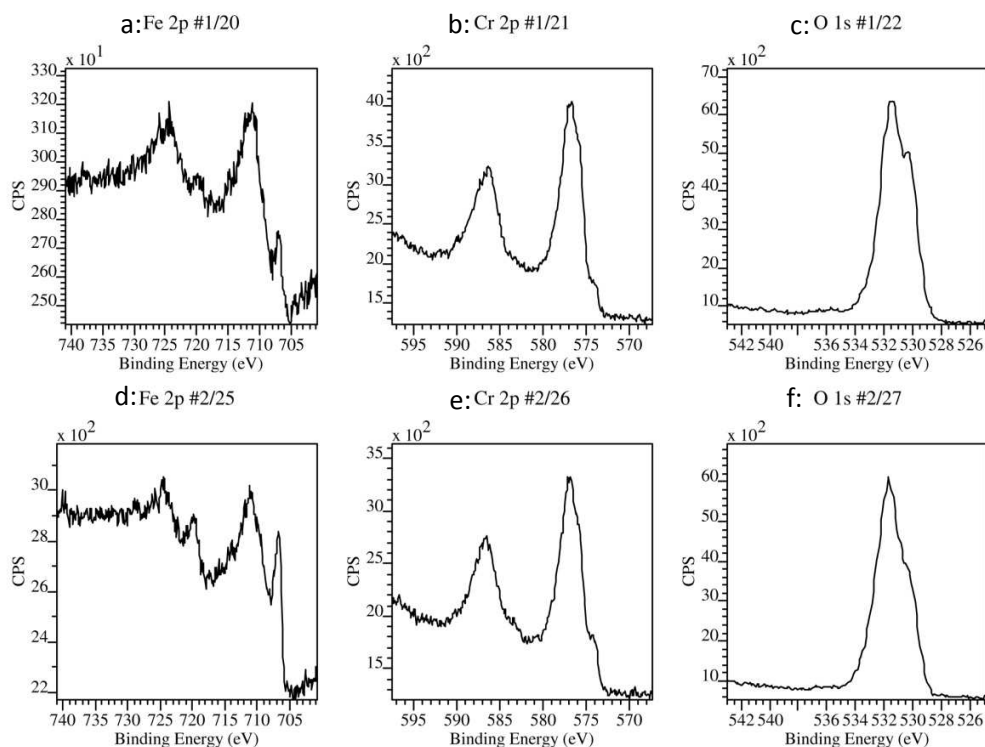


Fig. 7.12 XPS regional scan of Fe 2p, Cr 2p, O1s for the four alloys (a) Fe2p nc Fe-20Cr, (b) Cr 2p nc Fe-20Cr, (c) O1s nc Fe-20Cr, (d) Fe2p mc Fe-20Cr, (e) Cr 2p mc Fe-20Cr and (f) O1s mc Fe-20Cr

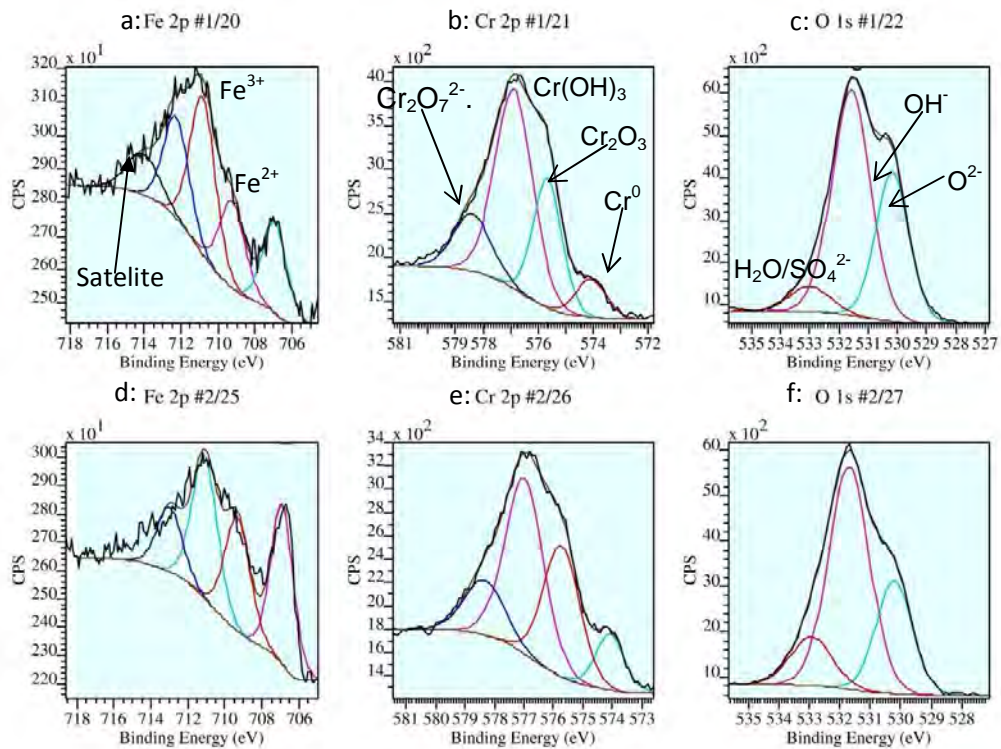


Fig. 7.13 XPS regional scan: curve fitting using casa XPS: (a) Fe 2p_{3/2} nc Fe-20Cr, (b) Cr 2p_{3/2} nc Fe-20Cr, (c) O 1s nc Fe-20Cr, (d) Fe 2p_{3/2} mc Fe-20Cr, (e) Cr 2p_{3/2} mc Fe-20Cr and (f) O 1s mc Fe-20Cr

7.4 CORROSION RESISTANCE IN THE PRESENCE OF CHLORIDE IONS

7.4.1 Potentiodynamic Polarization Tests

To investigate the effect of chloride ions on the corrosion resistance of nanocrystalline vis-à-vis microcrystalline Fe-20Cr alloys, potentiodynamic polarization tests were performed in 0.05M H₂SO₄+0.5M NaCl solutions and the potentiodynamic polarization curves are presented in Figure 7.14. Various parameters determined, using these curves, are presented in Table 7.6. It is evident from Table 7.6 and Figure 7.14 that the corrosion resistance of nanocrystalline Fe-20Cr alloy is superior to its microcrystalline counterpart too, in the presence of chloride ions, as evident from the smaller magnitudes of critical current density, passive current density and passivation potential for the

nanocrystalline Fe-20Cr alloy. Most interestingly, breakdown potential of nanocrystalline Fe-20Cr alloy in 0.05M H₂SO₄+0.5M NaCl solution (which was similar when nanocrystalline and microcrystalline Fe-10Cr alloys were tested in the absence of chloride ions) is much lower for the microcrystalline alloy, suggesting a superior resistance of passive film to the corrosion due to the Cl⁻ ions. In fact, it will be fair to say that, when tested in 0.05M H₂SO₄+0.5M NaCl solution, the microcrystalline alloy shows sign of active dissolution and hence the breakdown potential is not well-defined.

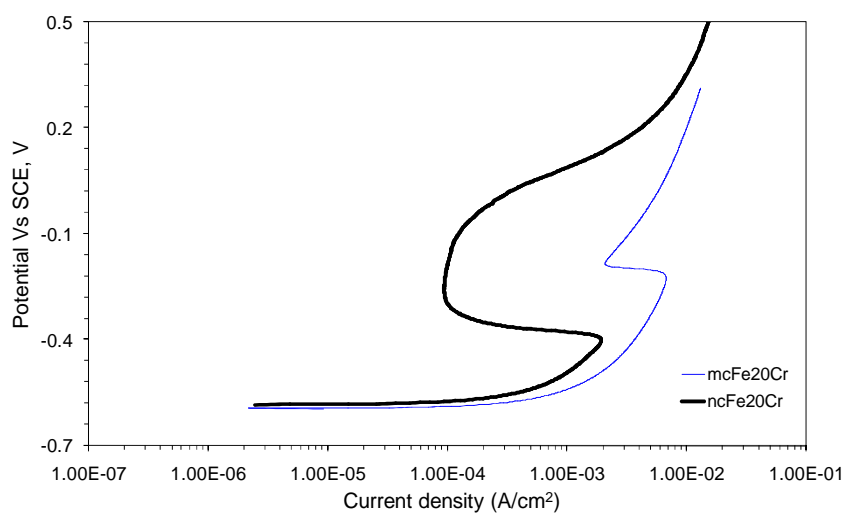


Fig. 7.14 Anodic polarization curves of nc and mc Fe-20Cr in 0.05M H₂SO₄+0.5M NaCl solution. (Reproducibility of these results is shown in Appendix-C Figure 5.)

Comparison of data presented in Tables 7.4 and 7.6 and Figures 7.8 and 7.14 would suggest that passivation potential does not change much due the addition of chloride ions to 0.05M H₂SO₄ solution. However, it causes a significant decrease in the breakdown potential both for nanocrystalline and microcrystalline alloys. However, the role of chloride ions in dissolution of passive film and decrease in breakdown potential is more prominent in the case of microcrystalline alloy. Addition of chloride ions increases both critical and passive current densities for the two alloys; however, passivation potentials do not change much.

Table 7.6 Electrochemical data from anodic polarization tests of nc Fe-20Cr and mc Fe-20Cr alloys in 0.05M H₂SO₄ +0.5M NaCl solutions. Reported data, E_{corr} : corrosion potential, E_{pp} : Potential where passivation starts, E_b : Potential where trans-passive region starts, i_{crit} : critical current density, are the averages of a number of experiments as shown in Figure 5 of Appendix C, and standard deviations of the data are shown in the bracket.

Test Materials	E_{corr} (mV)	E_{pp} (mV)	E_b (mV)	i_p ($\mu\text{A}/\text{cm}^2$)	i_{crit} (mA/cm^2)
nc Fe-20Cr/0.05M H ₂ SO ₄ +0.5NaCl	-590 (± 5)	-395 (± 3)	-70 (± 15)	100 (± 10)	1.5 (± 0.3)
mc Fe-20Cr/0.05M H ₂ SO ₄ +0.5NaCl	-590 (± 5)	-205 (± 10)	-179 (± 13)	1000 (± 500)	6.41

7.4.2 Surface studies using XPS after electrochemical tests

Samples preparation for XPS analysis was similar to the samples prepared in 0.05M H₂SO₄ solution. Nanocrystalline and microcrystalline Fe-20Cr alloys were polarized in the 0.05 M H₂SO₄+0.5M NaCl solution up to the potentials where, passive current density is minimum (-190 mV), and held for 30 minutes to reach steady state. Evolution of steady state current density is plotted as a function of time, as presented in the Figure 7.15. Similar to the tests without chloride addition, the curves distinctly show a superior corrosion resistance of nanocrystalline alloy.

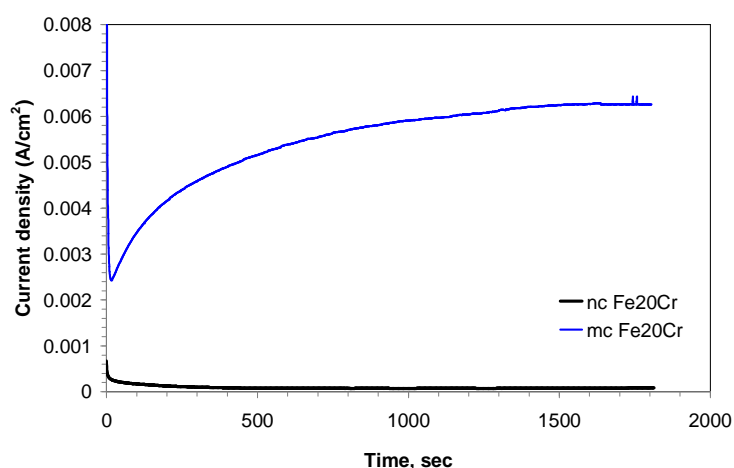


Fig. 7.15 Potentiostatic polarization curves of nc and mc Fe-20Cr alloys, at -190 mV in 0.05M H₂SO₄ + 0.5M NaCl solution. Before potentiostatic polarization, each of the samples was polarized potentiodynamically to -190 mV at a scan rate of 0.5 mV/sec

XPS survey scans of the corrosion film, developed during potentiostatic polarization of the nanocrystalline and microcrystalline Fe-20Cr alloys, were obtained at a takeoff angle of 0° and 30° . Survey scans, obtained at the takeoff angle of 0° , are presented in Figure 7.16. The spectrum shows the peaks of mainly Fe, Cr, O, Cl and S. XPS spectra (Figure 7.16) and also suggests relatively a higher Cr content for the corrosion film, developed on the nanocrystalline Fe-20Cr alloy, in comparison to microcrystalline Fe-20Cr alloy (Figure 7.16). Atomic fractions of the elements were determined using casaXPS software. Atomic ratio of Cr with respect to combined Fe and Cr (i.e., $\text{Cr}/(\text{Fe}+\text{Cr})$) were calculated using the atomic fractions, obtained from the survey scans, and are presented in Table 7.7. It is evident from the table 7.7 that the corrosion film developed on nanocrystalline form of the Fe-Cr alloys has significantly higher Cr to (Fe+Cr) ratio in comparison to that in their microcrystalline counterpart. Atomic ratio of Cr in both nanocrystalline and microcrystalline Fe-20Cr alloy (without any electrochemical treatment) is 0.21, whereas, XPS analysis of the corrosion film suggests the atomic ratio for the corrosion film of nanocrystalline (0.45) and microcrystalline (0.25) alloy to be considerably higher than the base alloy (0.21), and Cr enrichment for the corrosion film of nanocrystalline alloy is considerably higher than that of microcrystalline alloy. Interestingly Cl^- content in the passive film developed over nanocrystalline alloy is significantly higher (approximately 5 times greater) than that of microcrystalline alloy (Figure 7.16).

The above mentioned analysis was performed with a takeoff angle of 0° . To minimize the effect of base metal, survey scans were also obtained at a takeoff angle of 30° . $\text{Cr}/(\text{Fe}+\text{Cr})$ ratio obtained using a takeoff angle of 30° is presented in Table 7.7 and are consistent with the analysis performed at the takeoff angle of 0° .

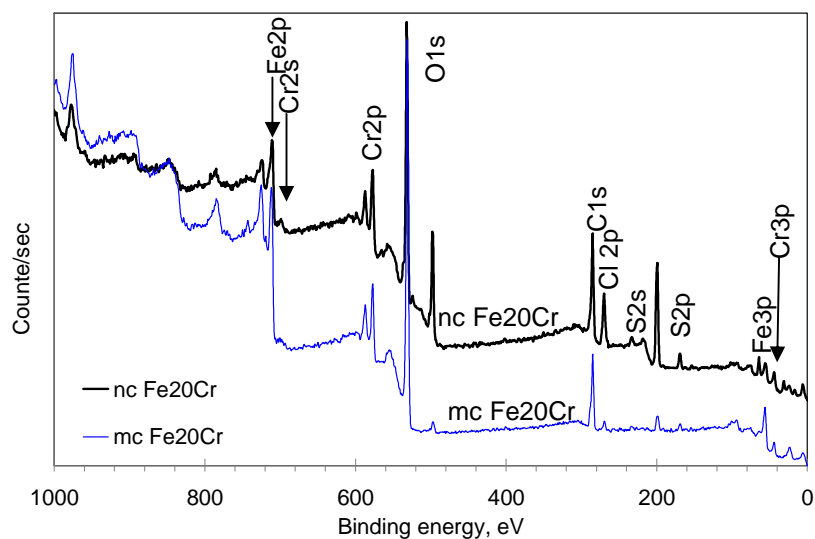


Fig. 7.16 Typical XPS survey scans spectra of the nc and mc Fe-20Cr alloys after potentiostatic polarization in 0.05M H_2SO_4 + 0.5M NaCl solution at -190 mV.

Table 7.7 Cr content as expressed as Cr ($Cr/(Fe+Cr)$) in the passive film of various alloy in 0.05M H_2SO_4 +0.5M NaCl solution

Test Materials	Passivation potential*	i_p ($\mu A/cm^2$)**	i_p ($\mu A/cm^2$)***	Cr/(Fe+Cr) ^a	Cr/(Fe+Cr) ^b
nc Fe-20Cr	-190	94	82	0.45	0.44
mc Fe-20Cr	-190	2140	6200	0.25	0.25

* Potential at which alloy was polarized for 30 minutes

** Passive current density obtained from potentiodynamic polarization (Figure 7.14)

*** Passive current density obtained after 30 minutes of polarization (Figure 7.15)

^a Survey scans obtained at a takeoff angle of 0°

^b Survey scans obtained with a takeoff angle of 30°

7.4.3 Surface studies using SEM after electrochemical tests

SEM micrographs of the nanocrystalline and microcrystalline Fe20Cr alloys after polarization to the potential, 50 mV more positive than the pitting potential of their respective alloys, are presented in the Figure 7.17. Greater pitting in the case of microcrystalline alloy (as noticed in the Figure 7.17) supports the potentiodynamic and potentiostatic polarization results.

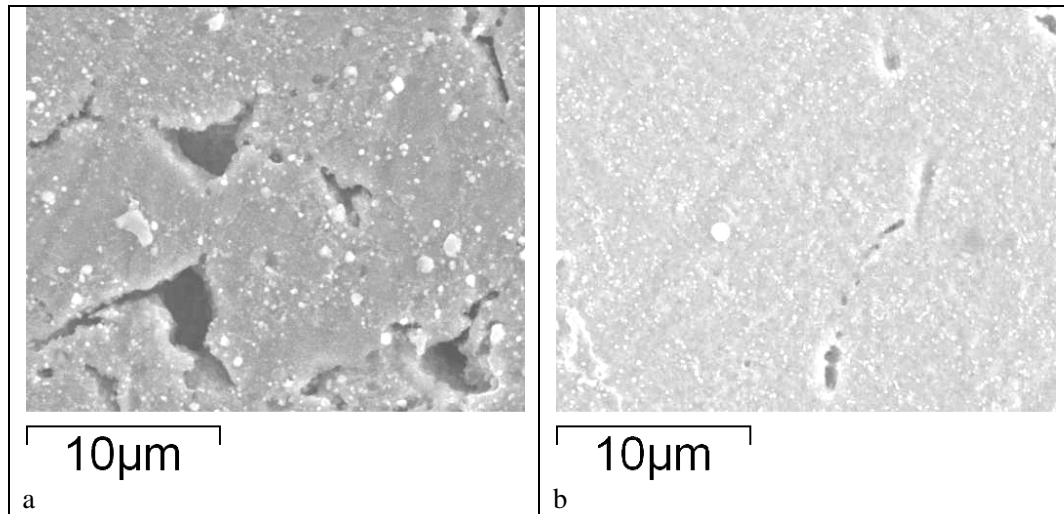


Fig. 7.17 SEM micrographs of nc and mc Fe20Cr alloys after potentiodynamic polarization to 50 mV above the pitting potential: (a) microcrystalline Fe20Cr and (b) nanocrystalline Fe20Cr alloy

7.5 Discussion

7.5.1 Value of the corrosion potential (E_{corr})

E_{corr} values (as represented by OCP) of both Fe-10Cr and Fe-20Cr nanocrystalline alloys were observed to be less positive than their microcrystalline counterparts. However, this difference, in some cases, is not large but, it is reproducible.

Nanocrystalline alloys possess comparatively large fraction of high energy sites (grain boundaries) which increases Gibbs Free Energy of the surface and, therefore, can be directly related to standard electrochemical potential of the surface as $\Delta G = -nFE$. Increase in the ΔG value of the nanocrystalline alloy should shift the E_{corr} value to the more negative direction. This argument would be one of the explanations of the decrease in the E_{corr} value as reported in some of the investigations.

7.5.2 Improved corrosion resistance of nanocrystalline form of the alloys

It is clear from the current investigation that Fe-Cr alloys (both Fe-10Cr and Fe-20Cr) show improved corrosion resistance in their nanocrystalline form. As evident from the Table 7.2, 7.5 and 7.7, Cr content in the passive film is considerably higher in nanocrystalline alloys which accounts for the improved corrosion resistance of nanocrystalline alloy, as described in the literature: the more the Cr enrichment the more would be the corrosion resistance. Possible mechanisms for the Cr enrichment of the passive film may be one or both of the following:

- (a) Considerably greater grain boundary area present in the nanocrystalline alloys would enhance the diffusivity of Cr by diffusion through the grain boundaries. Owing to the considerably greater grain boundary diffusivity, the overall diffusion coefficient in nanocrystalline alloy is reported [3] to be greater than the grain boundary diffusion coefficient in microcrystalline material of same composition. Previous section of the current study has demonstrated a considerably greater resistance to moderate temperature oxidation of an Fe-10Cr alloy in nanocrystalline state than in microcrystalline state because of the greater diffusion of the Cr in nanocrystalline state. However, the reported data on lattice and grain boundary diffusion in nanocrystalline and microcrystalline Fe-Cr system is available only for a higher temperature domain and diffusivity of Cr at room temperature is not available. Nevertheless, it may be interesting to note that because the grain boundary energy is far more enhanced in nanocrystalline alloys, one can argue that the temperature domain for the enhanced grain boundary diffusion may extend lower down to the normal temperatures. This view finds supporting evidence from the literature as the result of nanocrystalline state the corrosion resistance is reported to improve in the case of Fe-8Al, Fe₃₂-Ni₃₆-Cr₁₄-P₁₂-B, Ni-P and Co-P systems and enhanced grain boundary diffusivity of passivating element is attributed to improvement in the corrosion resistance. ,

(b) According to one of the passivity theories for stainless steels, passivity is obtained by the selective dissolution of Fe (at lower potentials) and formation of Cr oxide layer. Nanocrystalline alloys are comparatively more reactive due to the enhanced atomic energies, measured by reduced electron work function (EWF), may facilitate the selective dissolution of Fe and simultaneous accelerated formation of Cr oxide layer. This process leads to Cr enrichment of the passive film and passivity at lower potential.

Other factors that may add to the improved passivation behaviour of the nc Fe-20Cr alloys (as opposed to the microcrystalline alloy with same Cr content) are the formation of relatively more protective layer because of the following factors:

(a) Since, the passivation first starts on surface crystalline lattice defects, i.e., grain boundaries, triple points, dislocations etc. [396] and nanocrystalline materials have relatively a large fraction of grain boundaries and triple points on the surface. Therefore, it can be argued that high fraction of grain boundaries and triple points will provide an increased number of nucleation sites for the nucleation of the passive film and lead to a significant decrease in the lateral distance for the development of a contiguous protective layer. As a result, the passive film, developed over nc Fe-Cr alloy, exhibited comparatively more uniform layer and, therefore, improved corrosion behaviour over the mc alloys of similar chemical compositions.

(b) The passive film, formed on the nanocrystalline surface, should be more protective than on the microcrystalline counterpart because of the enhanced adhesion strength between passive film and the alloy surface due to the increase in the electron activity at grain boundaries and possible pegging of the passive film in to the grain boundaries. Theoretically and experimentally it has already been reported that nanocrystalline surfaces possess less electron work function and adhesive forces increase with decreases in the EWF. This view has been verified by Li and

Tao [253] on the electrodeposited nanocrystalline Cu, using micro-scratch test and electron work function (EWF) measurements.

- (c) Much greater adsorption of oxygen, which is the initial step for development of protective oxide, is accelerated on the nanocrystalline surface.
- (d) Electronic structure and the reactivity of the passive film developed over nanocrystalline alloys would be considerably different than that developed over microcrystalline alloys and may cause formation of more protective layer. Passive layer developed over nanocrystalline steels has shown higher electron work function than that on microcrystalline steel of similar chemical composition. Mott-Schottky's analysis performed over the nanocrystalline surface has shown considerable difference in electronic structure of the passive films developed over nc and mc form of the alloys. A p-n type of more protective passive film is reported in nanocrystalline alloys whereas, an n type of passive film is reported over mc alloy.

7.5.3 Improved resistance of nanocrystalline alloys in the presence of chloride ions

Similar to the improved corrosion behaviour shown in 0.5 M H₂SO₄ and 0.05 M H₂SO₄ solution, the nc Fe-20Cr alloy also shows improved corrosion resistance in the presence of chloride ions. As evident from the XPS analysis of passive film, the Cr enrichment of the passive film developed on the nanocrystalline surface is higher than that in microcrystalline alloy, suggesting formation of more protective corrosion films, which also show improved resistance to disruption in the passivity by Cl⁻ ions. Chloride ions are believed to lower the breakdown potential as a result of: a) the chloride ions penetrating into the corrosion film may increase the conductivity of the passive film, consequently decreasing the resistance offered against the migration of species involved in corrosion reaction,

and (b) chloride ions thin down the passive film by the reaction with passive film at passive film/solution interface, thus aiding the dissolution and (c) chloride ions reaching to the alloy surface causing localized corrosion.

7.6 conclusions

- 1) Corrosion resistance of nanocrystalline and microcrystalline Fe-10Cr and Fe-20Cr alloys (prepared by same processing route) was investigated in 0.5M H₂SO₄, 0.05M H₂SO₄ and 0.5M H₂SO₄+0.5M NaCl solutions by potentiodynamic and potentiostatic polarization experiments. Nanocrystalline alloys have shown improved corrosion resistance than their microcrystalline counterparts, as suggested by the lower passive current density, passivation voltage and critical current density in all the environments.
- 2) XPS analyses reveal that the relative Cr content in the passive film, developed on nanocrystalline alloy in each of the solutions, is considerably higher than that in their microcrystalline counterparts, which is responsible for the superior corrosion resistance.
- 3) Chloride ions lead to dramatic decrease in the corrosion resistance of both nc and mc alloys. However, deleterious effect of chloride ions on the corrosion resistance is comparatively less severe in the case of nanocrystalline alloy.

CHAPTER 8

SUMMARY AND FUTURE WORK

Major outcomes of the present study are summarised here:

- 1) This thesis presents a critical review on Fe and Fe- based nanocrystalline material which helps in developing the fundamental understanding of these novel materials and relating the structure of nanocrystalline materials to their properties.
- 2) Ball- milling is shown as a technique to produce Fe-Cr nanocrystalline alloys in powder form. After systematic study of grain growth behaviour of ball- milled nanocrystalline materials, it is established that a step of annealing prior to compaction helps in compaction of nanocrystalline Fe-Cr alloys and a technique to consolidate nanocrystalline Fe-Cr alloy powders is developed, which would be useful in compaction of nanocrystalline materials other than Fe-Cr alloys.
- 3) A comparison between the oxidation resistance of nanocrystalline and microcrystalline Fe-Cr alloys shows a greater oxidation resistance of nanocrystalline alloys over their microcrystalline counterparts. Most interestingly, the level of oxidation resistance obtained in microcrystalline Fe-20Cr alloy is obtained in Fe-10Cr alloy just by reducing the grain size to nano level. Characterization of oxide scale using SIMS and theoretical analysis attributes the formation of a passive Cr-oxide layer in case of nanocrystalline Fe-Cr alloys at lower Cr content (i.e. 10%Cr), therefore, higher oxidation resistance is observed in nanocrystalline alloys even at much lower

Cr contents. It further proves the hypothesis that passivity to oxidation can be achieved at lower Cr content by refining the grain size to nano range.

- 4) Electrochemical corrosion resistance of nanocrystalline and microcrystalline Fe-Cr alloys is compared and it is shown that nanocrystalline structure shows improved corrosion resistance in various electrolytes. Chemical compositional analysis of the corrosion film shows a greater Cr enrichment of the corrosion film in the case of nanocrystalline alloys which is attributed to greater corrosion resistance of nanocrystalline form of the alloys.

Proposed future work based on the present findings is as follows:

- 1) In- situ consolidation of nanocrystalline Fe-Cr alloys was not successful. However, as presented in the Appendix-D, initial success was obtained in the in-situ consolidation of Fe-Cr alloys by addition of Ni. Production of in-situ consolidated samples would enable to perform the mechanical tests and to develop the fundamental understanding of mechanical behaviour of nc alloys. In- situ consolidation would enable one to control grain size and would be possible to study the effect of grain size (below 10 nm, in fully dense samples) on the corrosion/oxidation resistance of nanocrystalline alloys.
- 2) It is clear from the Chapter 2 that the grain coarsening at elevated temperature has been a major issue with the nanocrystalline materials. Grain coarsening at higher temperature can be reduced significantly which is being shown in the Appendix A (section 3). The effect of addition of 1%Zr on the grain growth behaviour is clearly demonstrated in the Appendix A (Section 3).
- 3) Oxidation resistance of nanocrystalline and microcrystalline Fe-Cr alloys has to be studied at temperature higher than 400°C and it is anticipated that a higher oxidation resistance would be achieved. However, grain growth in Fe-Cr alloys would coarsen the grain to micron size. Grain

growth can be restricted by addition of secondary phase particles and the material could be used to higher temperatures.

- 4) Study of in- situ consolidated Fe-20Cr-10Ni alloys (as presented in Appendix D) would be very interesting as it offers an artifact free specimen with a grain size less than 10 nm where, effect of nanocrystalline structure is more profound. Various properties such as mechanical properties, electrochemical corrosion and oxidation properties should be considerably different than the specimen with a grain size of 50 nm. These in- situ consolidated samples would be used to investigate the structure of these materials using techniques such as HRTEM and would help in understanding the structure and its co-relation with the properties.

REFERENCES

- [1] Jones DA. Principles and Prevention of Corrosion. NJ: Prentice Hall.
- [2] Kaesche H. Corrosion of Metals: Physicochemical Principles and Current Problems Erlangen: Springer, 2003.
- [3] Wang ZB, Tao NR, Tong WP, Lu J, Lu K. Acta Mater 2003;51:4319.
- [4] Siegel RW. NanoStructured Materials 1994;4:121.
- [5] Suryanarayana C, Froes FH. Metal. Mater. Trans. A 1992;23A:1071.
- [6] Schaefer HE, Wurschum R, Birringer R, Gleiter H. Structure and Properties of nanometersized solids Physical research) to be published (reference from scripta metallurgica et materi. 24, 1990, 1347)
- [7] Griscom DL, Marquardt CL, Friebele EJ. J. Geophys. Res. 1975;80:2935.
- [8] Birringer R, Gleiter H, Klein H-P, Marquardt P. Phys. Lett. A 1984;102:365.
- [9] Gleiter H. Progress in Materials Science 1989;33:223.
- [10] Gleiter H, Marquardt P. Z. Metall. 1984;75:263.
- [11] Birringer R, Herr U, Gleiter H. Trans. Jpn. Inst. Met. (Suppl.) 1986;27:43.
- [12] Schaefer HE, Wurschum HE, Birringer R, Gleiter H. J. Less Common Metals 1988;140:161.
- [13] Yoshizawa Y, Oguma S, Yamauchi K. J. Appl. Phys. 1988;64:6044.
- [14] Yoshizawa Y, Yamauchi K. Mater. Trans. JIM 1990;31:307.
- [15] Siegel RW. NanoStructured Materials 1991;3:1.
- [16] Siegel RW. Annu. Rev. Mater. Sci. 1991;21:559.
- [17] Thomas GJ, Siegel RW, Eastman JA. Scripta matallurgica 1990;24:201.
- [18] Siegel RW. MRS Bull. 1990;15:60.
- [19] Siegel RW, Thomas GJ. Ultramicroscopy 1992;40.
- [20] Siegel RW. Mater Sci and Engineering 1993;A168:189.
- [21] Rosenhain W, Humfrey JCW. J. of the Iron and Steel Insitute 1913;87:219.
- [22] Rosenhain W, Ewen D. J. Of the Insitue of Metals 1913;10:119.
- [23] Phillpot SR, Wolf D. NanoStructured Materials 1995;8:1245.
- [24] Tanimoto H, Farber P, Wuerschum R, Valiev RZ, Schaefer HE. NanoStructured Materials 1999;12:681.
- [25] Zhu X, Birringer R, Herr U, Gleiter H. Phys. Rev. B 1987;35:9085.
- [26] Fecht HJ. NanoStructured Materials 1992;1:125.
- [27] Fecht HJ. Phys. Rev. Lett 1990;65:610.
- [28] Ferrante J, Smith JR, Rose JH. Phys. Rev. Lett 1983;50:1385.
- [29] Rose JH, Smith JR, Guinea F, Ferrante J. Phys. Rev. B 1984;29:2963.
- [30] Vinet P, Smith JR, Ferrante J, Rose JH. Phys. Rev. B 1987;35:1945.
- [31] Interface Science and Engineering, 1988.
- [32] Seeger A, G. S. Acta metall. 1959;7:495.
- [33] Smith DA, Vitek V, Pond RC. Acta metall. 1977;25:475.
- [34] Frost HJ, Ashby MF, Spaepen F. Scripta matallurgica 1980;14:1051.
- [35] Wolf D. Philos. Mag. B 1989;59:667.
- [36] Fecht HJ, Hellstern E, Fu Z, Johnson WL. Adv. Powd. Met 1989;2:111.
- [37] Hellstern E, Fecht HJ, Fu Z, Johnson WL. J. appl. Phys 1989;65:305.
- [38] Wallner G, Jorra E, Franz H, Peisl J, Birringer R, Gleiter H, Haubold T, Petry W. MRS Symp. Proc 1989;132:149.
- [39] Jorra E, Franz H, Peisl J, Wallner G, Petry W, Birringer R, Gleiter H, Haubold T. Philos. Mag. B 1989;60:159.

- [40] Zhao YH, Sheng HW, Lu K. *Acta Mater* 2001;49:265.
- [41] Panfilis Sd, Dacaptio F, Conrad H, J. Weissmuller, Boscherini F. *Phys. Lett. A* 1995;207.
- [42] Herr U, Jng J, Birringer R, Gonser U, Gleiter H. *Appl. Phys. Lett* 1987;50:472.
- [43] Fultz B, Kuwano H, Ouyang H. *J. appl. Phys* 1995;77:3458.
- [44] Schaefer HE, Wurschum R, Birringer R, Gleiter H. *Phys. Rev. B* 1988;38:9545.
- [45] Haubold T, Birringer R, Lengeler B, Gleiter H. *Phys. Lett. A* 1989;135:461.
- [46] Mutschele T, Kirchheim R. *Scripta materialia* 1987;21:1101.
- [47] Horvath J, Birringer R, Gleiter H. *Solid State Comm* 1987;62:319.
- [48] Wallner G, Jorra E, Franz H, Peisl J, Birringer R, Gleiter H, Haubold T, Petry W. *Mater. Res. Symp. Proc.* 1989;132:149.
- [49] Suryanarayana C. *Int. Mater. Rev.* 1995;40:41.
- [50] Lu K. *Mater. Sci. Engng. Rep* 1996;R16:161.
- [51] Loffler J, Weissmuller J. *Phys. Rev. B* 1995;52:7076.
- [52] Gleiter H. *Acta Mater* 2000;48:1.
- [53] Palumbo G, Thorpe SJ, Aust KT. *Scripta Metall Mater* 1990;24:2347.
- [54] Kirchheim R, Mutschele T, Kieninger W, Gleiter H, Birringer R, Koble TD. *Mater Sci and Engineering -A* 1988;99:457.
- [55] Bianco LD, Hernando A, Bonetti E, Navarro E. *Phys. Rev. B* 1997;56:8894.
- [56] Pulido E, Navarro I, Hernando A. *IEEE Tran. Magn.* 1992;28.
- [57] Cicco AD. *Materials Science Forum* 1995;195:1995.
- [58] Haubold T, Krauss W, Gleiter H. *Philos. Mag. Lett* 1991;63:245.
- [59] DiCicco A, Berrettoni M, Stizza S, Bonetti E, Cocco G. *Phys. Rev. B* 1994;12:386.
- [60] Cicco AD, Berrettoni M, Stizza S, Bonetti E. *Physica B* 1995;208-209:547.
- [61] Islamgaliev RK, Kuzel R, Obratzsova ED, Burianek J, Chmelik F, Valiev RZ. *Mater Sci and Engineering A* 1998;249:152.
- [62] Bonetti E, Pasquini L, Sanpaolesi E, Alvisi M. *J. Phys. (Paris) IV*, 6 1996;C8:345.
- [63] Wang J, Wolf D, Phillippot SR, Gleiter H. *Philos. Mag. A* 1996;73:517.
- [64] Chen D. *Mater Sci and Engineering A* 1995;190:193.
- [65] Chen D. *Materials Letters* 1994;21:405.
- [66] Gaffet E, Tachikart M, Kedim OE, Rahoudj R. *Materials Characterization* 1996;36:185.
- [67] Revesz A, Ungar A, Borbely A, Lendvai J. *NanoStructured Materials* 1996;7:779.
- [68] Chen Z, Ding J. *NanoStructured Materials* 1998;10:205.
- [69] Trudeau ML, Schulz R. *Mater Sci and Engineering A* 1991;134:1361.
- [70] Li DX, Ping DH, YE HQ, Qin XY, Lu XJ. *Materials Letters* 1993;18:29.
- [71] Siegel RW. *Encycl. of Appl. Physics* 1994;11, G.L. Trigg, ed.:173.
- [72] Trapp S, Limbach CT, Gonser U, Campbell SJ, Gleiter H. *Physical Review Letters* 1995;75:3760.
- [73] Takahashi T, Bassett WA. *Science* 1964;145:483.
- [74] Chen B, Penwell D, Kruger MB, Yue AF, Fultz B. *J. appl. Phys* 2001;89:4794.
- [75] Jiang J, Olsen JS, Gerward L. *Materials Transactions* 2001;42:1571.
- [76] Suryanarayana C. *Progress in Materials Science* 2001;46:1.
- [77] Murty BS, Ranganathan S. *Int. Mater. Rev.* 1998;43:101.
- [78] Natter H, Schmelzer M, Loeffler MS, Hempelmann R. *Mater. Sci. Forum* 2000;343:II:683.
- [79] Natter H, Schmelzer M, Loeffler MS, Krill CE, Fitch A, Hempelmann R. *Journal of Physical Chemistry B* 2000, 104:2467.
- [80] Michalski A. *NanoStructured Materials* 1997;8:725.
- [81] Lee DW, Yu JH, Jang TS, B.K.Kim. *Materials Letters* 2005;59:2124.
- [82] Korznikova GF, Korznikov AV, Syutina LA, Mulyukov KY. *Journal of Magnetism and Magnetic Materials* 1999;196:207.

- [83] Savader JB, Scanlon MR, Cammarata RC, Smith DT, Hayzelden C. *Scripta materialia* 1997;36:29.
- [84] Hernando A, Cebollada A, Menendez JL, Briones F. *Electronic transport in nanocrystalline iron: A low T magnetoresistance effect.* vol. 262. San Diego, CA, United States: Elsevier, 2003. p.1.
- [85] Fougere GE, Weertman JR, Siegel RW. *NanoStructured Materials* 1995;5:127.
- [86] Segers D, Petegem SV, Loffler JF, Swygenhoven HV, Wagner W, Dauwe C. *NanoStructured Materials* 1999;12:1059.
- [87] Sanchez-Lopez JC, Rojas TC, Espinos JP, Fernandez A. *Scripta materialia* 2001;44:2331.
- [88] Jang JSC, Koch CC, 1988;22:677 *CSM. Scripta metall. mater.* 1988;22:677.
- [89] Fecht HJ, Hellstern E, Fu Z, Johnson WL. *Metall. Mater. Trans. A* 1990;21A:2333.
- [90] Daroczi L, Beke DL, Posgay G, Zhou GF, Bakker H. *NanoStructured Materials* 1993;2:515.
- [91] Sinha P, Collins GS. *Hyperfine Interactions* 1994;92:949.
- [92] Bonetti E, Bianco LD, Pasquini L, Sampaolesi E. *NanoStructured Materials* 1999;12:685.
- [93] Bonetti E, Bianco LD, Fiorani D, Rinaldi D, Caciuffo R, Hernando A. *Physical Review Letters* 1999;83:2829.
- [94] Bonetti E, Scipione G, Valdre S, Enzo S, Frattini R, Macri PP. *Journal of Materials Science* 1995;30:2220.
- [95] Moelle CH, Fecht HJ. *NanoStructured Materials* 1995;6:421.
- [96] Malow TR, Koch CC, Miraglia PQ, Murty KL. *Mater Sci and Engineering* 1998;A252:36.
- [97] Malow TR, Koch CC. *Metall. Mater. Trans. A* 1998;29A:2285.
- [98] Malow TR, Koch CC. *Acta Mater* 1998;46:6459.
- [99] Malow TR, Koch CC. *Acta Mater* 1997;45:2177.
- [100] Szabo S, Beke DL, Harasztosi L, Daroczi L, Posgay G, Kis-Varga M. *NanoStructured Materials* 1997;9:527.
- [101] Elkedim O, Cao HS, Fluzin P. *Materials Science Forum* 1999;312.
- [102] Elkedim O, Cao HS, Meunier C, Gaffet E. *Materials Science Forum* 1998;269-272.
- [103] Tian HH, Atzmon M. *Acta Mater* 1999;47:1255.
- [104] Khan AS, Zhang H, Takacs L. *Int. J. Plasticity* 2000;16:1459.
- [105] Meszaros S, Vad K, Hakl J, Kerekes L, Gurin P, Kis-Varga M, Szabo S, Beke DJ, Chatel PFD. *Philosophical Magazine B: Physics of Condensed Matter; Statistical Mechanics, Electronic, Optical and Magnetic Properties* 2001;81:1597.
- [106] Sobczak E, Swilem Y, Dorozhkin NN, Nietubyc R, Dluzewski P, Slawska-Waniewska A. *J. Alloys Compd.* 2001;328:57.
- [107] Robertson A, Erb U, Palumbo G. *NanoStructured Materials* 1999;12:1035.
- [108] Natter H, Schmelzer M, Hempelmann R. *J. Mater. Res.* 1998;13:1186.
- [109] El-Sherik AM, Erb U. *J. Mater. Sci.* 1995;30:5743.
- [110] Cho SM, Kyungtae K, Moonjung K. *Materials Chemistry and Physics* 2006;96:278.
- [111] Natter H, Hempelmann R. *Journal of Physical Chemistry* 1996;100:19525.
- [112] Przenioslo R, Winter R, Natter H, Schmelzer M, Hempelmann R, Wagner W. *Physical Review B (Condensed Matter)* 2001;63:54408.
- [113] Saber K, Koch CC, Fedkiw PS. *Mater Sci and Engineering A* 2003;341:174.
- [114] Budevski E, Staikov G, Lorenz WJ. *Electrochemical phase transformation and growth.* Weinheim: VCH, 1996.
- [115] Cheung C, Djuanda F, Erb U, Palumbo G. *NanoStructured Materials* 1995;5:513.
- [116] Erb U PG, Szpunar B, Aust KT. *Nanostructured Materials* 1997;9:261.
- [117] Fougere GE, Riestler L, Ferber M, Weertman JR, Siegel RW. *Journal of Engineering and Applied Science* 1995;A204:1.
- [118] Jeong DH, Gonzalez F, Palumbo G, Aust KT, Erb U. *Scripta materialia* 2001;44:492.
- [119] Kim SH, Aust KT, Erb U, Gonzalez F, Palumbo G. *Scripta materialia* 2003;48:1379.

- [120] Choi CJ, Dong XL, Kim BK. Scripta materialia 2001;44:2225.
- [121] Dong XL, Choi CJ, Kim BK. J. appl. Phys 2002;92:5380.
- [122] Lee DW, Jang TS, Kim D, Tolochko OV, Kim BK. Glass and Physics Chemistry 2005;31:545.
- [123] Savader JB, Scanlon MR, Cammarata RC, Smith DT, Hayzelden C, Study of the Hall-Petch dependence in an annealed nanocrystalline iron thin film. vol. 403. Boston, MA, USA: Materials Research Society, Pittsburgh, PA, USA, 1996. p.157.
- [124] Benjamin JS. Met. Trans. 1970;1:1943.
- [125] Koch CC. "Mechanical Milling and Alloying" in Materials Science and Technology. In: Cahn RW, Haasen P, Kramer EJ, editors. Processing of metals and alloys, vol. 15. 1991. p.193.
- [126] Murty BS, Datta MK, Pabi SK. Sadhana - Academy Proceedings in Engineering Sciences 2003;28:23.
- [127] Giri AK. Advanced Materials 1997;9:163.
- [128] Gilman PS, Benjamin JS. Annu. Rev. Mater. Sci. 1983;13:279.
- [129] Witkin DB, Lavernia EJ. Progress in Materials Science 2006;51:1.
- [130] Koch CC. Mater Sci and Engineering A 1998;244:39.
- [131] Fecht HJ. In: Hadhipanayis GC, Siegel RW, editors. Nanophase materials, vol. 125. Kuwel Acad. Pub., 1994.
- [132] Koch CC. Rev. Adv. Mater. Sci 2003;5:91.
- [133] Gialanella S, Lutterotti L. In: Nalwa HS, editor. Nanoclusters and Nanocrystals. American Scientific Publishers, 2003.
- [134] Koch CC. NanoStructured Materials 1993;2:109.
- [135] Koch CC. NanoStructured Materials 1997;9:13.
- [136] Froes FH, Senkov ON, Baburaj EG. Mater Sci and Engineering A 2001;301:44.
- [137] Li S, Wang K, Sun L, Wang Z. Scripta Metall Mater 1992;27:437.
- [138] Suryanarayana C. Intermetallics 1995;3:153.
- [139] Mendez M, Mancha H, Cisneros MM, Mendoza G, Escalante JI, Lopez HF. Metal. Mater. Trans. A 2002;33A:3273.
- [140] Eckert J, Holzer JC, Krill CE, Johnson WL. J. Mater. Res. 1992;65:305.
- [141] Oleszak D, Shingu PH. J. appl. Phys 1996;79:2975.
- [142] Botcharova E, Freudenberge J, Schultz L. Journal of Alloys and Compounds 2004;365:157.
- [143] Alam SN. Mater Sci and Engineering A 2006;artile in press "Synthesis and characterization of W-Cu nanocompisted .."
- [144] Shen TD, Ge WQ, Wang KY, Quan MQ, Wang JT, Wei WD, Koch CC. NanoStructured Materials 1996;7:393.
- [145] Mohamed FA, Xun Y. Mater Sci and Engineering 2003;A354:133.
- [146] Mohamed FA. Acta Mater 2003;51:4107.
- [147] Perez RJ, Jiang HG, Dogan CP, Lavernia EJ. Metall. Mater. Trans. A 1998;29A:2468.
- [148] Zhou F, Witkin D, Nutt SR, Lavernia EJ. Mater Sci and Engineering in press
- [149] Moumeni H, Alley S, Greneche J.M., Journal of alloys and compounds, 2005, 386, 12
- [150] Xiong CS, Xiong YH, Zhu H, Sun TF, Dong E, Liu GX. NanoStructured Materials 1995;5:425.
- [151] Brun PL, Gaffet E, Froyen L, Delacy L. Scripta metall. mater. 1992;26:1743.
- [152] Fnidiki A, Lemoine C, Teillet J, Malandain JJ. Physica B 2003;327:140.
- [153] Rao MA, Bhargava S, Deva D. Metall. Mater. Trans. A 2005;36A:11.
- [154] Caer GL, Ziller T, Delcroix P, Bellourad C. Hyperfine Interactions 2000;130:45.
- [155] Fecht HJ. NanoStructured Materials 1995;6:33.
- [156] Xuan Y, Lavernia EJ, Mohamed FA. Metal. Mater. Trans. A 2004;35:573.
- [157] Murayama M, Howe jM, Hidaka H, Takai S. Science 2002;295:2433.
- [158] Dominguez O, Phillippot M, Bigot J. Scripta Metall Mater 1995;32:13.

- [159] Groza JR. "Nanocrystalline Powder Consolidation Methods" in Nanostructured Materials: Processing, Properties and Applications, ed. CC Koch, William Andrew Pub. Norwich, NY (2007).
- [160] Shapiro I, Kolthoff M. J. Phys. Colloid Chem 1947;51:483.
- [161] German R. Powder Metallurgy Science, MPIF.
- [162] Gupta RK, R.K. Singh Raman, Koch CC. Mater Sci and Engineering-A.
- [163] Guruswamy S, RL M, N. Srisukhumbowornchai, Michael KM, Joseph P. IEEE Trans 2000;36:3219.
- [164] Guduru RK, Scattergood RO, Koch CC, Murty KL, Guruswamy S, McCarter MK. Scripta materialia 2006;54:1879.
- [165] Kang S-jL. Sintering, Densification, Grain Growth and Microstructure, ELSEVIER.
- [166] Elkedim O, Cao HS, Guay D. Journal of Materials Processing Technology 2002;121.
- [167] Omuro K, Miura H, Ogawa H. Materials Science Forum 1999;318-320:701.
- [168] Youssef KM, Scattergood RO, Murty KL, Koch CC. Applied Physics Letters 2004:2004.
- [169] Cheng S, Ma E, Wang YM, Kecskes LJ, Youssef KM, Koch CC, Trociewitz UP, Han K. Acta Mater 2005;53:1521.
- [170] Elkedim O, Cao H, Guay D. Journal of Materials Processing Technology 2002;121:383 2002;121.
- [171] Rodeiguez-Baracaldo R, Benito JA, Cabrera JM, Prado JM. J. Mater. Sci. 2007;42:1757.
- [172] Rawers J, F.Biancanello, Jiggetts R, Fields R, Williams M. Scripta materialia 1999;40:277.
- [173] Wang N, Wang Z, Aust KT, Erb U. Mater Sci and Engineering 1997;A237:150.
- [174] Coble RL. J. appl. Phys 1963;34:1679.
- [175] Suryanarayana C, Koch CC. Hyperfine Interactions 2000;130:5.
- [176] Siegel RW, Fougere GE. NanoStructured Materials 1995;6:205.
- [177] Kumar KS, Swygenhoven HV, Suresh S. Acta Mater 2003;51:5743.
- [178] Padmanabhan KA. Mater Sci and Engineering A 2001;304-306.
- [179] Gutkin MY, Ovid'ko IA. Plastic deformation in Nanocrystalline Materials: Springer, 2004.
- [180] Gryaznov VG, Trusov LI. Progress in Materials Science 1993;37:289.
- [181] Tjong SC, Chen H. Materials Science and Engineering R 2004;45:1.
- [182] Koch CC, Scattergood RO, Murty KL, Guduru RK, Trichy G, Rajulapati KV. Materials Research Society Symposium - Proceedings 2003;791:51.
- [183] Taboor D. The hardness of the metals. Clarendon Press, Oxford 1951:95ff.
- [184] Armstrong RW. Yield Flow and Fracture of Polycrystals. In: Baker TN, editor. Applied Science, London. 1983. p.1.
- [185] Myres MA, Chawla KK. Mechanical Metallurgy - Principles and Applications, Prentice-Hall 1984.
- [186] Jang D, Atzmon M. J. appl. Phys 2003;93:9282.
- [187] Jang JSC, Koch CC. Scripta metall. mater. 1990;24:1599.
- [188] Cao HS. Materials Letters 2004;58:3564.
- [189] Hall EO. Proc. Phys. Soc. Kondon 1951;B64:747.
- [190] Petch NJ. J. Iron steel Inst. 1953;25:172.
- [191] Siegel RW. Materials Science Forum 1997;235-238:851.
- [192] Gutmanas EY, Trusov LI, Gotman I. NanoStructured Materials 1994;4:893.
- [193] Scattergood RO, Koch CC. Scripta metall. mater. 1992;27:1992.
- [194] Neith TG, J.Wadsworth. Scripta metall. mater. 1991;25:1991.
- [195] Lu K, Sui ML. Scripta metall. mater. 1993;28.
- [196] Lian J, Baudalet B. NanoStructured Materials 1993;2:415.
- [197] Gryaznov VG, Solov VA, Trusov LI. Scripta metall. mater. 1990;24.
- [198] Khan AS, Liang R. Int. J. Plasticity 1999;15:1089.
- [199] Suryanarayana C. The structure and Properties of Nanocrystalline Materials: Issues and Concerns. JOM 2002;54:24.
- [200] Kim K, Okazaki K. Mater. Sci. Forum 1992;88:553.

- [201] Chokshi AH, Rosen A, Karch J, Gleiter H. *Scripta metallurgica* 1989;23:1679.
- [202] Anderson E, King DLW, Spreadborough J. *Trans. TMS-AIME* 1968;242:115.
- [203] Thompson AW. *Acta Metall* 1975;23:1337.
- [204] Suryanarayana C, Mukhopadhyay D, Patnkar SN, Froes FH. *J. Mater. Res.* 1992;7:2114.
- [205] Koch CC, Cho YS. *NanoStructured Materials* 1992;1:207.
- [206] Lu K, Sui ML. *Scripta metall. mater.* 1993;28:1465.
- [207] Fougere GE, Weertman JR, Siegel RW. *Scripta metall. mater.* 1992;26:1879.
- [208] Shen TD, Koch CC. *Acta Mater* 1996;44:753.
- [209] Morris DG, Morris MA. *Acta metall. mater* 1991;39:1763.
- [210] Mishin OV, Gertsman VY, Valiev RZ, Gottstein G. *Mater. Sci. Forum* 1997;235-238:887.
- [211] Gertsman VY, Hoffmann M, Gleiter H, Birringer R. *Acta metall. mater* 1994;42:3539.
- [212] Gunther B, Baalman A, Weiss H. *Mater. Res. Symp. Proc.* 1990;195:611.
- [213] Nieman GW, Weertman JR, Siegel RW. *Mater. Res. Symp. Proc.* 1991;206:581.
- [214] Nieman GW, Weertman JR, Siegel RW. *J. Mater. Res.* 1991;6:1012.
- [215] Liang G, Li Z, Wang E. *J. Mater. Res.* 1996;31:910.
- [216] Aoki K, Itoh Y, Kawamura Y, Inoue A, Masumoto T. *Mater. Res. Symp. Proc.* 1997;460:153.
- [217] Jain M, Christman T. *Acta. metall. mater.* 1994;42:1901.
- [218] Kimura H. *NanoStructured Materials* 1997;9:93.
- [219] Dymek S, Dollar M, Hwang SJ, Nash P. *Mater Sci and Engineering* 1992;A152:60.
- [220] Bohn R, Oehring M, Pfuhlmann T, Appel F, Bormann R. *Processing and Properties of Nanocrystalline Materials*, ed. C. Suryanarayana, J. Singh and F.H. Froes TMS. Warrendale, Pennsylvania 1996:355.
- [221] Khan AS, Huang S. *Int. J. Plasticity* 1992;8:397.
- [222] Khan AS, Liang R. *Int. J. Plasticity* 2000;16:1443.
- [223] Weissmuller J. *Synthesis and processing of nanocrystalline powder* 1995;40:41.
- [224] Birringer R. *Mater Sci and Engineering* 1989;A117:33.
- [225] Natter H, Schmelzer M, Loffler MS, Hempelmann R. *Materials Science Forum* 2000;343-346:683.
- [226] Song X, Zhang J, Li L, Yang K, Liu G. *Acta Mater* 2006;54:5541.
- [227] Perez RJ, Jiang HG, Lavernia EJ. *NanoStructured Materials* 1997;9:71.
- [228] Huang B, Perez RJ, Lavernia EJ. *Mater Sci and Engineering* 1998;A255:124.
- [229] Eckert J, Holzer JC, Johnson WL. *J. appl. Phys* 1993;73:131.
- [230] Knsuth P, Charai A, Gas P. *Scripta metall. mater.* 1993;28:325.
- [231] Hofler HJ, Averback RS. *Scripta metall. mater.* 1990;24:2401.
- [232] Boylan K, Ostrander D, Erb U, Palumbo G, Aust KT. *Scripta metall. mater.* 1991;25:2711.
- [233] Gao Z, Fultz B. *NanoStructured Materials* 1994;5:327.
- [234] Witkin DB, Lavernia EJ. *grain growth. Progress in Materials Science* 2006;51.
- [235] Lu L, Wang LN, Ding BZ, Lu K. *Mater Sci and Engineering* 2000;A 286:125.
- [236] Rofagha R, Langer R, El-Sherik AM, Erb U, Palumbo G, Aust KT. *Scripta Metall Mater* 1991;25:2867.
- [237] Wang S, Rofagha R, Roberge PR, Erb U. *Electrochem Soc Proc* 1995;95-98:244.
- [238] Kim S, Gonzalez F, Panagiotopoulos G, G GP, Erb U, Aust KT. *American Electroplaters and Surface Finishers Society, AESF SUR/FIN 2001, Nashville, Orlando, FL, Session D. CD-Rom; 2001.*
- [239] Tang PT, Watanabe T, Anderson J, Bech-Nielsen G. *J. appl. Electrochem.* 1995;25:347.
- [240] Liu L, Li Y, Wang F. *Electrochimica acta* 2007.
- [241] Rofagha R, Splinter SJ, Erb U, Mcintyre NS. *NanoStructured Materials* 1994;4:69.
- [242] Ghosh SK, Dey GK, Dusane RO, Grover AK. *Journal of Alloys and Compounds* 2006;426:235.
- [243] Rofagha R, Erb U, Ostrander D, Palumbo G, Aust. K. *NanoStructured Materials* 1993;2:1.

- [244] Gonzalez F, Brennenstuhl AM, Palumbo G, Erb U, 1996;225–227:831. PCLMSF. Mater Sci Forum 1996;225-227:831.
- [245] Palumbo G, Gonzalez F, Brennenstuhl AM, Erb U, Shmayda W, Lichtenberger PC. NanoStructured Materials 1997;9:737.
- [246] Kim SH, Aust KT, Erb U, Ogundele G, Gonzalez F. American Electroplaters and Surface Finishers Society, AESF SUR/FIN 2002, Chicago, Orlando, FL, Session V; 2002. p. 225.
- [247] Wang L, Lin Y, Zeng Z, Liu W, Xue Q, Hu L, Zhang J. Electrochimica acta 2007;52:4342.
- [248] Jung H, Alfantazi A. Electrochimica acta 2006;51:236.
- [249] Cheng D, Tellkamp VL, Lavernia CJ, Lavernia EJ. Annals of Biomedical Engineering 2001;29:803.
- [250] Yu JK, Han EH, Lu L, Wei XJ. Journal of Materials Science 2005;40:1019.
- [251] Vindogradov A, Mimaki T, Hashimoto S, Valiev R. Scripta materialia 1999;41.
- [252] Vinogradov A, Mimaki T, Hashimoto S, Valiev R. Materials Science Forum 1999;312-314:641.
- [253] Tao S, Li DY. Nanotechnology 2006;17:65.
- [254] Heim U, Schwitzgebel G. NanoStructured Materials 1999;12:19.
- [255] Yamashita M, Mimaki S, Hashimoto S, Miura H. Philos. Mag. A 1991;63:707.
- [256] Mauer R, Erb U, Gleiter H. Mater Sci and Engineering 1984;63:L 13.
- [257] Aust. K, Erb U, Palumbo G. Mater Sci and Engineering A 1994;176:329.
- [258] Schneider M, Pischang K, Worch H, Fritsche G, Klimannek P. Materials Science Forum 200;343-346:873.
- [259] Aledresse A, Alfantazi A. Journal of Materials Science 2004;39:1523.
- [260] Kirchheim R, Huang XY, Cui P, Birringer R, Gleiter H. NanoStructured Materials 1992;1:167.
- [261] Vinogradov A, Mimaki T, Hashimoto S, Valiev R. Scripta materialia 1999;41:319.
- [262] Lopez-Hirata VM, Arce-Estrada EM. Electrochimica acta 1997;42:61.
- [263] Lu AQ, Zhang Y, Li Y, Liu G, Zang QH, Liu CM. Acta Metallurgica Sinica 2006;19:183.
- [264] Barbucci A, Farne G, Matteazzi P, Riccieri R, Cerisola G. Corrosion Science 1999;41:463.
- [265] Tong HY, Shi FG, Lavernia EJ. Scripta Metall Mater 1995;32:511.
- [266] Kedim OE, Paris S, Phigini C, Bernard F, Gaffet E, Munir ZA. Mater Sci and Engineering 2004;A369:49.
- [267] Thorpe SJ, Ramaswami B, Aust KT. Journal of Electrochemical Society 1988;135:2162.
- [268] Mohan P, Suryanarayana C, Desai V. Proc. Intl. Conf. Nano-Materials Kolkata Nov. 2004:171.
- [269] Mondal K, Murty BS, Chaterjee UK. Corrosion Science 2005;2005:2619.
- [270] Mondal K, Chaterjee UK, Murty BS. Corrosion and oxidation behaviour of amorphous and nanocrystalline phases in Ze alloys, Bangalore, India:Elsevier 2004;334-335:544.
- [271] Lu H-B, Li Y, Wang F-H. Surface and Coatings Technology 2006;201:3393.
- [272] Zander D, Koster U. Mater Sci and Engineering A 2004;375-377:53.
- [273] Fontana MG. Corrosion Science. New York: Mc Graw-Hill 1986.
- [274] Singh RKR. Metall. Mater. Trans. A 2004;35A:2525.
- [275] Mishra R, Balasubramaniam R. Corrosion Science 2004;46:3019.
- [276] Palumbo G, aust KT. Microstructural Science 1989;17:275.
- [277] Zhang XY, Shi MH, Li C, Liu NF, Wei YM. Mater Sci and Engineering A 2007;448:259.
- [278] Uhlig HH. Corrosion Science 1979;19:777.
- [279] Bollmann W. Philos. Mag. A 1984;49:73.
- [280] Bollmann W. Philos. Mag. A 1988;57:637.
- [281] Palumbo G, Aust KT. Mater Sci and Engineering A 1989;113:139.
- [282] King PF, Uhlig HH. Journal of Electrochemical Society 1959;63:2026.
- [283] Corrosion Handbook. Newyork: John Wiley and Sons, 1948.
- [284] Sedriks AJ. Corrosion of stainless steels: New York : Wiley, c1996.
- [285] Tomashov ND. Corrosion Science 1964;4:315.

- [286] Li P, Tan TC, Lee JY. *Corrosion Science* 1996;38:1935.
- [287] Doig P, Flewitt PEJ. *Mater Sci and Engineering* 1980;43:77.
- [288] McCafferty E. *Journal of Electrochemical Society* 2007;154:C571.
- [289] Schreiber A, Rosenkranz C, Lohrengel MM. *Electrochimica acta* 2007;52:7738.
- [290] Tronstad L, Borgmann C. *Trans. Faraday Soc.* 1934;30:349.
- [291] Faraday M. *Experimental researches in Electricity* reprinted 1965, Dover Pub, New York;2:243.
- [292] Bennett C, Burnham W. *Trans. Electrochem. Soc.* 1916;29:217.
- [293] Leistikow S, Wolf I, Grabke HJ. *Wekst. Korros* 1987;38:556.
- [294] Shida Y, Ohtsuka N, Muriama J, Fujino N, Fujikawa H. *Proc. JIMS-3, High Temp. Corros., Trans. Jap. Inst. Met.* 1983:631.
- [295] Fredenhagen C. *Z. Phys. Chem.* 1908;63:1.
- [296] Hittorf W. *Z. Phys. Chem.* 1899;30:485.
- [297] Hittorf W. *Z. Phys. Chem.* 1900;34:385.
- [298] Finklesstein A. *Z. Phys. Chem.* 1902;39:91.
- [299] Swinne R. *Z. Elektrochem.* 1925;31:417.
- [300] Fredenhagen C. *Z. phys. Chem.* 1903;43:1.
- [301] Langmuri I. *Trans. electrochem. Soc.* 1916;29:260.
- [302] Tammann G. *Z. anorg, allg. Chem.* 1919;107:236
- [303] Tammann G. *Stahl Eisen* 1922; 42:577
- [304] Norskov JK. *Rep. Prog. Phys.* 1990;53:1253.
- [305] Mulyukov RR. *Rev. Adv. Mater. Sci.* 2006;11:122.
- [306] Gleiter H, Weissmuller J, Wollersheim O, Wurschum R. *Acta Mater* 2001;49:737.
- [307] Smardz L, Jurczyk M, Smardz K, Nowak M, Makowiecka M, Obkonska I. *Renewable Energy* 2008;33:201.
- [308] Wang SG, Shen CB, Long K, Yang HY, Wang FH, Zhang ZD. *J. Phys. Chem. B* 2005;109:2499.
- [309] Shen CB, Wang SG, Yang HY, Long K, Wang FH. *Electrochimica acta* 2007;25:3950.
- [310] Lomayeva SF, Syugaev AV, Reshtetnikov SM, Sjuravin AS, Nemtsova OM, Aksenova VV. *Protection of Metals* 2007;43:194.
- [311] Wang XY, Li DY. *Electrochimica acta* 2002;47:3939.
- [312] Ye W, Li Y, Wang F. *Electrochimica acta* 2006;51:4426.
- [313] Pardo A, Merino MC, Otero E, Lopez MD, M'hich A. *Journal of non-crystalline solids* 2006;352:3179.
- [314] Meng G, Li Y, Wang F. *Electrochimica acta* 2006;51:4277.
- [315] Mordyuk BN, Prokopenko GI, Vasylyev MA, Iefimov MO. *Materials Science and Engineering A* 2007;458:253.
- [316] Ouzie EE, Li Y, Wang FH. *Electrochimica acta* 2007;52:6988.
- [317] Kwok CT, Cheng FT, Man HC, Ding WH. *Materials Letters* 2006;60:2419.
- [318] Giggins CS, Pettit FS. *Metall. Trans. AIME* 1969;245 2509.
- [319] Merz MD. *Metall. Trans.* 1979;10A:71.
- [320] Basu SN, Yurek GJ. *Oxid. Met.* 1991;36:28.
- [321] Jang LY, Yao YD, Chen YY, Hwu Y. *NanoStructured Materials* 1997;9:531.
- [322] Geng S, Wang F, Zhang S. *Surface and Coatings Technology* 2003;167:212.
- [323] Chen G, Lou H. *Scripta materialia* 2000;43:119.
- [324] Chen GF, Lou HY. *Materials Letters* 2000;45:286.
- [325] Liu L, Wang F. *Materials Letters* 2008;62:4081.
- [326] Wang F, Tian X, Li Q, Li L, Peng X. *Thin and solid films* 2008;516:5740.
- [327] Cao G, Geng L, Zheng Z, Naka M. *intermetallics* 2007;15:1672.
- [328] Koester U, Jastrow L. *Mater Sci and Engineering A* 2007;449-451:57.

- [329] May JE, Kuri SE, Nascente PAP. Mater Sci and Engineering A 2006;428:290.
- [330] Niu Y, Cao ZQ, F. G, Farne G, Randi G, Wang CL. Corrosion Science 2003;45:1125.
- [331] Wagner C. J. Electrochem. Soc. 1952;99:369.
- [332] Wagner C. J. Electrochem. Soc. 1956;103:571.
- [333] Wagner C. Z. Electrochem. 1959;63:772.
- [334] Lobb R, Evans H. Metal Science 1981:267.
- [335] Baker I, Liu F. NanoStructured Materials 1996;7:13.
- [336] Murugesan M, 1999;35:3499 HKHIToM. IEEE Transactions on Magnetics 1999;35:3499.
- [337] Lemoine C, Fnidiki A, Lemarchand D, Teillet J. Journal of Magnetism and Magnetic Materials 1999;203:184.
- [338] Delcroix P, Ziller T, Bellouard C, Caer GL. Mechanical alloying of an Fe_{0.30}Cr_{0.70} alloy from elemental powders. vol. 360-362. Oxford: Trans Tech Publications Ltd, 2001. p.329.
- [339] Fnidiki A, Lemoine C, Teillet J. Journal of Physics Condensed Matter 2002;14:7221.
- [340] Fnidiki A, Lemoine C, Teillet J, Nogues M. Physica B: Condensed Matter 2005;363:271.
- [341] Fnidiki A, Lemoine C, Teillet J. Physica B: Condensed Matter 2005;357:319.
- [342] Pandey B, Rao MA, Verma HC, Bhargava S. Journal of Physics: Condensed Matter 2005;17:7981.
- [343] Costa B, Caer GL, Begin-Colin S, Mendes PJ, Campos NAd. Journal of Materials Processing Technology 1999;92-93:395.
- [344] Costa BFO, Caer GL, Amado MM, Sousa JB, Journal of Alloys and Compounds 2000;308:49.
- [345] Zhu M, Fecht HJ. NanoStructured Materials 1995;6:921.
- [346] Massalski TB. Binary alloy phase diagrams Al.
- [347] Pfeiffer F, Radelhoff C. J. Magn. Mater. 1980;19:190.
- [348] Trudeau ML. NanoStructured Materials 1999;12:55.
- [349] Li J, Qin Y, Kou X, Huang J. Nanotechnology 2004;15:982.
- [350] Hylton TL, Coffey KR, Parker MA, Howard JK. J. appl. Phys 1994;75:7058.
- [351] Guenzberger D, Terra J. Phys. Rev. B 2005;72:024408.
- [352] Hongqi L, Ebrahimi F. Materials Science and Engineering A 2003;347:93.
- [353] Tcherdyntsev VV, Kaloshkin SD, Tomilin IA, Shelekhov EV, Baldokhin YV. NanoStructured Materials 1999;12:139.
- [354] Baldokhin YV, Tcherdyntsev VV, Kaloshkin SD, Kochetov GA, Pustov YA. Journal of Magnetism and Magnetic Materials 1999;203:313.
- [355] Hong LB, Fultz B. Journal of Applied Physics 1996;79:3946.
- [356] Kuhrt C, Schultz L. Journal of Applied Physics 1993;73:1975.
- [357] Zhu LH, Ma XM, Zhao L. Journal of Materials Science 2001;36:5571.
- [358] Zhu LH, Huang QW. Materials Letters 2003;57:4070.
- [359] Li-Hui Z, Qing-Wei H. Materials Letters 2003;57:4070.
- [360] Kuhrt C, Schultz L. Journal of Applied Physics 1999;73:6588.
- [361] Herzer G. IEEE Trans Magn 1989;MAG-25:3327.
- [362] Vitta S, Khuntia A, Ravikumar G, Bahadur D. Journal of Magnetism and Magnetic Materials 2008;320:182.
- [363] Leinartas K, Samuleviciene M, Bagdonas A, Juskenas R, Juzeliunas E. Surface and Coatings Technology 2003;168:70.
- [364] Enayati MH, Bafandeh MR.
- [365] Kaloshkin SD, Tcherdyntsev VV, Tomilin IA, Baldokhin YV, Skelekhov EV. Physica B: Condensed Matter 2001;299:236.
- [366] Koch CC, Youssef KM, Scattergood RO, Murty KL. Advanced Engineering Materials 2005;7:787.
- [367] Roy RA, Roy R. Mater. Res. Bull. 1984;19:169.
- [368] Karimpoor AA, Erb U, Aust KT, Palumbo G. Scripta materialia 2003;49:651.

- [369] Hibbard GD. Pros 15th Int Sympo: Processing and Fabrication of Advances Materials, Cincinnati 2006:297.
- [370] Seo JH. Mater. Sci. Forum 2005;475-479:3483.
- [371] Hibbard GD, Aust KT, Erb U. Mater Sci and Engineering A 2006.
- [372] Youssef KM, Scattergood RO, Murty KL, Horton JA, Koch CC. Appl. Phys. Lett 2005;87:1.
- [373] Youssef KM, Scattergood RO, Murty KL, Koch CC. Scripta materialia 2006;54:251.
- [374] Kedim OE, Cao HS, Guay D. Journal of Materials Processing Technology 2002;121:383.
- [375] Youssef KM, Koch CC, Fedkiw PS. Corrosion Science 2004;46:51.
- [376] R.K. Singh Raman, Metall. Mater. Trans. A 1995;26A:1847.
- [377] R.K. Singh Raman, Metall. Mater. Trans. A 1998;28A:577.
- [378] R.K. Singh Raman, Khanna AS, Gnanamoorthy JB. Tran. Indian Inst. Metals 1992;46:391.
- [379] R.K. Singh Raman, Khanna AS, Gnanamoorthy JB. J. Mater. Sci Letters 1990;9:353.
- [380] Kofstad P. High Temperature Corrosion. New York: Elsevier applied Science and publishers Ltd, 1988.
- [381] Wagner C. Corrosion Science 1965;5:751.
- [382] Kaur I, Gust W, Kozma L. handbook of grain and interphase boundary diffusion data: Stuttgart: Ziegler Press, p 523, 1989.
- [383] Bowen AW, Leak GM. Metall. Trans. 1970;1:1695.
- [384] Wang ZB, Tao NR, Tong WP, Lu J, Lu K. Defect and Diffusion Forum 1996;249:147.
- [385] Wood GC. Corrosion Science 1961;2:173.
- [386] Hossain MK. Corrosion Science 1979;19:1031.
- [387] Gao W, Liu Z, Li Z. Adv. Mater. 2001;12:1001.
- [388] Stringer J, Wright I. Oxid. Met. 1972;5:51.
- [389] Wang F. Oxidation of metals 1997;47:247.
- [390] Zeiger W, Schneider M, Scharnwber D, Worch H. NanoStructured Materials 1995;6:1013.
- [391] Hermas AA. Corrosion Science 2008;50:2498.
- [392] Brooks AR, Clayton CR, Doss K, Lu YC. J. Electrochem Soc 1986;133:2459.
- [393] Grosvenor AP, Kobe BA, M.C. B, N.S. M. Surface and Interface Analysis 2004;36:1564.
- [394] Lin T-C, Seshadri G, Kelber JA. Applied Surface Science 1997;119:83.
- [395] Langevoort JC, Sutherland I, Hanekamp LJ, Gellings PJ. Applied Surface Science 1987;28:1987.
- [396] Johansen NA, Adams GB, Rysselberhe PV. J. Electrochem Soc 1957;104:339.

Appendix A: Hardness of Nanocrystalline Fe-Cr alloys

Ball- milled nanocrystalline Fe-Cr alloys were compacted under a uni-axial pressure. Compacted alloys were polished carefully up to 0.3 micron using SiO₂ suspension, before microhardness measurements. Hardness data for the material measured after heat treatments are presented in the Table 1.

Table 1 (Appendix A) Microhardness of nanocrystalline and microcrystalline Fe-10 Cr and Fe-20Cr alloy

Material	Annealing Temp/time	Grain size (nm)	Hardness (GPa)
Fe-10Cr	Room temperature	13	9.1 (±0.3)
	600 °C/30min	40	6.8 (±0.2)
	600 °C /90min	52	6.6 (±0.2)
	840 °C /30min & 840 °C /30min	1500	1.7 (±0.1)
Fe-20Cr	Room temperature	14	9.2 (±0.3)
	600 °C/30min	42	6.9(±0.2)
	600 °C/90min	53	6.5(±0.2)
	840 °C /30min & 840 °C /30min	1500	1.7(±0.1)

Microhardness of the one of the pellets was also determined using nano-indentation technique. A load-displacement graph obtained in the nano-indentation using a range of applied load is shown in the Figure 1. The hardness data generated using two techniques are in good agreement.

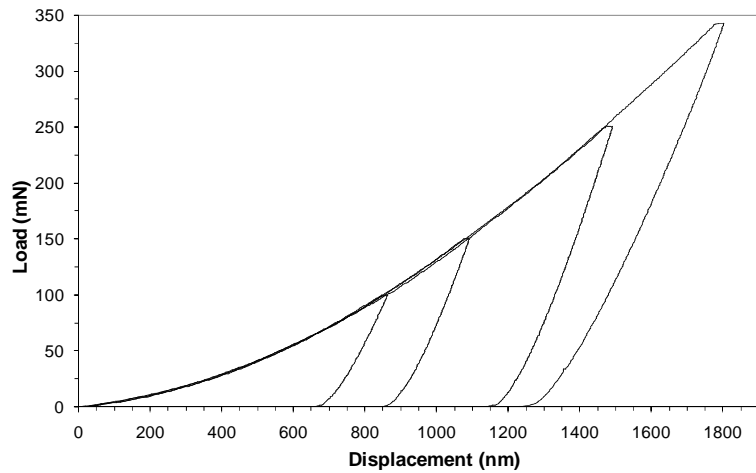


Fig.1 (Appendix A) Load Vs displacement curves obtained under different loading conditions

Microhardness of nanocrystalline Fe-Cr alloys, produced in the current study, is plotted as a function of grain size and is compared with the data in literature (Figure 2). The data presented in the Figure 2 suggest the hardness to increase with decrease in grain size and thus rules out the possibility of any inverse Hall –Petch relationship.

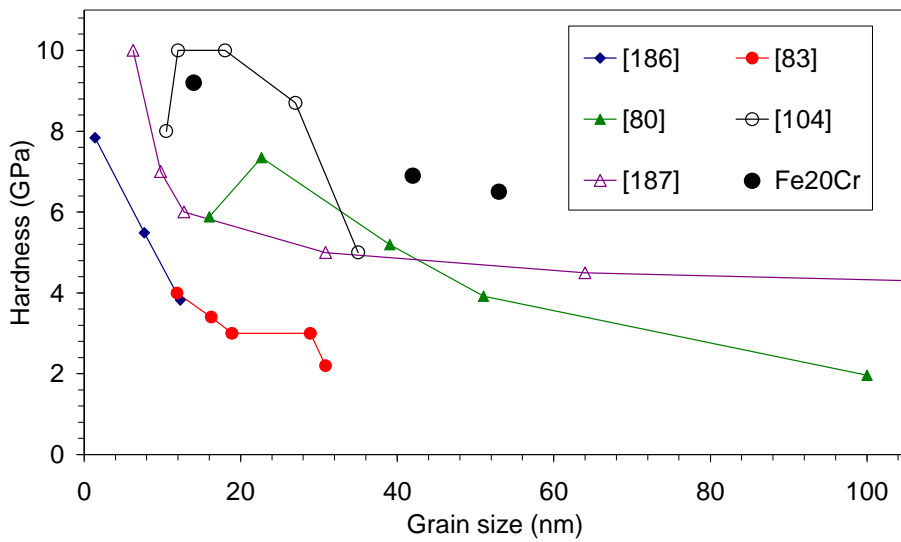


Fig. 2 (Appendix A) Variation of hardness with grain size, comparison of current finding with literature

Appendix B: Oxidation Kinetics

All the results concerning the kinetic curves (mass gain curves as a function of time), presented in Figures 6.1 to 6.4, clearly show that nanocrystalline form of the alloys possess improved oxidation resistance over their microcrystalline counterparts. To emphasize the effect of temperature on oxidation resistance clearly weight gain vs time graphs are plotted again (Figures 1a-3a). As expected, and as evident from the figures 1a and 2a, the oxidation rate increases with increase in the oxidation temperature.

To evaluate the kinetics of the oxidation square of weight gain/area is plotted against the oxidation time (Figure 2b) which clearly demonstrates that at the three temperatures, mc Fe-10Cr alloys follow parabolic oxidation kinetics, given by [380]:

$$(\Delta M/S)^2 = k_p t + a \quad 6.1$$

where S is the exposed area, ΔM is the weight change, k_p is the parabolic rate constant, t is the time and a is a constant. k_p can be expressed as [380]:

$$k_p = k_o \exp(-Q/RT) \quad 6.2$$

where k_o is a constant, Q is the activation energy for oxidation, T is the temperature in Kelvin, R is the gas constant.

The oxidation kinetics is more complex with the nc Fe-10Cr, and nc and mc Fe-20Cr alloys (Figures 2b and 3b). Nanocrystalline Fe-10Cr, and nc and mc Fe-20Cr alloys also follow the parabolic oxidation law but the oxidation kinetics is divided into two stages, characterized by a unique parabolic oxidation rate constant associated with the each stage of the oxidation (Figures 2b and 3b). The time dependent

parabolic oxidation rate constants (k_p) refer to a change in the oxidation mechanism over a period of time (which is also evident from the change in the colour as shown in the previous section). The critical time required for the onset of the second region in nc Fe-10Cr alloys increases with the increase in the oxidation temperature.

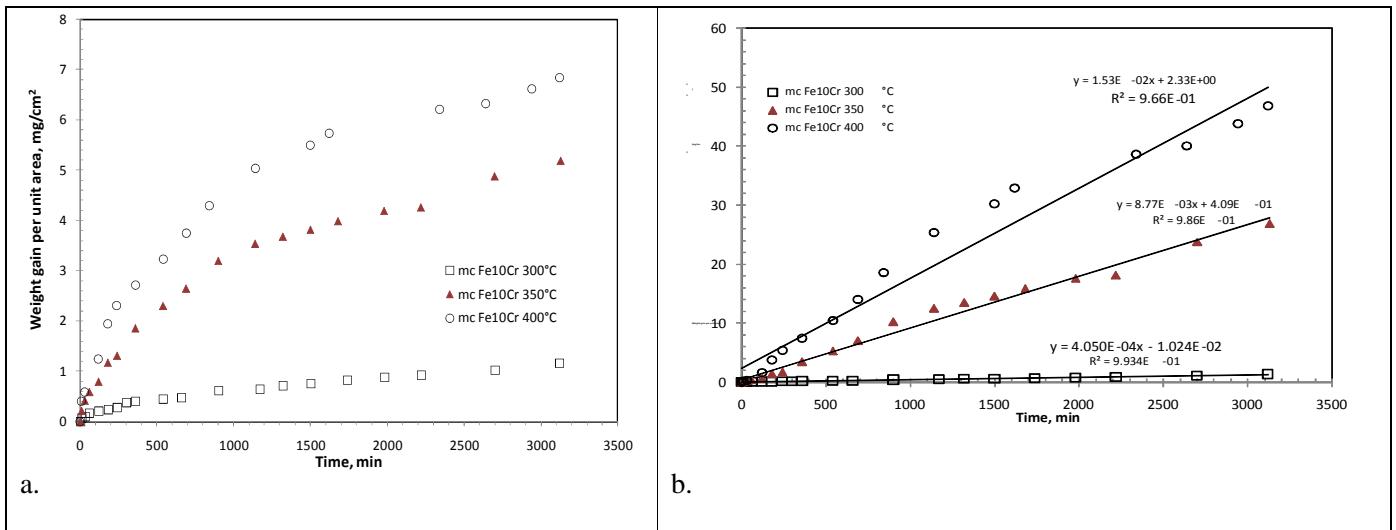


Fig. 1 (Appendix B) kinetics of oxidation for mc Fe10Cr alloy (a) weight gain vs oxidation time plot for mc Fe10Cr alloy for a range of temperatures. (b) $(\text{Weight gain})^2$ vs time plot for mc Fe10Cr alloys for a range of temperature

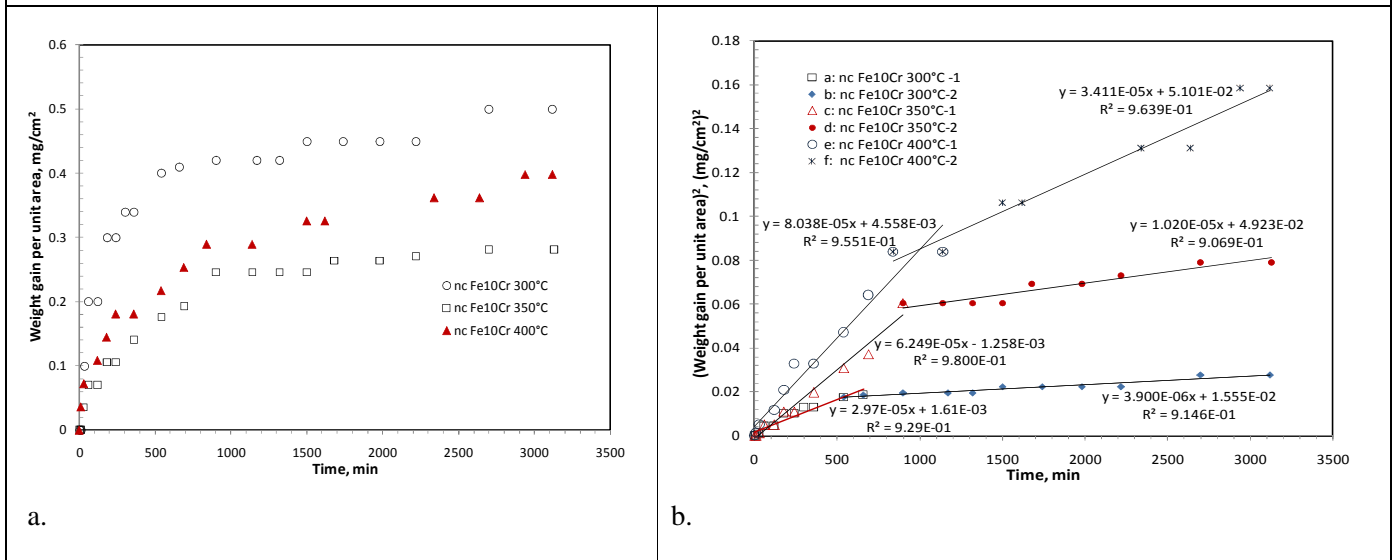


Fig. 2 (Appendix B) kinetics of oxidation for nc Fe10Cr alloy (a) weight gain vs oxidation time plot for nc Fe10Cr alloy for a range of temperatures. (b) $(\text{Weight gain})^2$ vs time plot for Fe10Cr alloys for a range of temperature, there are two stages of oxidation distinguished by the unique parabolic rate constant and described as 1 and 2 in the above graph.

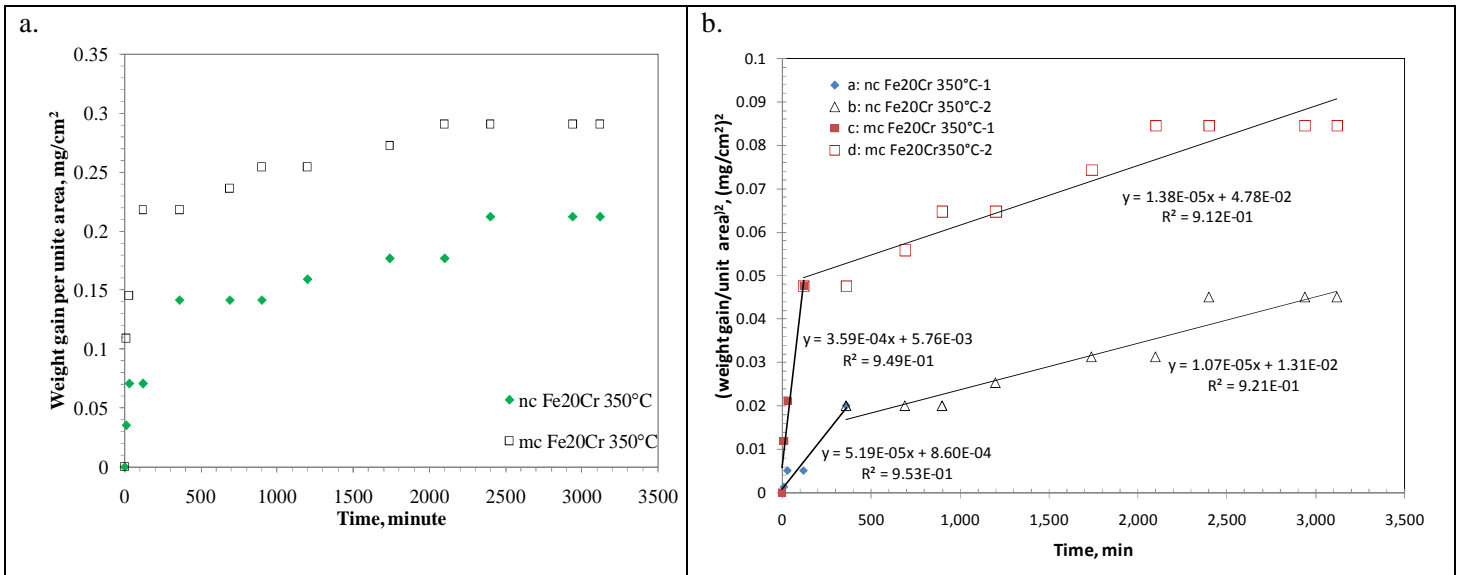


Fig. 3(Appendix B) kinetics of oxidation for nc and mc Fe20Cr alloy (a) weight gain vs oxidation time plot for nc and mc Fe20Cr alloy for a range of temperatures. (b) (Weight gain)² vs time plot for nc and mc Fe20Cr alloys for a range of temperature, there are two stages of oxidation distinguished by the parabolic rate constant and described as 1 and 2 in the above graph

Parabolic oxidation rate constants (k_p), obtained from the figures 1b, 2b and 3b are presented in Table 1.

Table 1 (Appendix C) Parabolic oxidation rate constants (k_p) values in $g^2 cm^{-4} s^{-1}$

	nc-Fe10Cr	mc- Fe10Cr	mc- Fe20Cr	nc-Fe20Cr
300°C	5.65×10^{-13} (1 st stage) and 7.42×10^{-14} (2 nd stage)	7.74×10^{-12}	--	--
350°C	1.04×10^{-12} (1 st stage) and 1.7×10^{-13} (2 nd stage)	1.46×10^{-10}	5.83×10^{-12} and 2.3×10^{-13}	8.65×10^{-13} and 1.72×10^{-13}
400°C	1.34×10^{-12} (1 st stage) and 5.69×10^{-13} (2 nd stage)	2.53×10^{-10}	--	--

Appendix C: Reproducibility of electrochemical corrosion data

Reproducibility of the electrochemical corrosion behaviour data as presented in Chapter 7 is presented in there:

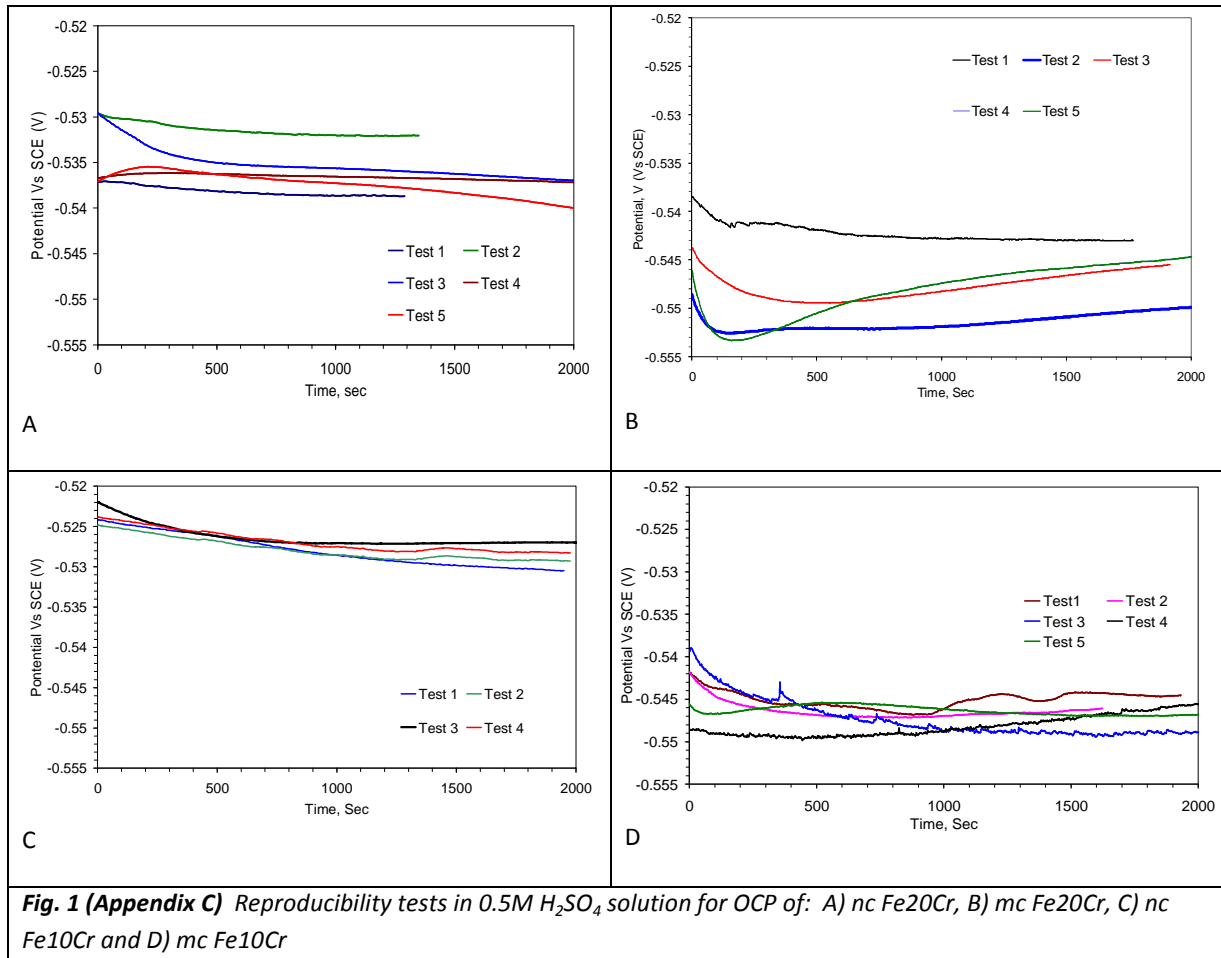
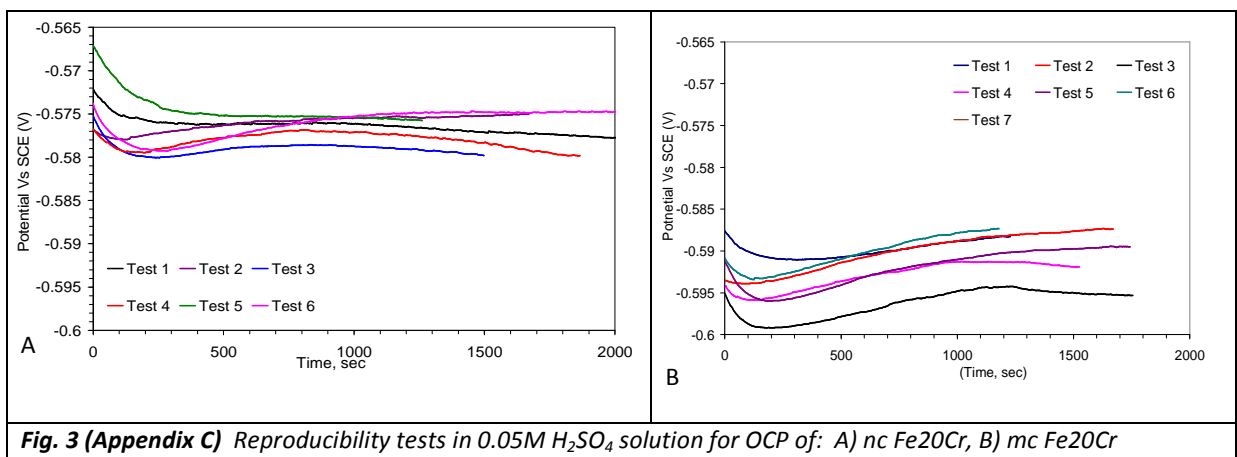
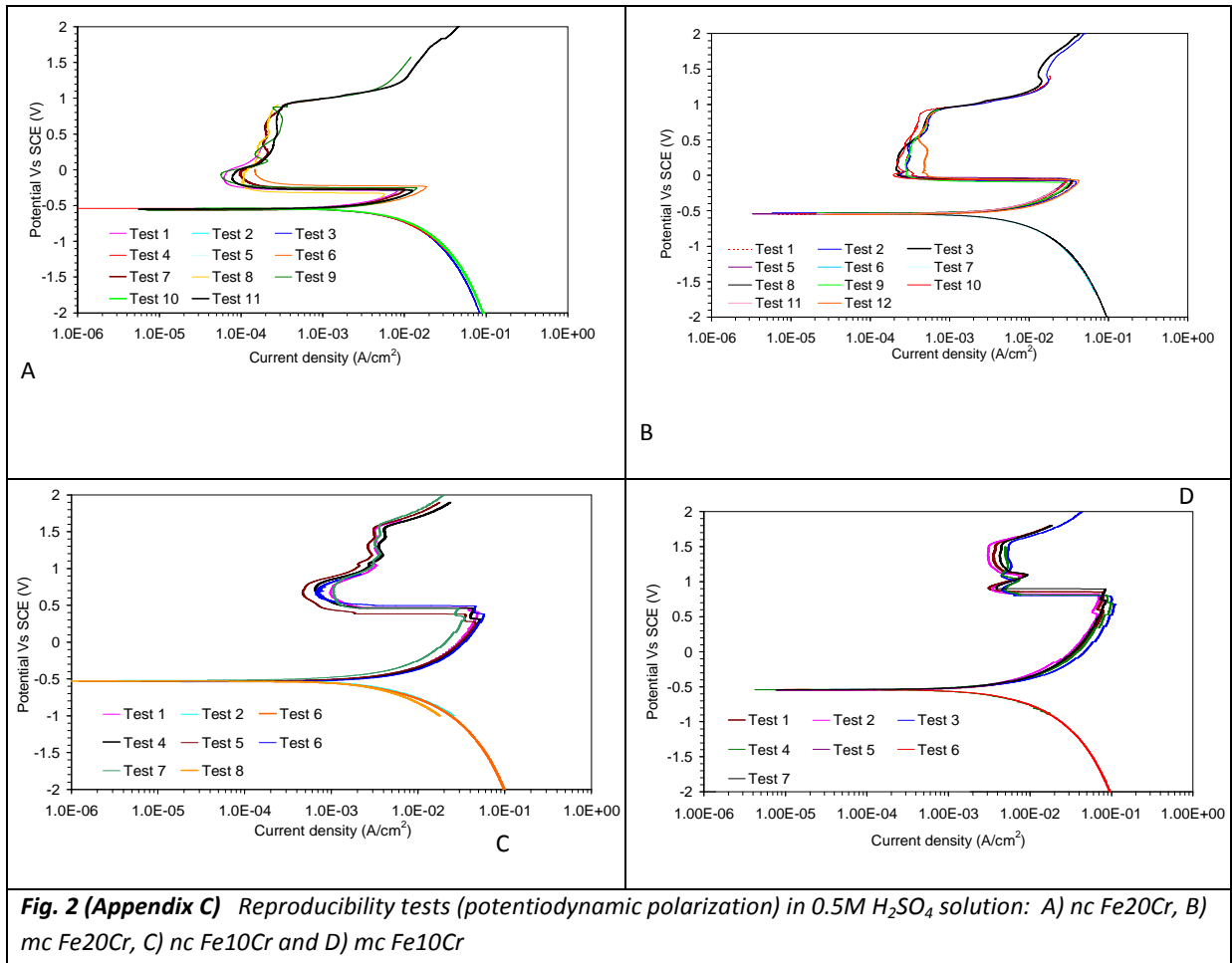
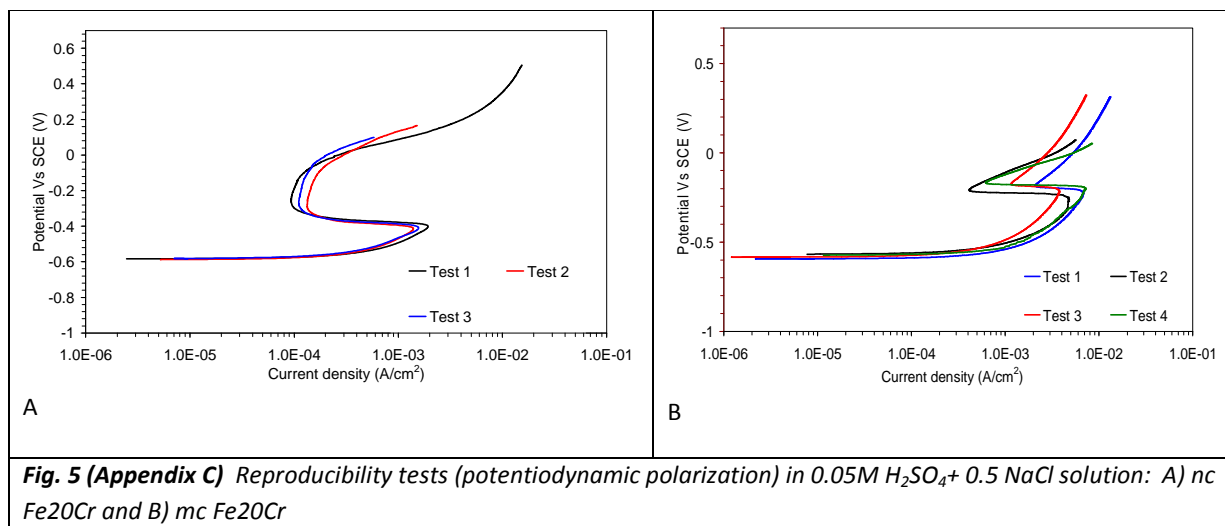
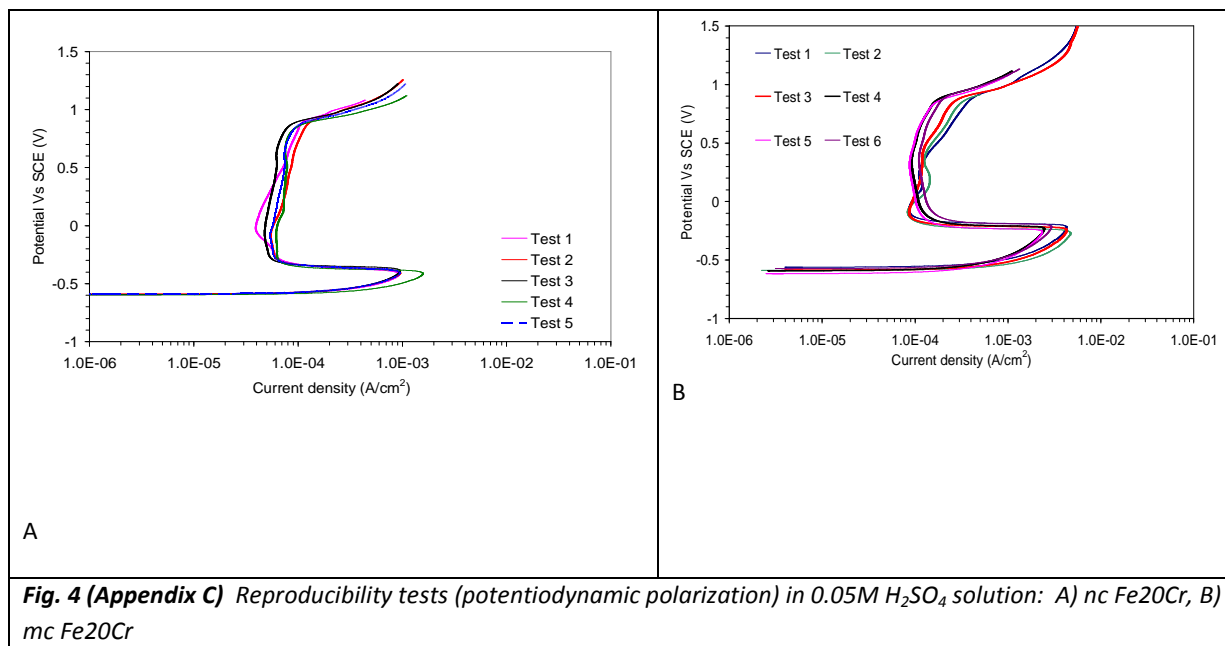


Fig. 1 (Appendix C) Reproducibility tests in 0.5M H_2SO_4 solution for OCP of: A) *nc Fe20Cr*, B) *mc Fe20Cr*, C) *nc Fe10Cr* and D) *mc Fe10Cr*





Appendix D: Attempts at in-situ consolidation

Nanocrystalline materials possess very less ductility which limits their real life application and processing of these novel materials. However, there are some debates whether loss of the ductility is an inherent property of nanocrystalline materials or a consequence of the artifacts introduced during processing. An in-situ consolidated nanocrystalline material may avoid the artifact and improve ductility, as shown in the case of nanocrystalline copper [366, 372, 373]

Some preliminary attempts were made to produce Fe-Cr based alloys using in-situ consolidation technique but it was not successful, probably because of the lack of ductility of Fe-Cr alloy system. Further in-situ consolidation was attempted with the addition of Ni which may stabilize austenitic phase and improve the ductility in the Fe-Cr-Ni alloy system.

There have been some initial successes in in-situ consolidation of Fe-20Cr-10Ni alloy. Elemental powders of Fe, Cr and Ni in appropriate proportion were ball-milled at room temperature for 15 hours followed by 3 hours of cryomilling. As shown in Figure 3a, in-situ consolidated small particles are obtained. A pressure of 8 tons was applied on these particles and they flatten into small discs (diameter=4 mm, thickness =0.5 mm) (Figure 3b), suggesting some ductility in the material. These discs can be useful to study mechanical properties and to make TEM samples for structural analysis of these materials

It was possible to prepare TEM samples from these small discs and the TEM investigations, carried out, have shown the grain size to be below 10 nanometers (Figure 4). Microhardness of the flat discs, as determined, was 7.8GPa (± 0.1)



Fig.1a (Appendix D) In-situ consolidated nc-Fe-20Cr-10Ni



Fig. 1b (Appendix D) After applying load of 12 tons

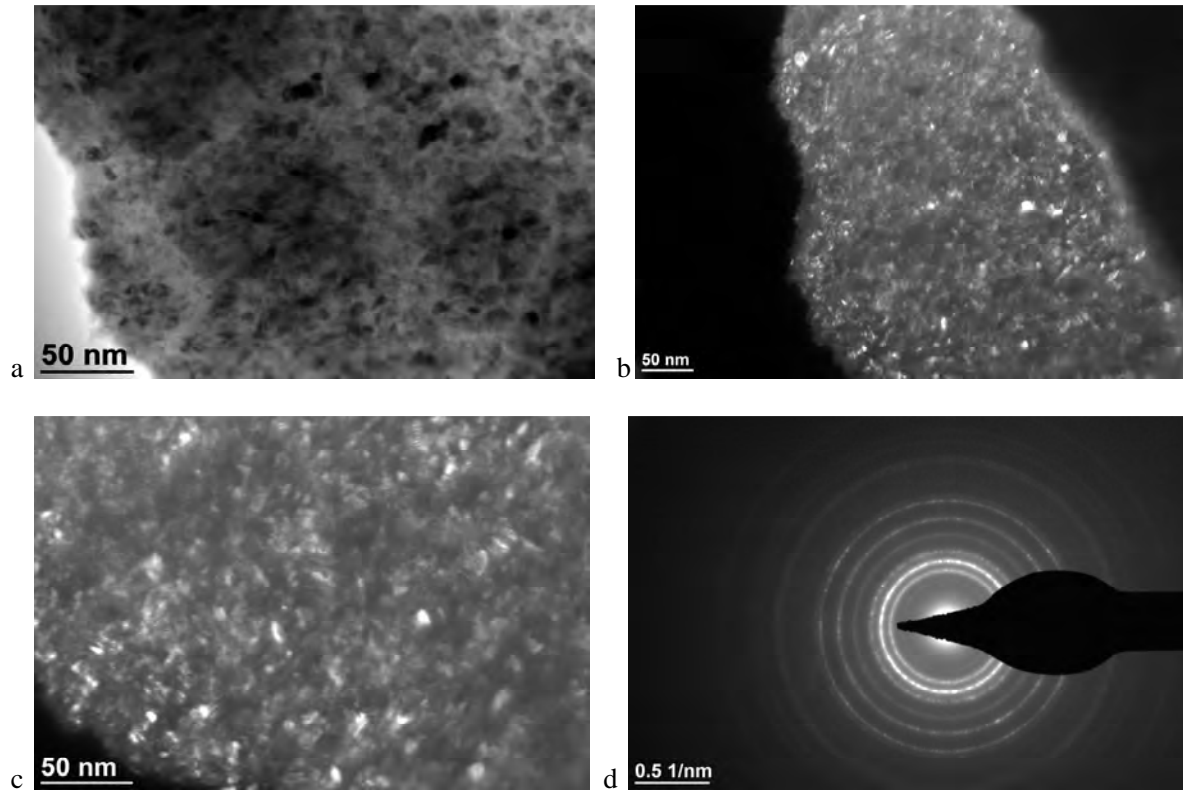


Fig.2 (Appendix D) TEM images of in-situ consolidated Fe20Cr10Ni alloy a) Bright field image, b) dark field image, c) dark field image of other region at higher magnification and d) selected area diffraction pattern